The History of Star Formation in Nearby Dwarf Galaxies

A DISSERTATION
SUBMITTED TO THE FACULTY OF THE GRADUATE SCHOOL
OF THE UNIVERSITY OF MINNESOTA
BY

Daniel Ray Weisz

IN PARTIAL FULFILLMENT OF THE REQUIREMENTS
FOR THE DEGREE OF
Doctor Of Philosophy

August, 2010

Acknowledgements

First, I want to thank my family. My parents and sister have provided me with unwavering support, despite not really understanding what I do. There is not much more one can ask of a family. I thank you for helping make this possible.

There are many people who have made my time in Minnesota fun and enriching. Some I have known for years, some I met only after returning. A special thanks to: Charles Eddleston, Richard Cargill, Daniel Kodet, Peter Bell, Erik Lundgren, Luke Anderson, Willie Ziegenhagen, Viktor Adamcseck, Pablo Viedma, Eric Singer, Ben Gaddis, and Sheila McGill.

I also thank the entire University of Minnesota astronomy department. The faculty, staff, and graduate students have made for a great environment in which to work toward my degree. Additionally, a number of professional astronomers have gone to great lengths to encourage, help, and advise me. Specifically, I would like to acknowledge the guidance of: Andy Dolphin, Julianne Dalcanton, Rob Kennicutt, Fabian Walter, John Cannon, and Henry Lee.

No one has been more important to my pursuit of a Ph.D. than my advisor Evan Skillman. Evan's infinite supply of patience (good thing I never had hard deadlines), good humor, and ability to see the bigger picture have greatly influenced my outlook and attitude toward astronomy. I have been tremendously fortunate to have had such a perfectly suited advisor.

Lastly, I acknowledge the support provided to me by the University of Minnesota and Russ Penrose. Their generous fellowships have allowed me to focus on my own research interests for my entirety of my graduate career.

Abstract

We present detailed analysis of color-magnitude diagrams (CMDs) of resolved stellar populations in nearby dwarf galaxies based on observations taken with the *Hubble Space Telescope* (HST). From the positions of individual stars on a CMD, we are able to derive the star formation histories (SFHs), i.e., the star formation rate (SFR) as a function of time and metallicity, of the observed stellar populations. Specifically, we apply this technique to a number of nearby dwarf galaxies to better understand the mechanisms driving their evolution.

The ACS Nearby Galaxy Survey Treasury program (ANGST) provides multi-color photometry of resolved stars in ~ 60 nearby dwarf galaxies from images taken with HST, This sample contains 12 dSph, 5 dwarf spiral, 28 dIrr, 12 dSph/dIrr (transition), and 3 tidal dwarf galaxies. The sample spans a range of ~ 10 in M_B and covers a wide range of environments, from highly interacting to truly isolated. From the best fit lifetime SFHs we find three significant results: (1) the average dwarf galaxy formed $\sim 60\%$ of its stars by z $\sim$ 2 and 70% of its stars by z $\sim$ 1, regardless of morphological type, (2) the only statistically significant difference between the SFHs of different morphological types is within the most recent 1 Gyr (excluding tidal dwarf galaxies), and (3) the SFHs are complex and the mean values are inconsistent with simple SFH models, e.g., single epoch SF or constant SFH. We find that an exponentially declining star formation model with $\tau \sim 6.4$ Gyr provides a reasonable representation of the mean SFHs. The dominance of the older stellar populations implies that the typical dwarf galaxy formed most of its stars at times similar to more massive galaxies. The sample shows a strong density-morphology relationship, i.e., the dSphs in the sample are less isolated than dIs. We find that the transition from a gas-rich to gas-poor galaxy cannot be solely due to internal mechanisms, e.g., stellar feedback, and is likely the result of external mechanisms, e.g., ram pressure and tidal stripping and tidal forces. The average transition dwarf galaxy is slightly less isolated and less gas-rich than the typical dwarf irregular. From a comparison between the ANGST and Local Group dwarf galaxy SFHs, we find consistency between the two samples, suggesting that the Local Group dwarf galaxies are a good representation of the broader universe. Both samples show a similarly strong

morphology-density relationship, further emphasizing the importance of environment in dwarf galaxy evolution.

We then present the recent ($\lesssim$ 1 Gyr) SFHs of nine M81 Group Dwarf Galaxies. Comparing the SFHs, birthrate parameters, fraction of stars formed per time interval, and spatial distribution of stellar components as a function of luminosity, we find only minor differences in SF characteristics among the M81 Group dIs despite a wide range of physical properties. We extend our comparison to select dIs in the Local Group (LG), with similar quality photometry, and again find only minor differences in SF parameters. The lack of a clear trend in SF parameters over a wide range of diverse environments suggests that SF in low mass systems may be dominated by stochastic processes. The fraction of stars formed per time interval for an average M81 Group and LG dI is consistent with a constant SFH. However, individual galaxies can show significant departures from a constant SFH. Thus, we find this result underlines the importance of stochastic SF in dIs. In addition to a statistical comparison, we examine possible formation scenarios of the less luminous and candidate tidal dwarfs in the M81 Group. The SFHs and the lack of an overdensity of associated red stars suggest that the Garland and Ho IX are not dIs and are potentially tidal dwarf galaxies. Interestingly, a noteworthy difference between the LG and the M81 Group is the lack of tidal dwarf candidates in the LG.

Comparing the recent SFHs and spatial locations of young stars with observations of the neutral interstellar medium (HI), we are able to gain new insight into the physics of stellar 'feedback'. We first make this type of comparison in IC 2754, a luminous dwarf irregular galaxy in the M81 Group with a $\sim$ 1 kpc supergiant HI shell. We find two significant episodes of SF inside the SGS from $200 - 300$ Myr and $\sim$ 25 Myr ago. Comparing the timing of the SF events to the dynamic age of the SGS and the energetics from the HI and SF, we find compelling evidence that stellar feedback is responsible for creating the SGS and triggering secondary SF around its rim.

We then conduct an extensive analysis of HI holes in M81 Group dwarf irregular galaxy, Holmberg II. From the deep photometry, we construct the CMDs and measure the SFHs for stars contained in HI holes from two independent holes catalogs, as well as select control fields, i.e., similar sized regions that span a range of HI column densities. The CMDs reveal young ($<$ 200 Myr) stellar populations inside all HI holes, which

contain very few bright OB stars with ages less than 10 Myr, indicating they are not reliable tracers of HI hole locations while the recent SFHs confirm multiple episodes of star formation within most holes. Converting the recent SFHs into stellar feedback energies, we find that enough energy has been generated to have created all holes. However, the required energy is not always produced over a time scale that is less than the estimated kinematic age of the hole. A similar analysis of stars in the control fields finds that the stellar populations of the control fields and HI holes are statistically indistinguishable. However, because we are only sensitive to holes $\sim$ 100 pc in diameter, we cannot tell if there are smaller holes inside the control fields. The combination of the CMDs, recent SFHs, and locations of young stars shows that the stellar populations inside HI holes are not coherent, single-aged, stellar clusters, as previously suggested, but rather multi-age populations distributed across each hole. From a comparison of the modeled and observed integrated magnitudes, and the locations and energetics of stars inside of HI holes, we propose a potential new model: a viable mechanism for creating the observed HI holes in Ho II is stellar feedback from multiple generations of SF spread out over tens or hundreds of Myr, and thus, the concept of an age for an HI hole is intrinsically ambiguous. For HI holes in the outer parts of Ho II, located beyond the HST/ACS coverage, we use Monte Carlo simulations of expected stellar populations to show that low level SF could provide the energy necessary to form these holes. Applying the same method to the SMC, we find that the holes that appear to be void of stars could have formed via stellar feedback from low level SF. We further find that Hα and 24μm emission, tracers of the most recent star formation, do not correlate well with the positions of the HI holes. However, UV emission, which traces star formation over roughly the last 100 Myr, shows a much better correlation with the locations of the HI holes.

Contents

List of Tables

List of Figures

Chapter 1

Introduction

1.1 Background

1.1.1 The Study of Galaxies

It nearly a century ago that galaxies were 'discovered' by Edwin Hubble. Hubble's realization that the bright nebulous objects he was observing may reside outside our own galaxy was truly revolutionary (Hubble, 1926). Since that time, the study of galaxy formation and evolution has grown tremendously. We now have cataloged photometric and spectral images of millions of galaxies both near and far (e.g., SDSS; Blanton et al., 2001).

Roughly speaking, galaxies are masses of dark matter, littered with small amounts of baryonic matter such as gas and stars. Because dark matter only interacts gravitationally, we are forced to infer much about the existence, composition, and evolution of galaxies from the trace amount of luminous matter, e.g., stars and gas, which we can observe.

The study of luminous matter has led to an impressive amount of insight into both the origin and evolution of galaxies and the universe as a whole. For example, within the past 15 years, exploding stars in distant galaxies have taught us that the universe is not only expanding, but also that its expansion is accelerating (e.g., Schmidt et al., 1998; Perlmutter et al., 1998) . The study of star formation in galaxies has also revealed much about how the universe has evolved since its origin 13.7 billion years ago. By

measuring the intensity of star formation in large number of galaxies, we now know that, on average, galaxies are currently forming stars with much less gusto than even a few billion years ago (e.g., Madau et al., 1996; Reddy et al., 2008). The universe would have looked very different to our telescopes only a few billion years ago!

Much of what we can infer about most galaxies in the universe is founded upon our detailed knowledge of nearby galaxies. Most galaxies are sufficiently far away that they appear unresolved, i.e., we cannot see individual features (much like the headlights of a distant car appear to be one light). However, the close proximity of nearby galaxies allows us to resolve individual stellar and gaseous components, allowing for highly detailed studies. Our understanding of the physics governing nearby galaxies can then be extrapolated to interpret observations of more distant galaxies (e.g., Leitherer et al., 1999).

The research presented in this thesis is focused on advances in understanding these nearby galaxies, specifically dwarf galaxies. The information provided in §1.1 is to give context for the more technical research presented in the subsequent sections. The amount of historical information on nearby galaxies is seemingly infinite. While the present text does not try to capture this rich history, it does aim to paint of picture of galaxies in the local universe which will (hopefully) help the reader understand the significance of the presented research.

1.1.2 The Importance of Dwarf Galaxies

Dwarf galaxies are the smallest, most common galaxy in the universe. With typical masses $\sim 10^3$–10^5 times less than those of normal spirals or ellipticals, dwarf galaxies typical outnumber their massive brethren several dozen (or more) to one (e.g., Karachentsev et al., 2004). In the hierarchical model of galaxy assembly, larger and more metal rich galaxies were primarily built by the merger of small satellite (dwarf) galaxies. The low masses and nearly pristine chemical composition of dwarf galaxies we see today make them the best known analogs to the building blocks of larger galaxies from the early universe.

Dwarf galaxies are relatively dynamically simple systems, which allows us to study the interaction between gas and stars, a process of fundamental importance to all of galaxy evolution. For example, dwarf irregular galaxies, those with recent star formation

and/or an appreciable level of neutral hydrogen (the raw material from which stars form), are solid body rotators (Skillman, 1996, e.g.,). That is, the stars and gas rotate in unison, without the complication of spiral density waves or sheer seen in larger galaxies. This property means that we can study both current and more evolved sites of star formation, which provides the opportunity for a complete picture of the physics and evolution of star-gas interactions (e.g., Dohm-Palmer et al., 1997; Weisz et al., 2009).

In brief, dwarf galaxies are exemplary laboratories for studying the fundamental processes driving both star formation and the evolution of galaxies.

1.1.3 The Role of Nearby Galaxies

By virtue of their low stellar masses, dwarf galaxies are quite faint. Detecting dwarf galaxies analogous to those seen in the immediate vicinity of the Milky Way, i.e., the Local Group, is quite challenging. To date, there does not exist a catalog of observed dwarf galaxies of comparable completeness to the Local Group. Thus, the study of dwarf galaxies is inherently limited to the nearby universe.

The distance limitation to studying nearby dwarf galaxies has both drawbacks and advantages. On one hand, we can observe the integrated light, i.e., the sum of all fluxes in a given filter, for distant galaxies. This allows us to directly measure *in situ* star formation of galaxies at different redshift. While this type of observation is both accessible and contains information about a galaxy, it does not allow a precise resolution of the history of star formation or a detailed study of interactions between individual stars and the surrounding gas.

In contrast, nearby galaxies provide us the opportunity to resolve their individual stars. Because every episode of star formation in a galaxy leaves an imprint on the stellar record, examining the resolved stellar populations of a galaxy is akin to looking at its fossil record. From this type of stellar archaeology, we can extract information about star formation over the history of a galaxy.

Photometric observations of individual stars allow them to be placed on a color-magnitude diagram (CMD), the fundamental unit used for understanding the stellar evolution of individual stars. By knowing the location of a star on a CMD, we can determine its age. Thus, by taking a census of all the individual stars with known ages in a galaxy, we can understand the history of star formation, and hence an important

evolutionary component, of that galaxy. The precise methodology is more rigorous than described here, and is detailed in §4.3.

1.1.4 The History of Star Formation in Nearby Dwarf Galaxies

The work presented in this thesis is based upon high spatial resolution observations of individual stars using images taken with the *Hubble Space Telescope*. From these images, we can place individual stars on a CMD and determine the star formation histories (SFHs) of nearby galaxies.

The SFHs can then be used to better understand the physics of star formation and the evolution of galaxies. In this thesis, I examine a number of related topics using the largest data set of nearby galaxies of its kind (Dalcanton et al., 2009). For example, I am able to address differences in the evolutionary histories of gas-rich and gas-poor dwarf galaxies – what drove some dwarf galaxies to lose all their gas and stop forming stars, while others have a gas supply that could allow them to form stars for billions of years? On a smaller scale, by comparing detailed accounts of star formation as a function of time and location, with the distribution of the surrounding gas supply, I am able to place constraints on the physics of star-gas interactions,. The work presented in this thesis is only a sampling of the new insight that can be gained into fundamental astrophysics by studying resolved stellar populations.

Chapter 2

Evidence for the Importance of Environment from the Global Star Formation Histories of 60 Dwarf Galaxies in the Local Volume

2.1 Introduction

Dwarf galaxies have come to play an increasingly important role in understanding how galaxies form and evolve. As the smallest, least luminous, and most common systems in the universe, dwarf galaxies span a wide range in physical characteristics and occupy a diverse set of environments (e.g., Mateo, 1998; van den Bergh, 2000; Karachentsev et al., 2004), making them excellent laboratories for direct studies of cause and effect in galaxy evolution. The low average masses and metallicities of dwarf galaxies suggest they may be the best available analogs to the seeds of hierarchical galaxy formation in the early universe.

Differences in the ancient patterns of star formation (SF) between high and low mass galaxies may be consistent with the 'downsizing' theory of galaxy formation

(e.g., Cowie et al., 1996; Thomas et al., 2005). Dwarf galaxies have also been considered as a potential solution for the faint blue galaxy problem (e.g., Babul & Ferguson, 1996; Ellis, 1997; Wyder, 2001; Skillman et al., 2003b), could also provide evidence of the impact of the re-ionization on SF in the early universe (e.g., Efstathiou, 1992; Navarro & Steinmetz, 1997; Dijkstra et al., 2004; Gnedin, 2000; Cole et al., 2007), and may hold clues to understanding gas accretion mechanisms for massive galaxies (e.g., Sancisi et al., 2008; Kauffmann et al., 2010).

A cohesive picture of the evolution of dwarf galaxies remains elusive. Historically, evolutionary scenarios have often been considered in the context of a dual morphological classification, namely dwarf spheroidals (dSphs; we include dwarf ellipticals in this general category) or dwarf irregulars (dIs), of which the latter exhibit current/recent SF activity and have a high gas fraction, and the former has neither gas nor significant levels of recent SF. So-called 'transition' dwarf galaxies, which have a high gas fraction yet little to no recent SF activity (e.g., Mateo, 1998; Miller et al., 2001; Dolphin et al., 2005; Young et al., 2007; Dellenbusch et al., 2008), may serve as an evolutionary link between dIs and dSphs (e.g., Grebel et al., 2003) or simply could be in between massive star forming events (e.g., Skillman et al., 2003a). Understanding the relationship between these three types of dwarf galaxies, specifically determining if and how dIs evolve into dSphs, is among the most pressing questions in dwarf galaxy evolution (e.g., Dekel & Silk, 1986; Binggeli, 1986; Skillman & Bender, 1995; Mateo, 1998; Dekel & Woo, 2003; Grebel et al., 2003; Mayer et al., 2006).

Resolved stellar populations have proven to be an incredibly powerful tool in observationally constraining scenarios of dwarf galaxy evolution. Past patterns of SF and chemical evolution are encoded in a galaxy's optical color-magnitude diagram (CMD), and a number of sophisticated algorithms (e.g., Tosi et al., 1989; Tolstoy & Saha, 1996; Gallart et al., 1996; Mighell, 1997; Holtzman et al., 1999; Hernandez et al., 1999; Harris & Zaritsky, 2001; Dolphin, 2002; Ikuta & Arimoto, 2002; Cole et al., 2007; Yuk & Lee, 2007; Aparicio & Hidalgo, 2009; Cignoni & Tosi, 2010) have been developed to measure the star formation history (SFH), i.e., the star formation rate (SFR) as a function of time and metallicity, by comparing observed CMDs with those generated from models of stellar evolution. The robustness of this method has become increasingly solidified with a variety of techniques and stellar models converging on consistent solutions for a range

of galaxies (e.g., Skillman & Gallart, 2002; Skillman et al., 2003b; Gallart et al., 2005; Monelli et al., 2010).

The resultant CMD-based SFHs have become particularly prevalent in understanding the formation and evolution of the Local Group (LG). The LG contains $\sim$ 50 dwarf galaxies ranging from highly isolated to strongly interacting (e.g., Mateo, 1998; van den Bergh, 2000; Tolstoy et al., 2009). Results from CMD-based SFHs of dwarf galaxies in the LG have revealed that both dSphs and dIs feature complex SFHs, typically with dominant stellar components older than 10 Gyr (e.g., Hodge, 1989; Grebel, 1997; Mateo, 1998; Dolphin et al., 2005). The SFHs of individual LG dwarf galaxies as well as aggregate compilations now serve as the basis for our understanding of the evolution of dwarf galaxies and have significantly advanced our knowledge of galactic group dynamics (e.g., Orban et al., 2008; Tolstoy et al., 2009; Mayer, 2010).

Beyond the LG, only a small subset of dwarf galaxies have explicitly measured CMD-based SFHs (e.g., Dolphin et al., 2003; Weisz et al., 2008; McQuinn et al., 2009, 2010a). Ground based observations of resolved stellar populations in more distant galaxies are challenging due to the need for longer exposure times and the effects of photometric crowding. However, observations from the Hubble Space Telescope (HST), particularly the Advanced Camera for Surveys (ACS; Ford et al., 1998), have revolutionized the field of resolved stellar populations, producing stunning CMDs of dwarf galaxies both in and beyond the LG. Outside the LG, HST observations of resolved stellar populations have been fairly piecemeal, with individual or small sets of galaxies the typical targets, and subsequent analysis often employing different methodologies or seeking different science goals. This also makes it challenging to place the results from LG studies in the context of the broader universe, as LG dwarf galaxies may not be representative of the typical universe (e.g., van den Bergh, 2000).

The ACS Nearby Galaxy Survey Treasury (ANGST; Dalcanton et al., 2009) was designed to help remedy this situation. Using a combination of new and archival imaging taken with the HST/ACS and Wide Field Planetary Camera 2 (WFPC2; Holtzman et al., 1995), ANGST provides a uniformly reduced, multi-color photometric database of the resolved stellar populations of nearby galaxies (D $\lesssim$ 4 Mpc) that are strictly outside the LG. Of the $\sim$ 70 galaxies in this sample, 60 are dwarf galaxies that span a range of $\sim$ 10 in M_B and reside in both isolated field and strongly interacting

group settings, providing an unbiased statistical sample in which to study the detailed properties dwarf galaxy formation and evolution.

In this paper, we present the uniformly analyzed SFHs of 60 dwarf galaxies based on observations, photometry, and artificial star tests produced by the ANGST program. The focus of this study is on the lifetime SFHs of the sample galaxies, with the recent (< 1 Gyr) SFHs the subject of a separate paper (D. Weisz et al., In Prep). We first briefly review the sample selection, observations, and photometry in §2.2. We then summarize the technique of measuring SFHs in §2.3. In §2.4, we discuss and compare the resultant SFHs in the context of both dwarf galaxy formation and evolution. We then explore our results with respect to the morphology–density relationship in §2.5. Cosmological parameters used in this paper assume a standard WMAP cosmology as detailed in Dunkley et al. (2009).

2.2 The Data

In this section, we briefly summarize the selection of the ANGST dwarf galaxy sample along with the observations and photometry. A more detailed discussion of the ANGST program can be found in Dalcanton et al. (2009).

2.2.1 Selection and Final Sample

We constructed the initial list of ANGST galaxies based on the Catalog of Neighboring Galaxies (Karachentsev et al., 2004), consisting exclusively of galaxies located beyond the zero velocity surface of the LG (van den Bergh, 2000). We selected potential targets with $|b| > 20^\circ$ to avoid observational difficulties associated with low Galactic latitudes. By simulating CMDs and crowding limits, we found that a maximum distance of $\sim$ 3.5 Mpc provides the optimal balance between observational efficiency and achieving the program science goals. Because the sample of galaxies within 3.5 Mpc contains predominantly field galaxies, we chose to extend the distance limits in the direction of the M81 Group. This added to the diversity of galaxies in the sample, while maintaining the goal of observational efficiency, due to the M81 Group's close proximity to the distance limit ($D_{M81} \sim 3.6$ Mpc) and low foreground extinction values. Similarly, we also included galaxies in the direction of the NGC 253 clump ($D_{N253} \sim 3.9$ Mpc) in the

Sculptor Filament (Karachentsev et al., 2003).

The final sample of ANGST dwarf galaxies in this paper is composed of 60 galaxies, from both new and comparable quality archival imaging. They range in M_B from -8.23 (KK 230) to -17.77 (NGC 55) and in distance from 1.3 Mpc (Sex A) to 4.6 Mpc (DDO165). The upper mass/luminosity cutoff for what constitutes a dwarf galaxy is somewhat ambiguous. For example, Mateo (1998) chose to exclude the LMC ($M_B = -17.93$) and SMC ($M_B = -16.35$) from the 'dwarfs' category. Similarly, we have included most galaxies considered dwarf galaxies in the literature in our analysis. However, analogous to Mateo (1998), we have not included NGC 3077 ($M_B = -17.44$), NGC 2976 ($M_B = -16.77$), and NGC 300 ($M_B = -17.66$), which would be among the brightest and most massive galaxies in the sample. Detailed studies of the SFHs of NGC 2976 (Williams et al., 2010) and NGC 300 (Gogarten et al., 2010) are available in the literature. A full list of sample galaxies and their properties are shown in Table 2.1 and Figure 2.1.

Although the sample of ANGST dwarf galaxies is extensive, it is not complete. Galaxies at low galactic latitudes have been intentionally excluded to avoid complications associated with high degrees of reddening. While SFHs can still be derived from CMD of such galaxies (e.g., McQuinn et al., 2009, 2010a), the effects of extreme reddening can lead to larger uncertainties and can require special analysis techniques (e.g., individual stellar line of sight reddening corrections), which detracts from a uniform approach to the data. In addition there have been a number of recently discovered dwarf galaxies in the M81 Group (Chiboucas et al., 2009), which have are not in the ANGST sample. Further, the ANGST sample does not include faint dwarf spheroidals (dSphs) which are likely located in close proximity to M81, i.e., analogs to Milky Way satellites such as Draco and Ursa Minor, but have yet to be detected due to their inherent faintness.

In this paper, we initially divide the sample of dwarf galaxies according to morphological type (de Vaucouleurs et al., 1991; Karachentsev et al., 2004), T, resulting in 12 dwarf galaxies with $T \leq 0$ (dwarf spheroidals), 5 with $T = 8$ or 9 (dwarf spirals; dSpirals), and 45 with $T = 10$ (dwarf irregulars; dIs). We have adopted nomenclature consistent with Mateo (1998), in which true dEs (e.g., NGC 147, NGC 185) are found to be rare, and dSphs are more common. Among the dIs, there could be some

ambiguity between bright dIs and dSpirals. For consistency, we defer to the T type morphological classification scheme, but note that the distinction between a bright dI and dSpiral is not always clear. Morphological type $T = 10$ further includes transition dwarf galaxies (dTrans), galaxies with reduced recent star formation but high gas fractions, and tidal dwarf galaxy candidates (dTidals), which appear to be condensing out of tidally disturbed gas. We classify subtypes, i.e., dTidal and dTrans, as follows: the three dTidals are Holmberg IX, A0952+069, and BK3N, all located in the M81 Group. For dTrans, we adopt the definition of Mateo (1998), namely, that a galaxy has $M_{HI}/L_B > 0.1$ and very little or no Hα flux. The final sample of dTrans has been drawn from HI and Hα measurements in the literature (Côté et al, 1997; Skillman et al., 2003a; Karachentsev et al., 2004; Karachentsev & Kaisin, 2007; Begum et al., 2008; Bouchard et al., 2009; Côté et al., 2009). We find 12 ANGST dwarf galaxies that satisfy the dTrans criteria: KK 230, Antlia, KKR 25 KKH 98, KDG 73, ESO294-10, ESO540-30, ESO540-32, KDG 52, ESO410-005, DDO 6, and UGCA 438, leaving the final tally of true dIs at 28.

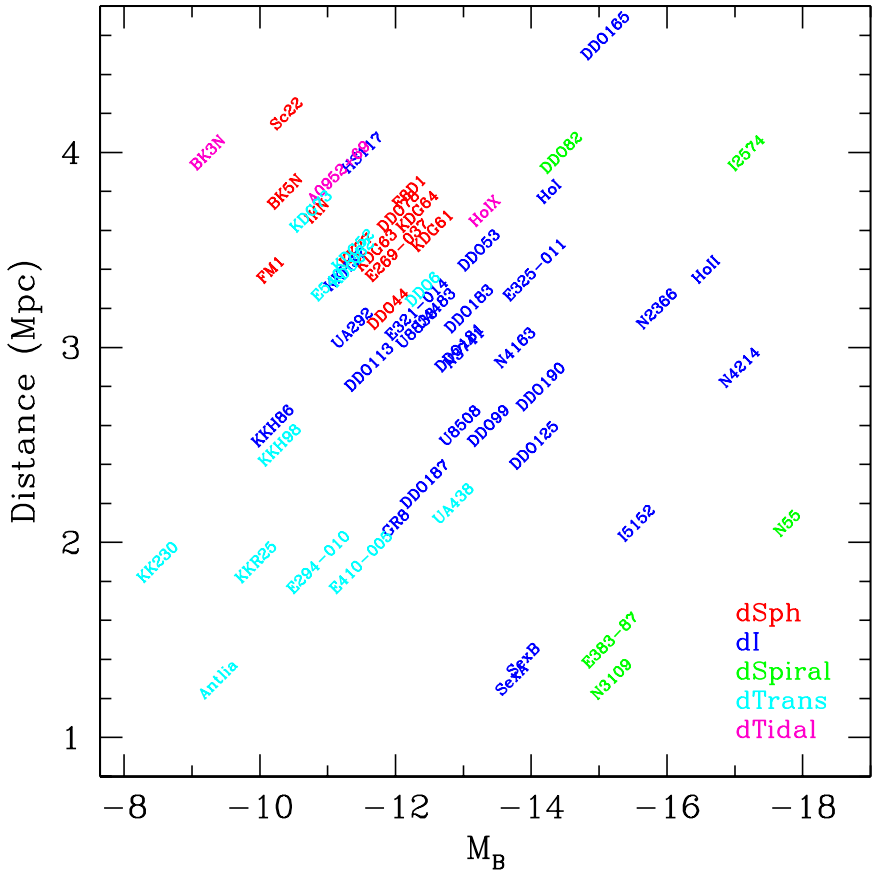

Figure 2.1 Distribution of the ANGST sample of dwarf galaxies in distance and M_B. Galaxies are color coded by morphological type: dSphs (red; T < 0), dIs (blue; T = 10), dSpirals (green; T = 8,9), dTrans (cyan; T = 10), and dTidals (magenta; T = 10) (de Vaucouleurs et al., 1991; Karachentsev et al., 2004). dTidals and dTrans have been identified based on previous literature analysis (see §2.2.1). We note there is likely some ambiguity in the classification of bright dIs and dSpirals (see §2.2.1).

Table 2.1: Properties of ANGST Dwarf Galaxies.

Galaxy Name (1)	Main Disturber (2)	M_B 3)	D (Mpc) (4)	A_V (5)	T (6)	Θ (7)	Optical Coverage Fraction (8)	Filters (9)	M_{F814W} 50% Comp. (mag) (10)	HST Proposal ID (11)
KK230	M31	-8.49	1.3	0.04	10	-1.0	12.0	F606W,F814W	0.62	9771
BK3N	M81	-9.23	4.0	0.25	10	1.0	18.0	F475W,F814W	-0.32	10915
Antlia	M31	-9.38	1.3	0.24	10	-0.1	1.20	F606W,F814W	1.75	10210
KKR25	M31	-9.94	1.9	0.03	10	-0.7	2.50	F606W,F814W	-0.18	11986
F6D1	M82	-10.16	3.4	0.24	-3	1.8	5.00	F606W,F814W	0.11	9884
KKH86	N5128	-10.19	2.6	0.08	10	-1.5	5.20	F606W,F814W	-1.3	11986
KKH98	M31	-10.29	2.5	0.39	10	-0.7	5.40	F475W,F814W	0.46	10915
BK5N–CENTRAL	N3077	-10.37	3.8	0.20	-3	2.4	7.60	F606W,F814W	-0.77	6964
BK5N–OUTER								F606W,F814W	-0.70	5898
Sc22	N253	-10.39	4.2	0.05	-3	0.9	5.70	F606W,F814W	0.30	10503
KK127	M31	-10.59	1.5	0.06	10	-0.8	4.53	F606W,F814W	-1.95	11986
KDG73	M81	-10.75	3.7	0.06	10	1.3	12.0	F475W,F814W	-0.38	10915
IKN	M81	-10.84	3.7	0.18	-3	2.7	0.58	F606W,F814W	-0.82	9771
E294-010	N55	-10.86	1.9	0.02	-3	1.0	4.60	F606W,F814W	1.80	10503
A0952+69	N3077	-11.16	3.9	0.26	10	1.9	1.20	F475W,F814W	-0.23	10915
E540-032	N253	-11.22	3.4	0.06	-3	0.6	2.30	F606W,F814W	0.10	10503
KKH37	I342	-11.26	3.4	0.23	10	-0.3	3.70	F475W,F814W	0.12	10915
E540-030	N253	-11.29	3.4	0.07	-1	0.4	2.70	F606W,F814W	0.32	10503
UA292	N4214	-11.36	3.1	0.05	10	-0.4	5.10	F475W,F814W	-0.37	10915
KDG52	M81	-11.37	3.5	0.06	10	0.7	2.30	F555W,F814W	0.37	10605
KK77	M81	-11.42	3.5	0.44	-3	2.0	0.83	F606W,F814W	0.28	9884
E410-005	N55	-11.49	1.9	0.04	-1	0.4	2.80	F606W,F814W	1.70	10503
HS117	M81	-11.51	4.0	0.36	10	1.9	2.70	F606W,F814W	-0.81	9771
DDO113	N4214	-11.61	2.9	0.06	10	1.6	1.80	F475W,F814W	0.08	10915
KDG63	M81	-11.71	3.5	0.30	-3	1.80	1.40	F606W,F814W	0.31	9884
DDO44	N2403	-11.89	3.2	0.13	-3	1.7	0.59	F475W,F814W	0.16	10915
GR8	M31	-12.00	2.1	0.08	10	-1.2	3.30	F475W,F814W	0.82	10915
E269-37	N4945	-12.02	3.5	0.44	-3	1.6	3.80	F606W,F814W	-1.8	11986

DDO78	M81	-12.04	3.7	0.07	-3	1.8	0.95	F475W,F814W	-0.27	10915
F8D1–CENTRAL	M81	-12.20	3.8	0.33	-3	3.8	0.84	F555W,F814W	-0.77	5898
F8D1–OUTER								F606W,F814W	-0.90	5898
U8833	N4736	-12.31	3.1	0.04	10	-1.4	5.00	F606W,F814W	-0.23	10210
E321-014	N5128	-12.31	3.2	0.29	10	-0.3	2.20	F606W,F814W	-0.84	8601
KDG64	M81	-12.32	3.7	0.17	-3	2.5	1.10	F606W,F814W	0.57	11986
DDO6	N253	-12.40	3.3	0.05	10	0.5	3.00	F475W,F814W	-0.02	10915
DDO187	M31	-12.43	2.3	0.07	10	-1.3	1.60	F606W,F814W	0.40	10210
KDG61	M81	-12.54	3.6	0.23	-1	3.9	1.10	F606W,F814W	0.33	9884
U4483	M81	-12.58	3.2	0.11	10	0.5	2.20	F555W,F814W	-1.36	8769
UA438	UA438	-12.85	2.2	0.05	10	-0.7	1.00	F606W,F814W	-1.7	8192
DDO181	M81	-12.94	3.0	0.02	10	-1.3	1.20	F606W,F814W	-0.31	10210
U8508	M81	-12.95	2.6	0.05	10	-1.0	2.10	F475W,F814W	0.39	10915
N3741	M81	-13.01	3.0	0.07	10	-0.8	1.60	F475W,F814W	-0.24	10915
DDO183	N4736	-13.08	3.2	0.05	10	-0.8	2.30	F475W,F814W	-0.46	10915
DDO53	M81	-13.23	3.5	0.12	10	0.7	1.60	F555W,F814W	-0.05	10605
HoIX	M81	-13.31	3.7	0.24	10	3.3	0.71	F555W,F814W	0.13	10605
DDO99	N4214	-13.37	2.6	0.08	10	-0.5	0.58	F606W,F814W	-0.95	10210
SexA	MW	-13.71	1.3	0.14	10	-0.6	0.06	F555W,F814W	0.80	7496
N4163	N4190	-13.76	3.0	0.06	10	0.1	1.20	F475W,F814W	-0.04	10915
SexB	MW	-13.88	1.4	0.10	10	-0.7	0.10	F606W,F814W	0.04	11986
DDO125	N4214	-14.04	2.5	0.06	10	-0.9	0.18	F606W,F814W	-1.3	11986
E325-11	N5128	-14.05	3.4	0.29	10	1.1	0.52	F606W,F814W	-0.58	11986
DDO190	M81	-14.14	2.8	0.04	10	-1.3	1.20	F475W,F814W	-0.01	10915
HoI	M81	-14.26	3.8	0.15	10	1.5	0.34	F555W,F814W	0.23	10605
DDO82	M81	-14.44	4.0	0.13	9	0.9	0.53	F475W,F814W	-0.32	10915
DDO165	N4236	-15.09	4.6	0.08	10	0.0	0.50	F555W,F814W	-0.7	10605
E383-87	MW	-15.16	1.5	0.24	8	-0.8	0.11	F606W,F814W	-2.14	11986
N3109-DEEP	Antlia	-15.18	1.3	0.20	9	-0.1	0.05	F606W,F814W	0.50	10915
N3109-WIDE2							0.05	F606W,F814W	0.09	11307
I5152	M31	-15.55	2.1	0.08	10	-1.1	0.10	F606W,F814W	-1.38	11986
N2366–1	N2403	-15.85	3.2	0.11	10	1.0	0.39	F555W,F814W	-0.16	10605
N2366–2							0.39	F555W,F814W	-0.05	10605

Ho II–1	M81	-16.57	3.4	0.10	10	0.6	0.12	F555W,F814W	-0.32	10605
Ho II–2							0.12	F555W,F814W	-0.21	10605
N4214	DDO113	-17.07	2.9	0.07	10	-0.7	0.03	F606W,F814W	-0.48	11986
I2574–SGS	M81	-17.17	4.0	0.11	9	0.9	0.05	F555W,F814W	-0.26	9755
I2574–1							0.05	F555W,F814W	-0.55	10605
I2574–2							0.05	F555W,F814W	-0.15	10605
N55–CENTRAL	N300	-17.77	2.1	0.04	8	0.4	0.01	F606W,F814W	-1.55	9765
N55–DISK							0.01	F606W,F814W	-0.42	9765

Throughout this paper, we adopt the tidal index, Θ (Karachentsev et al., 2004) as a measure of a galaxy's isolation. Θ describes the local mass density around galaxy i as:

$$\Theta_i = max[log(M_K/D_{ik}^3)] + C, i = 1, 2, \cdots, N \tag{2.1}$$

where M_k is the total mass of any neighboring galaxy separated from galaxy i by a distance of D_{ik}. The values of Θ we use in this paper have been taken from Karachentsev et al. (2004). Negative values correspond to more isolated galaxies, and positive values represent typical group members (see Table 2.1).

2.2.2 Observations and Photometry

HST observations of new ANGST targets were carried out in two phases due to the failure of ACS in 2007. Prior to the failure, we observed new targets using ACS with WFPC2 in parallel mode. Galaxies observed post-ACS failure were imaged with WFPC2 alone, as part of a 'supplemental' HST program (Proposal IDs 11307 and 11986 in Table 2.1). New ACS observations used the F475W (SDSS g) and F814W (I) filter combination, to optimize both photometric depth and temperature (color) baseline. A third filter in F606W (wide V) is also available for most galaxies. The low throughput in the bluer filters of WFPC2 led us to only use F606W and F814W for WFPC2 observations.

In most cases, a single HST field was sufficient to cover the main optical body of a galaxy, ensuring the SFHs are representative of the whole galaxy. In other cases, typically larger dSpirals, a smaller fraction of a galaxy's optical body was covered with HST imaging. To quantify this, we compute the ratio of the projected angular area of ACS or WFPC2 aperture to the angular area of the optical galaxy (Table 2.1). For the latter, we use the angular diameters and axial ratios presented in Karachentsev et al. (2004), which measure an optical area at a blue surface brightness level of ~ 25 mag arcsec^{-2} (or ~ 26.5 mag arcsec^{-2} in the case of the faintest galaxies; Karachentsev et al., 2004).

Several of the sample galaxies required multiple observations to cover a reasonable fraction of the optical galaxy, resulting in multiple fields, either overlapping for continuous arial coverage, or disjoint representative fields. In the case of overlapping fields

(NGC 2366, Holmberg II, IC 2574), we removed duplicate stars, ran the SFHs on each field, and combined the resultant SFHs. For non-overlapping fields (BK5N, F8D1) we verified the completeness functions among the fields were similar, and combined the photometry prior to measuring the SFHs.

In the case of NGC 55, we selected two non-overlapping fields, one in the center of the galaxy and one in the disk. The completeness functions were sufficiently different such that we did not combine photometry prior to computing the SFH. Instead, we derived the SFHs for each field separately, and combined then combined them. We adopted similar method of analysis for WFPC2 observations of NGC 3109, measuring the SFHs of a field in the center and disk, and combing the solutions. The fractional coverage listed in Table 2.1 takes into account the combined areas for galaxies with multiple fields.

As described in Dalcanton et al. (2009), both new and archival observations were processed uniformly beginning with image reduction via the standard HST pipeline. Using the ANGST data reduction pipeline, we performed photometry on each image with HSTPHOT[2] (Dolphin, 2000), designed for WFPC2 images, and DOLPHOT[3] , running in its ACS-optimized mode, for ACS observations, providing for a uniform treatment of all data. The resultant photometry for each data set was filtered to ensure our final photometric catalogs excluded non-stellar objects such as cosmic rays, hot pixels, and extended sources. For the purposes of this paper, we considered a star well measured if it met the following critera: a signal-to-noise ratio > 4 in both filters, a sharpness value such that $(sharp_1 + sharp_2)^2 \leq 0.075$, and a crowding parameter such that $(crowd_1 + crowd_2)^2 \leq 0.1$. To characterize observational uncertainties, we performed 500,000 artificial star tests on each image. Both the full and filtered (i.e., the '*gst*' files) photometric catalogs, HST reference images, CMDs can be found on the ANGST website[4] , while definitions and details of the effects of filtering criteria and observational strategies can be found in Dolphin (2000), Dalcanton et al. (2009), and Gilbert et al. (2010).

[2] http://purcell.as.arizona.edu/hstphot
[3] http://purcell.as.arizona.edu/dolphot
[4] http://www.nearbygalaxies.org

2.3 Method of Measuring SFHs

To ensure uniformity in the SFHs of the ANGST dwarf galaxies, we selected one SFH code (Dolphin, 2002) and one set of stellar evolution models (Padova; Marigo et al., 2008). The SFH code of Dolphin (2002) provides the user with robust controls over critical fixed input variables, e.g., IMF, binary fraction, time and CMD bin sizes, as well as the ability to search for the combination of metallicity, distance, and extinction values that produce a model CMD that best fits the observed CMD. The models of Marigo et al. (2008) combine updated AGB evolution tracks with the models of Bertelli et al. (1994) ($M \geq 7$ $M_{\odot}$) and Girardi et al. (2002) ($M < 7$ $M_{\odot}$).

Here, we briefly summarize the technique of measuring a SFH based on the full methodology described in Dolphin (2002). The user specifies an assumed IMF and binary fraction, and allowable ranges in age, metallicity, distance, and extinction. Photometric errors and completeness are characterized by artificial star tests. From these inputs, many synthetic CMDs are generated to span the desired age and metallicity range. For this work, we have used synthetic CMDs sampling stars with age and metallicity spreads of 0.1 dex. These individual synthetic CMDs are then linearly combined along with a model foreground CMD to produce a composite synthetic CMD. The linear weights on the individual CMDs are adjusted to obtain the best fit as measured by a Poisson maximum likelihood statistic; the weights corresponding to the best fit are the most probable SFH. This process can be repeated at a variety of distance and extinction values to solve for these parameters as well.

Uncertainties in the CMD fitting process fall into two categories: systematic and statistical. The systematic effects are due to uncertainties in the stellar isochrones and photometric zero points, and can be modeled in the CMD fitting process by allowing the program to solve SFHs for CMDs with small shifts in distance and extinction. Specifically, we chose to vary the best fit distance and extinction values by ± 0.05 mags, creating a grid of nine solutions, centered around the best distance and extinction values. The rms scatter of the different SFHs due to these slight offsets are indicative of the systematic uncertainties. We account for statistical uncertainties by redistributing the stars in each CMD bin on the best fit model according to a Poisson distribution and solving for a new SFH, fixing the distance and extinction to the best values, i.e., a Monte

Carlo test. The total statistical errors are standard deviation of the uncertainties from 50 Monte Carlo realizations. The systematic and statistical uncertainties are added in quadrature to produce the final error bars.

In order to minimize systematic effects for comparisons among the SFHs, we selected consistent parameters for measuring SFHs of all galaxies in the sample. All SFHs were measured using a single slope power law IMF with a spectral index of -1.30 over a mass range of 0.1 to 120 $M_{\odot}$, a binary fraction of 0.35 with a flat secondary mass distribution, 36 time bins ranging from $\log t = 6.6$–10.15, color and magnitude bins of 0.05 and 0.1 mags, and the most recent Padova stellar evolution models (Marigo et al., 2008). We designated the faint photometric limit to be equal to the 50% completeness limit in each filter (see Table 2.1). Initial values for the distances were taken from the TRGB distances measured in Dalcanton et al. (2009), while foreground extinction values were taken from the galactic maps of Schlegel et al. (1998). The SFH program was initially allowed to search for the best fit distance and extinction values without constraints, however we found no significant discrepancies between the assumed values and the best CMD fit distance and foreground extinction values, i.e., all were consistent within error. Final solutions were computed using the TRGB distances from Dalcanton et al. (2009) and foreground extinction values from Schlegel et al. (1998).

Selecting an appropriate time resolution is equally important to making meaningful comparisons. While deeper CMDs allow for higher time resolution at older ages, the ANGST dwarf galaxies sample a range of photometric depths. To place the data on equal footing, we selected five broad time bins, 0–1, 1–3, 3–6, 6–10, 10–14 Gyr ago, for the final SFHs. These time bins balance the depth considerations of the shallower CMDs with the interest of quantifying ancient (> 10 Gyr ago), intermediate (1–10 Gyr ago), and recent (< 1 Gyr ago) SFRs in sufficient detail for meaningful comparison.

Varying photometric depth also has an impact on the accuracy of the derived chemical evolution. CMD-derived metallicities are best constrained by the presence of the ancient main sequence (MS) turnoff (e.g., Dolphin et al., 2003; Gallart et al., 2005; Cole et al., 2007). Although the CMDs of most ANGST galaxies are too shallow to include the ancient MS turnoff, moderate constraints can be found by the inclusion of the red clump in the CMD fitting process. Without the red clump, the red giant branch (RGB) can suffer from significant age-metallicity degeneracies (e.g., Dolphin et al., 2003;

Cole et al., 2005; Gallart et al., 2005). To ensure physically realistic models of chemical evolution, i.e., to prevent scenarios in which the metallicity significantly increases or decreases rapidly over short time scales (e.g., $\sim$ 100 Myr), we required the metallicity to be consistent with a constant or monotonic increase as a function of time toward the present.

As an example of a typical CMD fit made by the SFH code, we compare the observed and synthetic CMDs of a representative ANGST dI, DDO 6 (Figure 2.2). Dalcanton et al. (2009) determined the TRGB distance of DDO 6 to be 3.31$\pm$0.06 Mpc while the foreground extinction maps of Schlegel et al. (1998) give values of $A_B = 0.07$ and $A_V = 0.06$. Allowing the SFH code to search for the best fit CMD, we find best fit values of D = 3.31$\pm$0.07 Mpc and $A_{F475W} = 0.05\pm0.04$, both in excellent agreement with the independently measured values. Examining the residual significance CMD, i.e., the difference between the data and the model weighted by the variance (panel (d) of Figure 2.2), we see a good, although not perfect fit. Notably, the area between the blue helium burning stars and young MS appears to be too cleanly separated in the model, which could be due to differential extinction effects from young stars in the known CMD. Additionally, the model red helium burning stars are too blue compared to the data, likely due to known inaccuracies in the massive star models (e.g., Gallart et al., 2005). However, even the most discrepant regions are fit within $\pm$ 5σ, which are indicated by black or white points. Overall, the model CMD appears to be in good agreement with the observed CMD, indicating that we have measured a reliable SFH. See Dolphin (2002) for a full discussion of the quality measures of this CMD fitting technique.

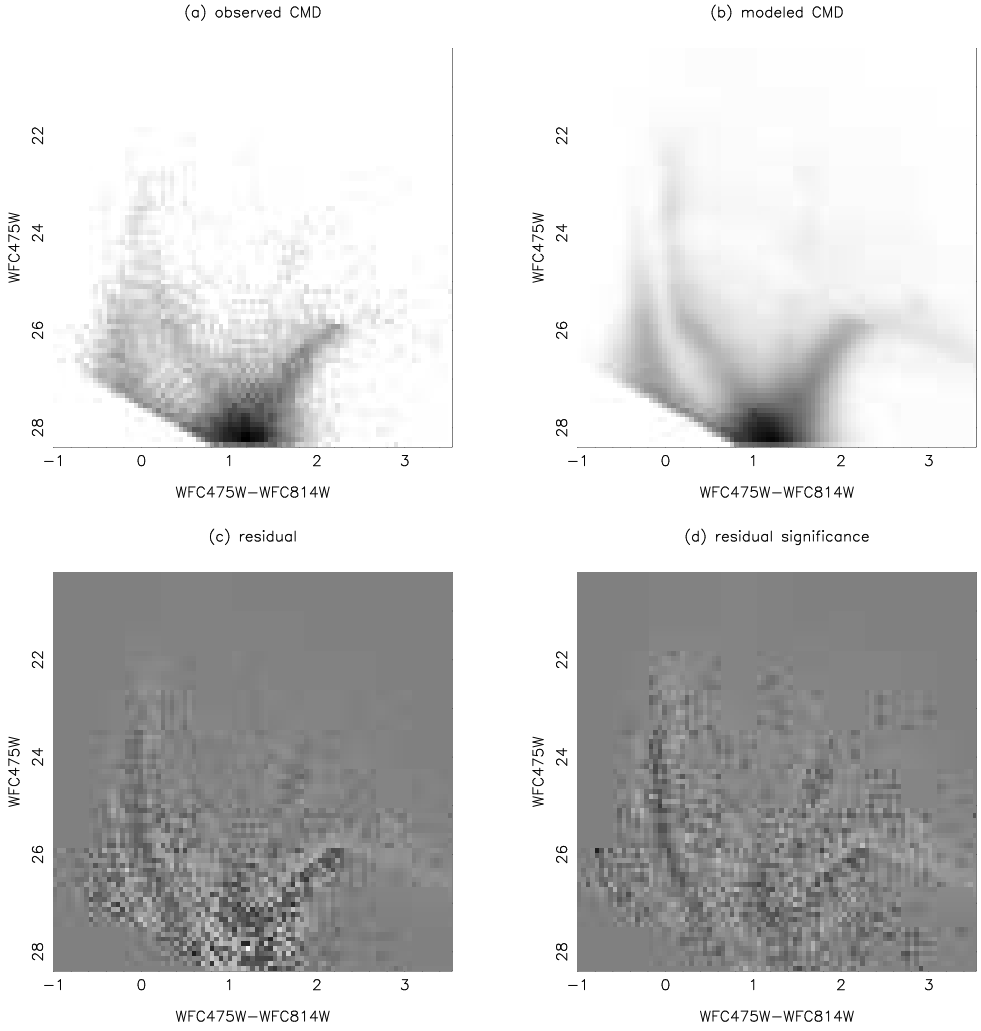

Figure 2.2 A comparison of the observed and model CMDs for ANGST sample dI DDO 6. The observed CMD is shown in panel (a) and the best matched model CMD in panel (b). The lower two panels are diagnostic CMDs used to determine the fit quality. Panel (c) shows the residual of data − model CMD, with black and white points representing $\pm$ 5σ. Panel (d) is the residual significance CMD, which is the data−model weighted by the variance in each CMD bin (Dolphin, 2002). Based on the residual significance CMD, we see that the overall fit is quite good, with only minor discrepancies, most notably between the main sequence and the blue helium burning stars, which is likely due to differential extinction effects, but only affects the SFH on time scales $<$ 1 Gyr.

2.4 The Extended Star Formation Histories of Dwarf Galaxies

In Figure 2.3, we present both the absolute SFHs, i.e., SFR(t), and the cumulative SFHs, i.e., the stellar mass formed during or previous to each time bin normalized to the integrated final stellar mass. The galaxies are sorted in order of increasing blue luminosity. A cursory inspection of Figure 2.3 reveals that dwarf galaxies have a wide variety of SFHs, despite often having similar luminosities, morphologies, or chemical compositions. This dispersion suggests that drawing broad conclusions about the nature of SF in dwarf galaxies can only be done with large samples, as selection of only a few galaxies may not be representative of the general population. Fortunately, the ANGST sample provides a statistically significant number of dwarf galaxies. In the following sections we consider galaxies with respect to morphological classification, and find that a number of trends begin to emerge.

In Figure 2.4, we present the unweighted mean specific SFHs per morphological type. That is, we selected the best fit SFH for each galaxy, divided by the total integrated stellar mass, and computed the mean SFH for all galaxies of each morphological type. The error bars in Figure 2.4 reflect the uncertainties in the mean values, and incorporate errors from the SFHs of each galaxy.

Comparing the mean SFHs among the different morphological types, we find they are consistent within the uncertainties for times $>$ 1 Gyr ago, with the exception of dTidals. Qualitatively, we find that a typical dwarf galaxy exhibits dominant ancient SF ($>$ 10 Gyr ago), and lower levels of SF at intermediate ages (1–10 Gyr ago). It is only within the most recent 1 Gyr that dSphs have significantly lower levels of SF relative to the other morphological types. While this is in agreement with conventional expectations of lower recent SFRs in dSphs, the sharp difference at 1 Gyr is interesting. The consistency of the SFHs before this epoch implies that as recently as 1 Gyr ago, many of the galaxies were star forming and were likely gas-rich, i.e., like present day dIs. The final transformation from a gas-rich to gas-poor state is relatively quick (see §2.5.1), but likely not as precisely synchronized as indicated in Figure 2.4. Indeed, SFHs of LG dwarf galaxies have shown that not all dSphs lost their gas $\sim$ 1 Gyr ago (e.g., Dolphin et al., 2005; Monelli et al., 2010). We also note that broad uncertainties in ages

and numbers of predicted AGB stars in low metallicity environments (see Girardi et al., 2010) do not allow higher time resolution at times $\gtrsim$ 1 Gyr ago without significantly increasing the errors in SFR, making the precise age for the drop in dSph SFRs and the degree of synchronization slightly uncertain.

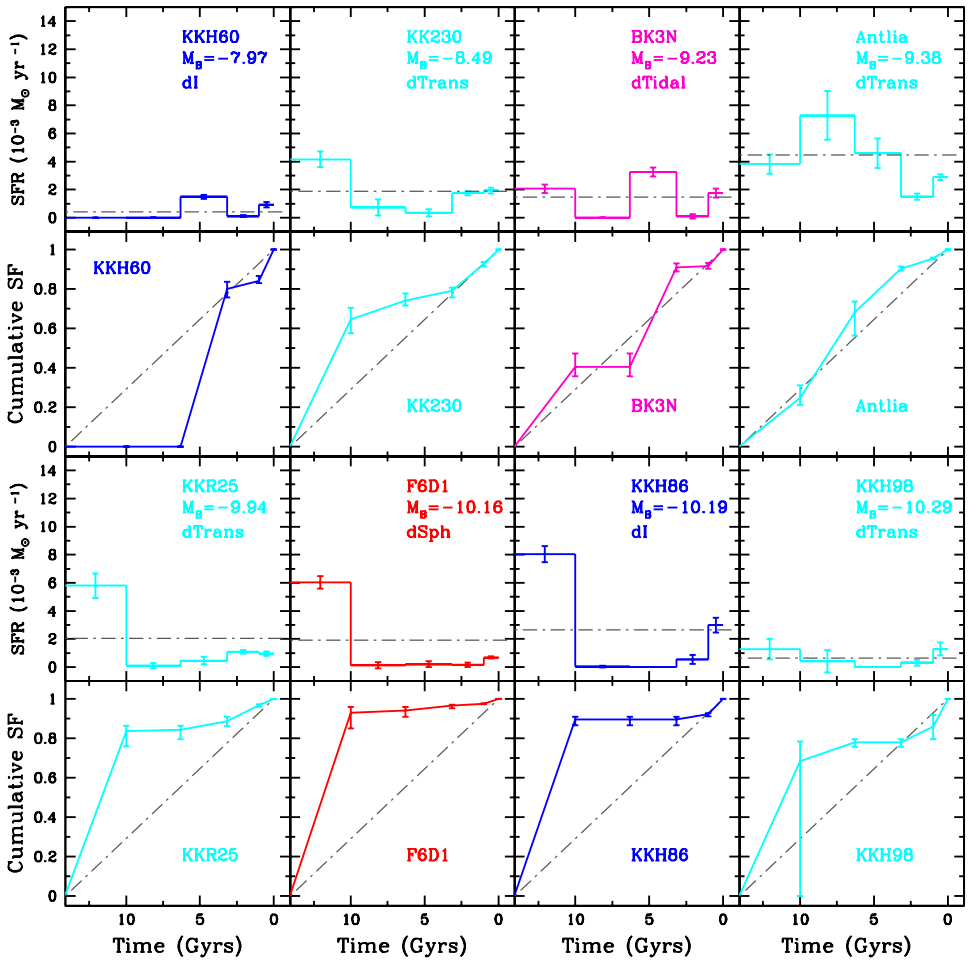

Figure 2.3 SFHs and cumulative SFHs, i.e., fraction of stellar mass formed normalized to the integrated stellar mass, of ANGST sample galaxies presented in order of increasing absolute blue luminosity. Each galaxy has been color-coded to indicated its morphological classification: dSphs (red), dI (blue), dTrans (cyan), dSpiral (green), dTidal (magenta). The grey dashed line in the SFH plots is the lifetime averaged SFR. In the cumulative SFHs, this same rate is also represented by the grey dashed line with a slope of unity, i.e., a constant SFH. The axes of the SFHs have been scaled so that galaxies of comparable luminosity are on similar scales. Some galaxies absolute SFHs have been scaled up to clarify details. The SFRs of KK 230, Anitlia, KKR 25, KKH 86, and Sex A have been increased by factor of 10. The optical coverage fraction (see Table 2.1) indicates how much of the optical galaxy a SFH represents. Note the wide variety of SFHs, along with the general inconsistency with simple models of SF, i.e., single epoch event or constant SFH.

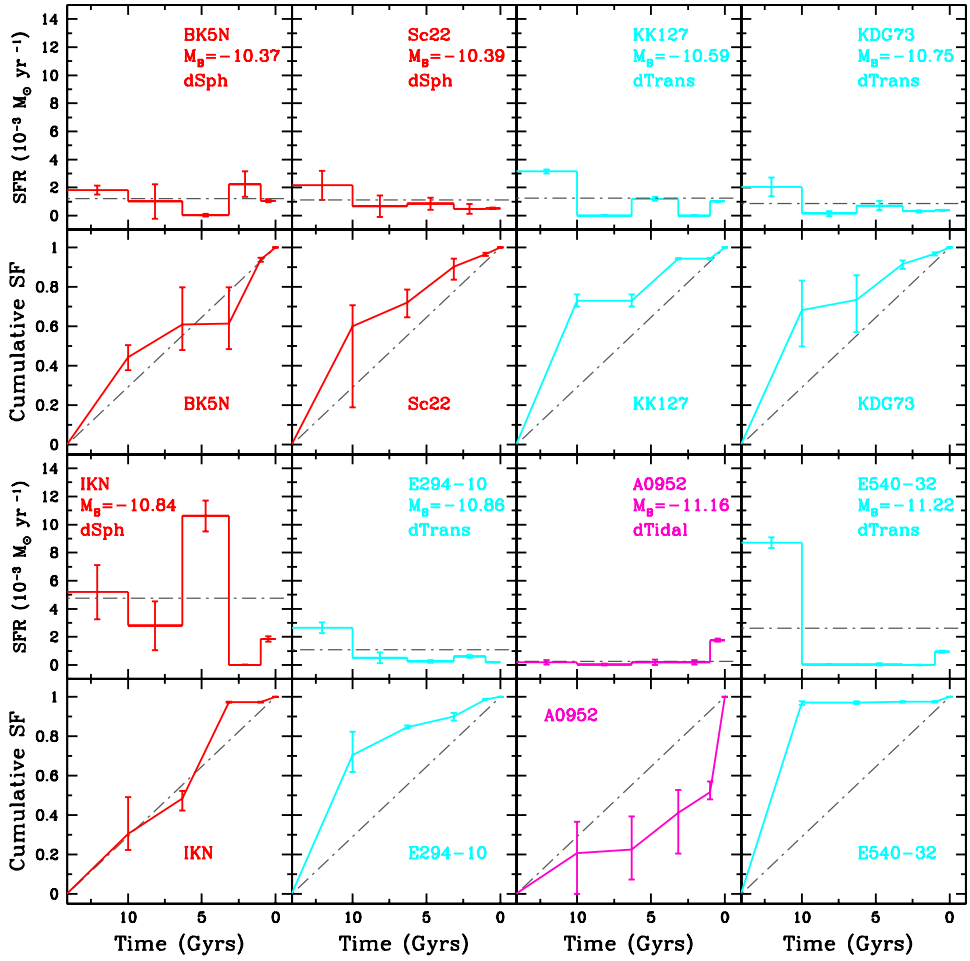

Figure 2.3 Continued

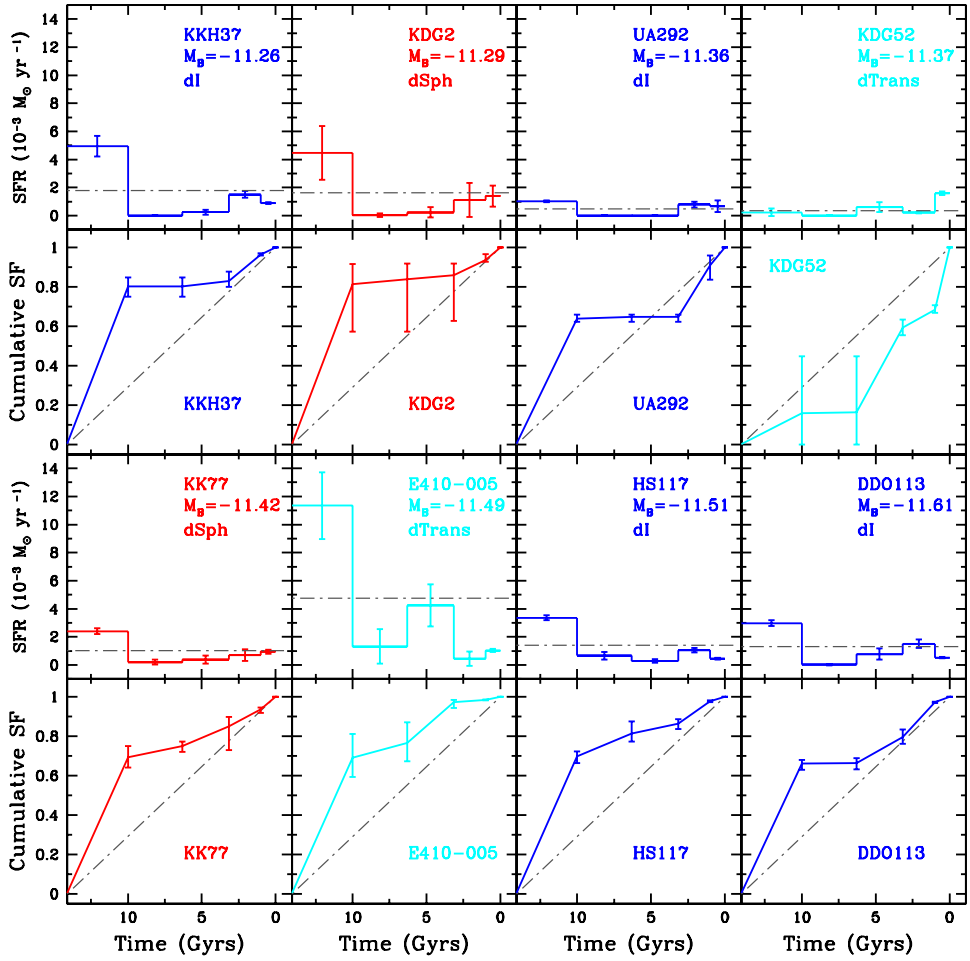

Figure 2.3 Continued

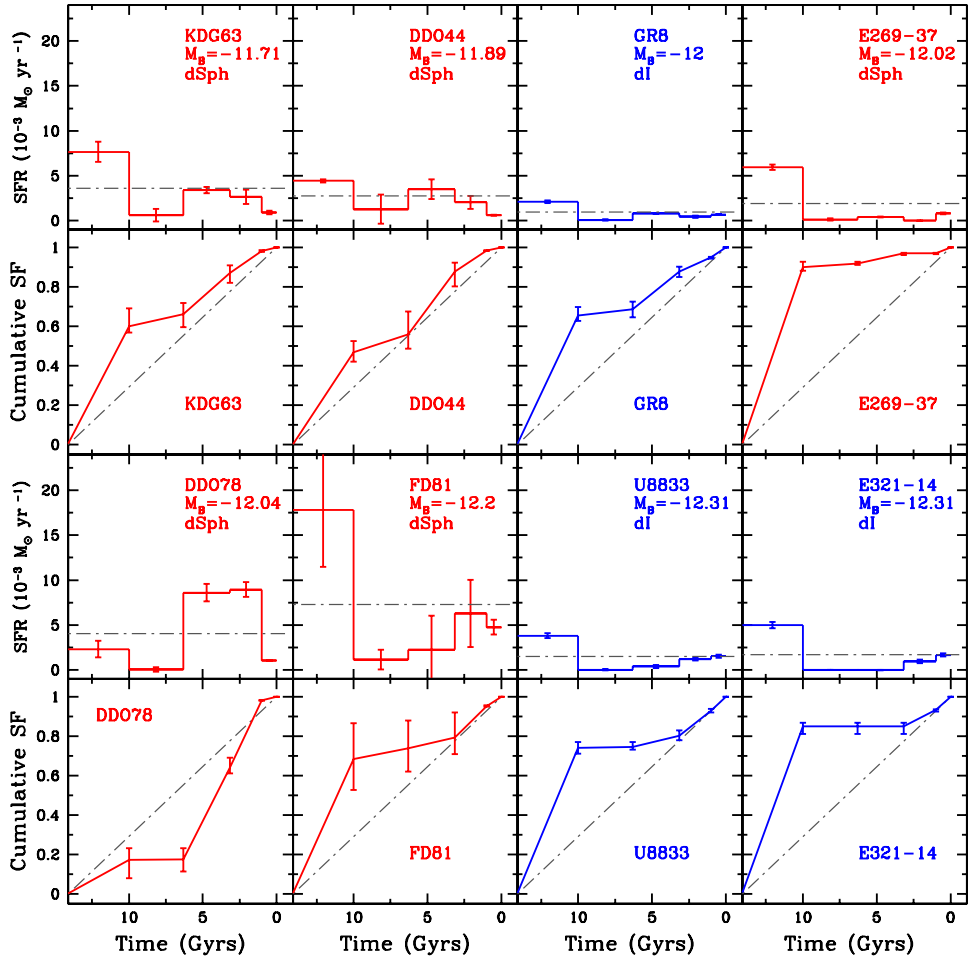

Figure 2.3 Continued

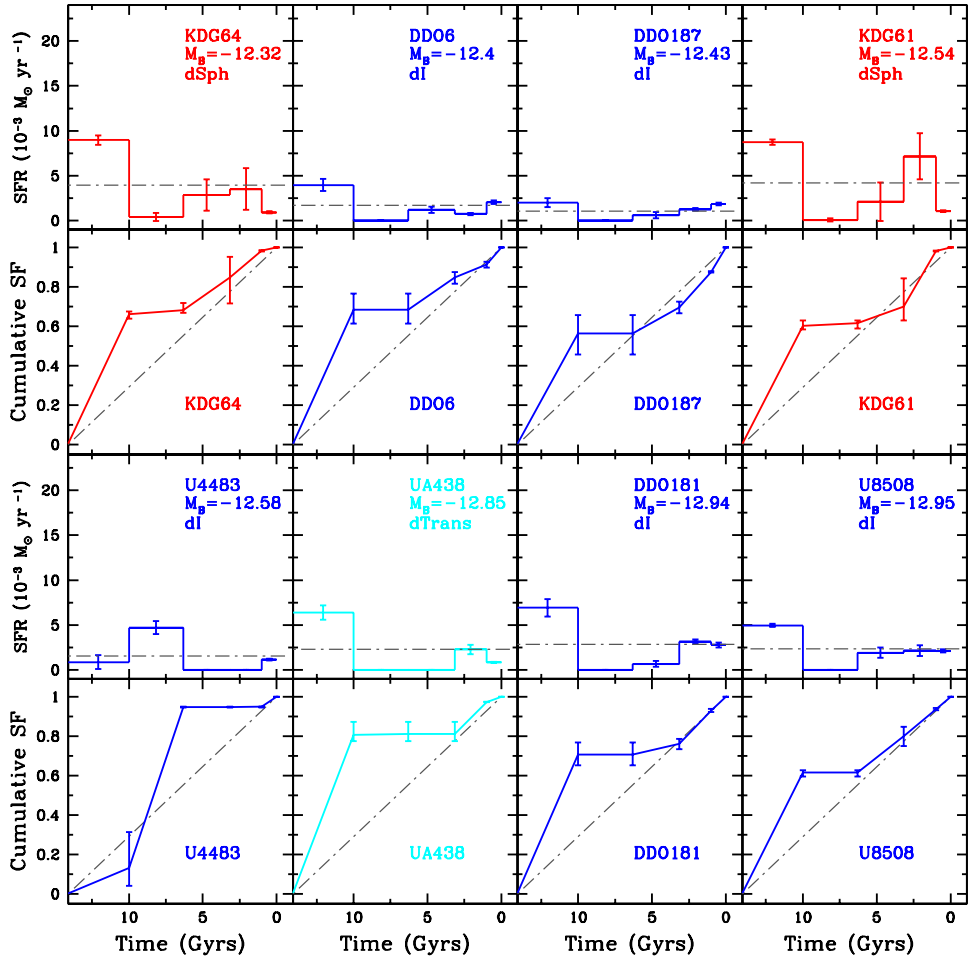

Figure 2.3 Continued

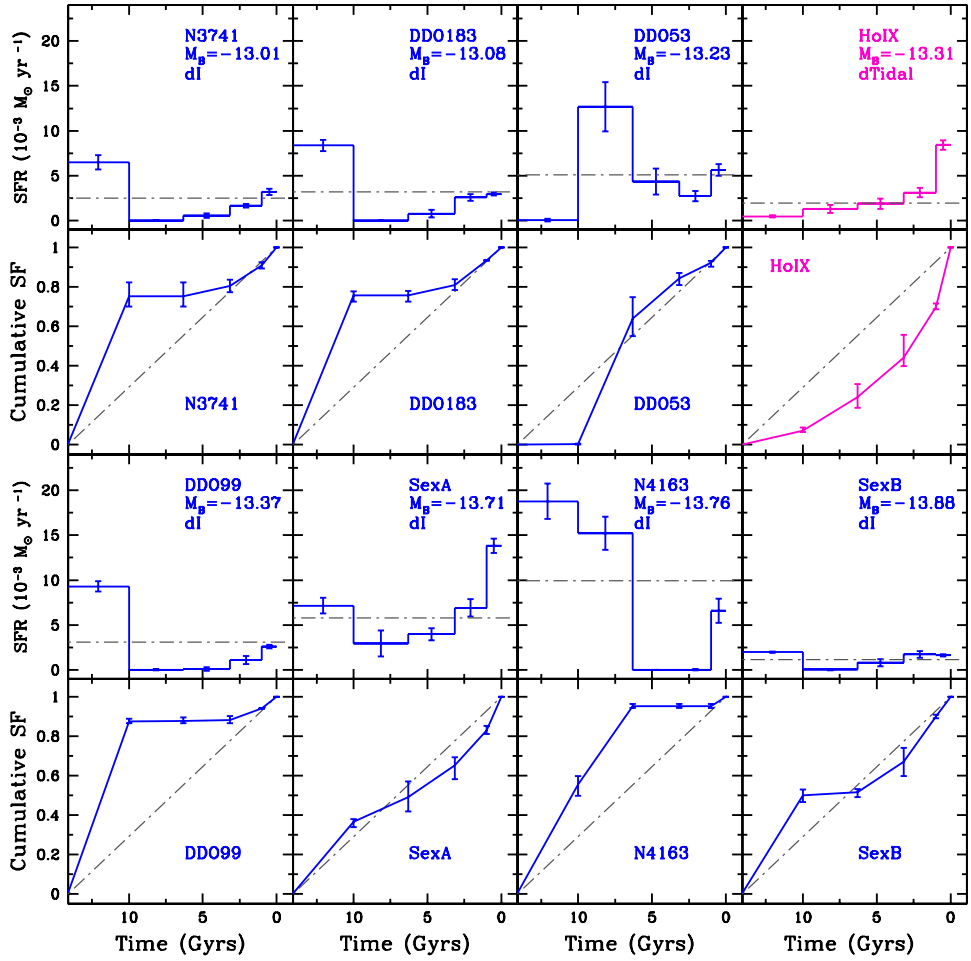

Figure 2.3 Continued

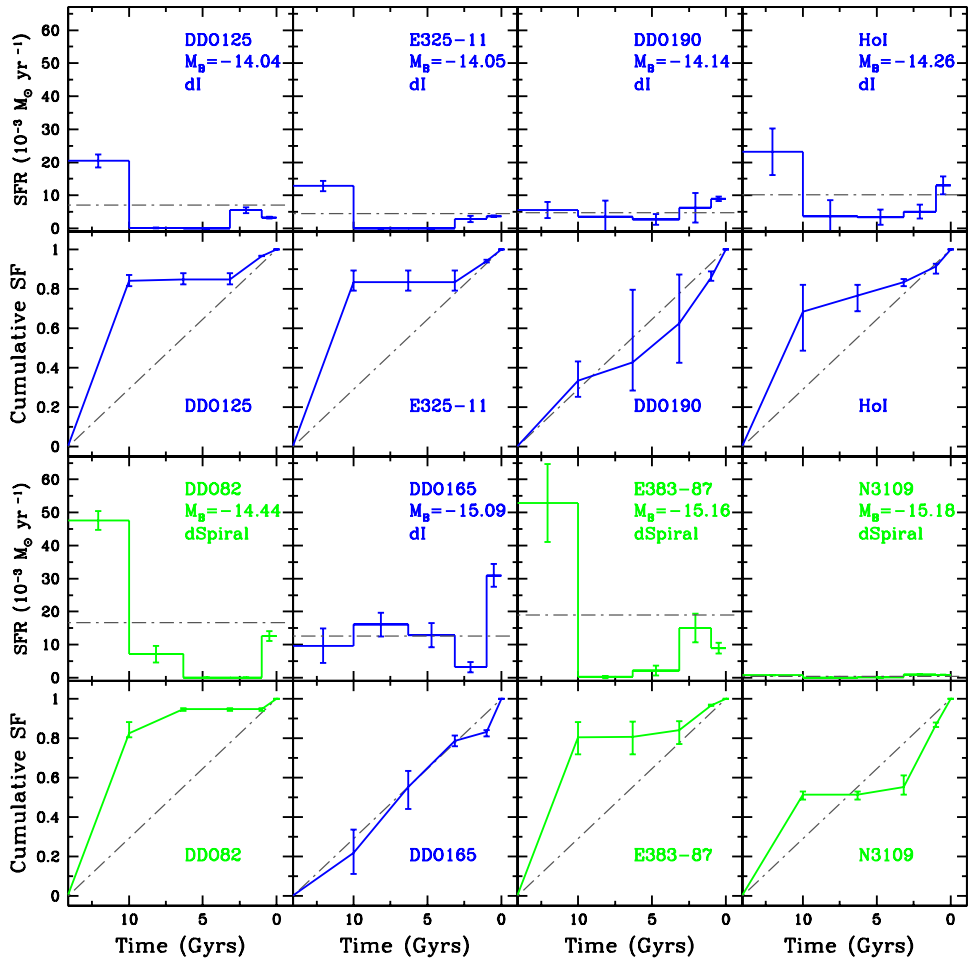

Figure 2.3 Continued

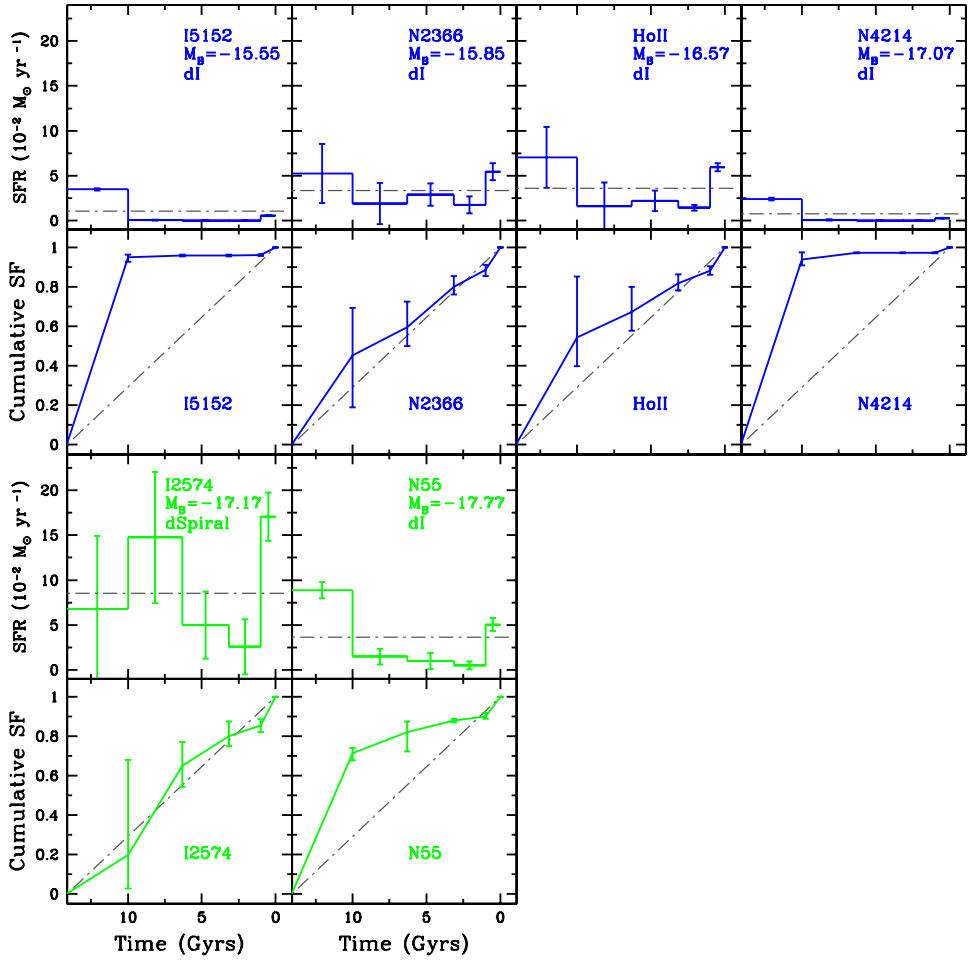

Figure 2.3 Continued

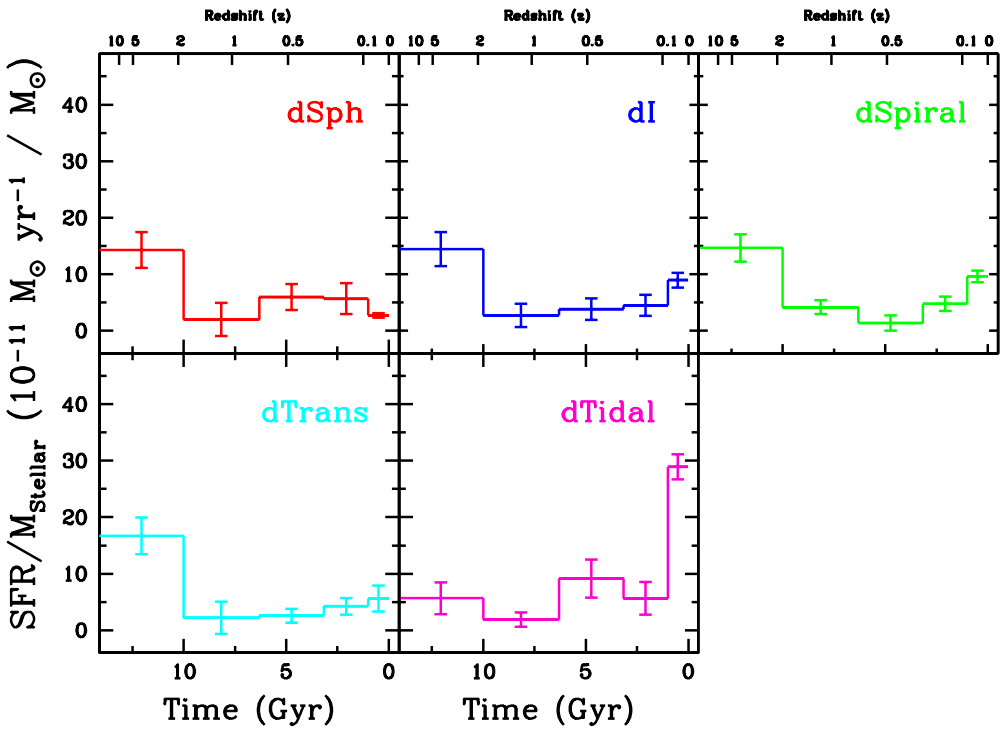

Figure 2.4 The mean specific SFHs, i.e., the SFH normalized to the integrated stellar mass, for each morphological type. The error bars reflect the uncertainties in the mean SFHs. Excluding dTidals, the average SFHs of the different types of galaxies are consistent with the uncertainties for times > 1 Gyr. Specifically, the typical dwarf galaxy had dominant early SF (> 10 Gyr), reduced intermediate age SF (1–10 Gyr), and suppressed (dSphs) or enhanced SF (dI, dSpiral, dTrans) in the most recent 1 Gyr. dTidals show a large increase in the SFR in the recent 1 Gyr, in agreement with expectations of a newly forming galaxy. However, the older SF may be due to contamination from background red stars (AGB, RGB) from M81. The redshift values shown assume a standard WMAP cosmology (Dunkley et al., 2009).

Cumulative SFHs allow galaxies of different masses to be readily compared. Like the absolute SFHs, the cumulative SFHs in Figure 2.5 show significant diversity within morphological classes (Table 2.2), yet converge on consistent mean values. Perhaps the most striking result is that the average dwarf galaxy formed $\sim 60\%$ of its total stellar mass by z $\sim$ 2, independent of morphological type. Specifically, the mean cumulative SFHs show that dSphs, dTrans, dIs, and dSpirals had all formed 61%, 68%, 63%, and 67% of their stellar mass by z $\sim$ 2, and 63%, 75%, 69%, and 72% by z $\sim$ 1, respectively. These percentages are consistent with one another at the 1-σ level. Within the most recent 1 Gyr, the typical dSph, dTrans, dI, and dSpiral formed 3%, 6%, 9%, and 8% of their present day stellar mass. The fraction of recent SF in dSphs is statistically inconsistent with the other galaxies at the 1-σ level.

The cumulative SFHs also allow for direct comparison with models of SF. The exponentially declining SF model (τ model) has been used as a simple analytic prescription for describing SFHs. We computed the cumulative SFH of the τ model for values of τ ranging from 0–14.1 Gyr, at a resolution of 0.1 Gyr. Comparing the resulting models with the data using a χ^2 test, we find that dSphs, dTrans, and dIs are best fit by τ values of 7.9, 6.8, and 5.3 Gyr, respectively. In all cases, the exponentially declining model predicted fewer stars formed by z $\sim$ 2 than the data, and over-predicted the fraction of stellar mass formed from 1–10 Gyr ago. For example, the data show that a typical dI formed 63% of its stars at z $\sim$ 2 and 91% by 1 Gyr ago. The best fit τ model for a dI predicts 52% and 97%, respectively. The models for dSphs and dTrans show a similar trend. In Figure 2.6, we show select τ models plotted along with the cumulative SFHs from the data. We have selected to plot the average best fit τ model (τ = 6.4 Gyr) as well as the τ model (τ = 4.9 Gyr) that best fits the data such that 60% of the stars must have formed prior to z $\sim$ 2. We also note that a both a constant SFH (τ = 14.1 Gyr) and an single epoch SFH (e.g., τ = 0.1 Gyr) are not consistent with the data. This comparison reveals that a τ models can produce a reasonable representation of the data, a more complex model is likely to provide a better fit.

The mean cumulative SFHs are also directly comparable to the observed cosmic SFH as measured using redshifted ultraviolet light from distant galaxies (Reddy et al., 2008). In Figure 2.6, we see that the cumulative cosmic SFH is in rough agreement with the mean SFHs of the ANGST dwarf galaxies at z $\sim$ 2. However, the cosmic SFH shows

a more rapid increase from z $\sim$ 1 to z $\sim$ 0.5 compared to the ANGST SFHs. We further see that the cosmic SFH shows only a small increase from z $\sim$ 0.5 toward the present, while all of the ANGST dwarfs show a steeper rise. Differences during this intermediate epoch could be attributed to physical effects, e.g., dwarf galaxies have more constant SFHs than more massive galaxies, or modeling effects, e.g., improved AGB star models could change the slope of the data. Williams et al. (2010b) presents a more detailed comparison of the cosmically and locally measured SFHs.

In Figure 2.7, we show the cumulative SFHs as a function of the total stellar mass and morphological type for each galaxy. While there appears to be some segregation in the integrated stellar masses among the morphological types, there does not appear to be a trend in the cumulative SFHs with total stellar mass.

The mean total stellar mass and fraction of stellar mass formed are overplotted for each of the morphological types in Figure 2.8. We see that the different morphological types show slight variations in mean total stellar mass, but only the dTidals are distinguishable in the mean fraction of stars formed as a function of lookback time. Interestingly, the average dTrans appears to be the least massive type of galaxy in the sample, which may provide a clue to the physical processes driving their evolution. However, we note that ambiguities in the definition of dTrans could also contribute to the lower mean total stellar mass (see §2.5.2 for further discussion).

The dominance of ancient SF in the typical dwarf galaxy suggests that dwarf galaxies may not readily fit into the theory of galaxy downsizing, i.e., the most massive galaxies form stars before less massive galaxies (e.g., Cowie et al., 1996). However, high redshift observations which support downsizing are only sensitive to massive L_*-type galaxies ($\gtrsim 10^{10}$ M$_\odot$), and do not sample the low end of the galaxy luminosity function, i.e., dwarf galaxies. Quantitatively, Thomas et al. (2005) find that higher mass galaxies have formed $\gtrsim$ 50% of their stellar mass density by z $\sim$ 1, with a significant decline of SFRs at younger ages. Comparing this result with the mean cumulative SFHs of ANGST dwarf galaxies (Figures 2.5 and 2.6) we find surprisingly similar trends. Namely, the typical dwarf galaxy appears to have undergone an intense period of early SF; $\sim$ 60% of its stellar mass formed by z $\sim$ 2, followed by a subsequent decline in the SFRs. Although the absolute SFRs are substantially lower, it appears that dwarf galaxies have a comparable fraction of stars in place by an earlier epoch. This suggests that

downsizing seen in many massive galaxies may not simply extrapolate into the lower mass galaxy regime.

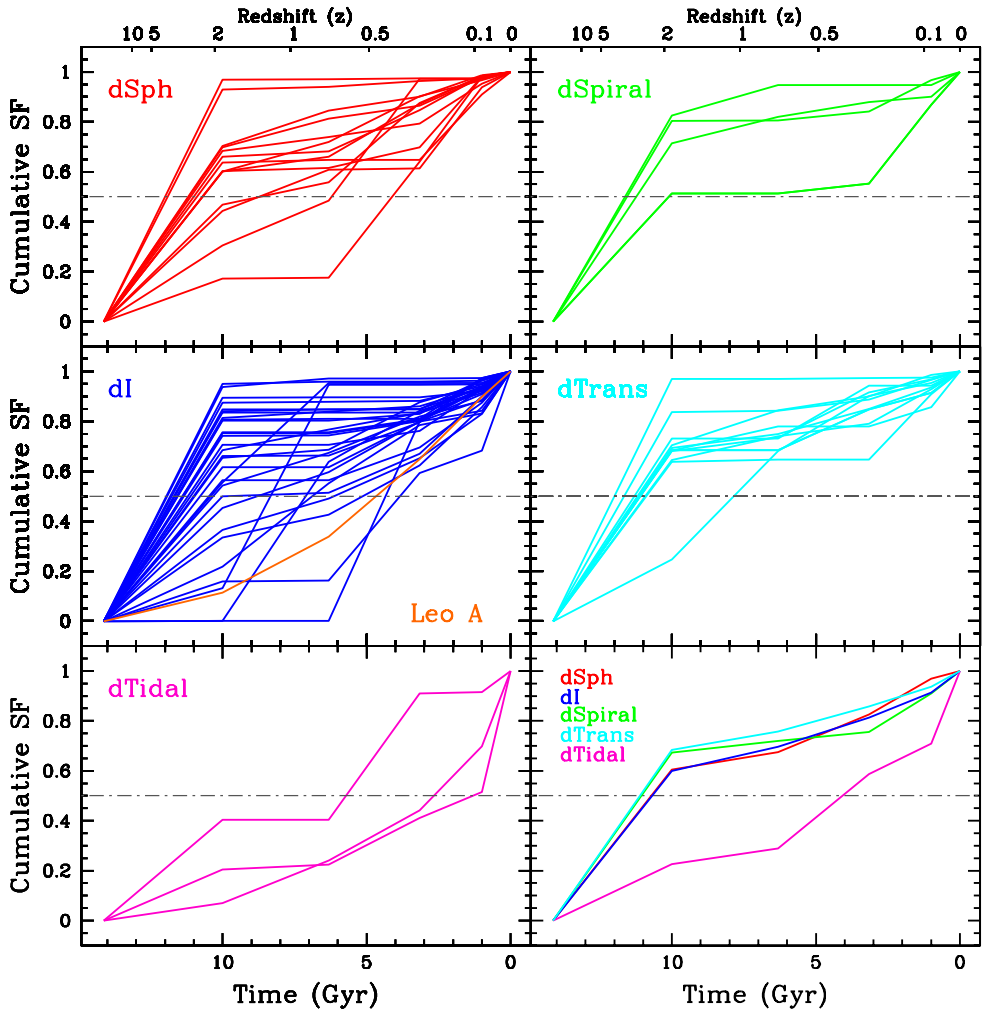

Figure 2.5 The individual and mean cumulative SFHs, i.e., the fraction of the total stellar mass formed as a function of time, per morphological type. Error bars have been omitted for clarity. The grey dashed line represents 50% of the total stellar mass. While the individual cumulative SFHs show a wide variety, the mean cumulative SFHs are remarkably similar. Most dwarf galaxies are not entirely old stellar populations, i.e., they have intermediate or recent SF, and none are consistent with simple models of SF, i.e., single epoch or constant SFHs. Excluding dTidals, the average dwarf galaxy formed $\sim 60\%$ of its stars by $z \sim 2$. The redshift values shown assume a standard WMAP cosmology (Dunkley et al., 2009).

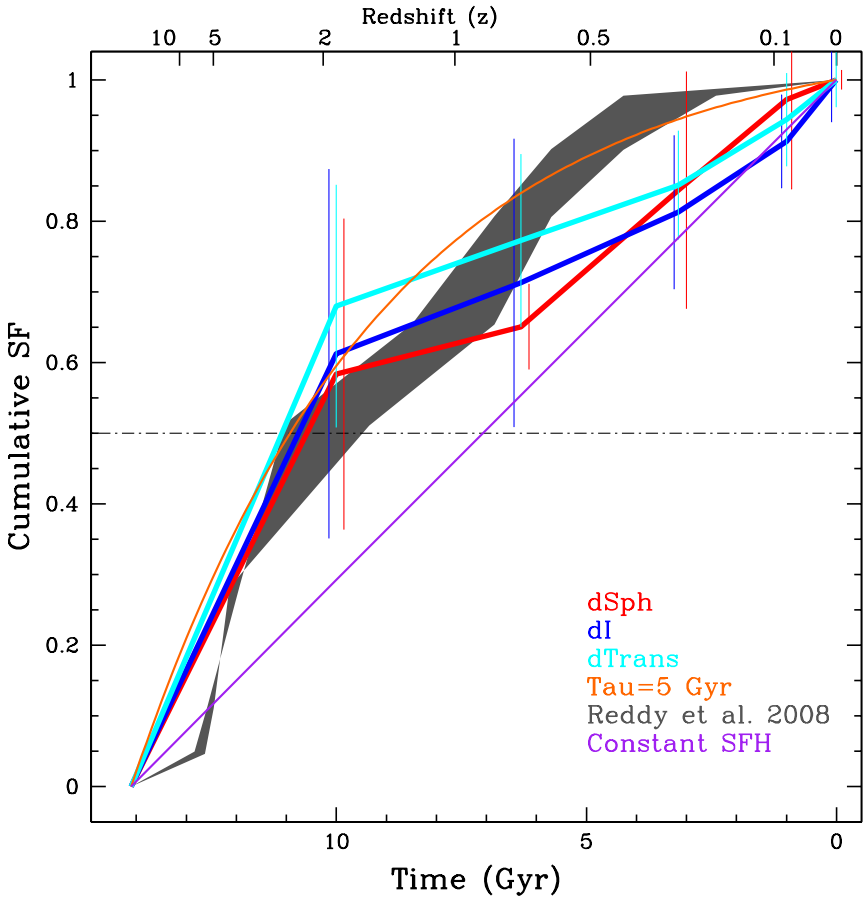

Figure 2.6 The mean cumulative SFHs, i.e., the fraction of total stellar mass formed, for dSphs (red), dIs (blue), and dTrans (cyan). The error bars represent the 1-σ dispersion in the mean values and the dashed line indicates 50% of the total stellar mass. For comparison, we have included different models of SF: constant SFH (purple) and exponentially declining with τ = 6.4 Gyr (green) and τ = 4.9 Gyr (orange). We see that while the constant SFH is not consistent with the data, exponential models provide a reasonable representation. The green line (τ = 6.4 Gyr) is the result of a best fit to the data, while the orange line (τ = 4.9 Gyr) is the largest τ value that produces 60% of the stars prior to z $\sim$ 2. Both τ models over-predict the fraction of stars formed from 1–10 Gyr relative to the data, indicating that an exponentially declining SF model cannot describe the measured SFHs (see §2.4). We also compare the cosmic SFH (grey shaded region) as measured from redshifted UV light (Reddy et al., 2008). We see consistency between the ANGST data and the cosmic SFH at z $\sim$ however, the comic SFH finds a higher fraction of stars forming at intermediate ages, and less SF in the most recent 1 Gyr. See §2.4 and Williams et al. (2010b) for further discussion.

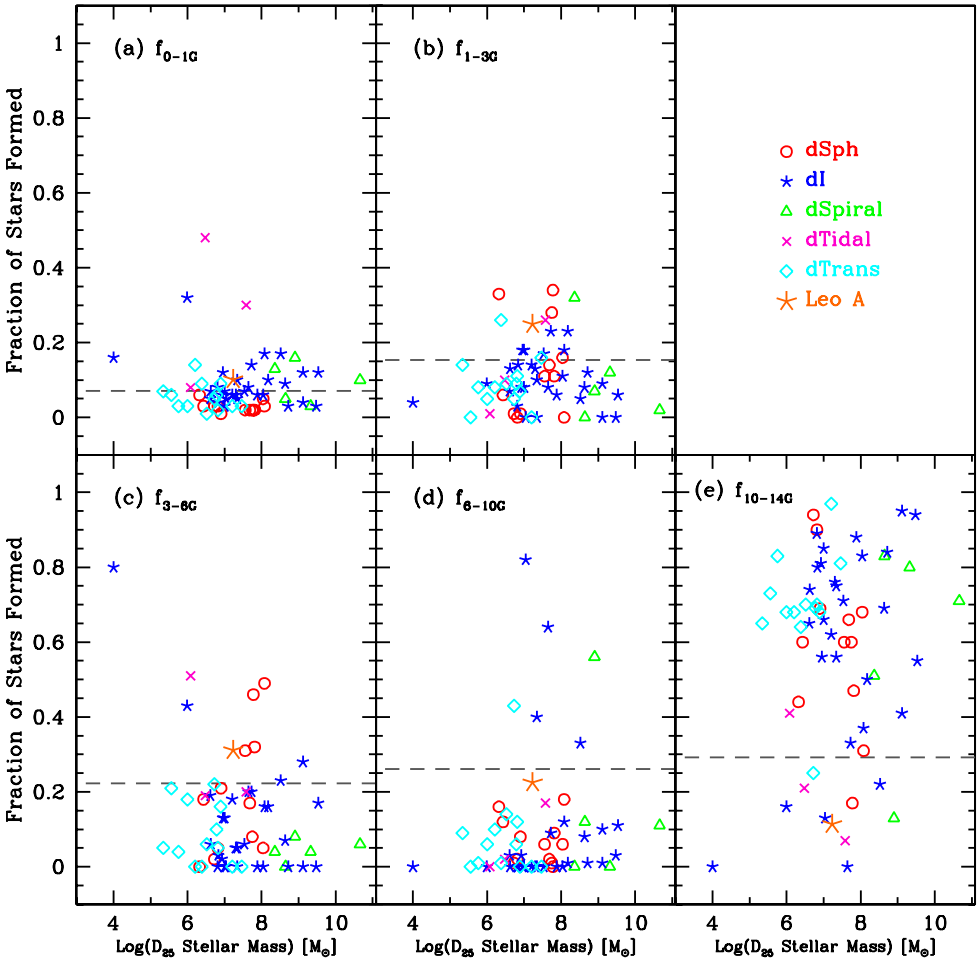

Figure 2.7 The cumulative SFHs, i.e., the fraction of total stellar mass formed, of each galaxy shown as a function of the total stellar mass and morphological type. The total integrated stellar masses are from the SFHs (Figure 2.3), normalized to D_{25} to account for differences in the observed areas. Time bins are such that f_{0-1G} = 0-1, f_{1-3G} = 1-3, f_{3-6G} = 3-6, f_{6-10G} = 6-10, f_{10-14G} = 10-14 Gyr ago. LG dI Leo A has been plotted for comparison, as it has a well constrained ancient SFH (Cole et al., 2007), which shows suppressed levels of ancient SF, $\lesssim$ 15% of total stellar mass formed. Very few of the the best fit SFHs of the ANGST galaxies show similarly low levels of ancient SF.

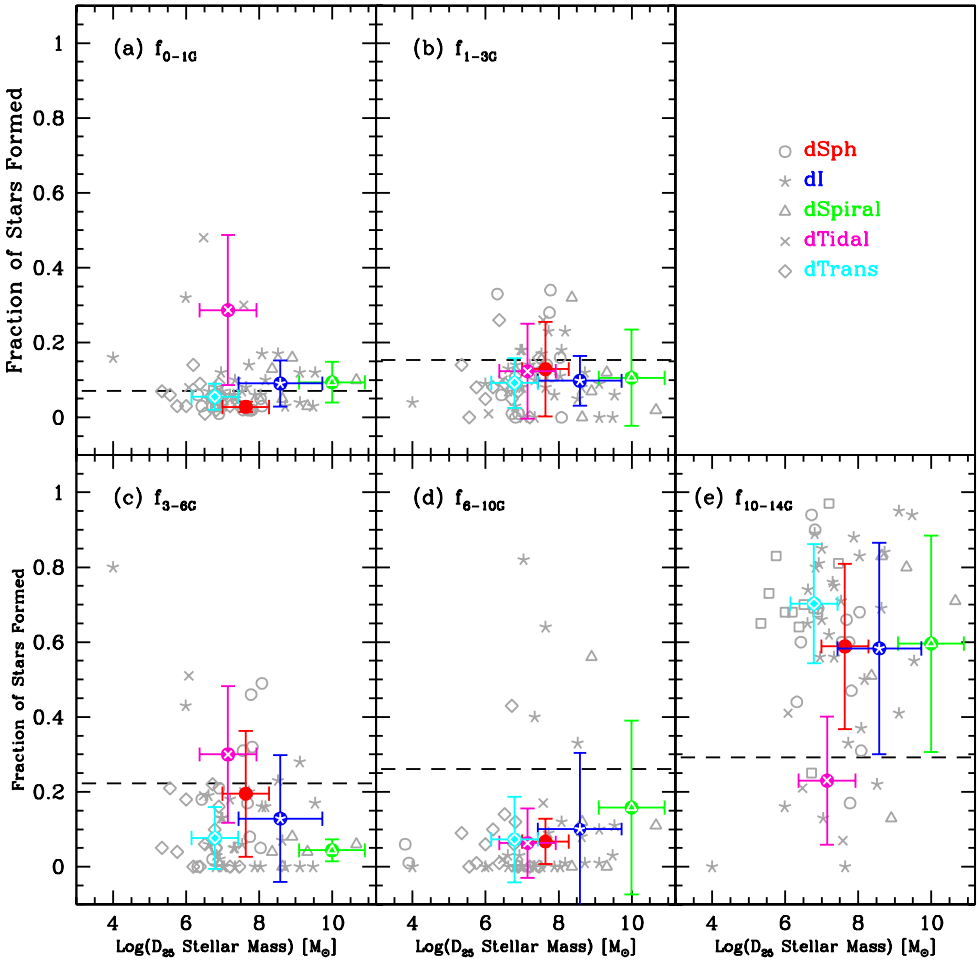

Figure 2.8 The cumulative SFHs, i.e., the fraction of total stellar mass formed, for each galaxy shown as a function of the total stellar mass and morphological type. The total integrated stellar masses are from the SFHs (Figure 2.3), normalized to D_{25} to account for differences in the observed areas. Time bins are such that f_{0-1G} = 0-1, f_{1-3G} = 1-3, f_{3-6G} = 3-6, f_{6-10G} = 6-10, f_{10-14G} = 10-14 Gyr ago. The grey points represent individual galaxies, while the colored points show the mean values per morphological type with 1σ error bars denoting the scatter. The different morphological types show slight differences in mean total stellar mass, but only the dTidals are distinguishable in mean fraction of stars formed as a function of lookback time.

Table 2.2: SFH Properties of ANGST Dwarf Galaxies

Galaxy	⟨SFR⟩	Total $M_\star$	f_{0-1G}	f_{0-1G}	f_{3-6G}	f_{6-10G}	f_{10-14G}
KK230	0.19	0.27	0.07	0.14	0.05	0.09	0.65
BK3N	1.50	2.1	0.08	0.01	0.51	0.00	0.41
Antlia	0.45	0.63	0.05	0.05	0.22	0.43	0.25
KKR25	0.21	0.29	0.03	0.08	0.04	0.01	0.83
FM1	1.90	2.7	0.03	0.01	0.02	0.01	0.94
KKH86	0.26	0.004	0.08	0.03	0.00	0.00	0.89
KKH98	0.62	0.88	0.14	0.08	0.00	0.10	0.68
BK5N	1.20	1.7	0.06	0.33	0.00	0.16	0.44
Sc22	1.10	1.6	0.03	0.06	0.18	0.12	0.60
KK127	0.13	0.18	0.06	0.00	0.21	0.00	0.73
KDG73	0.87	1.2	0.03	0.05	0.18	0.06	0.68
IKN	4.70	6.7	0.03	0.00	0.49	0.18	0.31
E294-010	1.10	1.5	0.01	0.09	0.06	0.14	0.70
A0952+69	0.26	0.36	0.48	0.10	0.19	0.02	0.21
E540-032	0.26	0.36	0.03	0.00	0.00	0.00	0.97
KKH37	1.80	2.5	0.04	0.14	0.03	0.00	0.80
KDG2	0.47	0.66	0.09	0.26	0.00	0.01	0.64
UA292	0.36	0.5	0.32	0.09	0.43	0.00	0.16
KDG52	1.00	1.4	0.06	0.09	0.10	0.06	0.69
KK77	4.70	7.0	0.01	0.01	0.21	0.08	0.69
E410-005	1.40	2.0	0.02	0.11	0.05	0.12	0.70
HS117	1.60	2.3	0.06	0.08	0.02	0.03	0.81
DDO113	1.30	1.9	0.03	0.18	0.13	0.00	0.66
KDG63	3.60	5.1	0.02	0.11	0.31	0.06	0.60
DDO44	2.80	3.9	0.02	0.11	0.32	0.09	0.47
GR8	0.94	1.3	0.05	0.07	0.19	0.03	0.65
E269-37	1.92	2.7	0.03	0.00	0.05	0.02	0.90
DDO78	4.10	5.7	0.02	0.34	0.46	0.00	0.17

F8D1	7.30	10.0	0.05	0.16	0.05	0.06	0.68
U8833	1.50	2.1	0.07	0.13	0.06	0.00	0.74
E321-014	1.73	2.4	0.07	0.08	0.00	0.00	0.85
KDG64	4.00	5.6	0.02	0.14	0.17	0.02	0.66
DDO6	1.70	2.4	0.09	0.07	0.16	0.00	0.68
DDO187	1.10	1.5	0.12	0.18	0.13	0.00	0.56
KDG61	4.20	6.0	0.02	0.28	0.08	0.01	0.60
U4483	1.60	2.2	0.05	0.00	0.00	0.82	0.13
UA438	2.30	3.2	0.03	0.16	0.00	0.00	0.81
DDO181	2.90	4.0	0.07	0.17	0.06	0.00	0.71
U8508	2.40	3.3	0.06	0.14	0.18	0.00	0.62
N3741	2.50	3.5	0.10	0.10	0.05	0.00	0.75
DDO183	3.20	4.6	0.06	0.13	0.05	0.00	0.76
DDO53	5.10	7.2	0.08	0.08	0.20	0.64	0.00
HoIX	2.00	2.8	0.30	0.26	0.20	0.17	0.07
DDO99	3.10	4.4	0.06	0.06	0.00	0.00	0.88
SexA	0.58	0.82	0.17	0.18	0.16	0.12	0.37
N4163	9.90	14.0	0.05	0.00	0.00	0.40	0.56
SexB	1.20	1.6	0.10	0.23	0.16	0.01	0.50
DDO125	7.10	10.0	0.03	0.12	0.00	0.01	0.84
e325-11	4.45	6.3	0.06	0.11	0.00	0.00	0.83
DDO190	4.70	6.7	0.14	0.23	0.20	0.09	0.33
HoI	10.0	14.0	0.09	0.08	0.07	0.08	0.69
DDO82	16.1	24.0	0.05	0.00	0.00	0.12	0.83
DDO165	12.6	18.0	0.17	0.05	0.23	0.33	0.22
e383-87	18.9	27.0	0.03	0.12	0.04	0.00	0.80
N3109	0.43	0.61	0.13	0.32	0.04	0.00	0.51
I5152	10.8	15.0	0.04	0.00	0.00	0.01	0.95
N2366	33.7	48.0	0.12	0.09	0.28	0.10	0.41
HoII	36.4	51. 0	0.12	0.06	0.17	0.11	0.55
N4214	7.50	11.0	0.03	0.00	0.00	0.03	0.94
I2574	86.3	120.0	0.16	0.07	0.08	0.56	0.13

N55	36.4	51.0	0.10	0.02	0.06	0.11	0.71

2.5 The Morphology-Density Relationship

Gas-poor galaxies are generally found to be less isolated than gas-rich galaxies (e.g., Dressler, 1980). This morphology–density relationship for dwarf galaxies (e.g., Mateo, 1998; Skillman et al., 2003a; Geha et al., 2006) provides a simple test for various models of dwarf galaxy evolution. In Figure 2.9, we see that dwarf galaxies in the ANGST volume clearly adhere to the morphology–density relationship. On average, dIs are significantly more isolated than dSphs, despite having similar mean total stellar masses. dTrans, on average, are slightly less isolated than dIs, but not to the same degree as dSphs (see §2.5.2). dSpirals are the most massive galaxies, and are also located in regions of intermediate isolation. These findings are in general agreement with earlier studies of LG dwarf galaxies (e.g., van den Bergh, 2000; Mateo, 1998; Tolstoy et al., 2009).

Models favoring internal mechanisms as the primary driver of gas loss (e.g., Dekel & Silk, 1986; Dekel & Woo, 2003) can reproduce a number of observed dwarf galaxy properties (e.g., surface brightness, rotation velocities; Woo et al., 2008). However, they are generally unable to account for the morphology–density relationship (e.g., Mayer, 2010). In contrast, models including the effects of tidal stirring have been able to reproduce a wide range of dwarf galaxy properties, including a canonical morphology–density relationship (e.g., Mayer et al., 2006; Mayer, 2010, and references therein). In the following sections, we directly compare results from the ANGST SFHs with different physical processes that affect the stellar and gas components in dwarf galaxies.

2.5.1 Comparing Stellar and Gas Masses

The relative amounts of gas and stellar mass along with SFHs can provide clues to the evolution of dwarf galaxies. In Figures 2.12 and 2.13, we show the gas mass and $M_{Gas}/M_{Baryonic}$, i.e., the sum of the gas and stellar masses, versus the total integrated stellar mass for each galaxy (excluding dTidals, as their HI content remains highly uncertain). Gas masses are HI masses taken from Karachentsev et al. (2004) that have been corrected by a factor of 1.4 to account for helium content. Stellar masses have been measured by integrating the SFHs and normalizing the observed area relative to D_{25}, to place all galaxies on equal footing.

In Figure 2.12, the gas-poor dSphs lie well below the $M_{Gas} = M_{Stellar}$ relation (grey dashed line. The remaining gas-rich galaxies generally follow this line, although there is significant dispersion. We also see that dTrans have lower stellar masses than dIs, and appear to more mass from stars than gas.

Figure 2.13 shows the gas mass fraction of the galaxies, color-coded by morphological type. The data show an upper envelope, defined by an increasing abundance of gas-rich galaxies at progressively higher masses. As expected, dSphs are dominated by stars rather than gas and dSpirals generally have low gas fractions. Comparatively, dIs show a large range in gas mass fractions, despite having similar stellar masses, and several galaxies have gas mass fractions approaching those of dSphs. dTrans typically have gas mass fractions below 0.5, indicating stars make up the majority of their baryonic mass.

Several galaxies are extreme outliers from the general trends in Figures 2.12 and 2.13. However, it is difficult to discern if this is the result of physical effects or incomplete observations. For example, HS 117 has an upper limit of $M_{HI} \sim 10^5$ $M_\odot$ (Huchtmeier et al., 2000), but uncertainties in the measurement make this value consistent with zero, which is the value reported in Karachentsev et al. (2004), who nevertheless classify it as a dI. Interestingly, Karachentsev & Kaisin (2007) detect low level Hα in HS 117, which reinforce the dI classification, but based on the lack of HI, they deem this a dSph. DDO 113 does not have a reliable HI detection in the literature. These galaxies do not have sufficiently well measured HI content for us to confidently interpret their position on these plots in a physical context.

Excluding the outliers, the general trends in Figure 2.12 allow us to assess the impact of internal and external drivers of gas loss/consumption on the evolutionary tracks of a present day gas-rich dwarf galaxy. By itself, SF will increase the stellar mass and decrease the HI mass, moving a galaxy down and to the right in Figure 2.12. The SF process will eventually halt as the gas densities become too low to continue forming stars (e.g., Kennicutt, 1989), leaving remnant gas. Stellar feedback is an appealing method for gas removal (e.g., Dekel & Silk, 1986), but it has shortcomings. Although stellar feedback would, in principle, remove gas with minimal effect on the stellar content (down on Figure 2.12), simulations show that the gravitational potentials of most dwarf galaxies are too deep for gas to completely escape (e.g., Mac Low & Ferrara, 1999; Marcolini et al., 2006; Revaz et al., 2009), making this a implausible mechanism

for gas removal in dwarf galaxies. A galaxy could move up in Figure 2.12 by adding gas through interaction with another low mass galaxy, inflow, and/or accretion (e.g., Kereš et al., 2005), however the details of gas acquisition by galaxies in the low mass regime considered in this paper are still not entirely clear. It is also important to note that stellar feedback and SF processes alone cannot reproduce the morphology–density relationship, suggesting that external processes must play a critical role in gas loss and dwarf galaxy evolution.

Models of external interactions, notably 'tidal stirring' (e.g., Mayer et al., 2001a, b), hold promise for explaining gas loss in dwarf galaxies. Tidal stirring posits that a combination of ram pressure stripping and gravitational forces exerted on a dwarf galaxy by a nearby massive galaxy can turn a gas-rich into a gas-poor galaxy. Specifically, tidal stirring models show that both gas and stellar mass can be removed during a close passage, which would move a galaxy down and left in Figure 2.12. Not only does this provide a simple gas removal mechanism, it also naturally produces dSphs. In the SF and stellar feedback scenario, a present day gas-rich galaxy could only lose gas mass and gain stellar mass (down and right in Figure 2.12). Thus, gas-rich dwarf galaxies with larger stellar masses could only produce more massive gas-poor dSphs, which are not commonly observed. Instead, tidal stirring modeling indicates that massive gas-rich dwarf galaxies could lose sufficient stellar and gas mass through repeated interactions to become a lower mass dSph. The morphology–density relationship is thus a natural product of this model. In addition, as tidal stirring only impact galaxies during interactions, SF can proceed as expected in all non-interacting galaxies, and thus dwarf galaxies would generally have extended SFHs and follow the observed mass–metallicity relationship.

One tenable scenario for gas loss and dwarf galaxy evolution would be that a gas-rich galaxy consumes gas through SF and enriches the ISM through stellar feedback. A close passage to a massive galaxy could then remove stellar and/or gas mass from the dwarf galaxy. The extended SFHs of the typical dwarf galaxy suggests that it would take multiple close passages for a galaxy to lose its entire gas supply. Thus, once the dwarf galaxy is no longer interacting with the massive galaxy, it could resume the SF process. Further, the dwarf galaxy could also accrete gas while not interacting with the massive galaxy which would replenish its gas supply (moving up in Figure 2.12). Repetition of this process could provide a simple explanation for the sustained but episodic SFH of

most observed dwarf galaxies.

When comparing tidal indices to the gas mass fractions (Figure 2.14) we find that all dwarf galaxies in dense environments ($\Theta \gtrsim 1.5$) are gas-poor, suggesting that there may be a critical density for the transition from gas-rich to gas-poor. More detailed modeling of dwarf galaxy group dynamics, including properties of individual dwarf galaxies (e.g., Peñarrubia et al., 2008), are needed to quantify the specifics of these speculative scenarios.

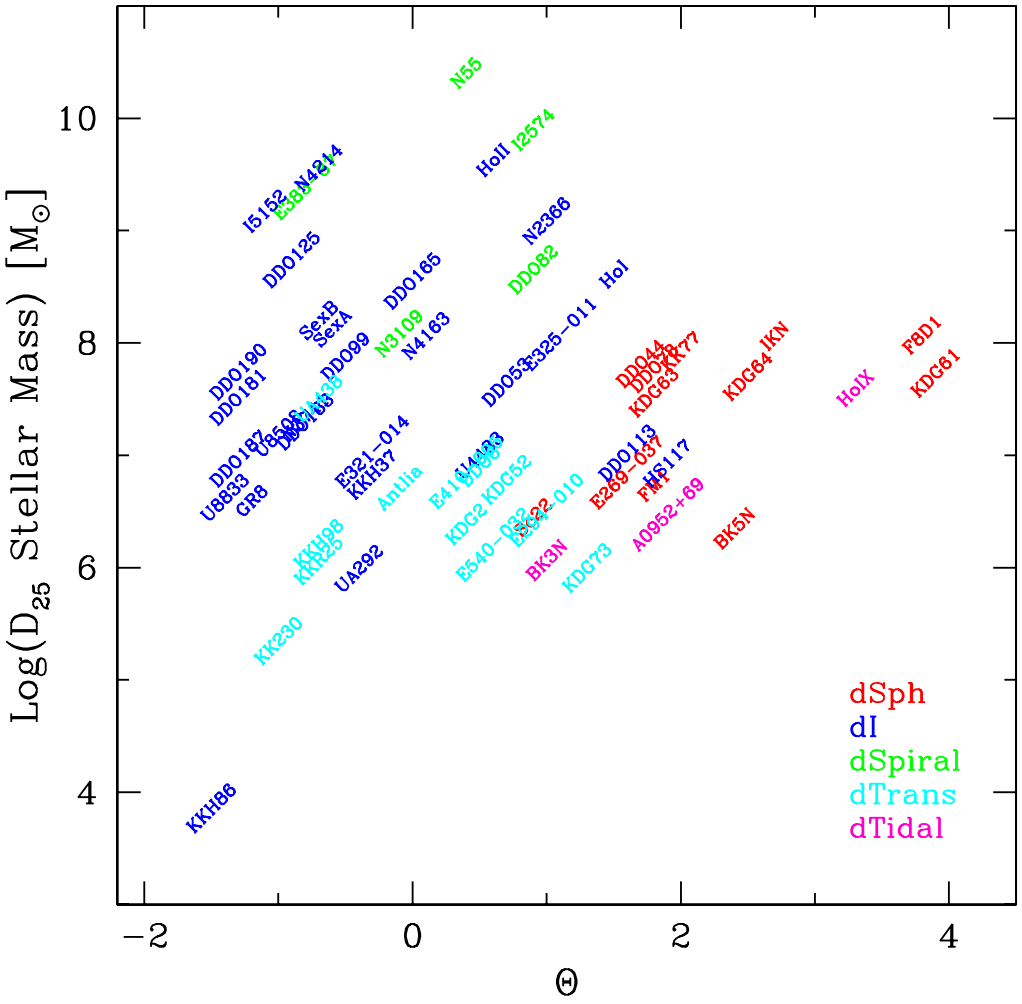

Figure 2.9 The observed morphology–density relationship for the ANGST dwarf galaxies. Integrated stellar masses have been derived from the SFHs in Figure 2.3, and normalized to $D_{stellar}$ to account for differences in the observed areas. The tidal indices, Θ, have been taken from Karachentsev et al. (2004). Negative values of Θ represent isolated galaxies, while positive values represent typical group members. We note dSphs, dIs, and dTrans have similar stellar masses, despite being located in different environments. This is in agreement with studies of dwarf galaxies in both the LG and SDSS samples (e.g., Mateo, 1998; Geha et al., 2006).

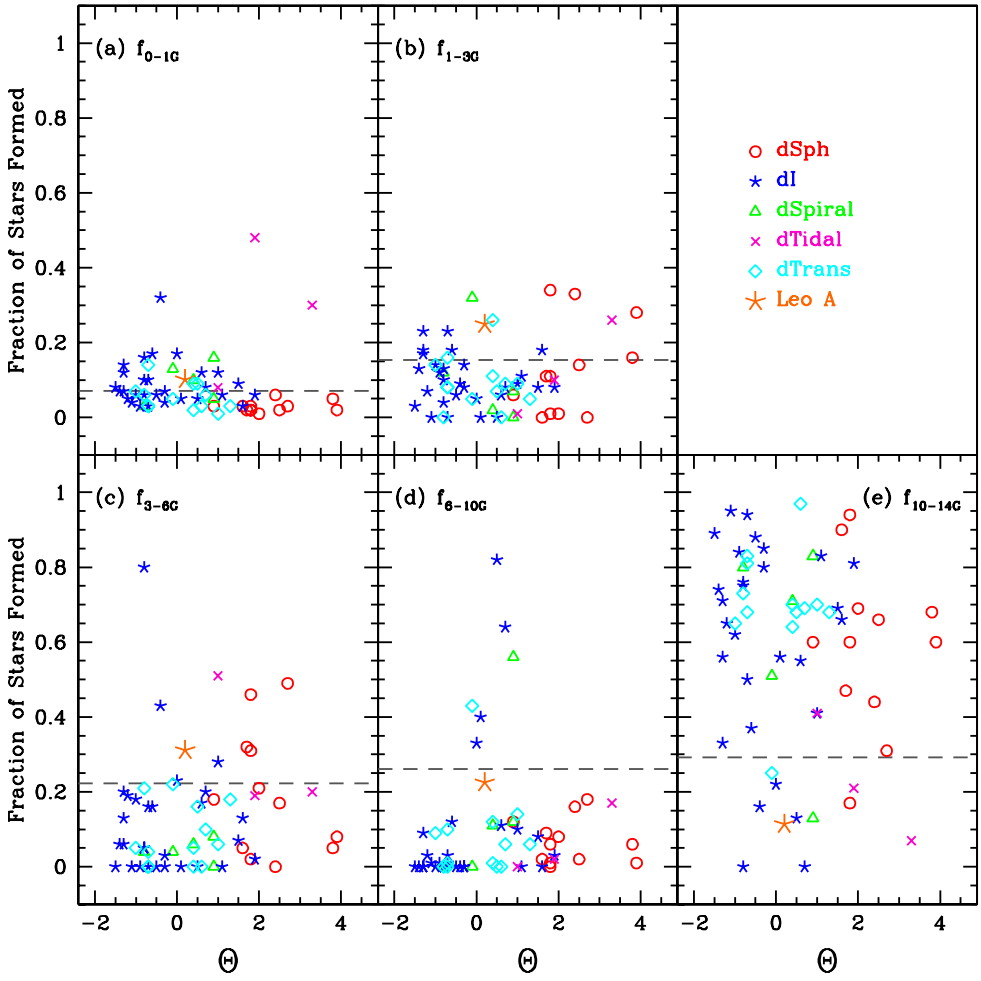

Figure 2.10 The cumulative SFHs, i.e., the fraction of total stellar mass formed, for each galaxy shown as a function of the tidal index Θ and morphological type. The time bins are such that f_{0-1G} = 0-1, f_{1-3G} = 1-3, f_{3-6G} = 3-6, f_{6-10G} = 6-10, f_{10-14G} = 10-14 Gyr ago. The tidal indices, Θ, have been taken from Karachentsev et al. (2004). Negative values of Θ represent isolated galaxies, while positive values represent typical group members. LG dI Leo A has been plotted for comparison, as it has a well constrained ancient SFH (Cole et al., 2007), which shows suppressed levels of ancient SF, $\lesssim 15\%$ of total stellar mass formed. Very few of the the best fit SFHs of the ANGST galaxies show similarly low levels of ancient SF.

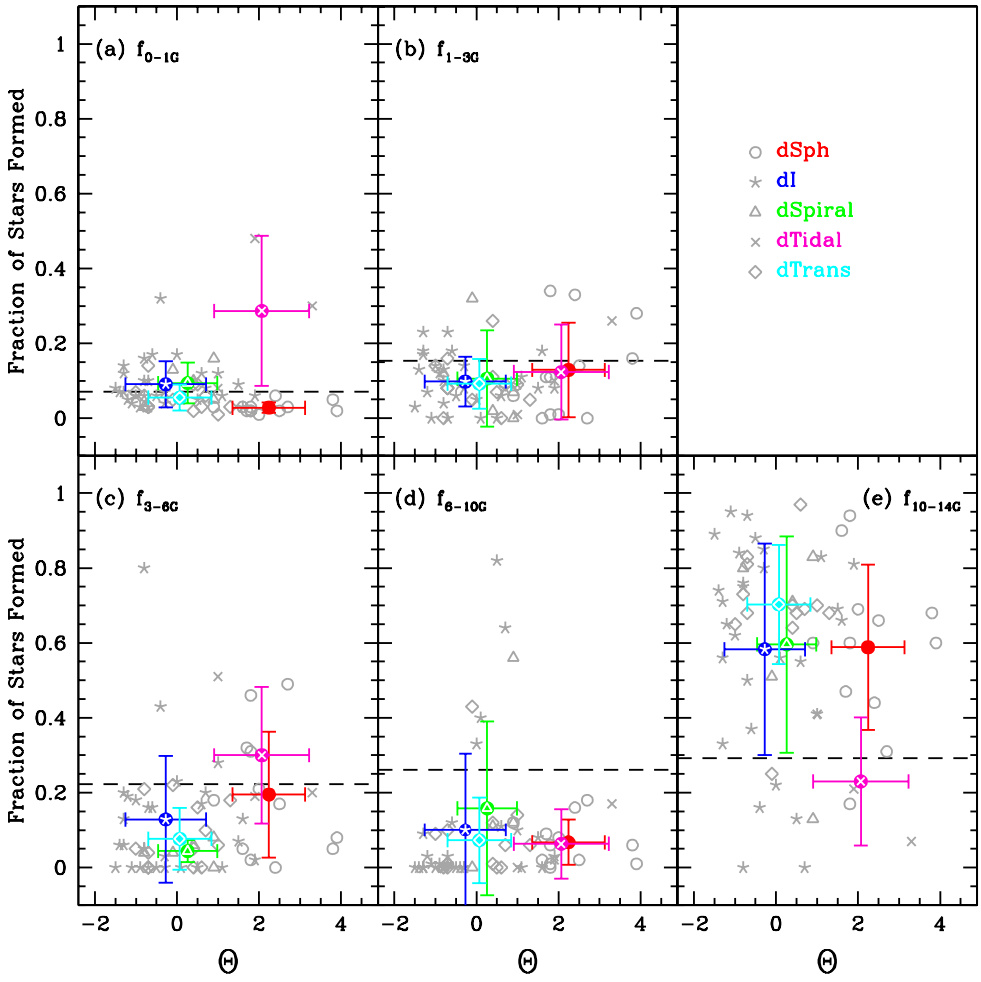

Figure 2.11 The dwarf galaxy morphology–density relationship represented by the cumulative SFH, i.e., the fraction of total stellar mass formed, as a function of tidal index, Θ, and morphological type. The time bins are such that f_{0-1G} = 0-1, f_{1-3G} = 1-3, f_{3-6G} = 3-6, f_{6-10G} = 6-10, f_{10-14G} = 10-14 Gyr ago. The tidal indices, Θ, have been taken from Karachentsev et al. (2004). Negative values of Θ represent isolated galaxies, while positive values represent typical group members. The grey points are the individual galaxies, the colored points and the mean values with 1σ error bars showing the scatter in both Θ and fraction of stars formed. While the dIs tend to be more isolated than other galaxies, i.e., more negative values of Θ, the fraction of stars formed in each time bin is generally consistent with a notable difference in the most recent time bin. The mean values of the dTrans galaxies indicate they are in between dIs and dSphs in their isolation and SF characteristics.

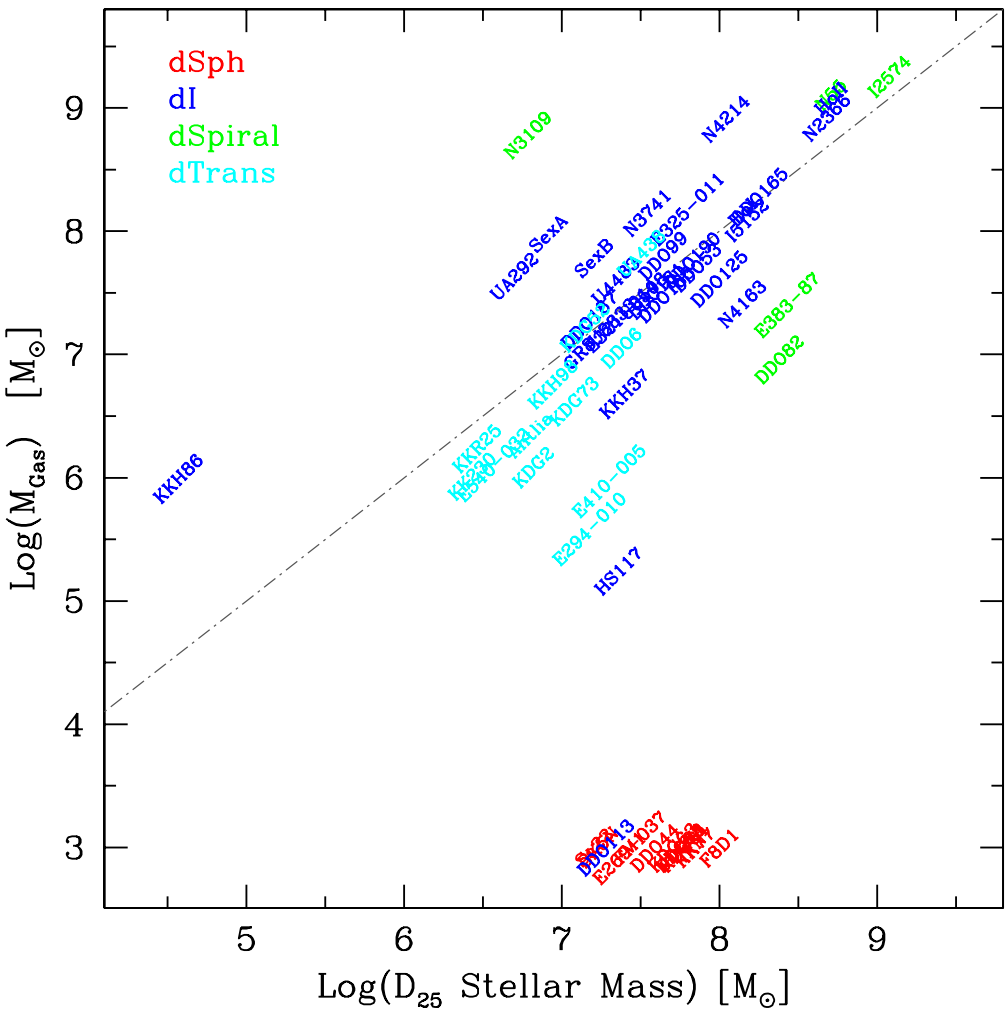

Figure 2.12 M_{Gas} plotted versus $\log(M_{stellar})$, the total integrated stellar mass from the SFHs (Figure 2.3), normalized to D_{25} to account for differences in the observed areas. We computed M_{Gas} by correcting the HI masses from Karachentsev et al. (2004) by a factor of 1.4 to account for helium content. The grey dashed line represents $M_{Gas} = M_{stellar}$. Considering a present day gas-rich galaxy, SF will increase the stellar mass and decrease the gas mass, moving the galaxy down and to the right. Gas removal will move a galaxy downward, while gas addition, e.g., accretion, moves a galaxy up. Stellar mass loss moves a galaxy to the left. SF and stellar feedback alone cannot transform a gas-rich galaxy into a dSph, however models including external effects, e.g., ram pressure stripping and tidal forces, can remove sufficient stellar and gas mass to transform a gas-rich into a gas-poor galaxy (see §2.5.1).

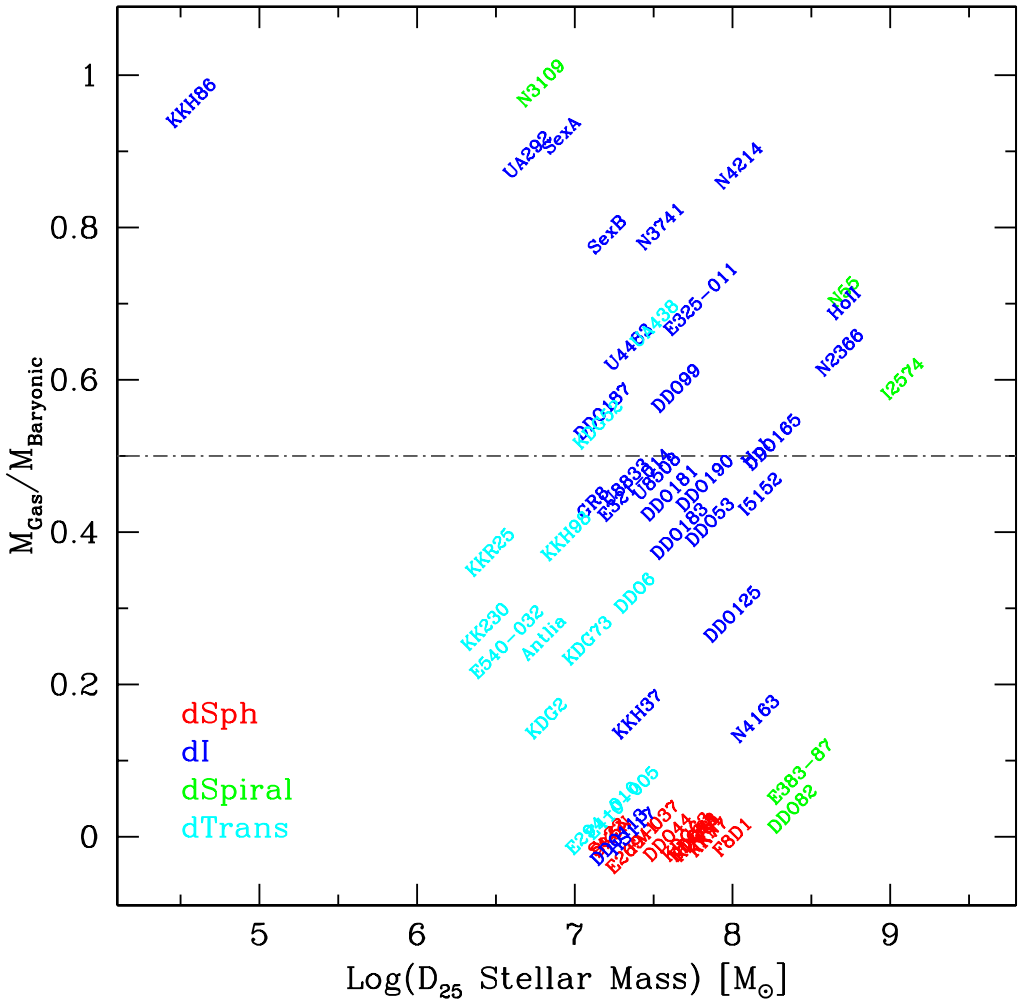

Figure 2.13 The ratio of gas mass to total baryonic mass (i.e., the gas fraction; M_{Gas} to M_{Gas} + $M_{stellar}$) plotted versus the total stellar mass. We computed M_{Gas} by correcting the HI masses from Karachentsev et al. (2004) by a factor of 1.4 to account for helium content. The total integrated stellar masses are from the SFHs (Figure 2.3), normalized to D_{25} to account for differences in the observed areas. The mean stellar masses for dSphs, dIs, and dTrans are comparable. Both dIs occupy a broad dynamic range in gas fraction, dTrans typically have gas fractions < 0.5, and dSphs are devoid of gas.

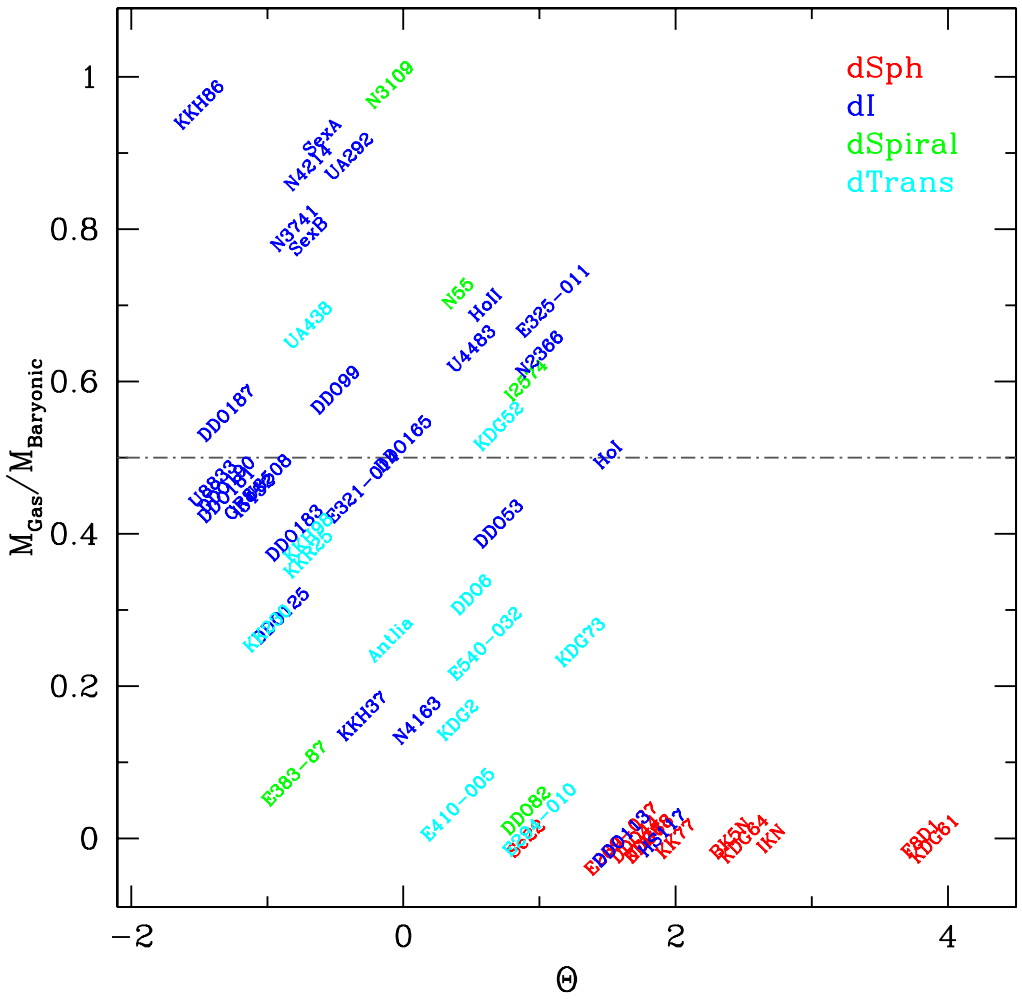

Figure 2.14 The ratio of gas mass to total baryonic mass (i.e., the gas fraction; M_{Gas} to $M_{Gas} + M_{stellar}$) plotted versus the tidal index, Θ. The tidal indices, Θ, have been taken from Karachentsev et al. (2004). Negative values of Θ represent isolated galaxies, while positive values represent typical group members. HI masses have been taken from Karachentsev et al. (2004). We computed M_{Gas} by correcting the HI masses from Karachentsev et al. (2004) by a factor of 1.4 to account for helium content. The total integrated stellar masses are from the SFHs (Figure 2.3), normalized to D_{25} to account for differences in the observed areas. Gas-poor galaxies typically have positive tidal indices, while gas-rich galaxies have predominantly negative values. It is interesting to note that for $\Theta \gtrsim 1.5$, there are no gas-rich galaxies.

2.5.2 The Role of Transition Dwarf Galaxies

With little evidence of recent SF, yet detectable amounts of HI, dTrans may hold clues to the transformation of gas-rich to gas-poor galaxies. Synthesizing several previous studies, there are two favored scenarios for their origins, namely that dTrans are either in the last throes of SF or are observed during temporary lulls between episodes of elevated SF (e.g., Côté et al, 1997; Mateo, 1998; Grebel et al., 2003; Skillman et al., 2003a; Côté et al., 2009).

Ambiguity in the classification of dTrans can make understanding their properties difficult. For the sake of consistency, we adopt the definition presented in Mateo (1998), which classified transition dwarf galaxies to be those with $M_{HI}/L_B > 0.1$ and no evidence of *significant* SF as traced by Hα. Though this definition has provided a quantitative discriminant for identifying transition galaxies, it does suffer some shortcomings. Specifically, Hα, which measures SF from ionizing photons over timescales $\lesssim$ 10 Myr, may not be able to distinguish between a temporary lull in ongoing SF and a longer quiescent period (e.g., McQuinn et al., 2009, 2010a). Further, an underpopulated upper stellar IMF (e.g., Lee et al., 2009; Meurer et al., 2009) could also lead to no Hα detection, despite other evidence of very recent SF. D. Weisz et al. (In Prep) will explore the detailed CMDs and recent SFHs of dTrans, providing a more robust view of SF processes in these galaxies and reconciling conflicting literature classifications for some galaxies. However, for the scope of this paper we retain the classification scheme of Mateo (1998).

Compared to dIs, on average, dTrans are slightly less isolated, have lower M_{HI}/L_B, and have formed a smaller percentage of their stellar mass in the most recent 1 Gyr (Figures 2.11, 2.15, and 2.16). Combining the tidal indices with the gas fractions and stellar masses (Figures 2.13 and 2.14), we find that dTrans with lower gas-fractiona typically have higher tidal indices. ESO294-10 and ESO410-5 both have low gas fractions and are among the least isolated dTrans ($\Theta > 0$). However, KDG 73 has a high gas fraction and the most positive tidal index among dTrans. This suggests that KDG 73 could be in the process of making a close passage to M81. Galaxies with intermediate gas fraction values (i.e., ~ 0.5; Antlia, DDO 6, ESO540-32, KDG 2) generally have tidal indices of ~ 0. The dTrans with the highest gas fractions ($\gtrsim 0.6$; KKR 25, UA 438, KKH 98, KK 230) generally have negative tidal indices. KDG 52 is the exception as it

has a gas fraction of ~ 0.7 with a positive tidal index.

We find that these general trends are in agreement with both models in the literature. Namely, that there are two ways to produce a dTrans: either through gaps in the current SF episodes, which can explain gas-rich and isolated dTrans or through a close passage to a massive galaxy, in which a previously gas-rich galaxy may now be in the process of becoming a gas-poor dSph. KDG 73 could be one such gas-rich galaxy that may soon undergo a significant transformation. The evolutionary scenario for KDG 52 remains a bit of mystery. We do note that despite the recent major interaction in the M81 Group, the HI maps of KDG 73 and KDG 52 show no evidence of tidal disruption (Ott et al., 2008).

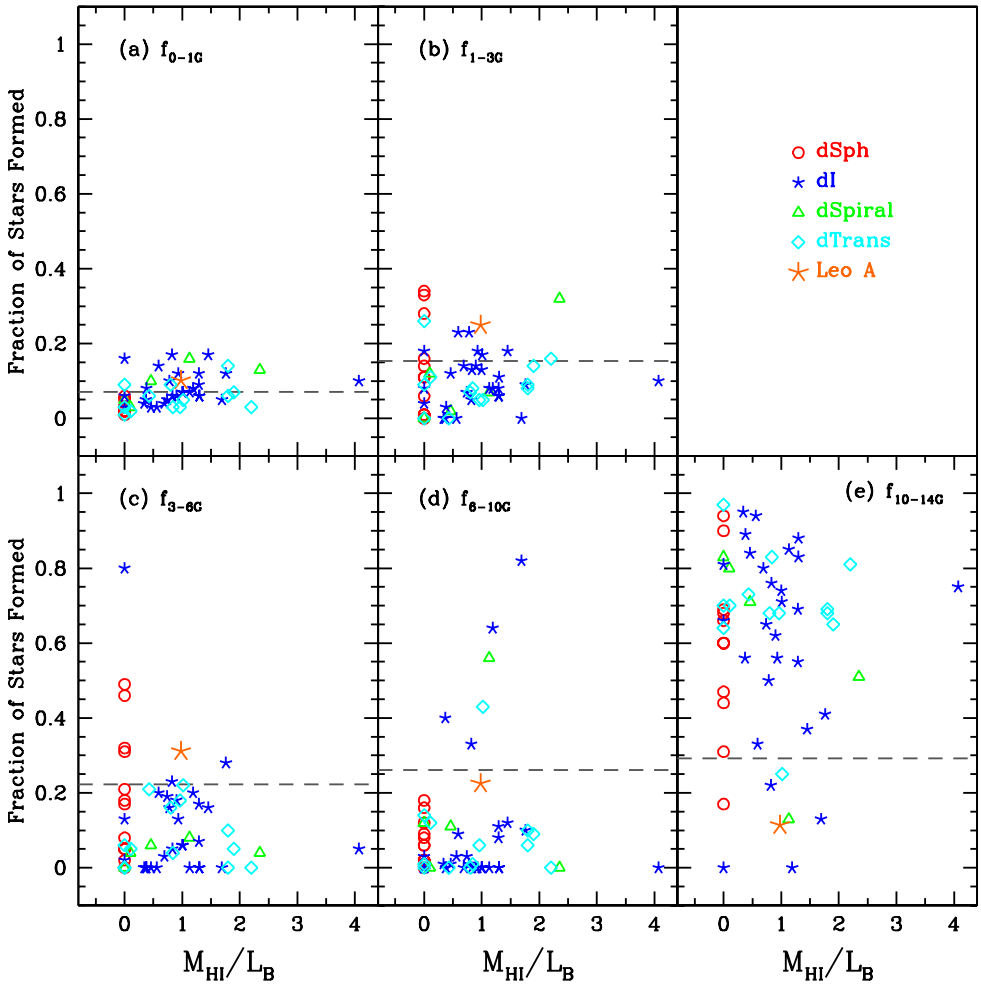

Figure 2.15 The cumulative SFHs, i.e., the fraction of total stellar mass formed, for each galaxy shown as a function of M_{HI}/L_B (Karachentsev et al., 2004) and morphological type. The time bins are such that f_{0-1G} = 0-1, f_{1-3G} = 1-3, f_{3-6G} = 3-6, f_{6-10G} = 6-10, f_{10-14G} = 10-14 Gyr ago. Mateo (1998) employ the following criteria to identify dTrans: $M_{HI}/L_B > 0.1$ and no significant level of recent SF as indicated by Hα.

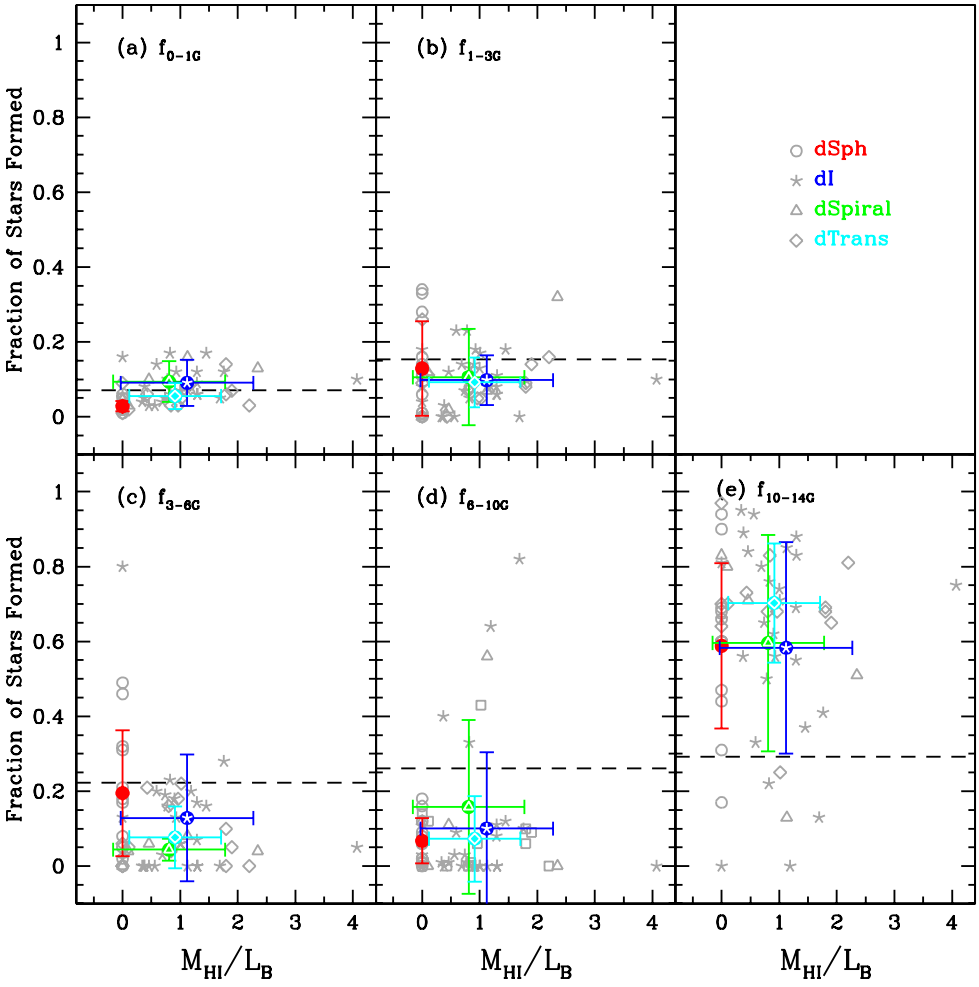

Figure 2.16 The cumulative SFHs, i.e., the fraction of total stellar mass formed, for each galaxy shown as a function of M_{HI}/L_B (Karachentsev et al., 2004) and morphological type The time bins are such that f_{0-1G} = 0-1, f_{1-3G} = 1-3, f_{3-6G} = 3-6, f_{6-10G} = 6-10, f_{10-14G} = 10-14 Gyr ago. The grey points represent individual galaxies, while the colored points show the mean values per morphological type with 1σ error bars denoting the scatter. The dTrans galaxies are generally consistent with dIs in both SF and $\mathrm{M}_{HI}/\mathrm{L}_B$ values.

2.6 Summary

We uniformly analyzed SFHs of 60 dwarf galaxies in the nearby universe based on observations and data processing done as part of the ANGST program. While the SFHs of individual galaxies sare quite diverse, we find that the mean SFHs of the different morphological types are indistinguishable outside the most recent $\sim$ 1 Gyr. On average, the typical dwarf galaxy formed $\sim$ 60% of its stellar mass by z $\sim$ 2, consistent with findings in more massive galaxies (e.g., Thomas et al., 2005). The only clear difference in the SFHs per morphological type is seen in the more recent 1 Gyr, where the average dSph has a statistically significant lower level of SF. Further, simple models of SFHs, e.g., constant, single epoch, declining exponential, are inconsistent with most dwarf galaxy SFHs.

The dwarf galaxies in the ANGST sample show a strong morphology–density relationship. This suggests that internal mechanisms, e.g., stellar feedback, cannot solely account for gas-loss in dwarf galaxies, as the corresponding models are unable to produce this observed relationship. Instead, we find best consistency with the model of 'tidal stirring' (e.g., Mayer et al., 2006), which can broadly explain the extended SFHs as well as the observed morphology–density relationship. Similarly, the consistency of the SFHs suggests that dIs and dSphs should have similar RGB metallicities, in contrast with the findings of Grebel et al. (2003).

We also identify 13 dTrans in the sample, based on the literature definition of present day gas fraction and SF as measured by Hα (e.g., Mateo, 1998). Within this sample of dTrans, we find that high gas fraction is associated with more isolated galaxies, while lower gas fractions are less isolated. This suggests that there are two mechanisms that can produce the observed dTrans characteristics: the isolated gas-rich galaxies are simply between episodes of SF due to the stochastic nature of SF in low mass galaxies, while the less isolated galaxies could be in the process of interacting with a massive companion.

Chapter 3

How Typical Are the Dwarf Galaxies of the Local Group?

3.1 Introduction

Dwarf galaxies in the Local Group (LG) are among the most well-studied galaxies in the universe. Detailed determinations of their kinematics, metallicities, and stellar contents serve as a basis for much of what we understand about the formation and evolution of both individual and groups of galaxies (see reviews by Mateo, 1998; van den Bergh, 2000; Tolstoy et al., 2009). In particular, Hubble Space Telescope (HST) observations of resolved stellar populations in LG dwarf galaxies have resulted in high quality color-magnitude diagrams (CMDs) from which we can directly determine the history of star formation and chemical evolution for individual galaxies (e.g., Tolstoy et al., 2009).

Although we often draw on results from LG studies to explain the evolution of galaxies in the broader universe, whether LG dwarf galaxies are representative of all dwarf galaxies remains an open question (e.g., van den Bergh, 2000). The LG is a relatively dense environment with a specific history of mass accretion and interaction. Thus it is difficult to definitively ascribe the observed properties of LG dwarf galaxies to any particular mechanism. Quantifying precisely how typical LG dwarf galaxies are provides a crucial foundation for understanding dwarf galaxies in the broader universe.

Directly comparing the stellar contents of LG dwarf galaxies to those in the nearby universe requires uniform data sets of comparable quality and size. Historically, studies

of resolved stellar populations in nearby dwarf galaxies have focused on small samples or individual galaxies, and employed different analysis techniques, leading to larger systematic uncertainties when comparing different studies. Recent projects described by Holtzman et al. (2006) and Dalcanton et al. (2009) have resulted in two uniform multi-color photometric databases of the resolved stellar populations of dwarf galaxies in the LG and Local Volume, which, for the first time, allows a direct unbiased study of dwarf galaxies in a large volume, spanning a wide range of environments.

The Local Volume contains a diverse set of galaxies and environments, some of which have no analogs in the LG. For example, the M81 Group is known to have undergone a recent major interaction (e.g., Yun et al., 1994; Yun, 1999), which has likely influenced star formation and gas-loss in the M81 Group dwarf galaxies (e.g., Weisz et al., 2008), and may even be responsible for the creation of new tidal dwarf galaxies (e.g., Makarova et al., 2002). At the opposite extreme in density, isolated 'field' dwarf galaxies may have fewer or no interactions with more massive companions, which could result in distinctly different patterns of star formation and chemical evolution when compared to typical group members.

In this paper, we present a comparison of the SFHs and morphology–density relationships of dwarf galaxies in the LG and the local universe. We measured the SFHs from uniformly processed photometry, as well as identical selections of SFH code and stellar evolution models, minimizing the effects of potential systematics. In §3.2, we summarize the sample selection and data. The technique of measuring SFHs from optical CMDs is briefly reviewed in §3.3. In §6.5, we compare the SFHs and examine the morphology–density relationship for both LG and nearby dwarf galaxies. Cosmological parameters used in this paper assume a standard WMAP cosmology (Dunkley et al., 2009).

3.2 The Data

3.2.1 The Local Group Dwarf Galaxy Sample

For this comparison, we consider a sample of LG dwarf galaxies based on those discussed in Mateo (1998) (see Table 3.1). All galaxies have multi-color optical imaging taken with either the Advanced Camera for Surveys (ACS; Ford et al., 1998) or the Wide

Field Planetary Camera 2 (WFPC2; Holtzman et al., 1995) aboard HST. Following the convention of Mateo (1998), we have excluded the LMC and SMC from this paper. Similarly, we have omitted NGC 3109, NGC 205, NGC 6822, and NGC 55 as these are sufficiently large galaxies that their status as true dwarf galaxies is ambiguous. Additionally, HST imaging of these galaxies only subtends a small fraction ($\lesssim 10\%$) of the total optical body, and may not be representative of the entire galaxy's SFH. Similarly, we have excluded 'ultra-faint LG dwarf galaxies (e.g., Belokurov et al., 2006) and Andromeda companions discovered more recently than And VII (e.g., Zucker et al., 2004) from this comparison. These sets of galaxies do not yet have publicly available photometry that has been identically processed as the galaxies we consider in this paper. The resulting LG sample covers a range of M_B from -7.13 (Ursa Minor) to -15.57 (IC1613).

We divide the sample into three categories, dwarf spheroidal (dSph), dwarf irregular (dI), and transition dwarf (dTrans) galaxies according to the morphological classifications in Mateo (1998). For the purpose of comparing the SFHs, we merge dwarf elliptical (dE; NGC 147 and NGC 185; e.g., Mateo, 1998) into a canonical gas-poor galaxy (dSph) category. Following the convention of Mateo (1998), we designate dTrans as those which have $M_{HI}/L_B > 0.1$ and no *significant* recent star formation, as measured by Hα. We note that Mateo (1998) classifies Pegasus as a dTrans, but Skillman et al. (2003a) detect significant levels of Hα, and thus we consider it to be a dI. In total, the LG sample has 19 dSphs, 7 dIs, and 4 dTrans (Table 3.1).

The SFHs used for this comparison are based on CMDs presented in Dolphin et al. (2005), but have been re-measured (A. Dolphin et al., In Prep) with updated Padova stellar evolution models (Marigo et al., 2008). These SFHs are based on photometry of HST/WFPC2 imaging which was uniformly processed using HSTPHOT (Dolphin, 2000) as part of the Local Group Stellar Populations Archive[2] (Holtzman et al., 2006). Five of the galaxies (Cetus, Tucana, IC 1613, Leo A, and LGS3) were more recently observed with ACS as part of the Local Cosmology with Isolated Dwarfs program (LCID; Gallart et al., 2007), and have significantly deeper CMDs compared to the corresponding WFPC2 photometry (e.g., Cole et al., 2007; Monelli et al., 2010). Photometry of

[2] http://astronomy.nmsu.edu/holtz/archival/html/lg.html

ACS observations was performed with DOLPHOT[3] , a version of HSTPHOT with an ACS specific module, which allows us to include these five SFHs without compromising uniformity.

Table 3.1: The LG Sample of Dwarf Galaxies

Galaxy Name (1)	Main Disturber (2)	M_B (3)	D (Mpc) (4)	A_V (5)	Type (6)	Θ (7)
UrsaMin	MW	-7.13	0.08	0.11	dSph	3.3
LGS3	M31	-7.96	0.61	0.14	dTrans	1.7
And V	M31	-8.41	0.78	0.41	dSph	2.8
Draco	MW	-8.74	0.09	0.09	dSph	3.0
Carina	MW	-8.97	0.10	0.21	dSph	2.7
Leo II	MW	-9.23	0.20	0.06	dSph	1.7
And III	M31	-9.30	0.72	0.19	dSph	3.5
And II	M31	-9.33	0.65	0.21	dSph	2.4
Antlia	M31	-9.38	1.30	0.24	dTrans	-0.1
Sculptor	MW	-9.77	0.08	0.06	dSph	2.8
Cetus	M31	-10.18	0.77	0.10	dSph	0.5
Phoenix	MW	-10.22	0.41	0.05	dTrans	0.8
And VI	M31	-10.80	0.83	0.21	dSph	1.7
And I	M31	-10.87	0.76	0.18	dSph	3.7
Leo I	MW	-10.97	0.25	0.12	dSph	1.5
DDO210	M31	-11.09	0.94	0.17	dTrans	1.6
Pegasus	M31	-11.47	0.95	0.22	dI	1.2
SagDIG	MW	-11.49	1.11	0.40	dI	-0.3
Fornax	MW	-11.50	0.14	0.07	dSph	2.3
AndVII	M31	-11.67	0.94	0.64	dSph	2.0
LeoA	MW	-11.70	0.79	0.07	dI	0.1
IC10	MW	-12.60	0.81	5.0	dI	1.8

[3] http://purcell.as.arizona.edu/dolphot/

Sagittarius	MW	-12.80	0.03	0.40	dSph	4.0
Tucana	MW	-12.94	0.86	0.11	dSph	-0.1
SexA	MW	-13.71	1.30	0.14	dI	-0.6
SexB	MW	-13.88	1.40	0.10	dI	-0.7
WLM	M31	-13.95	0.93	0.12	dI	0.3
N185	M31	-14.76	0.61	0.61	dSph/dE	3.5
N147	M31	-14.79	0.72	0.58	dSph/dE	3.0
IC1613	M31	-15.57	0.74	0.08	dI	0.9

3.2.2 The ANGST Dwarf Galaxy Sample

The ACS Nearby Galaxy Survey Treasury (ANGST; Dalcanton et al., 2009)[4] sample contains dwarf galaxies that are located beyond the zero velocity surface of the LG and within $D \sim 4$ Mpc (see Table 3.2). The sample contains a mixture of field and group galaxies, the latter of which are located in the M81 Group ($D_{M81} \sim 3.6$ Mpc) and in the direction of the NGC 253 clump ($D_{N253} \sim 3.9$ Mpc) in the Sculptor Filament (Karachentsev et al., 2003). For comparison, we have selected all dSphs, dIs, and dTrans from the ANGST sample, as defined in D. Weisz et al. (In Prep). We note that several ANGST galaxies (Antlia, GR8, Sex A, Sex B, IC 5152, and UGCA 438) are considered in the LG of Mateo (1998). Of these galaxies, Antlia, Sex A, and Sex B are on the periphery of the LG, and we classify them as part of the LG sample. TRGB distance determinations (e.g., Dalcanton et al., 2009) place IC 5152, Gr8, and UA 438 clearly beyond the zero velocity surface of the LG, and we thus include them in the ANGST sample for this comparison.

The ANGST sample contains several reported dEs in the M81 Group: F8D1, BK5N, KDG 61, KDG 64, KK 77, FM 1, and DDO 71 (Caldwell et al., 1998; da Costa, 2007), which we included in the dSph category. Although the term dE has often been used to describe early type dwarf galaxies outside the LG (e.g., Geha et al., 2006), here we adopt the term dSph, which has historically been used in LG studies (e.g., Mateo, 1998, and references therein) as a number of the early type ANGST dwarf galaxies have luminosities and CMDs that are similar to dSphs in the LG. We note that the

[4] http://archive.stsci.edu/prepds/angst/

ANGST sample includes 3 putative tidal dwarf galaxies (Holmberg IX, A0952+69, and BK3N; Makarova et al., 2002; Sabbi et al., 2008; Weisz et al., 2008), which have no counterparts in the LG. Their status as true galaxies is ambiguous (e.g., Weisz et al., 2008), and we thus exclude them from this comparison. Similar to the LG sample, we also exclude comparably massive ANGST galaxies (IC 2574, DDO 82, ESO383-87, NGC 4214; i.e., morphological T types of 8 or 9; Karachentsev et al., 2004) from this comparison.

The faint end of the ANGST galaxy luminosity function is likely not complete due to a selection biases against identifying faint low luminosity surface brightness galaxies. For example, the ANGST sample does not include a number of recently discovered low surface brightness M81 Group galaxies (Chiboucas et al., 2009), as they do not yet have HST imaging publicly available. The final sample of ANGST galaxies in this paper includes 12 dSphs, 25 dIs, and 11 dTrans, spanning a range in M_B from -8.49 (KK230) to -16.57 (Ho II).

The SFHs of the ANGST dwarf galaxies are presented in D. Weisz et al. (In Prep). Data reduction and analysis, i.e., photometry and SFHs, have been done in a manner consistent with the LG sample, making it possible to directly compare the data with that of the LG sample.

Table 3.2: The ANGST Sample of Dwarf Galaxies

Galaxy Name (1)	Main Disturber (2)	M_B (3)	D (Mpc) (4)	A_V (5)	Type (6)	Θ (7)
KK230	M31	-8.49	1.3	0.04	dTrans	-1.0
KKR25	M31	-9.94	1.9	0.03	dTrans	-0.7
FM1	M82	-10.16	3.4	0.24	dSph/dE	1.8
KKH86	N5128	-10.19	2.6	0.08	dI	-1.5
KKH98	M31	-10.29	2.5	0.39	dTrans	-0.7
BK5N	N3077	-10.37	3.8	0.20	dSph/dE	2.4
Sc22	N253	-10.39	4.2	0.05	dSph/dE	0.9
KDG73	M81	-10.75	3.7	0.06	dTrans	1.3

IKN	M81	-10.84	3.7	0.18	dSph	2.7
E294-010	N55	-10.86	1.9	0.02	dTrans	1.0
E540-032	N253	-11.22	3.4	0.06	dTrans	0.6
KKH37	I342	-11.26	3.4	0.23	dI	-0.3
KDG2	N253	-11.29	3.4	0.07	dTrans	0.4
UA292	N4214	-11.36	3.1	0.05	dI	-0.4
KDG52	M81	-11.37	3.5	0.06	dTrans	0.7
KK77	M81	-11.42	3.5	0.44	dSph/dE	2.0
E410-005	N55	-11.49	1.9	0.04	dTrans	0.4
HS117	M81	-11.51	4.0	0.36	dI	1.9
DDO113	N4214	-11.61	2.9	0.06	dI	1.6
KDG63	M81	-11.71	3.5	0.30	dSph	1.80
DDO44	N2403	-11.89	3.2	0.13	dSph	1.7
GR8	M31	-12.00	2.1	0.08	dI	-1.2
E269-37	N4945	-12.02	3.5	0.44	dSph	1.6
DDO78	M81	-12.04	3.7	0.07	dSph	1.8
F8D1	M81	-12.20	3.8	0.33	dSph/dE	3.8
U8833	N4736	-12.31	3.1	0.04	dI	-1.4
E321-014	N5128	-12.31	3.2	0.29	dI	-0.3
KDG64	M81	-12.32	3.7	0.17	dSph/dE	2.5
DDO6	N253	-12.40	3.3	0.05	dTrans	0.5
DDO187	M31	-12.43	2.3	0.07	dI	-1.3
KDG61	M81	-12.54	3.6	0.23	dSph/dE	3.9
U4483	M81	-12.58	3.2	0.11	dI	0.5
UA438	N55	-12.85	2.2	0.05	dTrans	-0.7
DDO181	M81	-12.94	3.0	0.02	dI	-1.3
U8508	M81	-12.95	2.6	0.05	dI	-1.0
N3741	M81	-13.01	3.0	0.07	dI	-0.8
DDO183	N4736	-13.08	3.2	0.05	dI	-0.8
DDO53	M81	-13.23	3.5	0.12	dI	0.7
DDO99	N4214	-13.37	2.6	0.08	dI	-0.5
N4163	N4190	-13.76	3.0	0.06	dI	0.1

DDO125	N4214	-14.04	2.5	0.06	dI	-0.9
E325-11	N5128	-14.05	3.4	0.29	dI	1.1
DDO190	M81	-14.14	2.8	0.04	dI	-1.3
Ho I	M81	-14.26	3.8	0.15	dI	1.5
DDO165	N4236	-15.09	4.6	0.08	dI	0.0
IC5152	M31	-15.67	1.9	0.08	dI	-1.1
N2366	N2403	-15.85	3.2	0.11	dI	1.0
Ho II	M81	-16.57	3.4	0.10	dI	0.6

3.3 Measuring the Star Formation Histories

We briefly summarize the technique of measuring a SFH from a CMD, based on more detailed discussions of the methodology described in Dolphin (2002), Dolphin et al. (2005), and D. Weisz et al. (In Prep). The user specifies an assumed IMF and binary fraction, and allowable ranges in age, metallicity, distance, and extinction. Photometric errors and completeness are characterized by artificial star tests. From these inputs, many synthetic CMDs are generated to span the desired age and metallicity range. For this work, we have used synthetic CMDs sampling stars with age and metallicity spreads of 0.1 dex. These individual synthetic CMDs are then linearly combined along with a model foreground CMD to produce a composite synthetic CMD. The linear weights on the individual CMDs are adjusted to obtain the best fit as measured by a Poisson maximum likelihood statistic; the weights corresponding to the best fit are the most probable SFH. This process can be repeated at a variety of distance and extinction values to solve for these parameters as well.

To minimize systematic effects, we selected identical input parameters for each of the galaxies. Specifically, we chose a single power law stellar IMF with a spectral index of -1.30 with mass limits of 0.1 to 100 $M_{\odot}$ and a binary fraction of 0.35. Due to age-metallicity degeneracies in shallow CMDs (e.g., Gallart et al., 2005; Cole et al., 2005), we required metallicity to increase as a monotonic function of time, except in the case of the LCID galaxies, where chemical evolution was well determined without this constraint (e.g., Gallart et al., 2005; Cole et al., 2007; Monelli et al., 2010). Distances for the LG galaxies were taken from TRGB and CMD fits in Dolphin et al. (2005), while

we used TRGB distances from Dalcanton et al. (2009) for ANGST galaxies. Foreground extinction values for all galaxies were taken from the maps of Schlegel et al. (1998).

Uncertainties in the SFHs are the quadrature sum of systematic and statistical effects. The systematic errors are indicative of the uncertainties in the model isochrones. Statistical errors reflect counting statistics in each CMD bin, and are measured using 50 Monte Carlo realizations. See Dolphin (2002), Dolphin et al. (2005), and D. Weisz et al. (In Prep) for a more detailed discussion of errors in the SFHs. The error bars considered in this paper represent 1-σ scatter in the mean of the best fit SFHs.

3.4 Discussion

3.4.1 Comparing the Star Formation Histories

Cumulative SFHs, i.e., the fraction of stellar mass formed before a given time, allow a direct comparison between the SFHs of galaxies of different masses. In Figure 3.1, we plot the unweighted mean cumulative SFHs of the ANGST and LG dwarf galaxies, for each morphological type. The uncertainties shown represent the 1-σ scatter in the mean of the best fit SFHs. For each morphological type, we see that the two samples are consistent within uncertainties for all times considered. Specifically, a typical LG or ANGST dwarf galaxy formed $\sim$ 50–60% of its total stellar mass $\gtrsim$10 Gyr ago (z $\sim$ 2) and 30–40%, 1–10 Gyr ago (see Table 3.3). Thus the morphological differences between the dSph and dI classes are due to relatively recent changes in the SFHs over the past $\sim$ 1 Gyr.

We find that dSphs systematically lack young stars, relative to dIs and dTrans, for both the ANGST and LG sample. The average dSph formed only 1–3% of its total stellar mss in the most recent 1 Gyr compared to 7–9% for a typical dI and 4–6% for the average dTrans (see Table 3.3).

We have no ability to compare SFHs prior to z $\sim$ 2. At early these epochs, only ultra-deep CMDs reaching the ancient main sequence turnoff can reliably decipher the details of the ancient SFHs, e.g., epoch of the peak ancient SFR. Thus, while the two samples show excellent consistency in their cumulative SFHs, studies of the detailed ancient SFHs indicate that galaxies can show wide variation in their patterns of star formation at the oldest epochs (e.g., Cole et al., 2007; Monelli et al., 2010). These early variations

may show correlations with environment or other galaxy properties. However, we are not able to discern such differences for the vast majority of galaxies in our samples.

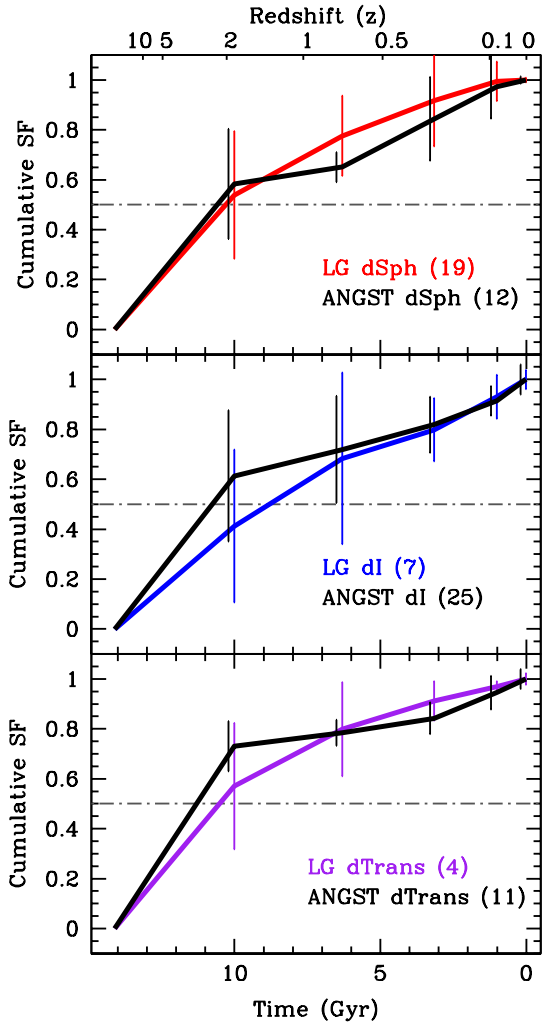

Figure 3.1 The mean cumulative SFHs, i.e., the fraction of the total stellar mass formed prior to a given time, for the LG and ANGST dwarf galaxies. We have divided them according to morphological type, indicating the LG values in color (dSphs: red; dIs: blue; dTrans: purple). The error bars represent the 1-σ scatter in the mean cumulative SFHs of the individual galaxies. The grey dashed-line indicates 50% of the total stellar mass. The SFHs of the LG and ANGST galaxies are consistent at all times. On average, a typical dwarf galaxy from either sample forms 50–60% of its stellar mass $\gtrsim$ 10 Gyr ago (z $\sim$ 2), and 30–40% 1–10 Gyr ago. The SFHs significantly differ among the morphological types only in the most recent 1 Gyr. dSphs have formed only 1–3% of their stellar mass, compared with 7–9% for dIs and 4–6% for dTrans.

Table 3.3: The Mean Cumulative SFHs of the LG and ANGST Dwarf Galaxies

Group	$f_{10-14Gyr}$	$f_{6-10Gyr}$	f_{3-6Gyr}	f_{1-3Gyr}	f_{0-1Gyr}
(1)	(2)	(3)	(4)	(5)	(6)
LG dSphs	0.54±0.26	0.24±0.16	0.14±0.18	0.08±0.09	0.01±0.01
ANGST dSphs	0.58±0.22	0.07±0.06	0.19±0.17	0.13±0.13	0.03±0.01
LG dIs	0.41±0.31	0.27±0.34	0.12±0.13	0.13±0.09	0.07±0.04
ANGST dIs	0.61±0.26	0.10±0.20	0.10±0.11	0.10±0.07	0.09±0.06
LG dTrans	0.57±0.25	0.23±0.19	0.11±0.08	0.05±0.05	0.04±0.02
ANGST dTrans	0.73±0.10	0.05±0.05	0.06±0.06	0.10±0.07	0.06±0.04

3.4.2 The Morphology–Density Relationship

In the LG, gas-rich dwarf galaxies are typically found to be more isolated than gas-poor dwarf galaxies (e.g., Mateo, 1998; van den Bergh, 2000). This relationship has been shown to hold true for dwarf galaxies in the broader universe (e.g., Geha et al., 2006; D. Weisz et al., In Prep), including dTrans in the Sculptor Group (Skillman et al., 2003a). In Figure 3.2, we compare the morphology–density relationships for LG and ANGST dwarf galaxies. As a measure of isolation, we use the tidal index of each galaxy as reported in Karachentsev et al. (2004), where more negative values indicate a higher degree of isolation. Typical group members have $\Theta \sim 0$. We also include points from ~ 250 galaxies from Karachentsev et al. (2004) with $M_B > -18.5$, to demonstrate the broader morphology-density relationship. Due to a likely high degree of incompleteness and uncertainties in the Θ values for a number of more distant galaxies, we only include these galaxies to provide a qualitative context.

The LG and ANGST samples show clear and well-matched morphology–density relationships. The dIs in both samples span a broad range of predominantly negative tidal indices, indicating that dIs are preferentially found away from dense environments. This result is consistent with previous studies of both the LG (e.g., Mateo, 1998; van den Bergh, 2000) and galaxies in the wider universe (e.g., Geha et al., 2006).

The ANGST sample has more dIs with $\Theta < -1.5$, which is due to the large field population of the sample. dSphs in the two samples typically have positive tidal indices and fainter values of M_B when compared to the dIs. A Kolmogorov-Smirnov (KS) test confirms that dIs and dSphs are not drawn from the same distribution in either environment or luminosity, with a less than 4×10^{-5} probability of having identical distributions.

In contrast with the sharp division in properties between dIs and dSphs, dTrans have properties that are intermediate between the two classes. dTrans galaxies occupy environments that are statistically indistinguishable from those of dIs, according to a KS test. Their environments are statistically distinct from those occupied by dSphs, with only a 2×10^{-6} probability of being drawn from the same distribution of Θ. The luminosities of the dTrans galaxies have the opposite behavior. Their luminosities are statistically indistinguishable from those of dSphs, but are statistically lower luminosity than dIs, with only a 10^{-5} probability of being drawn from the same distribution of luminosities. Thus, in many respect transitional dwarfs appear to be the low luminosity end of the dIrr class.

The combined sample of $\sim$ 80 LG and ANGST dwarf galaxies all show a clearly defined morphology–density relationship, which underlines the importance of environmental effects in the evolution of dwarf galaxies. Suggestions that the transition from a gas-rich to a gas-poor state, i.e., dI to dSph, is primarily due to internal effects, e.g., stellar feedback, (Dekel & Silk, 1986; Dekel & Woo, 2003; Woo et al., 2008) are unable to account for the morphology–density relationship. Instead, models incorporating effects of tidal forces and stripping, along with ram pressure stripping, e.g., 'tidal' stirring (e.g., Mayer et al., 2001a,b), appear to provide a more comprehensive explanation for evolution of dwarf galaxies, while broadly accounting for the morphology–density relationship. See D. Weisz et al. (In Prep) for further discussion of dwarf galaxy SFHs and gas-loss models.

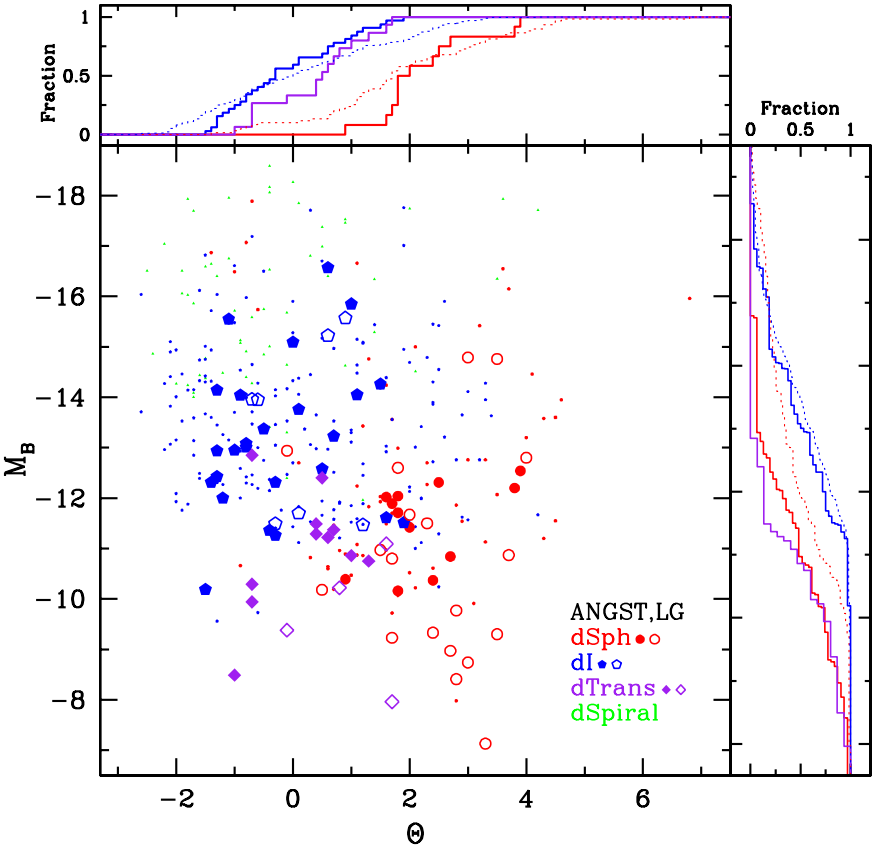

Figure 3.2 The observed morphology–density relationship for the LG (open symbols) and ANGST (filled symbols) dwarf galaxies.The small symbols are represent $\sim$ 250 galaxies in the Local Volume with $M_B > -18.5$ from the catalog of Karachentsev et al. (2004). The green points indicate dwarf spirals (dSpiral), which have a morphological T type of 8 or 9. We note that there may be ambiguity in the classification of right dIs an faint dSprials. The tidal indices, Θ, have also been taken from Karachentsev et al. (2004). Negative values of Θ represent isolated galaxies, while positive values represent typical group members. Solid lines in the cumulative panels are for the combined LG and ANGST sample, while the dashed lines represent sample from Karachentsev et al. (2004), minus the LG and ANGST galaxies. We see that both LG and ANGST dIs typically have negative tidal indices, while dSphs generally have positive tidal indices. dTrans have intermediate values, namely that they have a similar luminosity distribution to dSphs, but are location in low density regions, similar to dIs (see §3.4.2). The strong morphology–density relationship supports suggestions that environmental factors are important in the evolution of dwarf galaxies.

3.5 Summary

We compared uniformly derived SFHs of dwarf galaxies in the LG and ANGST samples. The cumulative SFHs are indistinguishable among the two samples, independent of morphological type, suggesting that LG dwarf galaxies accurately represent those in the nearby universe. First, the typical dwarf galaxy formed 50–60% of its total stellar mass $\gtrsim$ 10 Gyr ago (z $\sim$ 2), and 30–40%, 1–10 Gyr ago. Thus, the mean stellar age of dwarf galaxies is old, regardless of their current morphology, SFR, or environment. Second, the SFHs among the morphological types show the most significant difference in the most recent 1 Gyr. On average, during this time, dSphs formed 1–3% of their total stellar mass, compared to 7–9% for dIs and 4–6% for dTrans. These statistics suggest that complete gas loss in a typical gas-poor dwarf galaxy is a recent phenomena.

Both samples show consistent and well-defined morphology–density relationships, with dIs showing higher degrees of isolation than dSphs. A KS test reveals that dTrans occupy similar environments to dIs but have luminosities comparable do dSphs. This suggests that dTrans could be the low luminosity end of the dI class. The excellent agreement between the two samples, and among the broader universe, underlines the importance of environmental factors in the evolution of dwarf galaxies.

Chapter 4

The Recent Star Formation Histories of M81 Group Dwarf Irregular Galaxies

4.1 Introduction

4.1.1 The M81 Group Dwarf Galaxy Project

The ability to translate resolved stellar populations into star formation histories (SFHs) has become an increasingly powerful method for understanding how star formation (SF) shapes galaxy evolution (e.g., Gallart et al., 2005). The power of the Hubble Space Telescope (HST) is truly being realized as we are able to resolve the stellar components of increasingly distant galaxies. With the continuing expansion of the sample of galaxies with measured SFHs from resolved stars (e.g., the ACS Nearby Galaxy Survey Treasury (ANGST); Dalcanton et al., 2009), we are able to study how a wide variety of galaxies evolve both individually and in their respective environments.

Of particular interest are star forming galaxies that sample the faint end of the galactic luminosity function. Characteristics of SF in this regime are not as well studied as brighter, more massive galaxies, due to completeness limits of large galaxy surveys (e.g., SDSS). For example, Lee et al. (2007) and Kennicutt et al. (2008) empirically find an increased dispersion in the Hα equivalent width (EW) measurements, the normalized

SFR over the past 5 Myr, of star forming galaxies fainter than $M_B \sim -15$ compared to brighter galaxies. The cause behind the increased dispersion is not clear, and we could simply be observing the galaxies at different points in their SF duty cycle. Alternatively, different physical mechanisms could be responsible for the observed dispersion. There are several candidate theories that have distinct signatures: stochastic effects (cf., Mueller & Arnett, 1976; Gerola & Seiden, 1978), internal feedback (stellar winds, supernovae, e.g., Pelupessy et al., 2004; Stinson et al., 2007), external interactions (mergers, tidal influence, e.g., Toomre & Toomre, 1972; Gnedin, 1999), or a combination thereof. Direct observational evidence of recent SF episodes can shed light into the role of each process.

Specifically, dwarf irregular galaxies (dIs) are excellent environments for probing the mechanisms which regulate SF. By number, dIs dominate the faint star forming galaxy count and span a wide range in mass, luminosity, metallicity, and SFR (Mateo, 1998). They are solid body rotators (Skillman et al., 1988), so that features resulting from past SF episodes are preserved and not destroyed as they are in larger galaxies with differential rotation (Skillman, 1996). Thus, SFHs based on resolved stellar populations of dIs directly probe the physical mechanisms that govern SF in low mass galaxies.

Additionally, dIs are useful for understanding galaxy interactions within a group environment. Because SFHs trace the evolution of each galaxy over the history of the universe, we can measure the fraction of stellar mass formed at different epochs, which is directly comparable to models of galaxy interactions within groups (e.g., Ricotti & Gnedin, 2005; Orban et al., 2008). At more recent times, SFHs of dIs can be used to quantify patterns and duty cycles of SF over the past ~ 1 Gyr and compare them to theoretical predictions and amongst different groups of galaxies.

Comparing nearby galaxy groups, an interesting feature of the M81 Group is the presence of suspected tidal dwarfs (e.g., Makarova et al., 2002; Karachentsev et al., 2004), which have no counterparts in the Local Group. A three body interaction between larger galaxies in the M81 Group (M81, M82, and NGC 3077) occurred ~ 300 Myr ago, and there have been numerous observations of HI tidal debris leftover from this event (e.g., van der Hulst, 1979; Yun et al., 1994). Young stellar systems have been observed in these tidal remnants, and we may be witnessing the formation of new dwarf galaxies (i.e., tidal dwarfs) in the nearby universe (e.g., Walter & Heithausen, 1999;

Makarova et al., 2002).

In this paper, we introduce the observations, color-magnitude diagrams (CMDs), and SFHs of nine dIs in the M81 Group based on HST/ACS imaging. While our focus is on the recent temporal SFHs, we can also place loose constraints on the ancient SFHs and use red and blue star density maps to trace locations of past SF episodes. Using the recent SFHs, we are able to quantify and compare the strength and duration of SF episodes amongst the sample and to similarly observed galaxies in the LG. We use this paper to establish analysis techniques that we anticipate applying to a larger sample in the future. Here, we present a limited comparison of the SFHs to observations in other wavelength regimes (e.g., Hα, ultraviolet (UV), infrared (IR), HI), and in our future work we will compare the spatially resolved recent SFHs to HI observations and calibrate different SFR indicators to our CMD based SFHs.

4.1.2 The M81 Group Dwarf Galaxy Sample

The M81 Group presents an excellent environment for the study of resolved stellar populations and SFHs. The M81 Group is a prominent group of galaxies close enough to the Local Group (with distances typically $\sim$ 3.8 Mpc, Karachentsev et al., 2002) that the HST/ACS easily resolves the bright, young stellar populations. Further, the kinematic state of the M81 Group is very dynamic. HI observations and related models of the M81 Group (Yun et al., 1994; Yun, 1999) reveal a recent ($\sim$ 300 Myr) interaction between the major member galaxies and the presence of tidal streams and debris. A three dimensional map as well as detailed structural and kinematical information of the M81 Group are presented in Karachentsev et al. (2002).

The sample of nine M81 Group dIs was selected from galaxies which had excellent ancillary observations, starting with galaxies observed as part of the Spitzer Infrared Nearby Galaxies Survey (SINGS; Kennicutt et al., 2003). There are eight M81 Group dIs in both the SINGS and The HI Nearby Galaxy Survey (THINGS; Walter et al., 2008). This list was augmented by adding NGC 2366 (which had similar quality ancillary observations, although not part of the SINGS survey), the Garland (for which HST/ACS observations already existed, GO-9381, PI: Walter), and UGC 4483, which is a dwarf starburst galaxy (cf., Skillman et al., 1994; van Zee et al., 1998). Two galaxies were subsequently dropped from the sample. UGC 4483 was observed on December 31, 2006,

but the observation failed; this was shortly followed by the failure of the ACS, so we have no new observations for it and it was dropped from the sample. M81 Dwarf B was dropped from the sample after we found it to be significantly more distant than the other galaxies in agreement with other recent analysis (e.g., 5.3 Mpc, Karachentsev et al., 2002). The final sample of nine M81 Group dIs spans a wide range of properties including 6 magnitudes in luminosity, a factor of 1000 in current star formation rate (SFR), and 0.5 dex in metallicity (see Table 4.1).

In Figure 4.1 we have highlighted the dIs from this paper (M81 Group dIs in blue and LG dIs in black) in the context of the Local Volume star-forming galaxy sample (Lee et al., 2007; Kennicutt et al., 2008). The galaxies here are shown in the $M_B-H\alpha$ equivalent width (EW) plane, which traces mass and current normalized SFR, respectively. Lee et al. (2007) find an empirical transition at $M_B \sim -15$ based on the dispersions in Hα EW. Our sample of dIs straddles both sides of this division, allowing us to probe differences in SF characteristics in both luminosity regimes over a wide range of current SFRs.

Within our sample, we have two candidate tidal dwarf galaxies, the Garland and Ho IX. We will adopt that label throughout this paper, recognizing that the status of these features as true galaxies is controversial (e.g., van Driel et al., 1998; Makarova et al., 2002; Karachentsev et al., 2002) and they may simply be stellar systems forming in the outskirts of their larger companions (see Figure 4.2). We chose to exclude the candidate tidal dwarfs from our statistical analysis because of we find them to be fundamentally different than dIs in the sample.

Table 4.1 The M81 Group Dwarf Galaxy Sample

Galaxy	Alternate	M_B	$Log(M_{HI})$	Dmod	A_V	Z	Field	RA	Dec
Garland		−11.40	7.54	27.75	0.22	...		10:03:51.70	+68:41:25
Dwarf A	K52	−11.49	7.12	27.75	0.07	...		08:23:56.00	+71:01:45
DDO 53	UGC 4459, VII Zw 238	−13.37	7.61	27.76	0.12	−1.04		08:34:07.20	+66:10:54
Ho IX	UGC 5336, DDO66, K62	−13.68	8.50	27.84	0.26	−0.42		09:57:32.00	+69:02:45
Ho I	UGC 5139, DDO63	−14.49	8.12	27.92	0.16	−0.96		09:40:32.10	+71:11:12
DDO165	UGC 8201	−15.09	8.14	28.30	0.08	...		13:06:26.40	+67:42:24
NGC 2366	DDO42	−16.02	8.85	27.52	0.12	−0.75			
							1	07:28:43.96	+70:42:04
							2	07:28:59.60	+69:14:15
Ho II	UGC 4305, DDO50	−16.72	8.99	27.65	0.11	−0.74			
							1	08:18:58.96	+70:42:04
							2	08:19:20.50	+70:43:40
IC 2574	DDO81, UGC 5556	−17.46	9.23	28.02	0.12	−0.57			
							1	10:28:43.14	+68:27:04
							2	10:28:23.07	+68:24:36
							3	10:27:50.00	+68:22:55

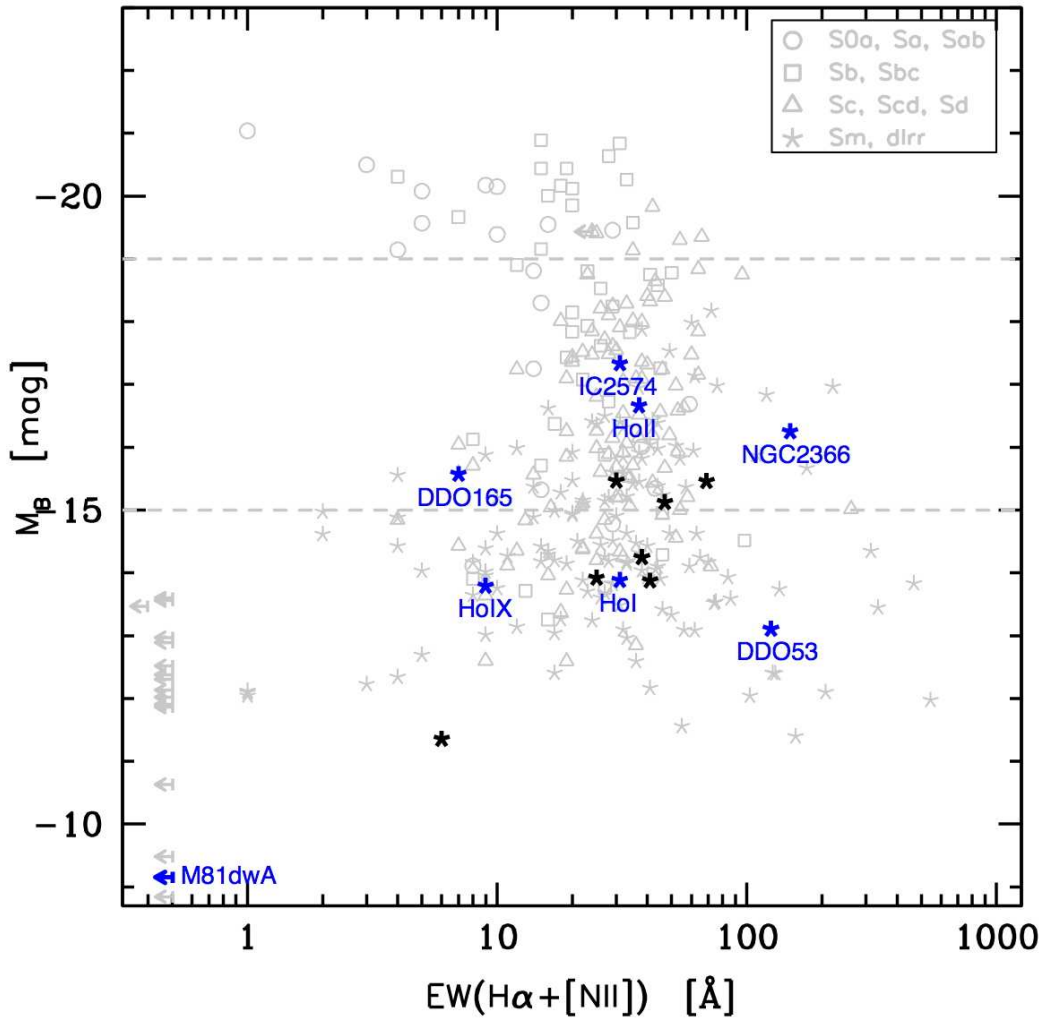

Figure 4.1 The Local Volume star-forming galaxy sequence plotted as as Hα EW vs. M_B (Lee et al., 2007; Kennicutt et al., 2008). The M81 Group dIs in this paper are shown in blue, and the Local Group dIs in this paper are shown in black. Note the wide range of luminosities and current SFRs (Hα EW) that the dIs in our sample span.

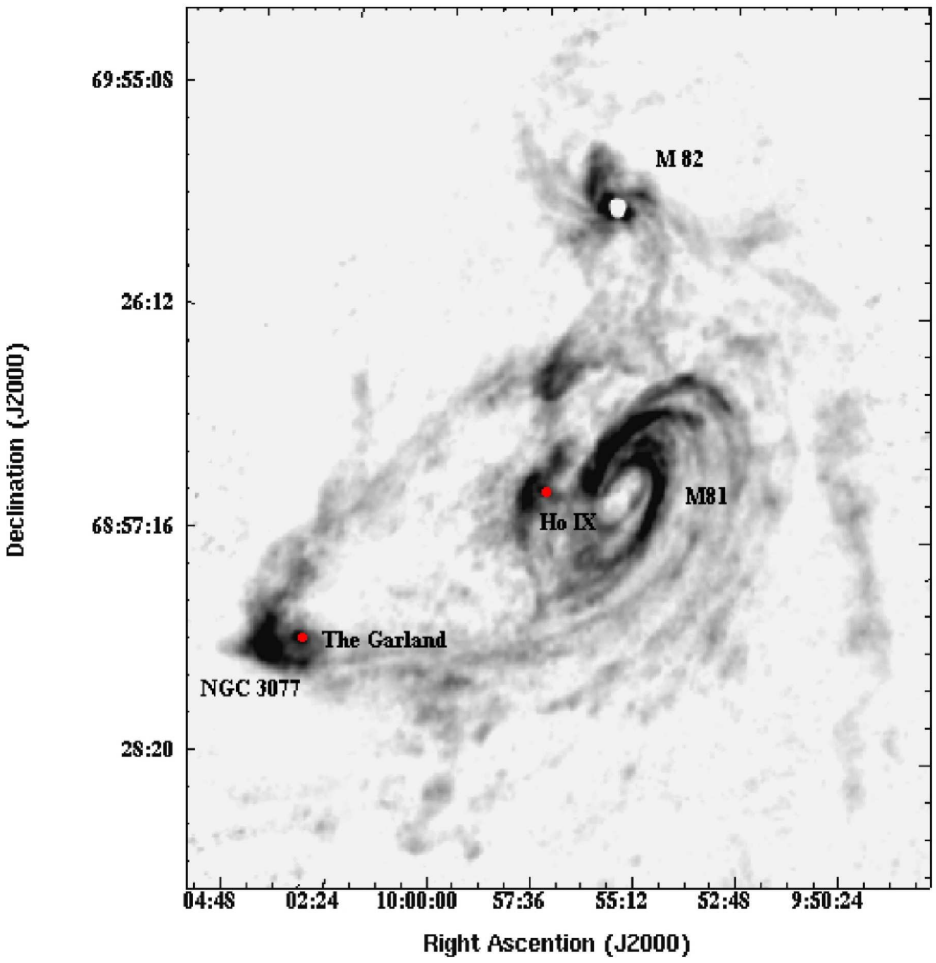

Figure 4.2 A high resolution HI image of the M81 Group (Yun et al., 1994) with the locations of the three larger galaxies (M81, M82, and NGC 3077) and two candidate tidal dwarfs (the Garland and Ho IX) indicated.

4.2 Observations and Photometry

We obtained HST/ACS (Ford et al., 1998) images of seven of the nine M81 Group dIs with ACS/WFC between January 27, 2006 and December 30, 2006 (GO-10605) using the filter combination of F555W (V) and F814W (I) in order to optimize the combination of photometric depth and temperature baseline (represented by stellar color in the observation plane). The requisite photometric depth of a signal to noise ratio of ~ 5 at $M_V = -0.5$ allows us to sufficiently resolve CMD features that give us leverage on the recent SFHs (Dohm-Palmer & Skillman, 2002a). The selection of filters is important because a larger difference in the central wavelengths of two selected filters provides for a clearer separation between features in the CMD. While observing at very blue and red wavelengths (e.g., U or B and I) would provide for a greater color difference, it also makes the integration time to the same photometric depth increase greatly. Thus, to optimize both color separation and photometric depth we observed the M81 Group dIs using F555W and F814W.

For most of the galaxies, a single ACS field was sufficient to cover a significant fraction of the stars, for the larger galaxies, NGC 2366 and Ho II, we observed two fields each, and for IC 2574, an ACS field from the HST Archive was supplemented by two additional fields. The ninth galaxy, the Garland, was also added from the HST archive. Both of these galaxies were observed in the same filter combination for comparable integration times. All observations were CR-split to reduce the impact of cosmic rays and dithered to cover the chip gap. Most of the M81 Group is also in the HST's continuous viewing zone, making for very efficient observing strategies (e.g., Caldwell et al., 1998).

After the images were processed with the HST pipeline, we performed photometry using DOLPHOT, a version of HSTphot (Dolphin, 2000) optimized for ACS observations. Cosmic rays, hot pixel residuals, and extended objects were all rejected based on their brightness profiles. Remaining objects were then subject to further photometric tests (signal to noise, crowding, and sharpness) resulting in catalogs of only well-measured stars (signal-to-noise > 5, $|F555W_{sharp} + F814W_{sharp}| > 0.27$, and $F555W_{crowd} + F814W_{crowd} < 1.0$), where sharpness and crowding follow the defitions in Dolphin (2000). Artificial star tests were performed to determine the completeness

limit for each field and these values are listed in Table 4.2.

The faintest well measured stars in our photometry have $M_V \sim 0$, which is adequate for recent SFHs, but only allows us to place weak constraints on the ancient (> 6 Gyr) SFHs. The main restriction resulting from shallower CMDs is the loss of time resolution at older ages (Dolphin, 2002). For example, the study of the Local Group galaxy Leo A by Tolstoy et al. (1998) used similar depth photometry ($M_V \sim 0$) to infer that bulk of the SF in Leo A occurred at later (more recent) times. This conclusion was verified by the very deep photometry, including the oldest MS turnoffs, presented by Cole et al. (2007). While the emphasis of our work is to constrain the recent SFHs, for which we have sufficient photometric depth (e.g., Dohm-Palmer et al., 1997), we can place loose constraints on the ancient SFHs by placing all SF > 6 Gyr into a single old age time bin.

Table 4.2: Observations and Completeness

Galaxy	Field	Int Time. F555W (secs)	Int. Time F814W (secs)	Stars in CMD	50% Comp. F555W	50% Comp. F814W
Garland		9600	19200	127,778	28.6	28.1
Dwarf A		5914	5936	17,450	28.4	27.8
DDO 53		4768	4768	67,903	28.1	27.8
Ho IX		4768	4768	68,373	28.3	27.7
Ho I		4446	5936	121,198	28.0	27.8
DDO 165		4768	4768	120,281	28.0	27.2
NGC 2366	1	4780	4780	246,750	27.8	27.4
	2	4780	4780	232,569	27.9	27.4
Ho II	1	4660	4660	239,742	27.8	27.3
	2	4660	4660	226,602	27.9	27.5
IC 2574	1	6400	6400	253,736	28.2	27.7
	2	4784	4784	234,369	27.7	27.0
	3	4784	4784	159,169	28.1	27.6

4.3 Methodology

4.3.1 Features on the CMD

In order to highlight important features on the CMD, we present a simulated CMD (Figure 4.3) made with the stellar evolution models of Marigo et al. (2008). We have also overplotted the timescales from the theoretical isochrones on the young stellar sequences to demonstrate the relationship between age and magnitude. Here, we provide a brief overview of main features of the CMD. For a more thorough review see Gallart et al. (2005). The main sequence (MS) stars burning hydrogen in their cores are marked by the green line. Immediately to the right of the MS are the blue helium burning stars (BHeBs), indicated by the blue line. These are intermediate mass stars ($\sim 2 - 15$ $M_{\odot}$) that have evolved off the MS and are burning helium in their cores. In a parallel track to the right of the BHeBs are the red helium burning stars (RHeBs), denoted by the red line. The HeB phase of stellar evolution is very short lived, making the HeB stars excellent chronometers for SF episodes as discussed in §3.2. Note the BHeBs are roughly 2 magnitudes brighter than their corresponding MS stars of the same age. In the orange box to the right of the RHeBs are asymptotic giant branch stars (AGBs) which are low to intermediate mass evolved stars burning both hydrogen and helium in shells. The magenta line marks the red giant branch stars (RGBs), which are low to intermediate mass stars that have evolved off the MS and are burning hydrogen in shells surrounding the cores. The tip of the red giant branch (TRGB), where the helium core of RGBs ignite, is an excellent distance indicator as it has a virtually invariant absolute I magnitude at low metallicities (Lee et al., 1993). The red clump (RC) is a phase where low and intermediate mass stars lie on the CMD as they burn helium in their cores and is enclosed by the cyan circle. Note that the RC overlaps with RGB stars and also merges with the BHeBs at (at $\sim$ 1 Gyr old BHeBs) and RHeBs (at $\sim$ 500 Myr for RHeBs) on the bright side, making this a very dense region on the CMD.

4.3.2 Connecting CMDs to Recent SFHs

An important step in verifying the accuracy of any derived SFH is being able to relate features of a given CMD to the corresponding SFH. We have constructed an instructional aid by simulating two CMDs from simple input SFHs and color-coding the ages

of the stars (see Figure 4.4). Similar diagrams can be found in the literature (e.g., Gallart et al., 2005), but here we emphasize the *recent* SF by limiting our input SFH to the last 5 Gyr. These CMDs were created with the code of Dolphin (2002) and stellar evolution models of Marigo et al. (2008) using a power law initial mass function (IMF) with a spectral index of $\gamma = -1.30$ (i.e., $\gamma \propto \frac{dn}{d(\log(m))}$, where $\gamma = -1.35$ represents the Salpeter IMF, Salpeter, 1955), between 0.15 and 100 $M_{\odot}$, a binary fraction (BF) of 0.35, zero foreground reddening, and a constant metallicity (of a typical dI) of $[M/H] = -1.0$ (i.e., Z = 0.1 $Z_{\odot}$ and where $[M/H]$ is the logarithmic relative abundance of heavier elements, M, with respect to hydrogen, H, relative to the solar value).

The CMDs in the left column of Figure 4.4 were created assuming a constant SFR of 0.005 $M_{\odot}$ yr^{-1} (typical for a dI) for the past 5 Gyr. To more clearly demonstrate the positions of younger stars on the CMD, the CMDs in the right column were created with an increasing SFR over the past 5 Gyr, such that $SFR_{5Gyr} = 0.005$ $M_{\odot}$ yr^{-1} and $SFR_{Present} = 0.1$ $M_{\odot}$ yr^{-1}. Because our emphasis is primarily on recent SF, we will not analyze the contributions of AGB and RGB stars because they are indicators of SF older than $\sim$ 1 Gyr.

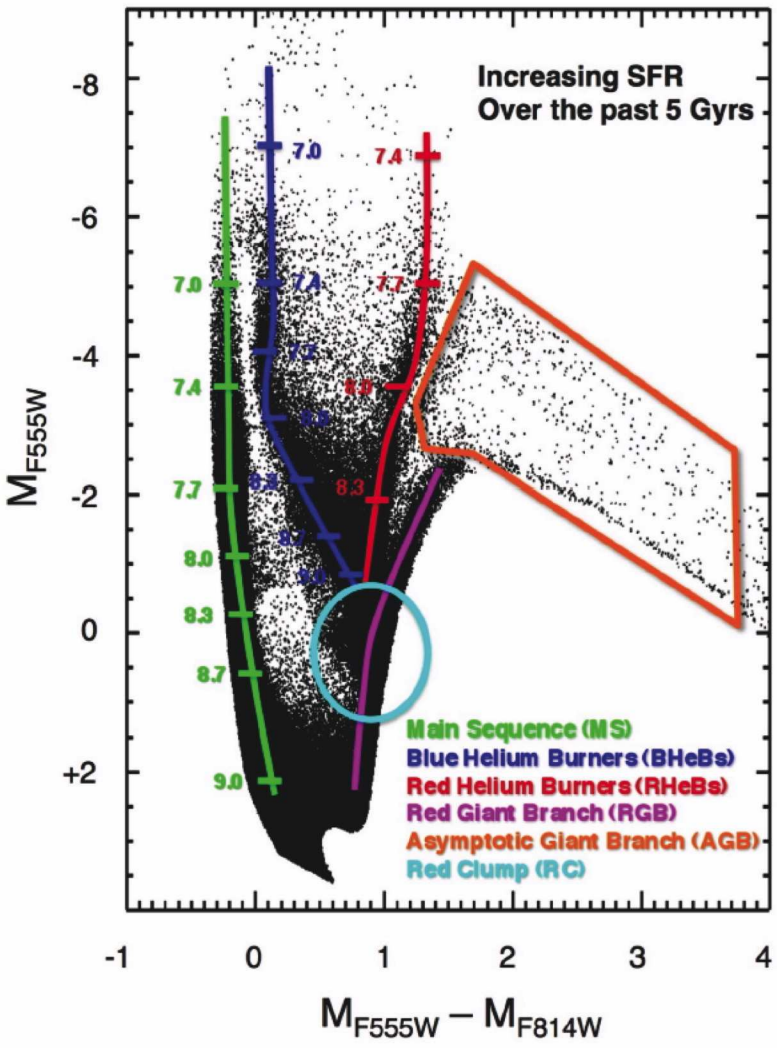

Figure 4.3 A simulated CMD of increasing SF over the past 5 Gyr. Important features on the CMD are highlighted: Main Sequence (MS, green), Blue Helium Burners (BHeBs, blue), Red Helium Burners (BHeBs, red), Asymptotic Giant Branch (AGB, orange), Red Giant Branch (RGB, magenta), and Red Clump (RC, cyan). For the MS, BHeBs, and RHeBs we overlay the logarithmic ages of stars at a given magnitude (Marigo et al., 2008).

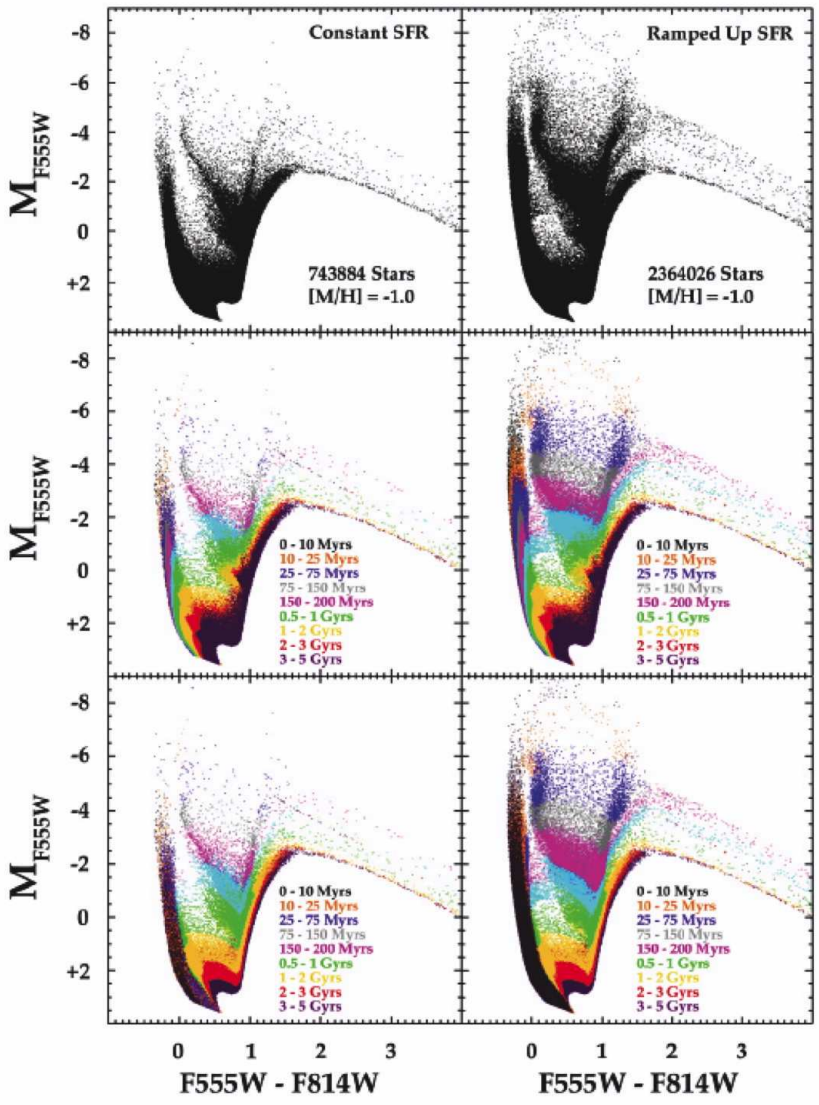

Figure 4.4 Simulated CMDs using models of Marigo et al. (2008) that demonstrate the power of HeBs as chronometers of SF within the last $\sim$ 1 Gyr. Panels on the left were constructed using a constant SFR (0.005 $M_\odot$ yr^{-1}), while panels on the right represent a ramped up SFR (0.005 $-$ 0.1 $M_\odot$ yr^{-1}). The stars are color coded by age and middle and bottom panels are plotted in opposite order. The points are plotted in reverse order to demonstrate the physical reality that HeBs, particularly BHeBs, of different ages do not have overlapping magnitudes and colors, making them very accurate chronometers for recent ($<$ 1 Gyr) SF. In contrast, MS stars of different ages can overlap in magnitude and color, which provide limited leverage on SF over the past $\sim$ 1 Gyr.

In the top two panels of Figure 4.4 we present the CMDs as they would appear as if we were to observe this simulated galaxy. We present the same CMDs with the stars color-coded by ages in the lower four panels.

In the center panels of Figure 4.4, we present the constant SFR (left panel) and increasing SFR (right panel) CMDs with color coded ages. Evident in both panels are the distinct age divisions of the MS and BHeB stars as a function of magnitude. That is, the youngest stars ($0 - 10$ Myr, black points) are located at the brightest magnitudes and older stars are located at fainter magnitudes (i.e., $10 - 25$ Myr, orange points; $25 - 75$ Myr, blue points; $75 - 150$ Myr, grey points, etc) and they are divided into fairly distinct age divisions. The MS shows these divisions all the way back to 5 Gyr, the oldest age of these CMDs, while the BHeBs extend back to ~ 1 Gyr, where they merge into the RC. The RHeBs also demonstrate a similar magnitude-age relationship, but blend into the RC at a brighter magnitude, or younger age.

Considering only the MS in Figure 4.4, we see stars of different ages can have the same magnitude and color. For example, while the magenta points ($150 - 300$ Myr) appear as a distinct age division on the MS, this is only a stripe of the brightest magenta MS colored stars. The fainter magenta colored MS stars are obscured on this CMD by older, fainter MS stars. Even stars of ages younger than 150 Myr ($0 - 10$ Myr, black points; $10 - 25$ Myr, orange points; $25 - 75$ Myr, blue points; $75 - 150$ Myr, grey points) can have the same color and magnitude as the magenta colored stars. To further emphasize this important degeneracy, in the lower panels we plot the same CMDs, only with the plotting order of the points reversed (young on top of old vs. old on top of young). The reversal of the plotting order demonstrates that stars with the same magnitude and color on the MS can have vastly different ages such that the youngest stars ($0 - 10$ Myr, black points) populate the entire MS to very faint magnitudes, and can occupy the same CMD space as 5 Gyr old MS stars.

In contrast, the BHeBs are particularly powerful chronometers for recent SF episodes because BHeBs of different ages have distinct magnitudes and colors. Consider the magenta points ($150 - 300$ Myr) on the BHeB sequence in the two center panels of Figure 4.4. There are no stars of any other age that have the same color and magnitude as the magenta colored BHeB stars. This fact is further accentuated by the reverse plotted CMDs in the lower two panels. Whereas the MS stars do not retain the same

neat age divisions between the center and lower panels, the BHeBs do. A slight caveat applies to the boundaries between the different generations of BHeBs. There is a slight overlap of different age stars in these regions, but this effect is on order of 10% according to simulations we have conducted. Thus, the BHeBs provide us with extremely powerful leverage to accurately measure the recent SFH of a galaxy.

4.3.3 Method of Measuring SFHs

Technological and theoretical advances in the past decade have made it possible to derive SFHs of stellar populations with unprecedented detail and accuracy. Sophisticated programs (Tosi et al., 1989; Tolstoy & Saha, 1996; Gallart et al., 1996; Mighell, 1997; Holtzman et al., 1999; Hernandez et al., 1999; Dolphin, 2002; Ikuta & Arimoto, 2002; Yuk & Lee, 2007) enable us to directly compare observed stellar populations with model stellar populations and measure the corresponding SFH.

Explicitly, a SFH is the SFR as a function of time and metallicity (i.e., SFR(t,Z)). To derive the SFH of each M81 Group dI in our sample, we used the maximum likelihood method of Dolphin (2002). The program creates synthetic CMDs using the models of Marigo et al. (2008) for every combination of fixed (IMF, BF, etc.) and searchable (distance, extinction, metallicity, and SFR) variables. The synthetic CMDs are then compared to the observed CMD using a modified χ^2 parameter. The best fit synthetic CMD yields the most likely SFH of the galaxy. See Dolphin (2002) for a full description of the SFH measurement algorithm.

Along with the SFR, metallicity information is extracted from the best fit isochrone at each age. These fits yield a mean value of $[M/H]$ in each time bin allowing us to trace the chemical evolution of a galaxy. Because our photometry does not reach the ancient MS turnoff, it is hard to place tight constraints on the chemical evolution from CMD fitting alone. To aid in our solutions, we require that the program fit monotonically increasing metallicities. For deeper CMDs this assumption would not be necessary.

To ensure that we have a robust SFH, we compute both systematic and statistical uncertainties of the SFR in each time bin. The systematic uncertainties are a product of the stellar evolution isochrones and are manifested as a degeneracy between distance and extinction. To account for this form of uncertainty, we re-solve for new SFHs allowing the distance and extinction values to vary slightly from the values associated with the most

likely SFH. The uncertainties in the SFRs for each variation are added in quadrature to produce the systematic component of our uncertanties. The statistical uncertainties are a result of counting statistics in each CMD bin. We use Monte Carlo tests to re-solve for SFHs after redistributing the stars in each bin according to a Poisson distribution. The resultant systematic and statistical uncertainties are added in quadrature to produce the error bars in our final SFHs. A more detailed discussion of the calculation and interpretation of uncertainties in SFHs can be found in Dolphin (2002).

4.4 CMDs, SFHs, and Stellar Spatial Distributions

The three main tools for our analysis are CMDs, SFHs, and stellar density maps for blue and red stars. The combination of these three products aids in our analysis of the temporal and spatial properties of the SFHs for each galaxy. In this section, we present the CMDs of each ACS observation, the lifetime and recent SFHs of each galaxy, and the stellar density maps for each galaxy. As a setup for our later comparison of SF based on luminosity, the sample is divided into two luminosity regimes with a dividing line of $M_B = -15$.

We present four-panel figures in order to demonstrate provide spatial context of our analysis of each galaxy in our sample (Figures 4.5 − 4.13). Panel (a) shows an R-band DSS image with the ACS field(s) of view overlaid in blue with the chip gap position shown in red. Panel (b) shows a color image of each ACS field, created (and combined, for multiple pointings) using drizzled images from the HST pipeline. Panels (c) and (d) are density maps of the blue (young) and red (old) stars, respectively, in each galaxy. The density plots of blue and red stars give a sense of the spatial distribution of young and old stars in the each galaxy. Red stars are defined as having a color (i.e., m_{F555W}-m_{F814W}) between 0.6 and 3.0 and a magnitude fainter than the TRGB, to exclude the young RHeBs, but include RGB, RC, and AGB stars. We defined the blue stars to have a color less than 0.6 and include MS and BHeBs. We also exclude faint spurious detections by considering stars that are only brighter than the 60% F814W completeness limit as determined by the artificial star tests. To create the maps, we binned the stars and smoothed the resulting distribution using a Gaussian kernel such that the final image resolution is 7.5".

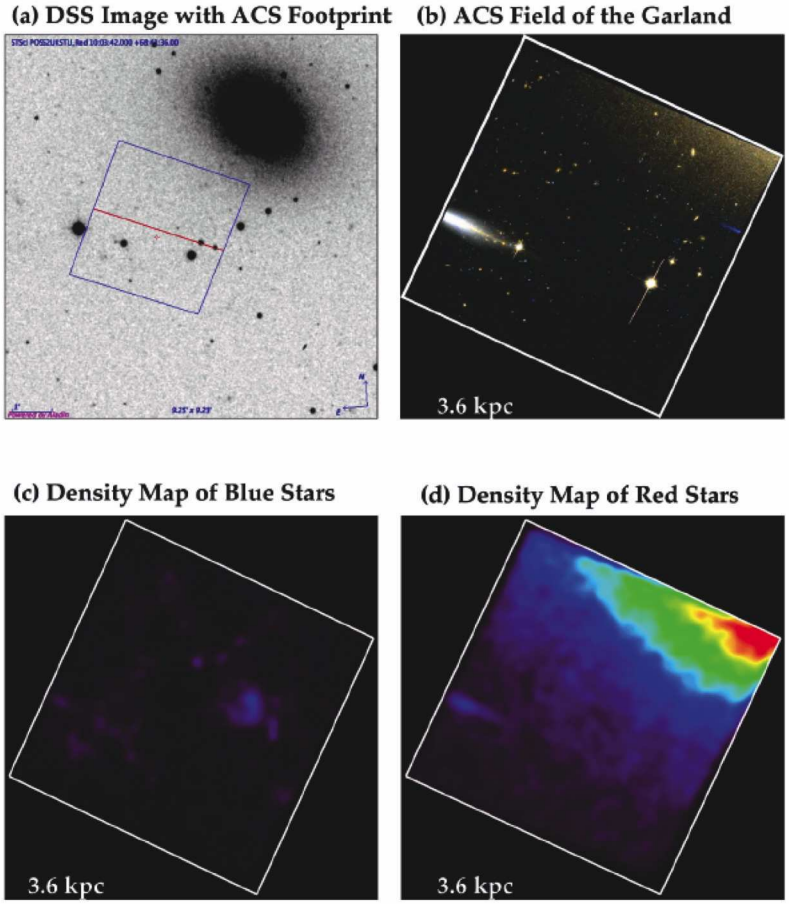

Figure 4.5 A four panel figure of the Garland showing the ACS footprint in blue with the chip gap direction in red over the R-Band DSS image (a), the color ACS image (b), and stellar density maps of blue (c) and red stars (d) as determined by their positions on the CMD. The blue stars have a color < 0.6 and magnitude $> 60\%$ completeness in F814W. The red stars are defined as $0.6 \leq$ color ≤ 3.0 and a magnitude range between the TRGB and 60% completeness in F814W. The highest density regions are the red contours and the lowest are in purple. Note our ACS observation of the Garland contains a significant number of red stars from NGC 3077 (see §4.1 for further discussion).

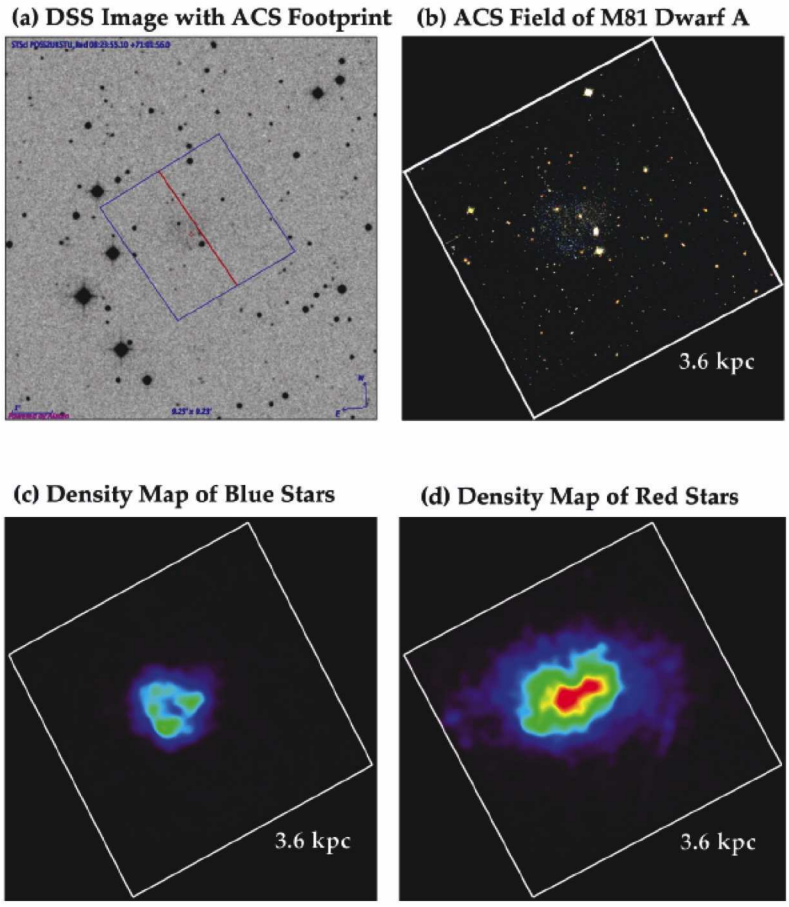

Figure 4.6 A four panel figure of the M81 Dwarf A showing the ACS footprint in blue with the chip gap direction in red over the R-Band DSS image (a), the color ACS image (b), and stellar density maps of blue (c) and red stars (d) as determined by their positions on the CMD. The blue stars have a color < 0.6 and magnitude $>$ 60% completeness in F814W. The red stars are defined as $0.6 \leq$ color ≤ 3.0 and a magnitude range between the TRGB and 60% completeness in F814W. The highest density regions are the red contours and the lowest are in purple.

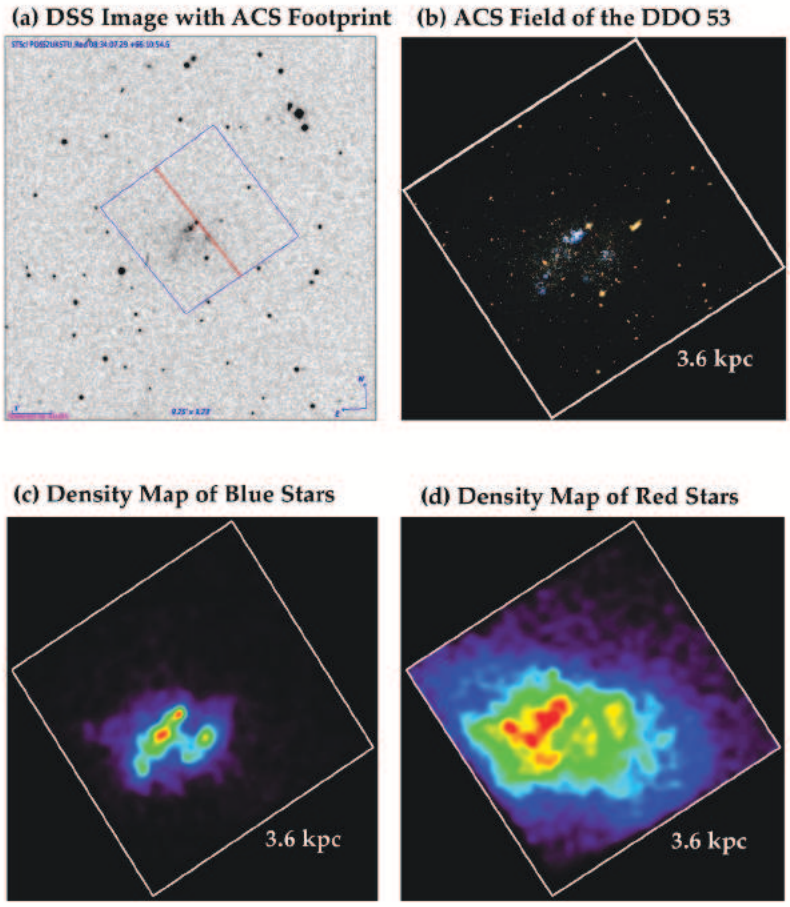

Figure 4.7 A four panel figure of the DDO 53 showing the ACS footprint in blue with the chip gap direction in red over the R-Band DSS image (a), the color ACS image (b), and stellar density maps of blue (c) and red stars (d) as determined by their positions on the CMD. The blue stars have a color < 0.6 and magnitude $>$ 60% completeness in F814W. The red stars are defined as $0.6 \leq$ color ≤ 3.0 and a magnitude range between the TRGB and 60% completeness in F814W. The highest density regions are the red contours and the lowest are in purple.

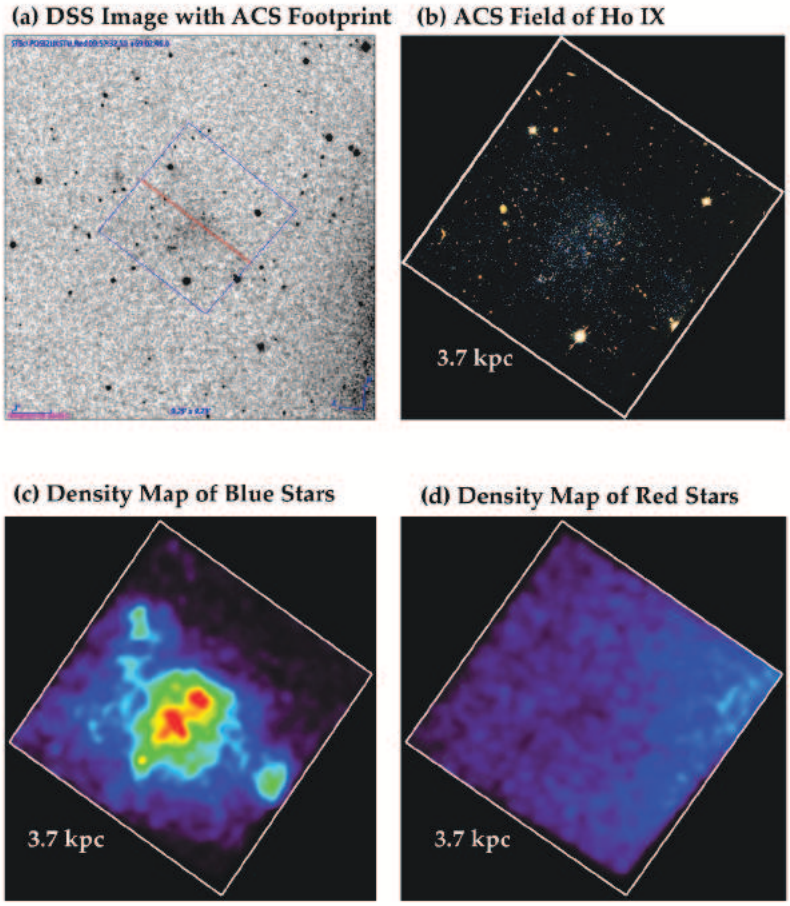

Figure 4.8 A four panel figure of the Ho IX showing the ACS footprint in blue with the chip gap direction in red over the R-Band DSS image (a), the color ACS image (b), and stellar density maps of blue (c) and red stars (d) as determined by their positions on the CMD. The blue stars have a color < 0.6 and magnitude $>$ 60% completeness in F814W. The red stars are defined as $0.6 \leq$ color ≤ 3.0 and a magnitude range between the TRGB and 60% completeness in F814W. The highest density regions are the red contours and the lowest are in purple. Note that our ACS field of Ho IX contains red stars from M81 (see §4.1 for further discussion).

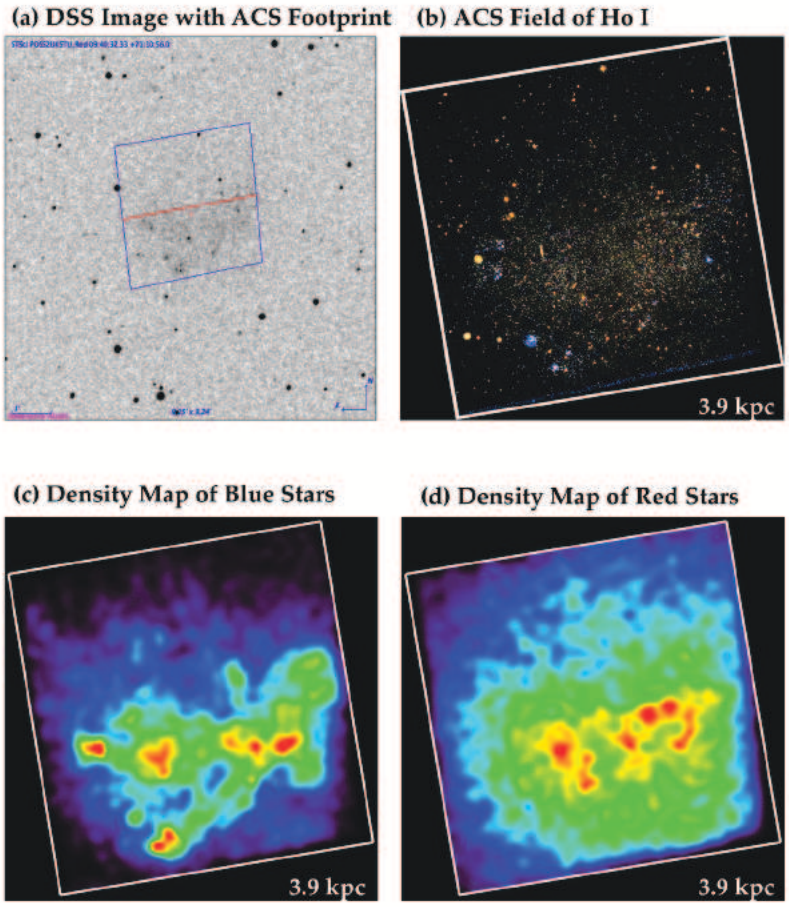

Figure 4.9 A four panel figure of the Ho I showing the ACS footprint in blue with the chip gap direction in red over the R-Band DSS image (a), the color ACS image (b), and stellar density maps of blue (c) and red stars (d) as determined by their positions on the CMD. The blue stars have a color < 0.6 and magnitude $> 60\%$ completeness in F814W. The red stars are defined as $0.6 \leq$ color ≤ 3.0 and a magnitude range between the TRGB and 60% completeness in F814W. The highest density regions are the red contours and the lowest are in purple.

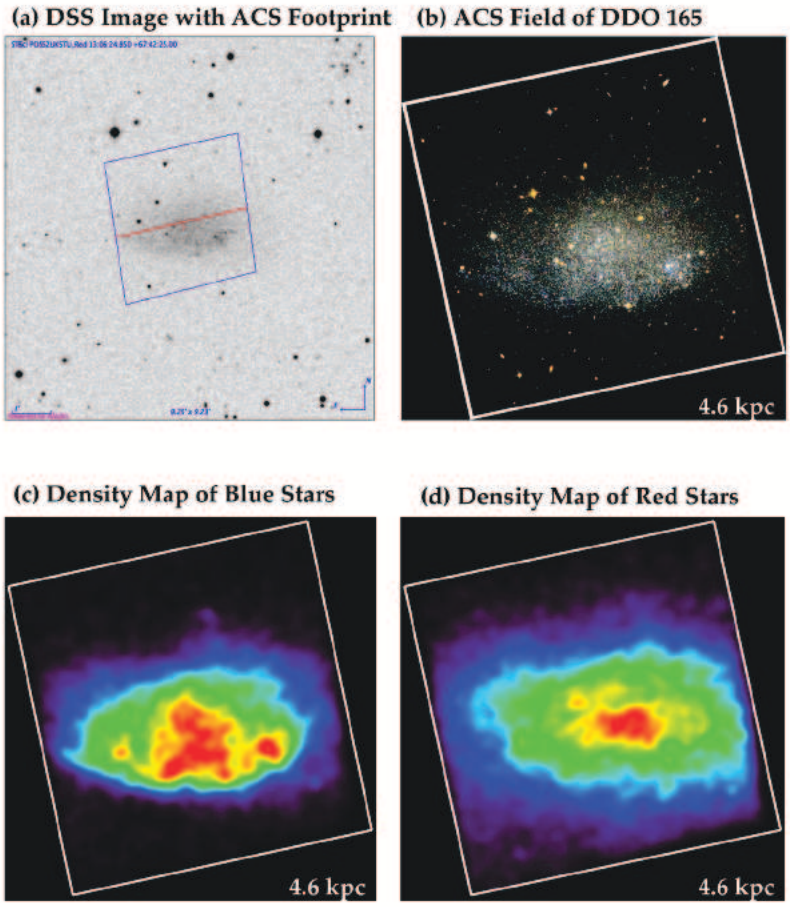

Figure 4.10 A four panel figure of the DDO 165 showing the ACS footprint in blue with the chip gap direction in red over the R-Band DSS image (a), the color ACS image (b), and stellar density maps of blue (c) and red stars (d) as determined by their positions on the CMD. The blue stars have a color < 0.6 and magnitude $>$ 60% completeness in F814W. The red stars are defined as $0.6 \leq$ color ≤ 3.0 and a magnitude range between the TRGB and 60% completeness in F814W. The highest density regions are the red contours and the lowest are in purple.

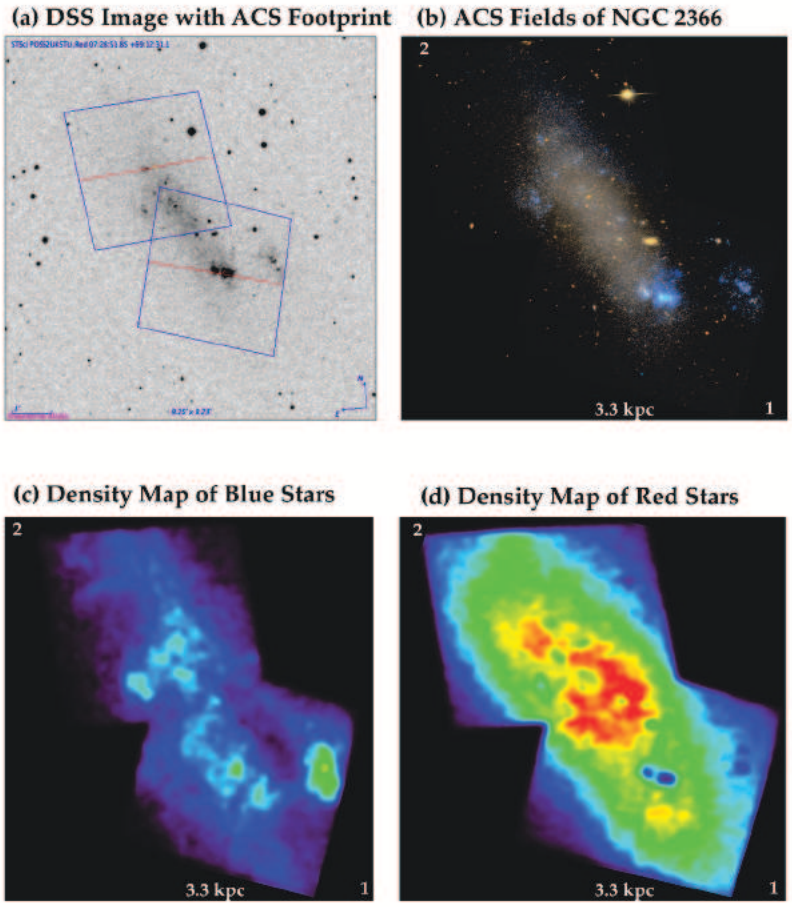

Figure 4.11 A four panel figure of the NGC 2366 showing the ACS footprints in blue with the chip gap directions in red over the R-Band DSS image (a), the color ACS image (b), and stellar density maps of blue (c) and red stars (d) as determined by their positions on the CMD. The blue stars have a color < 0.6 and magnitude $>$ 60% completeness in F814W. The red stars are defined as $0.6 \leq$ color ≤ 3.0 and a magnitude range between the TRGB and 60% completeness in F814W. The highest density regions are the red contours and the lowest are in purple.

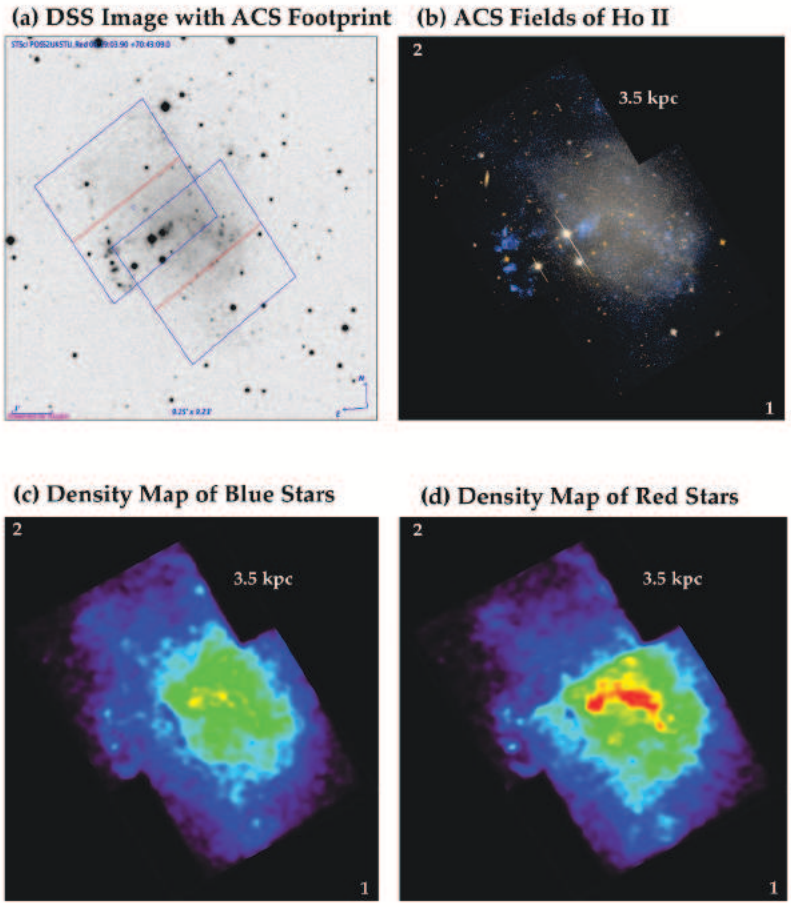

Figure 4.12 A four panel figure of the Ho II showing the ACS footprints in blue with the chip gap directions in red over the R-Band DSS image (a), the color ACS image (b), and stellar density maps of blue (c) and red stars (d) as determined by their positions on the CMD. The blue stars have a color < 0.6 and magnitude $>$ 60% completeness in F814W. The red stars are defined as $0.6 \leq$ color ≤ 3.0 and a magnitude range between the TRGB and 60% completeness in F814W. The highest density regions are the red contours and the lowest are in purple.

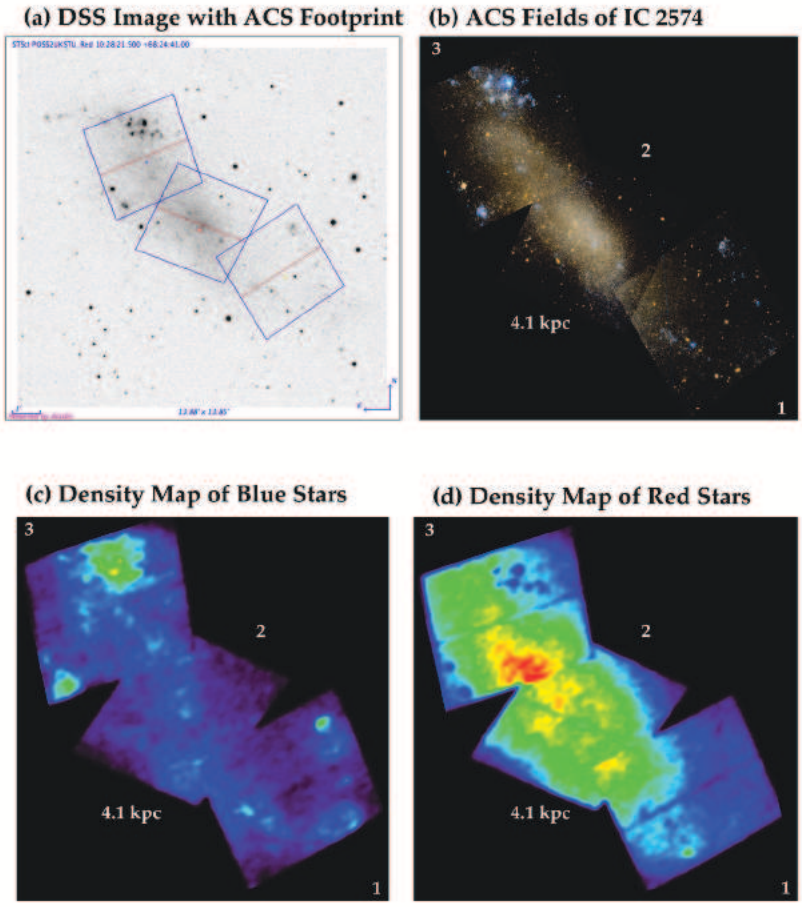

Figure 4.13 A four panel figure of the IC 2574 showing the ACS footprints in blue with the chip gap directions in red over the R-Band DSS image (a), the color ACS image (b), and stellar density maps of blue (c) and red stars (d) as determined by their positions on the CMD. The blue stars have a color < 0.6 and magnitude $>$ 60% completeness in F814W. The red stars are defined as $0.6 \leq$ color ≤ 3.0 and a magnitude range between the TRGB and 60% completeness in F814W. The highest density regions are the red contours and the lowest are in purple.

The CMDs of each ACS field are shown as density contours to reveal greater detail in otherwise crowded regions of the CMD (Figures 4.14 − 4.17). These CMDs were made using a nearest neighbor plotting algorithm such that regions with a stellar density $\geq$ 4 stars dmag^{-2} (decimags, 0.1 magnitudes) are shown as contours with the contour levels spaced uniformly by a factor of 2. Stars are plotted as individual points when the density $<$ 4 stars dmag^{-2}.

The lifetime (Figures 4.18 and 4.19) and recent (Figures 4.20 and 4.21) SFHs show the SFHs of each galaxy for both the history of the universe and the most recent 1 Gyr with different time resolutions. The typical time resolution for the lifetime SFHs is Δ log(t) $\sim$ 0.3, while the recent SFHs have a 10 Myr resolution in the most recent time bin and a $\sim$ 250 Myr resolution for the oldest time bin. We note that the recent SFHs appear different from the most recent 1 Gyr of the lifetime SFHs due to the choice of binning, although they are equivalent SFHs. We chose a finer time resolution for the most recent 1 Gyr because of excellent leverage on the recent SF afforded by the BHeBs, allowing us to study pattens of recent SF in greater detail.

Similar to the different appearance of the lifetime and recent SFHs, the value of the SFR error bars also vary with time bin resolution. This effect is most evident in the oldest age bin of the lifetime SFHs. Although the photometry only allows us to place weak constraints on the ancient SFHs, the error bar appears quite small. This is because we bin all SF $>$ 6 Gyr into a single coarse bin as opposed to multiple bins of finer time resolution. If we had selected finer time resolution, we would have increased the uncertainty in the SFR in each time bin. Despite being able to quantify the ancient SFH, we can only do so with very low time resolution (6 − 14 Gyr), which equates to placing a loose constraint on SF at this epoch.

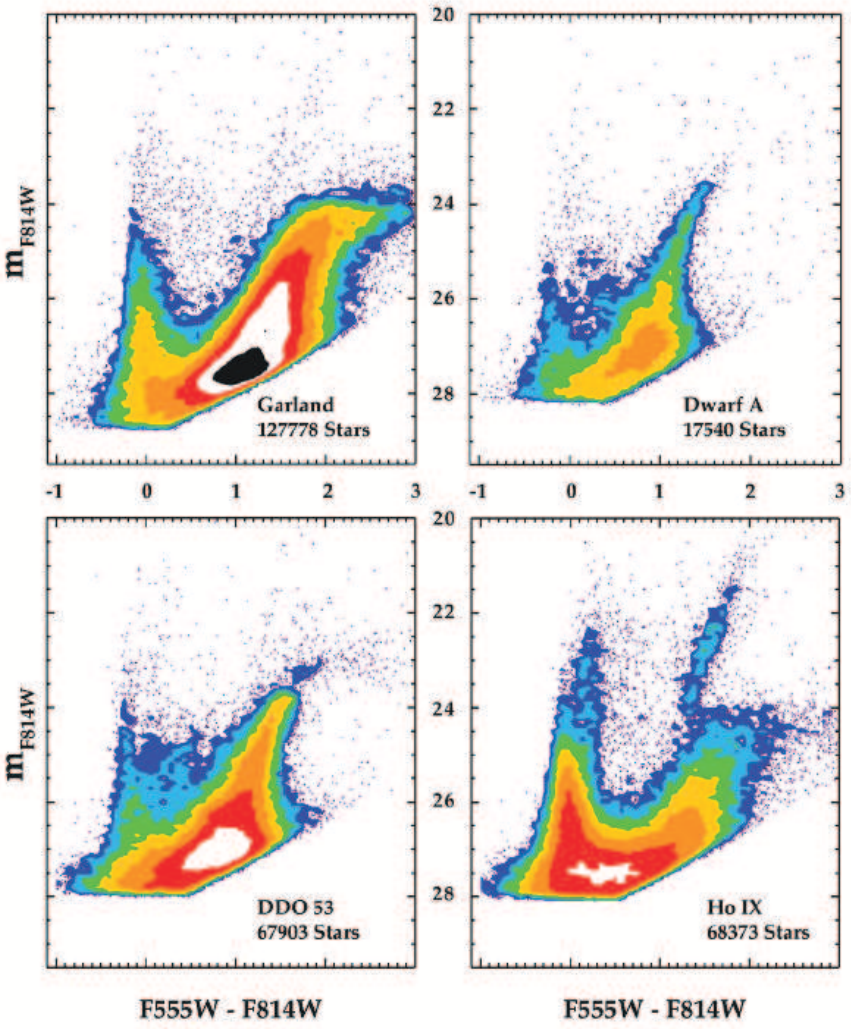

Figure 4.14 The HST/ACS CMDs of M81 Dwarf A, the Garland, DDO 53, and Ho IX presented in ACS instrumental filters F555W and F814W, contoured by stellar density on the CMD. Regions of density less than 4 stars dmag^{-2} (0.1 $\times$ 0.1 magnitudes bins) are plotted as points. Contours are spaced by factors of 2 to show the detailed structure of the CMDs.

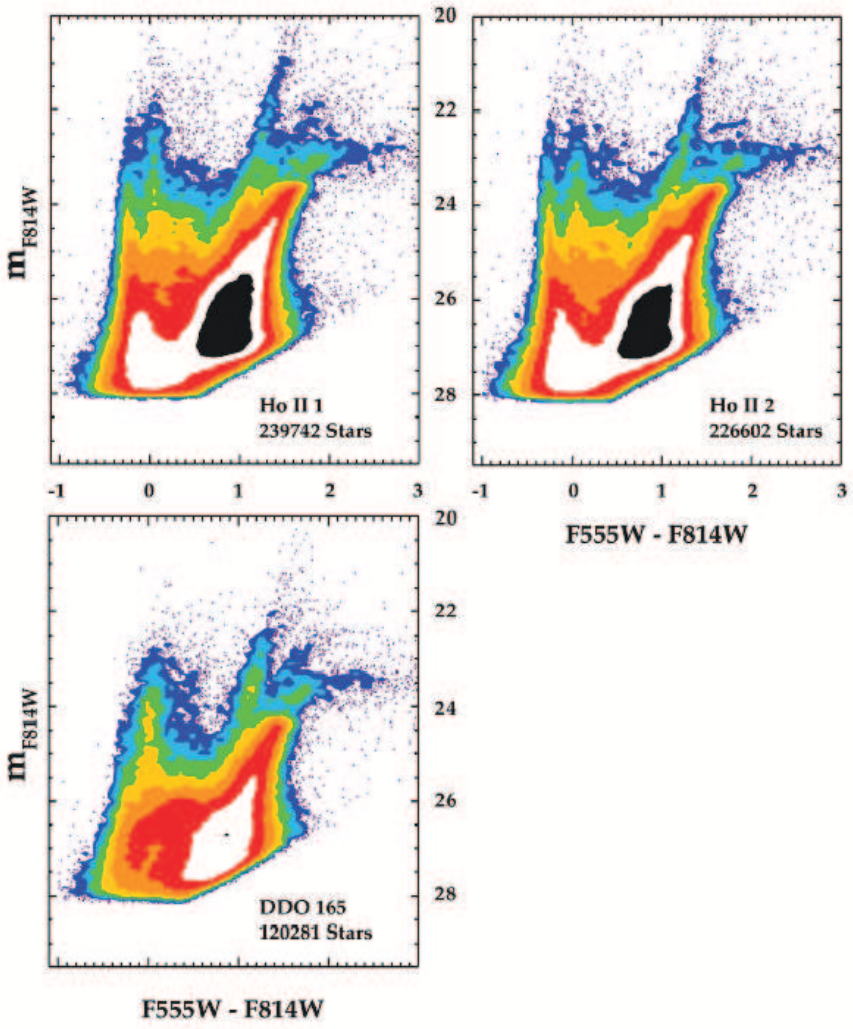

Figure 4.15 The HST/ACS CMDs of both fields of Ho II and DDO 165 presented in ACS instrumental filters F555W and F814W, contoured by stellar density on the CMD. Regions of density less than 4 stars dmag^{-2} (0.1 $\times$ 0.1 magnitudes bins) are plotted as points. Contours are spaced by factors of 2 to show the detailed structure of the CMDs.

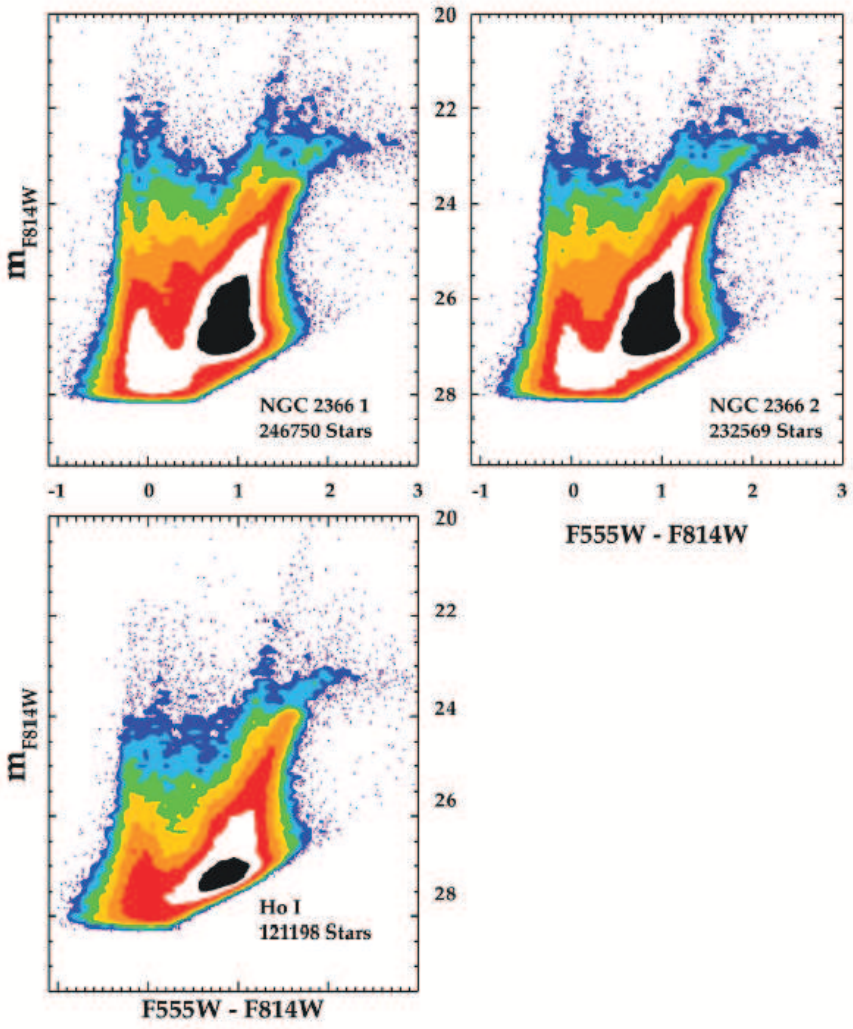

Figure 4.16 The HST/ACS CMDs of both fields of NGC 2366 and Ho I presented in ACS instrumental filters F555W and F814W, contoured by stellar density on the CMD. Regions of density less than 4 stars dmag^{-2} (0.1 $\times$ 0.1 magnitudes bins) are plotted as points. Contours are spaced by factors of 2 to show the detailed structure of the CMDs.

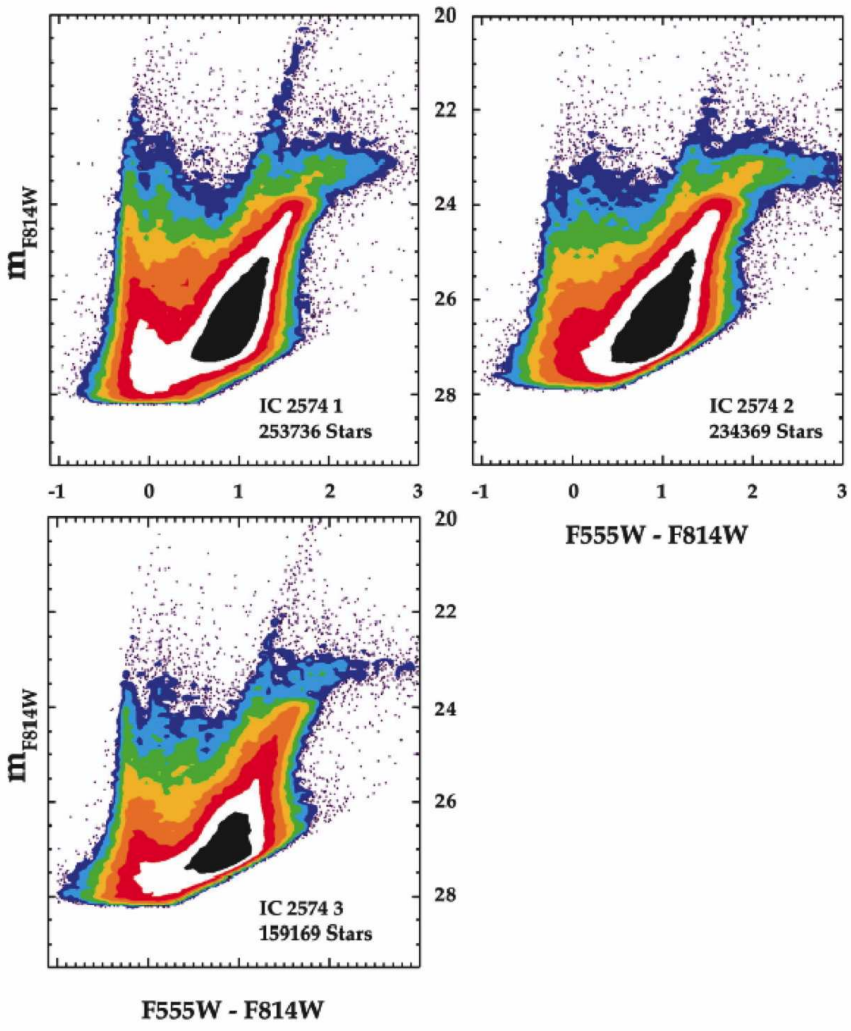

Figure 4.17 The HST/ACS CMDs of all three field of IC 2574 presented in ACS instrumental filters F555W and F814W, contoured by stellar density on the CMD. Regions of density less than 4 stars dmag^{-2} (0.1 $\times$ 0.1 magnitudes bins) are plotted as points. Contours are spaced by factors of 2 to show the detailed structure of the CMDs.

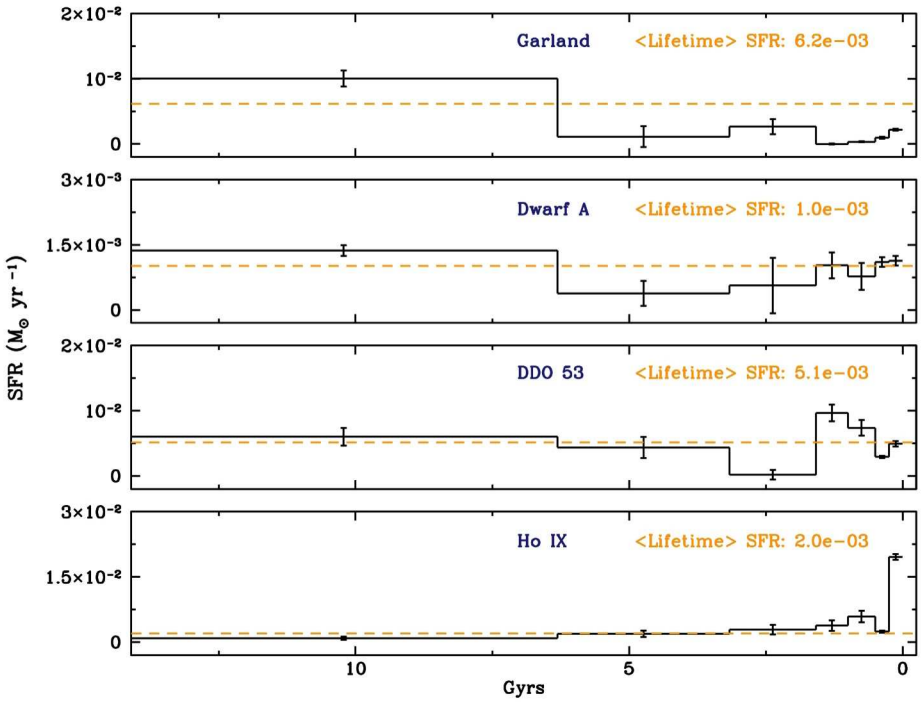

Figure 4.18 The lifetime SFHs of the Garland, M81 Dwarf A, Ho IX, and DDO 53 with a time resolution of $\sim \log(t) \sim 0.3$. The orange dashed line represents the SFH averaged over the lifetime of the of galaxy. The error bars reflect both systematic and statistical uncertainties.

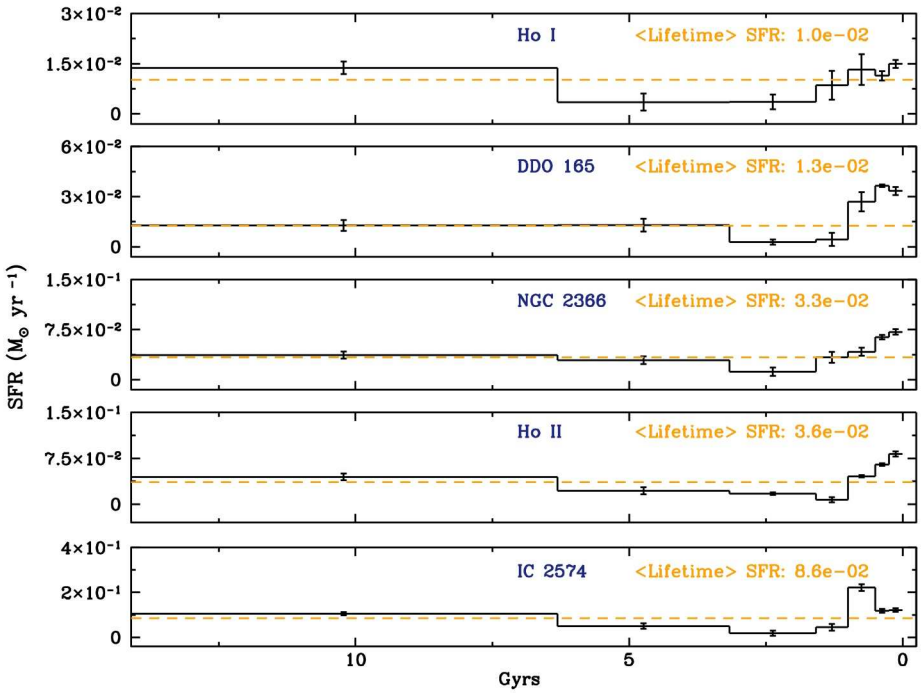

Figure 4.19 The lifetime SFHs of Ho I, DDO 165, NGC 2366, Ho II, and IC 2574 with a time resolution of $\sim \log(t) \sim 0.3$. The orange dashed line represents the SFH averaged over the lifetime of the of galaxy. The error bars reflect both systematic and statistical uncertainties.

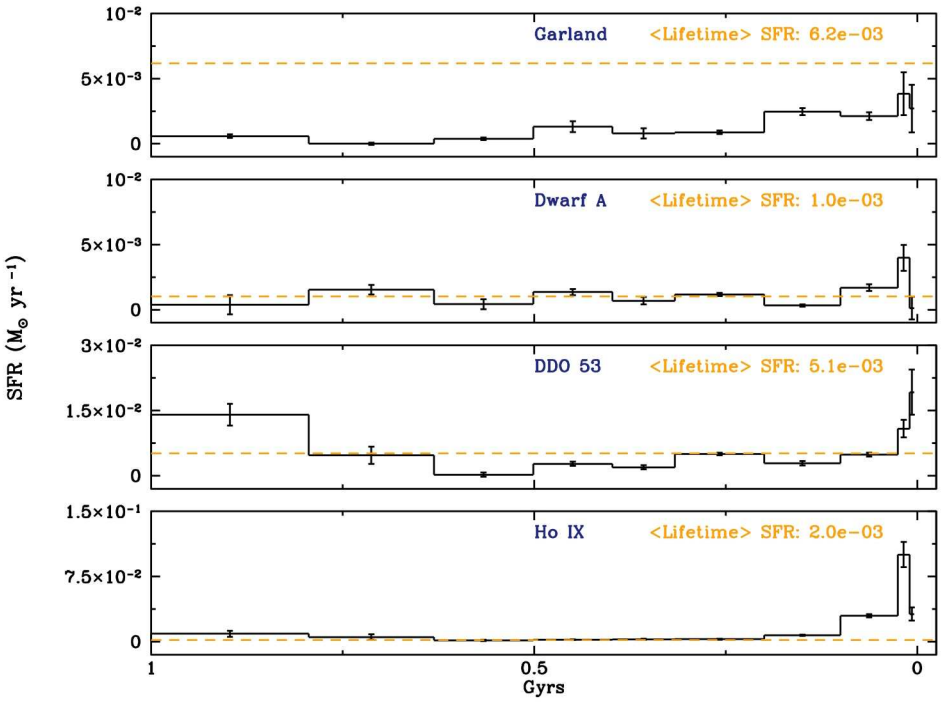

Figure 4.20 The recent SFHs of the Garland, M81 Dwarf A, Ho IX, and DDO 53 with a time resolution ranging from 10 Myr in the most recent time bin to $\sim$ 250 Myr in the oldest bin. The orange dashed line represents the SFH averaged over the lifetime of the of galaxy. The error bars reflect both systematic and statistical uncertainties.

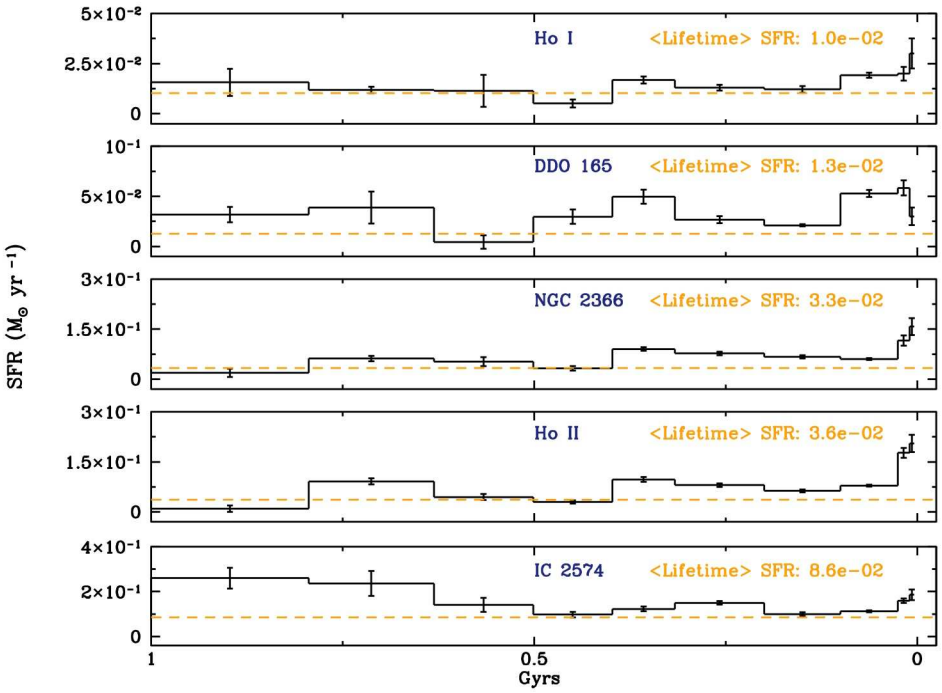

Figure 4.21 The recent SFHs of Ho I, DDO 165, NGC 2366, Ho II, and IC 2574 with a time resolution ranging from 10 Myr in the most recent time bin to $\sim$ 250 Myr in the oldest bin. The orange dashed line represents the SFH averaged over the lifetime of the of galaxy. The error bars reflect both systematic and statistical uncertainties.

To quantitatively compare the SFHs, we employ the two parameters. The first, f, is the fraction of stars formed over a given time period. Specifically, we compute f_1, f_6, and f_{14}, the fraction of stars formed from $0 - 1$ Gyr, $1 - 6$ Gyr, and $6 - 14$ Gyr (see Table 4.3). By comparing the fraction of stars we can assess how active the galaxy has been at recent, intermediate, and ancient times (e.g., for a constant SFR, $f_1 = 0.07$, $f_6 = 0.36$, and $f_{14} = 0.57$). The second set of parameters we compute are the 'birthrate' parameters, i.e., the ratio of the current SFR to the lifetime averaged SFR (cf., Scalo, 1986; Kennicutt, 1998), for recent time intervals of 100 Myr, 500 Myr and 1 Gyr. The birthrate parameter b_{100} represents the SFH of a galaxy averaged over the past 100 Myr normalized to the lifetime average, and, similarly, b_{500} and b_{1G} are the birthrate parameters for the past 500 Myr and 1 Gyr respectively (see Table 4.3). A galaxy that forms stars at a constant rate would have a birthrate parameter of unity. Birthrate parameters greater than unity show that the SFR is a higher than average at that time.

4.4.1 Galaxies with $M_B > -15$

In this section we present the CMDs, spatial stellar distribution, and SFHs for each of the galaxies with $M_B > -15$ in increasing order of luminosity. We discuss and compare the formation and evolution of these galaxies in §6.

The Garland – As shown in Figure 4.5, the Garland is located in close proximity to the southeast of NGC 3077. The Garland is very hard to discern in both the DSS and color ACS images, but is more prevalent in the density maps. There is a dense red star component (panel (d)) in the ACS field which decreases away from NGC 3077 implying that these stars are associated with the larger galaxy. In contrast, the blue stellar density map (panel (c)) reveals several regions of concentrated blue stars in agreement with Sakai & Madore (2001). The region of highest blue star concentration overlaps with the the outer red stars and it is not possible from the ACS observations alone to determine if these blue stars are a separate system or merely young stars in the outer part of NGC 3077. We also note that there does not appear to be an overdensity of red stars associated with any of the concentrations of blue stars.

In Figure 4.14 we show the CMD of the entire ACS field of the Garland. The high stellar density and breadth of the RGB are due to the red stars from the outer part of NGC 3077. Young stars are present in the form of MS stars and a very sparse

distribution of HeBs.

The lifetime and recent SFHs of the Garland are shown in Figures 4.18 and 4.20. To produce a more accurate SFH, we isolated the Garland from NGC 3077 by subtracting out the stars that lie in the green through red contour shown in panel (d) of Figure 4.5.

The lifetime SFH shows an ancient SFR which exceeds the average lifetime SFR ($\sim$ 0.006 $M_\odot$ yr^{-1}) and is presumably due to the inclusion of red stars from NGC 3077; only 1% of the stars in the ACS image have been formed within the more recent Gyr. The additional red stars have the effect of increasing the lifetime average SFR of the Garland. Over the most recent 1 Gyr, we see that the SF remains roughly constant until $\sim$ 300 Myr ago when there was an increase in the SFR that continues to the present. We quantify this increase in SFR by computing $\frac{b_{100}}{b_{1G}} \sim 2.5$, done so to eliminate the dependence on the contaminated lifetime average SFR (see Table 4.3). To further aid in measuring the SFH, we did not require the metallicity to monotonically increase with time. The Garland is best fit with more metal poor isochrones over the past 1 Gyr ($[\frac{M}{H}] = -1.0$) and more metal rich ancient ($[\frac{M}{H}] = -0.4$) and intermediate age ($[\frac{M}{H}] = -0.3$) components. This metallicity distribution is consistent with the old and intermediate age stars coming from the more massive NGC 3077, while the young stars in the Garland come from metal poor gas.

M81 Dwarf A – The ACS observation and stellar density maps of M81 Dwarf A are shown in Figure 4.6. We see from panel (d) in Figure 4.6 that the red stars are highly concentrated in the center, with a slight elongation in the southeast-northwest direction. The highest blue star concentrations form a ring shape and are aligned with the densest region of rest stars (panel (c)).

From the CMD of M81 Dwarf A (Figure 4.14) we see a prominent RGB and very few AGB stars. The MS and BHeB sequences are distinct and both moderately populated, although their absence at brighter magnitudes suggests that there is little, if any, recent SF.

The lifetime and recent SFHs of M81 Dwarf A are shown in Figures 4.18 and 4.20. The lifetime SFH shows the oldest stars were formed at a rate higher than the lifetime average (0.001 $M_\odot$ yr^{-1}), $f_{14} = 0.75$, followed by intermediate age SF at a rate lower than the lifetime average ($f_6 = 0.19$) until the last $\sim$ 2 Gyr. Within the last 1 Gyr the SFH is consistent with the lifetime average, $b_{1G} = 0.92$ and $b_{500} = 1.08$, with a

significant increase in the SFR in the past $\sim$ 100 Myr ($b_{100} = 1.84$). In the most recent time bin, $0 - 10$ Myr, the SFR significantly drops off, which is confirmed by the absence of Hα emission, indicating M81 Dwarf A is not forming stars at the present (Lee, 2006; Kennicutt et al., 2008).

DDO 53 – Figure 4.7 shows the ACS observations and stellar density maps of DDO 53. The red stellar density map, shown in panel (d), reveals an elongated distribution of red stars in the northeast-southwest direction that appears to extend to the east beyond the ACS field of view. The highest concentration of blue stars (panel (c)) is coincident with the highest concentration of red stars, and does not seem to suffer from truncation as the red stars do. The asymmetric distribution of red stars could be due to an interaction and is discussed in greater detail in §6.

The CMD of DDO 53 (Figure 4.14) shows high density RC and RGB stars, with a smaller population of AGB stars. There is a bright MS of moderate stellar density and HeBs are present but more so at fainter magnitudes, which are indicative of recent SF ($<$ 25 Mrs).

The lifetime and recent SFHs are shown in Figures 4.18 and 4.20. The lifetime SFH shows ancient and intermediate SF consistent with the lifetime average of $\sim$ 0.005 $M_\odot$ yr^{-1} ($f_{14} = 0.64$ and $f_6 = 0.28$). Over the most recent 1 Gyr DDO 53 has formed 8% of its stars and the birthrate parameters are very near the lifetime average, except over the past 100 Myr ($b_{100} = 1.24$, see Table 4.3). The cause of this rise in birthrate is due to an elevated SFR within the past 25 Myr, which is in excellent agreement with the presence of more young MS than HeB stars, the latter of which do not appear before 25 Myr.

Holmberg IX – The blue and red stellar density maps reveal a wealth of information about Ho IX (see Figure 4.8). The highest concentration of red stars (panel (d)) is along the western edge of the ACS field and decreases in density across the field to the east. It is unclear whether the low level of red stars (purple contours in panel (d)) that occupy the majority of the field are due to background or the very outer reaches of M81. The blue stars (panel (c)) are very prominent in the blue stellar density map as they show a very high density concentration of stars in the center of the ACS field. Similar to the Garland, we do not find a concentration of red stars associated with the blue stars of Ho IX.

In Figure 4.14 we show the CMD of the entire ACS field for Ho IX. Much like the Garland, Ho IX has a relatively broad RGB, which is due to contamination from red stars associated with M81. What makes the CMD of Ho IX especially interesting is the clustered dense nature of the HeBs, which is the signature of a recent burst of SF activity. The lack of bright MS stars tells us that Ho IX very recently stopped forming stars.

The lifetime and recent SFHs of Ho IX are shown in Figures 4.18 and 4.20. In a similar manner as for the Garland, we excluded the stars associated with M81 (roughly, we removed most of the blue and cyan contoured stars in panel (d) of Figure 4.8) and measured the SFH of Ho IX based on the remaining stars. We also did not require a monotonically increasing metallicity in the CMD fitting routine. Like the Garland, Ho IX is best fit with a more metal rich old component and a more metal poor young component (see Table 4.3).

The lifetime SFH shows that Ho IX has ancient and intermediate age SFRs consistent with the lifetime average SFR (~ 0.002 $M_\odot$ yr^{-1}). We find that Ho IX formed a significant fraction of its stars within the past 1 Gyr ($f_1 = 0.30$) with SFRs up to the most recent $\sim$ 250 Myr consistent with the lifetime average SFR. Even more recently, we see that $b_{100} \sim 20$, which implies a large fraction of stellar mass in Ho IX was formed within the past 100 Myr. The most recent time bin, $0 - 10$ Myr, shows a significant decline in the SFR, and Hα observations show an anomalously low Hα EW of 9Å, which is the signature of a post-burst galaxy (Lee, 2006; Kennicutt et al., 2008). The combined SFH and Hα, which is sensitive to $\sim 0 - 6$ Myr SF, are evidence that Ho IX is in a post-burst state and has just stopped forming stars within the last $\sim$ 10 Myr. We discuss the formation and evolution of Ho IX in more detail in §6.

Ho I – Figure 4.9 shows the ACS observation and stellar density maps of Ho I. The ACS field has captured most of the galaxy, although the red stellar distribution appears to be truncated to the south and west (panel (d)). There is a high density concentration of red stars in the center of the field, with a more moderate density component occupying the rest of the field. The blue stars are centrally located in the field, with several areas of very high density (panel (c)).

The CMD of Ho I is shown in Figure 4.16. The RGB and RC are densely populated due to ancient SF and the presence of a more sparsely populated AGB sequence implies

lower levels of intermediate age SF. The HeB and MS tracks share roughly the same densities and together tell us the Ho I has recently been forming stars.

The lifetime and recent SFHs of Ho I are shown in Figures 4.19 and 4.21. The ancient SFR is slightly greater than the lifetime average SFR (~ 0.01 $M_\odot$ yr^{-1}), while the intermediate age SFRs are lower than the lifetime average SFR ($f_{14} = 0.76$, $f_6 = 0.15$). Within the past 1 Gyr, we find the SFRs are slightly greater ($b_{1G} = 1.26$) than the lifetime average and that the most significant deviation from the lifetime average SFR occurs within the past 100 Myr, $b_{100} = 1.88$. Hα observations confirm that Ho I is presently forming stars (Ott et al., 2001; Lee, 2006; Kennicutt et al., 2008).

4.4.2 Galaxies with $M_B \leq -15$

In this section we present the CMDs, spatial stellar distribution, and SFHs for each of the galaxies with $M_B \leq -15$in order of increasing luminosity. We do not provide extensive comments and comparison with other wavelengths on individual features in the larger galaxies. In future work, we will conduct more detailed analysises of the spatial resolved recent SFHs of these galaxies.

DDO 165 – Figure 4.10 shows the ACS observation and stellar density maps of DDO 165. The red stellar density map (panel (d)) shows a distribution of red stars elongated in the east-west direction, with the highest density centrally located. The red stars appear to extend beyond the ACS field of view on the west side. There is a high density central concentration of blue stars (panel (c)) that cover a larger area than the central concentration of red stars. The blue stars are also elongated along the east-west axis.

The CMD of DDO 165 is shown in Figure 4.15. We see fairly well populated RGB and AGB tracks, indicators of old and intermediate SF. The young stars in this galaxy are particularly interesting and unusual. On the blue side, we do not see separate MS and BHeB tracks, rather, there is just one fairly dense blue star feature. We are able to conclude that this feature is indeed composed of BHeBs based on the empirical work of Dohm-Palmer & Skillman (2002a), which show that in Local Group dI Sextants A, that the ratio of BHeBs to RHeBs is greater than unity on average. The fact that the HeBs are so dominant over the MS is evidence that DDO 165 must have had recent SF activity, but is no longer forming stars.

The lifetime and recent SFHs of DDO 165 are shown in Figures 4.19 and 4.21. The ancient and intermediate age SFRs are mostly consistent with the lifetime average SFR (~ 0.013 $M_\odot$ yr^{-1}) with $f_{14} = 0.55$ and $f_6 = 0.28$. Over the past 1 Gyr, DDO 165 has formed 17% of its stars, the highest fraction in our sample outside of Ho IX (Table 4.3). We see that the birthrate parameters are consistently higher the unity ($b_{1G} = 2.43$, $b_{500} = 2.74$, and $b_{100} = 3.95$), with a significant increase over the past 100 Myr. There is little Hα emission in DDO 165, indicating very little, if any current SF. Further, the low Hα equivalent width (EW) classifies DDO 165 as post-burst, in excellent agreement with our SFH (Lee, 2006; Kennicutt et al., 2008).

NGC 2366 – Two ACS fields were required to cover most of NGC 2366 (Figure 4.11). We created a mosaic of the entire galaxy from the ACS observations (panel (b)) using Multidrizzle (Koekemoer et al., 2002) . The red stellar density map (panel (d)) reveals an elliptical distribution of red stars with the major axis in the northeast-southwest direction with a central high density concentration. The blue stars (panel (c)) are scattered through the main body, with a few highly concentrated regions. Field 1 (southern field) contains the powerful star forming HII region, NGC 2363 (**?**), seen as the large blue central region in panel (b). Coincident with this region is a dense concentration of blue stars (panel (c)) and a deficiency of red stars (panel (d)). This may either be a true lack of red stars or, more likely, a photometric effect, due to the high stellar density and extended HII emission in the F555W filter. To the west of NGC 2366, we find another concentration of blue stars, with no associated clustering of red stars, which is unlikely due to a photometric effect, because the region of extended HII emission is not very large.

We show the CMDs of Fields 1 and 2 in Figure 4.16. The similarity of the RGB, RC, and AGB components of the two fields reflect the symmetry of the spatial red star distribution in the galaxy. Field 1, which contains NGC 2363, contains MS and HeB tracks that are more densely populated at brighter magnitudes, indicating the southern half of the galaxy has stronger recent SF.

The lifetime and recent SFHs of NGC 2366 are shown in Figures 4.19 and 4.21 for Fields 1 and 2 combined. The ancient and intermediate SFRs are mostly consistent with the lifetime average SFR (~ 0.03 $M_\odot$ yr^{-1}) with $f_{14} = 0.59$ and $f_6 = 0.29$. Over the past 1 Gyr, the birthrate parameters range from $\sim 1.5 - 2$ and $f_1 = 0.12$, indicating

NGC 2366 has been very actively forming stars.

Ho II – Ho II required two ACS fields to cover a significant fraction of the galaxy (Figure 4.12). The color ACS figure (panel (b)) was created using Multidrizzle. Even with the two fields, there is still some truncation of both blue (panel (c)) and red (panel (d)) stars in the northwest direction, due to the galaxy extending beyond the ACS fields. Neither the red nor blue stars show preferential elongation along any axis. The red stars are centrally concentrated and coincident with the highest concentration of blue stars. In the color ACS image (panel (b)), we see several prominent blue regions of HII emission on the eastern side of the galaxy. Each of these blue regions has an associated overdensity of blue and red stars, suggesting these regions have been forming stars more than just at recent times.

The CMDs of Field 1 (south) and 2 (north) of Ho II are shown in Figure 4.16. The RC, RGB, and AGB sequences are similarly populated, which is in line with the symmetry of the galaxy's red stellar spatial distribution (panel (d)). The MS and HeBs are also virtually identical on the CMD, although Field 2 contains a more densely populated bright MS, indicative of stronger recent SF in Field 2.

The lifetime and recent SFHs of the combined fields of Ho II are shown in Figures 4.19 and 4.21. The ancient and intermediate SFRs of Ho II are consistent with or below the lifetime average (~ 0.04 $M_\odot$ yr^{-1}) with $f_{14} = 0.67$ and $f_6 = 0.21$. The birthrate parameters of Ho II range from $1.6 - 2.7$ and $f_1 = 0.12$ (see Table 4.3). We see a dramatic rise in the SFR over the past 50 Myr.

IC 2574 – IC 2574 is the largest and most metal rich of the dIs in the sample. We used two ACS fields to cover the southern and central regions and added a previous observation from the HST archive to the north to give us close to full coverage (Figure 4.13). We combined the three fields using Multidrizzle to create the color ACS mosaic image in panel (b). Panel (d) shows that the red stars are elliptically distributed with a major axis in the northeast-southwest direction. The highest concentration of red stars are located in the northern part of field 2 (center field) and southern part of field 3 (upper field). The blue stars (panel (c)) are scattered throughout the main body of the galaxy, ranging from low density in the Field 3 (lower field) to extremely prominent in the field 1. The high density concentration of blue stars in the northern field are associated with an HI supergiant shell (SGS; Walter & Brinks, 1999).

The CMDs of each of the three fields are shown in Figure 4.17. The RC, RGB, and AGB sequences of Fields 2 and 3 are virtually identical, a sign of the symmetric spatial distribution of red stars in these fields. Field 1 contains less stars in these same regions, primarily because this field does not contain as large a section of the optical galaxy as the other two fields. The MS and HeBs are most prominent in Field 3, which is expected due to the young stellar association near the SGS. Fields 1 and 2 are mostly occupied by a low density of blue stars, with a few concentrated regions, which is reflected in the CMDs and blue density map.

The lifetime and recent SFHs of the three combined fields of IC 2574 are shown in Figures 4.19 and 4.21. The oldest SFR is slightly higher than the lifetime average ($\sim$ 0.09 $M_\odot$ yr^{-1}), while the intermediate age SFR is lower than the lifetime average (f_{14} = 0.65 and $f_6 = 0.20$). We see from both the lifetime and recent SFH plots that a large SF event occurred at $\sim$ 1 Gyr and continued to form stars at a rate above the lifetime SFR for $\sim$ 500 Myr ($b_{1G} \sim 2$ and $f_1 = 0.15$). Over the most recent 500 Myr, the SFR is still above the lifetime average ($b_{500} \sim b_{100} \sim 1.4$), but recently, IC 2574 is not forming stars as strongly as over the 500 Myr $-$ 1 Gyr period.

Table 4.3 M81 Dwarfs: Star Formation Properties

Galaxy	Global Average SFR 10^{-2} $(M_{\odot}yr^{-1})$	b_{100}	b_{500}	b_{1G}	f_{1G}	f_{6G}	f_{14G}	$[\frac{M}{H}]_{1G}$	$[\frac{M}{H}]_{6G}$	$[\frac{M}{H}]_{14G}$	Θ
Garland	0.61	0.37	0.25	0.15	0.01	0.09	0.91	−1.0	−0.3	−0.4	4.0
Dwarf A	0.10	1.84	1.08	0.92	0.06	0.19	0.75	−1.3	−1.3	−1.6	0.7
DDO 53	0.52	1.24	0.76	1.08	0.08	0.28	0.64	−1.2	−1.2	−1.2	0.7
Ho IX	0.19	19.83	5.46	4.21	0.30	0.46	0.24	−1.4	−0.8	−1.1	3.3
Ho I	1.03	1.88	1.27	1.26	0.09	0.15	0.76	−1.2	−1.3	−1.4	1.5
DDO 165	1.27	3.95	2.74	2.43	0.17	0.28	0.55	−1.3	−1.4	−1.7	0.0
NGC 2366	3.37	2.14	1.99	1.61	0.12	0.29	0.59	−1.2	−1.3	−1.4	1.0
Ho II	3.64	2.70	2.00	1.63	0.12	0.21	0.67	−1.3	−1.3	−1.4	0.6
IC 2574	8.63	1.38	1.38	1.97	0.15	0.20	0.65	−1.0	−1.1	−1.2	0.9
Leo A	0.02	3.39	2.37	2.05	0.11	0.59	0.30	−1.3	−1.4	−1.4	0.2
WLM	0.08	1.73	2.08	2.24	0.10	0.44	0.46	−1.0	−1.0	−1.3	0.3
Sex A	0.18	5.06	2.28	1.70	0.15	0.28	0.57	−1.4	−1.4	−1.6	−0.6
IC 1613	0.10	1.61	0.95	0.83	0.06	0.41	0.53	−0.7	−1.0	−1.7	0.9
NGC 6822	0.17	2.59	1.12	1.12	0.07	0.56	0.37	−0.5	−0.8	−1.9	0.6
NGC 3109	0.56	1.36	1.05	0.75	0.05	0.03	0.92	−0.8	−0.9	−1.2	−0.1
IC 10	0.87	0.34	1.05	0.81	0.04	0.48	0.48	−0.4	−0.5	−0.8	1.8

4.5 Comparison of SFHs and SF Parameters

In this section we examine the fraction of stars formed and birthrate parameters as both a function of luminosity and in comparison to the Local Group. We divide the sample of galaxies based on their absolute blue magnitude with the dividing line at $M_B = -15.0$, an empirical separation used by Lee et al. (2007) based on Hα EW measurements. Additionally, we exclude both the Garland and Ho IX from this analysis because they are likely to be stellar systems forming from tidal debris and not independent galaxies. This leaves us with seven galaxies from the M81 sample for analysis. While this sample is in the regime of small number statistics, we are able to compensate by probing SF at a variety of ages, something Hα, UV, and IR flux surveys are unable to do. Additionally, we are developing this analysis in anticipation of a larger number of galaxies with similar data quality (e.g., ANGST), where the number of galaxies will be a factor of ten larger.

Similar to Lee et al. (2007) and Kennicutt et al. (2008) we present the mean and dispersion of the birthrate parameters as well as the fraction of stars formed in two magnitude regimes, $M_B > -15$ and $M_B \leq -15$ (see Table 4.4). Comparing the M81 Group galaxies in the two magnitudes regimes, we find that both types of galaxies formed comparable fractions of stars at ancient and intermediate times (see Table 4.4). The fraction of stars formed in the most recent Gyr is slightly higher in the more luminous galaxies ($\langle f_1(M_B \leq -15)\rangle = 0.14$ and $\langle f_1(M_B > -15)\rangle = 0.08$). This difference may reflect that the SFH correlates with mass, or that a higher fraction of recent SF boosts the luminosity of a galaxy increasing the probability that it will have $M_B < -15$.

Within the past Gyr, we can use the birthrate parameters to characterize the patterns of recent SF. For the fainter dIs we find $\langle b_{500}\rangle$ and $\langle b_{1G}\rangle \sim 1$, consistent with the lifetime average SFR. At more recent times, the SFR is elevated with $b_{100} \sim 1.6$. Looking at the larger dIs, we find a similar increase of b_{100} with $\langle b_{1G}\rangle$ and $\langle b_{500}\rangle \sim 1.9$ and $\langle b_{100}\rangle \sim 2.3$. Despite the differences in the mean values of the birthrate parameters of the two classes of galaxies, the fractional increase in the birthrate parameter in the past 100 Myr is ~ 1.5 for both types of galaxies. Overall, the fraction of stars formed and birthrate parameters are consistent with one another in the two luminosity regimes.

Examining the dispersions in the birthrate parameters, we find that the values for $\sigma(\log(b_{500}))$ and $\sigma(\log(b_{1G}))$ are roughly equal for both types of galaxies, but over the

past 100 Myr the dispersion in the birthrate parameters is ~ 1.5 times greater for the brighter galaxies. The increase in both dispersion and mean birthrate parameters in the past 100 Myr is not too surprising because the sample of dIs was selected to span a wide range of current SFRs as measured by Hα emission (Figure 4.1 Lee et al., 2007; Kennicutt et al., 2008). However, the resultant dispersions are subject to our sample selection bias, and will be more meaningful with an expanded sample.

4.5.1 Comparison with the Local Group

An interesting application of measured SFHs is to compare the properties of galaxies in different groups. The M81 Group is a more massive analog to the Local Group (LG) and experienced a major interaction within the last ~ 300 Myr. In the previous section, we explored the properties of the SFHs of the M81 Group dIs and found minor differences in the two luminosity regimes in both the fraction of star formed and birthrate parameters. We apply the same statistics to select LG dIs with similar quality photometry and compare the results to those of the M81 Group dIs.

To assemble a sample of LG galaxies, we selected those galaxies in the Local Group Photometry Archive (Holtzman et al., 2006) whose WFPC2 photometry is of comparable quality to our M81 Group dwarf observations. The sample consists of Leo A, WLM, Sex A, IC 1613, NGC 6822, NGC 3109, and IC 10. The SFHs of both sets of galaxies were computed using the same method to allow for uniform comparison (Dolphin et al., 2005). As we can see, the mean lifetime averaged SFR of the LG sample, ~ 0.001 $M_{\odot}$ yr^{-1}, is lower than that of the M81 Group sample, ~ 0.02 $M_{\odot}$ yr^{-1}. Of course our selection of galaxies for comparison is based on photometric quality and not on physical characteristics and thus is subject to a selection bias. For example, the samples are not comprable in their luminosity distributions.

Comparing the fraction of stars formed in M81 Group dIs and LG dIs, we find very little difference between the two groups (Figure 4.22 and Table 4.4). While individual galaxies do not share the same f values, the averages in the two luminosity regimes are very similar. We extend this comparison by examining the average values of the composite sample with the expected values for a constant SFH (i.e., $f_1 = 0.07$, $f_6 = 0.36$, and $f_{14} = 0.57$). While very few of the individual galaxies (Table 4.3) are consistent with the constant SFR f values, the average of the composite sample, in both luminosity

regimes, is in excellent agreement with a constant SFH. It is important to note that this result does not imply that a constant SFH is a good model for any given dI. Rather, this result emphasizes that dIs have SFHs that deviate randomly from a constant SFH model. Additionally, we searched for a correlation between our f parameters and Θ, the tidal index (see §6 and Karachentsev et al., 2004), as well as our f parameters and the center of mass of the respective groups, and found none.

Similarly, we compare the birthrate values for the M81 dIs and LG dIs, finding little difference between the composite values in the two luminosity regimes (Figure 4.23 and Table 4.4). On average the the faint LG galaxies have higher mean birthrate parameters than their M81 counterparts. Conversely, the bright M81 Group dIs have higher mean birthrate parameters than the bright LG dIs. Examining the composite values, we find that they are consistent with one another and are well above what we would expect for a constant SFH (i.e., $b = 1$). This conclusion suggests that the birthrate parameters for dIs are not correlated with luminosity and are randomly distributed. However, we need to examine a larger sample to support this conclusion. We also examined trends between our b parameters and Θ and between our b parameters and the center of mass of the respective groups, but found no clear correlation.

Table 4.4: Star Formation Statistics for the M81 Dwarfs

	M81 Group		Local Group		M81 + LG	
	> -15	≤ -15	≤ -15	> -15	> -15	≤ -15
$\langle f_1 \rangle$	0.08	0.14	0.11	0.05	0.09	0.10
$\langle f_6 \rangle$	0.21	0.25	0.43	0.36	0.34	0.29
$\langle f_{14} \rangle$	0.71	0.61	0.46	0.59	0.57	0.61
$\sigma(f_1)$	0.02	0.02	0.04	0.02	0.03	0.05
$\sigma(f_6)$	0.07	0.05	0.12	0.29	0.15	0.18
$\sigma(f_{14})$	0.07	0.06	0.12	0.29	0.16	0.17
$\langle \log(b_{100}) \rangle$	0.21	0.37	0.42	0.03	0.33	0.23
$\langle \log(b_{500}) \rangle$	0.01	0.29	0.26	0.03	0.15	0.18
$\langle \log(b_{1G}) \rangle$	0.03	0.27	0.20	-0.06	0.13	0.13
$\sigma(\log(b_{100}))$	0.10	0.19	0.24	0.45	0.21	0.35
$\sigma(\log(b_{500}))$	0.11	0.12	0.19	0.02	0.20	0.17
$\sigma(\log(b_{1G}))$	0.07	0.08	0.20	0.09	0.17	0.19

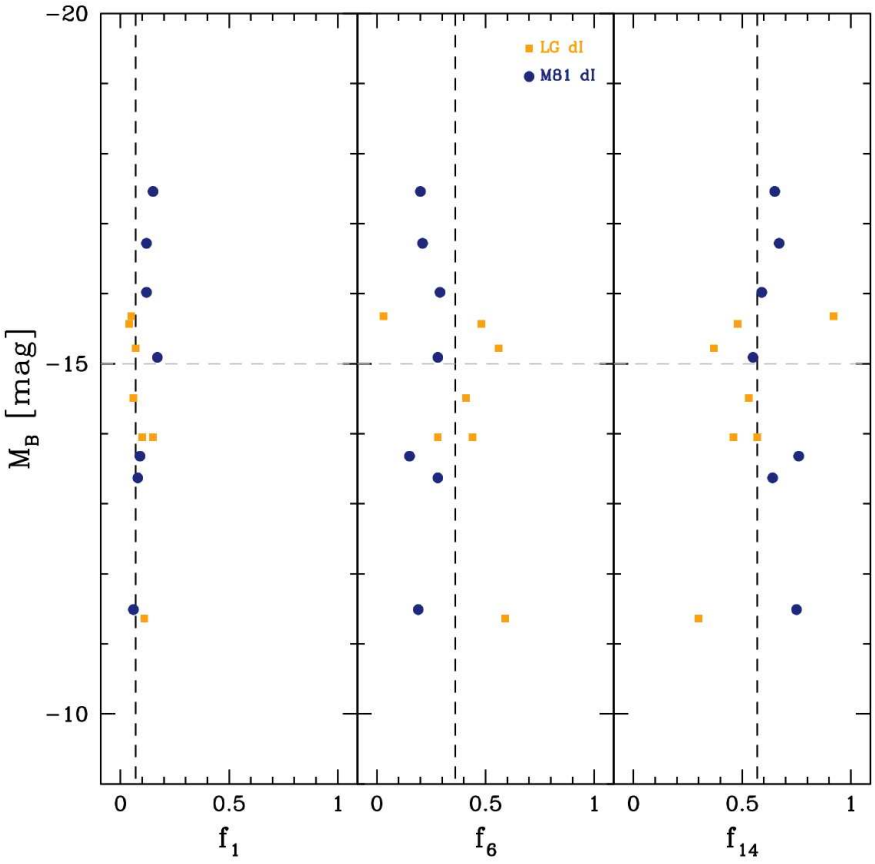

Figure 4.22 The fraction of stars formed in the past $0 - 1$ Gyr (f_1), $1 - 6$ Gyr (f_6), and $6 - 14$ Gyr (f_{14}) plotted versus M_B for both M81 Group (orange triangles) and Local Group (blue circles) galaxies. The grey dashed line represents a transition luminosity noted by Lee et al. (2007) based on Hα EW measurements.

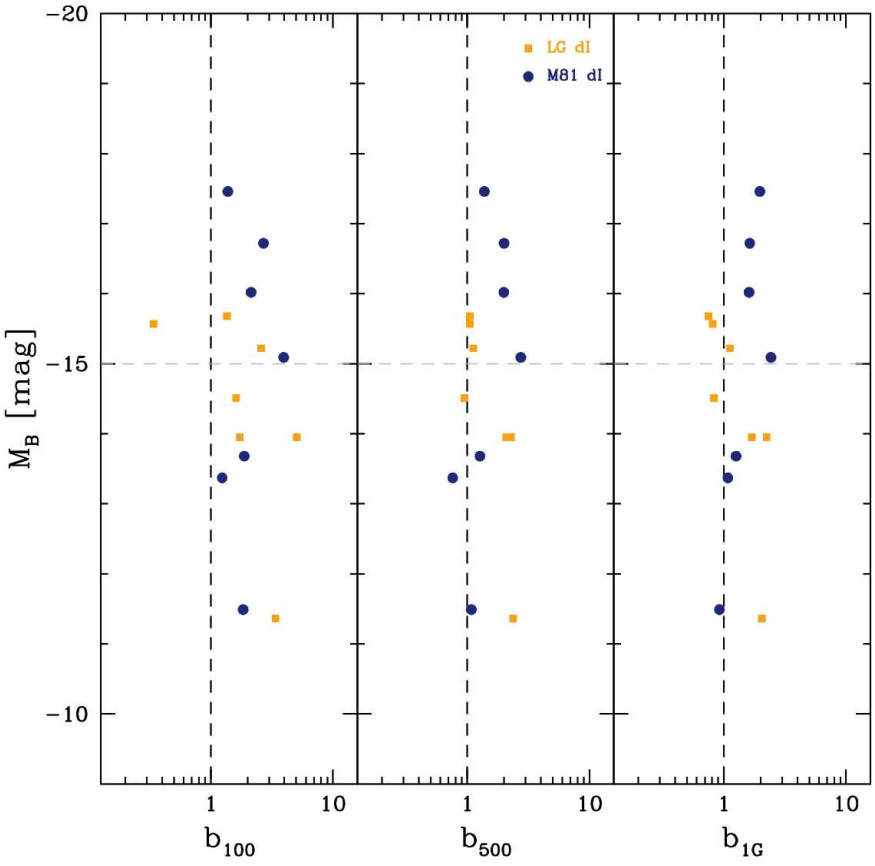

Figure 4.23 The birthrate parameters plotted versus M_B for both M81 Group (orange triangles) and Local Group (blue circles) galaxies. The grey dashed line represents a transition luminosity noted by Lee et al. (2007) based on Hα EW measurements.

4.6 Formation and Evolution of Small and Potential Tidal Dwarfs

Of the 4 faintest galaxies, there is evidence that the Garland and Ho IX are tidal dwarfs (Yun, 1999; Makarova et al., 2002). There have also been suggestions that DDO 53 is the result of a merger (Begum et al., 2006), and that M81 Dwarf A may be of tidal origin

(Bureau et al., 2004). All of these galaxies share a common feature an of increased SFR over the past 100 Myr, which may be due to induced SF as a result recent interactions. We now assess the evidence to determine which of these galaxies may be recently formed tidal dwarfs and which may be genuinely old, but with recent SFR enhancements.

Close interactions between galaxies are capable of leaving tidal debris that may be the raw material for the formation of new stellar systems, perhaps even new independent galaxies (e.g., Zwicky, 1956; Toomre & Toomre, 1972; Duc et al., 1997). In the M81 Group, HI observations (Yun et al., 1994) reveal evidence of tidal streams and debris indicative of a recent interaction of larger galaxies within the group. Subsequent modeling of the group dynamics (Yun, 1999) find the three large galaxies (M81, M82, and NGC 3077) had an interaction $\sim$ 250 Myr for M81 and NGC 3077 and $\sim$ 220 Myr ago for M81 and M82. Within this tidal debris around NGC 3077, we find the Garland, an overdensity of young stars (see Figure 4.2), also coincident with peaks in HI and CO (van der Hulst, 1979; Walter & Heithausen, 1999; Yun et al., 1994). Based on our SFH, we find a rise in the SFR at $\sim$ 250 Myr, slightly more recently than the proposed interaction timescale. Similar to the Garland, Ho IX is located in the inner tidal arm of M81 (see Figure 4.2), and also experienced a rise in SFR, $b_{100} \sim 20$, slightly more recently than the interaction time of 220 Myr. Further, these two systems have large tidal indices, $\Theta_{Garland} = 4.0$ and $\Theta_{Ho\ IX} = 3.3$, which indicate the relative amount of gravitational disturbance from a neighboring galaxy (see Equation 8 in Karachentsev et al., 2004). Large positive values indicate a high degree of disturbance and more negative numbers imply a larger degree of isolation.

While it is difficult to determine if the Garland and Ho IX are tidal dwarfs, it is reasonably straightforward to see that the Garland and Ho IX are not dIs. Comparing red star distributions with the two faint dIs in the sample, we see that both DDO 53 and M81 Dwarf A have prominent red star components that are distinct from the background and coincident with the high density of blue stars. However, the Garland and Ho IX (Sabbi et al., 2008) do not show any evidence of a red star overdensity coincident with the blue stars. From this we can conclude that the Garland and Ho IX are not dIs.

Beyond comparing the Garland and Ho IX to dIs, we cannot distinguish if the Garland and Ho IX are true tidal dwarfs or alternatively stellar systems forming in their larger companion. A primary criteria for determination of a tidal dwarf is a

low mass-to-light ratio, due to the absence of dark matter (e.g., Barnes & Hernquist, 1992; Duc et al., 2000), which we cannot measure from the resolved stellar component. Without this measurement, we can only conclude that these are possible tidal dwarf galaxies.

HI observations and analysis by Bureau et al. (2004) suggest that M81 Dwarf A may also be of tidal origin formed from tidal debris originally belonging to Ho II. However, M81 Dwarf A shows no dramatic increase in the recent SFH and the older stellar population is centrally concentrated, both unlike the candidate tidal dwarfs in our sample. Examining the SFH, neither the ancient nor recent SFHs show evidence of tidal formation. M81 Dwarf A formed 75% of its stars $6 - 14$ Gyr ago, which is unlike Ho IX. The Garland does show a higher fraction of stars formed in the same bin, but this is likely due to red star contamination from NGC 3077. At recent times, M81 Dwarf A does show an increasing trend in birthrate parameters toward the present, but there is not a sudden increase in the SFR as is the case with the other candidate tidal dwarf galaxies in the M81 Group sample. Spatially, the red star distribution is fairly symmetric, which is not like that of the other tidal dwarfs. Similarly, the HI component of M81 Dwarf A does not show an asymmetry toward or any connection to a nearby companion (Begum et al., 2006; Walter et al., 2008). In agreement with these observations, M81 Dwarf A has a tidal index of 0.7 (Table 4.3), which indicates it is fairly isolated. Thus, M81 Dwarf A is not a tidal dwarf candidate like the Garland or Ho IX.

The unusual kinematics of the HI in DDO 53 led Begum et al. (2006) to speculate that DDO 53 may be a product of a recent merger between two fainter dwarfs. The HI kinematics are comparable to other galaxies thought to be late-stage mergers (Hunter & Wilcots, 2002; Koribalski et al., 2003). From our spatial analysis (Figure 4.7), we do find that the red stars are not symmetric, which could be due to a merger or at least gravitational influence of another galaxy. The blue stars are centrally concentrated and align well with peaks in both Hα and HI observations (Walter et al., 2008; Begum et al., 2006), but they do not follow the distribution of red stars, which we might expect if there was a recent gravitational disturbance. The recent SFH of DDO 53 reveals that it is forming stars at a higher rate at the present than any other time within the more recent 1 Gyr. Outside of this dramatic increase, DDO 53 has been

forming stars at or below the lifetime average over the past 1 Gyr, which would not be consistent with a merger in this timeframe. Similarly, with a tidal index of 0.7, DDO 53 is a relatively isolated galaxy and does not appear to have been gravitationally disturbed recently. It is possible that DDO 53 is the result of a merger, but such an interaction would have had to take place more than 1 Gyr ago according to our observations and analysis.

We can also compare the the chemical evolution measured from the SFH fitting method to search for differences between the small and candidate tidal dwarfs. M81 Dwarf A and DDO 53 show very little evolution in their chemical abundances over their lifetimes (see Table 4.3) and DDO 53 has a 1 Gyr value close to the observed abundance (Tables 4.1 and 4.3). The galaxies underwent very little in the way of chemical evolution over their lifetimes, which would be consistent with isolated, i.e., non-interacting galaxies. In contrast, the candidate tidal dwarfs have significant chemical evolution (e.g., Barnes & Hernquist, 1992). As previously mentioned, for the candidate tidal dwarfs we did not require the chemical evolution to monotonically increase. The motivation for this was to help find evidence if there truly were two populations of stars in these fields. The difference in the ancient and recent metallicity values (0.6 dex for the Garland and 0.3 dex for Ho IX) and the fact that the younger components are relatively metal poor are both signs, albeit indirect, that there are mixed populations in those fields; the more metal rich stars from the large companion and the more metal poor stars formed from tidal debris.

4.7 Conclusions

From HST/ACS imaging we use resolved stellar populations to study the temporal and spatial properties of nine diverse dIs in the M81 Group. Photometry from the HST/ACS images was used to create CMDs and trace the temporal evolution of each galaxy via measured SFHs. From the CMD, we isolated red (old) and blue (young) stars and created stellar density maps to better understand the stellar spatial components. Notably, we analyze two candidate tidal dwarf galaxies, the Garland and Ho IX, and find that they are clearly different from any of the other galaxies in the sample, both in their SFHs and spatial stellar distributions, despite having similar luminosities. They

are particularly interesting because they are two of the nearest candidate tidal dwarf galaxies in the universe, as we do not have similar galaxies in the Local Group.

In addition to analyzing the galaxies on an individual basis, we divided the sample into two groups, based on an empirical separation in luminosity of star forming galaxies in the Local Volume (Lee et al., 2007; Kennicutt et al., 2008). Based on this division, we compute the fraction of stars formed and birthrate parameters, and compare these values between the two regimes, finding very little difference. We extend our comparison of dIs to the LG, selecting LG galaxies with similar quality photometry for comparison. Again, comparing the M81 Group dIs and LG dIs, we find very little difference in their SF characteristics (i.e., fraction of stars formed and birthrate parameters). Analyzing the composite population of the M81 and LG dIs, we find that the average values of the fraction of stars formed in both luminosity regimes are consistent with that of a constant SFH. Importantly, we note that individual galaxies are not well modeled by a constant SFH. We interpret this result to mean that the fraction of stars formed in each galaxy is essentially random (or stochastic), but that with a larger sample, the mean values converge on those consistent with a constant SFH. We searched for trends in the birthrate parameters as a function of luminosity, but found none, supporting the idea that stochastic SF is important in dIs. With our future work, we will explore the same type of analysis with a larger sample, as well as comparing spatially resolved SFHs to multi wavelength observations to give us further insight into the impact of SF on the evolution of low mass galaxies.

Chapter 5

Triggered Star Formation and the Creation of the Supergiant HI Shell in IC 2574

5.1 Introduction

Vigorous (SF) is one mechanism thought to be responsible for the creation of the holes and shells observed in the interstellar medium (ISM) of a wide variety of galaxies. Following a strong episode of SF, energy input into the ISM from young massive stars (e.g., stellar winds, Type II supernovae) can provide sufficient mechanical energy to create these holes and shells and may even trigger secondary SF around the edges (e.g., Tenorio-Tagle & Bodenheimer, 1988; Puche et al., 1992). Although observations of young stellar clusters inside these ISM features confirm that this is one possible scenario, a majority of holes and shells do not contain bright associated young clusters (e.g., van der Hulst, 1996; Rhode et al., 1999; Pasquali et al., 2008). One explanation is that only a select few ISM holes and shells have been observed with sufficient photometric depth to detect the associated clusters. Alternatively, a number of competing theories suggest the origins of holes and shells in the ISM are from mechanisms other than stellar feedback, e.g., high velocity cloud collisions (e.g., Kamphuis et al., 1991), interactions (e.g., Bureau et al., 2004), gamma ray bursts (e.g., Loeb & Perna, 1998),

stochastic SF propagation (Harris & Zaritsky, 2008).

Dwarf irregular galaxies (dIs) provide excellent environments in which we can study the creation mechanisms of these ISM features. Larger galaxies exhibit differential rotation and sheer, which can destroy the holes and shells in the ISM on timescales as short as 10^7 year. However, dIs are typically solid body rotators (e.g., Skillman et al., 1988; Skillman, 1996), which allows features in the ISM to grow to large sizes ($\sim$ 1 kpc) and stay coherent over longer time scales (e.g., Walter & Brinks, 1999).

Nearby dIs are particularly convenient probes of the interplay between SF and the ISM, because we can directly compare the resolved stellar populations to the HI component to better understand mechanisms of feedback. At a distance of $\sim$ 4 Mpc (Karachentsev et al., 2002), IC 2574, an M81 Group dI, contains a "supergiant shell" (SGS) (denoted by the red ellipse in panels (a) and (b) of Figure 5.1; Walter et al., 1998; **?**) and is an excellent candidate for specifically studying both the formation of the SGS and subsequent triggered SF around its rim. Walter & Brinks (1999) classify the SGS as an ellipse ($\sim$ 1000 $\times$ 500 pc), however note that many of the holes and shells in IC 2574 are elongated due to projection effects (the de-projected diameter is $\sim$ 700 pc). They further note there is some evidence that the SGS is a superposition of two merged shells (Walter & Brinks, 1999), which could account for its elliptical shape. In addition to the shape, the expansion of the SGS is somewhat uncertain. Walter & Brinks (1999) measure an HI expansion velocity of 25 km s^{-1} from a break in the PV-diagram, which is only an indirect measure of expansion, and in fact is consistent with stalled expansion as well. We discuss the implications of these scenarios in §5.3.1. UV observations show a young stellar cluster ($\sim$ 11 Myr old, Stewart et al., 2000) inside the SGS, but no Hα emission is observed from the interior. Around the rim, strong Hα (and mid-IR) emission is observed (see panel (c) of Figure 5.1, e.g., Walter et al., 1998; Cannon et al., 2005) indicating SF at these locations within the past $\sim$ 5 Myr.

In this paper, we use deep HST/ACS imaging of the resolved stellar populations of the SGS to measure its recent SFH ($<$ 500 Myr). We use the unique properties of resolved blue helium burning stars (BHeBs) to trace the spatial locations of the SF episodes, resulting in a movie that shows how SF propagated in the vicinity of the SGS over the past 500 Myr. From these lines of evidence, we are able to directly explore the SF event(s) responsible for the creation of the SGS and triggering of secondary SF.

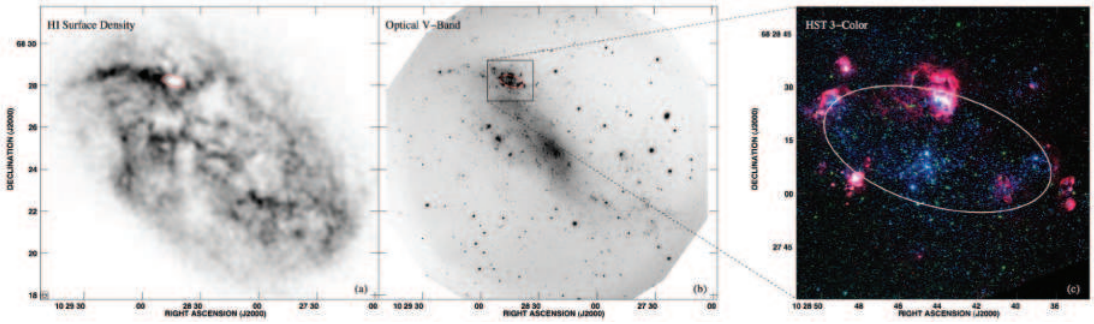

Figure 5.1 (a) HI image (Walter & Brinks, 1999); (b) optical V-band (Walter & Brinks, 1999); and (c) color ACS image of the SGS region in IC 2574 we use for analysis in this paper. The ellipse in each image is the outline of the SGS and is likely elliptical due to projection effects. It has a de-projected diameter of $\sim$ 700 pc.

5.2 Observations and Photometry

We used HST/ACS to observe the region of IC 2574 containing the SGS on 2004, February 6 in three wide band filters F435W (B), F555W (V), and F814W (I). The images were processed using the HST pipeline and photometry was extracted using DOLPHOT, a version of HSTPHOT (Dolphin, 2000) with an ACS specific module. To account for photometric completeness, we performed artificial star tests. After filtering out cosmic rays, hot pixels, and extended sources from the photometry we had 253,736 well measured stars in the ACS field of view. Subsequently, we isolated the SGS region and found 24,912 well measured stars in the F555W and F814W filters. The limiting magnitude of our photometry in this region is $M_V \sim 0$, which gives us excellent leverage on SF in the past $\sim$ 1 Gyr (Gallart et al., 2005; Weisz et al., 2008). The photometry was carried out as part of a larger study of M81 Group dIs and full details of the observations, photometry, and completeness can be found in Weisz et al. (2008).

5.3 The Star Formation History

We measured the SFH of the SGS region (the entirety of panel (c) in Figure 5.1) of IC 2574 from the HST/ACS based color-magnitude diagram (CMD) using the code of Dolphin (2002). This method constructs synthetically generated CMDs, using the stellar

evolution models of Marigo et al. (2008), and compares them to the observed CMD using a maximum likelihood technique. To obtain this solution, we used a combination of fixed (e.g, binary fraction, initial mass function) and searchable (e.g., distance, extinction) parameters. For consistency, we set all our parameters to the values found for IC 2574 listed in Table 2 of Weisz et al. (2008). To quantify the uncertainties of the SFH, we added the systematic uncertainties from the isochrones and the statistical uncertainties from Monte Carlo tests in quadrature (see Weisz et al. 2008 for details).

We used the CMD of the SGS region (see Figure 5.2) as input into the SFH code. The SFH of the SGS region over the past 500 Myr is shown in the top panel of Figure 5.3. For reference, we show the SFR of the SGS region averaged over the lifetime of the galaxy as the red dashed line. We see that over the past 500 Myr, the SFR is always higher than the lifetime averaged SFR, with notable increases at $\sim 200 - 300$ Myr and within the last ~ 25 Myr. From the most recent time bin ($0 - 10$ Myr) we see a dramatic increase in the SFR, which is in agreement with the Hα derived SFR for this region (e.g., Miller & Hodge, 1994; Cannon et al., 2005). Because the SGS region, i.e. all of panel (c) in Figure 5.1, is larger than the SGS itself, we tested for the possibility that SF from the additional area influenced our SFH. We measured the SFH interior to the SGS only and found differences which were deemed insignificant.

5.3.1 Spatially resolved SFH of the SGS

BHeBs are powerful tools for studying both the ages and locations of SF from $\sim 10 - 500$ Myr (c.f. Dohm-Palmer et al., 1997, 2002b; Weisz et al., 2008). They provide us leverage because (a) this evolutionary phase is very short relative to the main sequence lifetime and (b) BHeBs of different ages do not overlap on the CMD (Dohm-Palmer et al., 1997; Gallart et al., 2005; Weisz et al., 2008). The result is that we can create density maps of BHeBs at different ages, which trace the spatial location of SF events over time. Inherently uncertainties in distance, extinction, photometry, and isochrones can all affect the precise ages of the BHeBs. Because of the low metallicities in dIs and the high quality of our ACS data, we find the observational related uncertainties to be small, and have calculated isochrone based errors to be $\sim 10\%$ (Weisz et al., 2008). In addition to uncertainties in ages, the locations of the BHeBs can be influenced by proper motions of the stars. The stars we consider are thought to belong to clusters

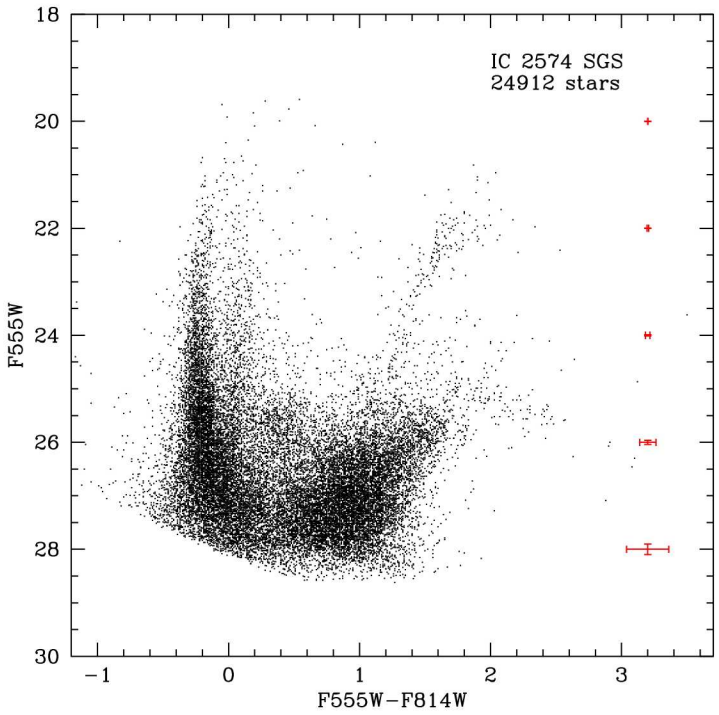

Figure 5.2 The HST/ACS CMD of the SGS region (panel (c) in Figure 5.1) corrected for foreground extinction.

and are thus bound by gravity. Although they will not remain gravitationally bound indefinitely, the time scale for dissipation of such stellar associations is $\sim$ 600 Myr to 1 Gyr (Dohm-Palmer et al., 1997), much longer than the time scale we consider for the SGS. To transform the density of BHeBs to a SFR per area, we multiply each density map by the corresponding SFR, measured using the code of Dolphin (2002), divide by the image area, and interpolate in both space and time to create a spatially resolved SFH movie. The final spatial resolution of the movie is $\sim$ 8", similar to that of the HI observations, and the movie frames are then interpolated onto a grid with 5 Myr sampling.

Figure 5.4 shows selected still frames from the spatially resolved SFH movie of the SGS region; the outline of the SGS is indicated by the white ellipse. We can see that

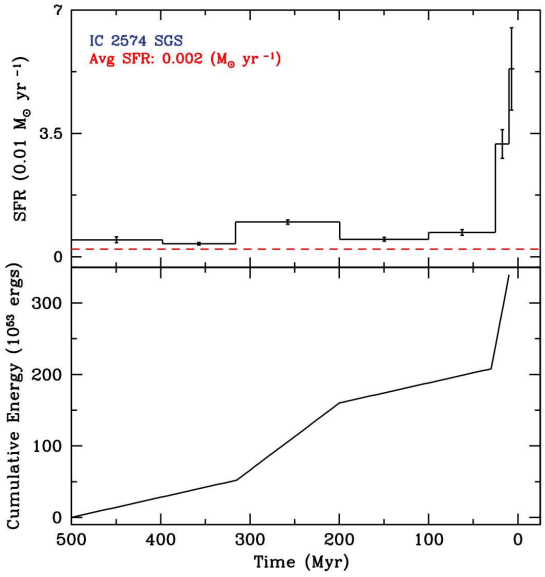

Figure 5.3 (*top*) The SFH of the SGS region over the past 500 Myr. The red dashed line indicates the SFR of the SGS averaged over the lifetime of the galaxy; (*bottom*) The cumulative energy from SF in the SGS over the past 500 Myr calculated with STARBURST99.

in the oldest frames, 500 and 350 Myr, there is no major SF going on in the region. From $200 - 300$ Myr, we see that there is an elevated period of SF in the center of the SGS. A period of relative quiescence lasts until ~ 100 Myr, when a SF event begins to strengthen inside the central regions of the SGS. The peak strength of this central event is at ~ 25 Myr, after which SF subsides centrally, but increases in intensity on the rim.

The location of the SF events in the center of the SGS and on the rim are in excellent agreement with observations from other wavelengths. The central event coincides well with UV observations by Stewart et al. (2000). The triggered SF on the rim is traced by Hα and Spitzer IR imaging (e.g., Cannon et al., 2005) and is in excellent agreement with our 10 Myr frame. The $200 - 300$ Myr event is beyond the look back time of the UV and IR fluxes, and is only traceable with the deep photometry presented here.

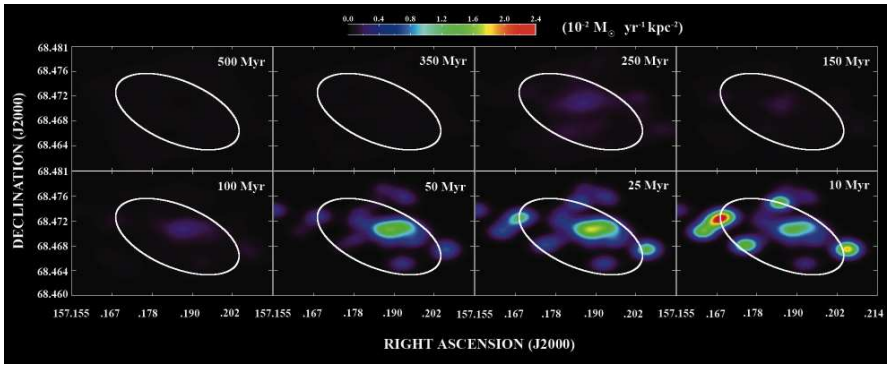

Figure 5.4 Selected still frames from the spatially resolved recent SFH of the SGS region. The white ellipse corresponds to the elliptical outline of the SGS itself shown in Figure 5.1. The spatial resolution of the images is $\sim$ 8", similar to that of the HI observations.

5.4 Discussion

To understand the current state of the SGS, we consider the energetics of both the HI and SF, the role of triggered SF, and the timing of the events that led to the evacuation of the HI and secondary SF around the rim. To do this we examine the efficiency of energy, i.e. the feedback efficiency, transfered from stellar feedback into moving the ISM in the context of both an expanding and stalled shell.

Following the model of Chevalier (1974), one can compute the energy necessary to evacuate the HI mass interior to the SGS to be $\sim 2\times10^{53}$ erg (e.g., Walter et al., 1998; Walter & Brinks, 1999; Cannon et al., 2005). Using STARURST99 (Leitherer et al., 1999), we can independently calculate the energy associated with SF in the SGS region by inputting our SFH and assuming the same IMF as was used to measure the SFH (see Weisz et al. 2008). We computed the total cumulative kinetic energy (i.e., stellar winds and SNe) of the SGS region over the past 500 Myr to be $\sim 3\times10^{55}$ erg (Figure 5.3). Because of our relatively coarse time resolution, we need to consider that our elevated SF periods, may be shorter bursts averaged out over a longer time. Thus, we used STARBURST99 to model the SFH as both a series of constant episodes of SF, as well instantaneous bursts for the elevated SF episodes and found the energetics to be consistent.

At first pass, it may seem that SF generates an unreasonably large amount of energy compared to the HI energy requirement. However, by considering the feedback efficiency we can reconcile the apparent discrepancy. Assuming that each SN imparts 10^{51} erg in into moving the ISM we find a $\sim 1\%$ stellar feedback efficiency, which is on the low end of the spectrum that ranges from $\sim 1 - 20\%$ (e.g., Theis et al., 1992; Cole et al., 1994; Padoan et al., 1997; Thornton et al., 1998). However, we have really computed a lower limit on the efficiency, as the HI energy is a lower bound, and the SF energy is an upper bound. The HI energy was computed using an assumed smooth uniform HI distribution inside the SGS. Given that the central SF event in the SGS was extremely powerful, it is likely that there was a higher density of gas interior to the SGS in the past (e.g., Oey et al., 2002). For example, the model of Chevalier (1974) predicts that an increase in a factor of 10 in the gas density would change our feedback efficiency to $\sim 10\%$. When we consider the energy input into the ISM due to SF, only a fraction of this energy is used to move the ISM, with the rest lost to heating and radition. Simulations suggest $\sim 10^{50}$ erg per SN is a more realistic amount of SN energy imparted into moving the ISM (Cole et al., 1994; Thornton et al., 1998), which also increases our feedback efficiency. Finally, if the SGS has stalled expansion and broken out of the plane of the galaxy, the energy from SF simply escapes and does not go into moving the ISM. Despite the large uncertainties in the calculations of both energy quantities, we find that our feedback efficiency falls in the range of the values typically calculated from simulations, indicating the SF generated an appropriate amount of energy for creation of the SGS.

The SGS presents a clear case of not only sequential SF, but also triggered (i.e., causally connected) SF. From the spatially resolved SFH movie (Figure 5.4), we see clearly that the central burst predates the SF on the rim, which is in excellent agreement with age estimates in the literature (e.g., Walter et al., 1998; Cannon et al., 2005; Pasquali et al., 2008). Establishing a causal relationship between SF events is generally non-trivial and only a handful of cases of triggered SF have been established (see Oey et al. 2005 and references therein). In the case of the SGS, we have a recent SF episode interior to the SGS, which peaked ~ 25 Myr ago and the bulk of the recent SF on the rim is < 10 Myr old, indicated by both the SF movie and the Hα observations. Thus, it appears that the central SF event initiated the expansion of the shell, which swept up the ISM, and when the gas on the rim becomes sufficiently dense, secondary

SF began. As a slight twist to this scenario, we can speculate about the role of the older ($200 - 300$ Myr), central SF event. Because of the location of the older event and energy input into the ISM, it is possible that this older event cleared out some or all of the SGS, and the more recent event simply served to accelerate the expansion and trigger the SF around the rim. Or perhaps the older event created one spherical shell, which merged with a younger shell to account for the ellipticity of the SGS. To better our understanding of the role of both young and old SF events in reshaping the ISM, we will need to employ similar analysis techniques on a statistically significant sample of holes and shells in the ISM of nearby dIs.

Chapter 6

Does Stellar Feedback Create HI Holes? An HST/VLA Study of Holmberg II

6.1 Introduction

The role of star formation (SF) in creating structure and shaping the interstellar medium (ISM) is an important but unresolved topic. Studies of the neutral hydrogen (HI) component in a wide variety of nearby galaxies, including our own, reveal numerous holes, shells, and bubbles (for simplicity, we will refer to all types as holes throughout the paper), which span a great range in size and age (e.g., Heiles, 1979; Brinks & Bajaja, 1986; Puche et al., 1992; Oey & Massey, 1995; Kim et al., 1999; Walter & Brinks, 1999; Muller et al., 2003; Relaño et al., 2007; Chu, 2008; Bagetakos et al., 2009). The origin of these ISM features has long been attributed to stellar feedback from massive stars, i.e., stellar winds and Type II supernovae (SNe) (Weaver et al., 1977; Cash et al., 1980; McCray & Kafatos, 1987; Tenorio-Tagle & Bodenheimer, 1988, and references therein). Typical ages of these ISM features, measured from the hole diameters and HI expansion velocities, range from $\sim 10^6 - 10^8$ yr (e.g., Oey & Massey, 1995; Walter & Brinks, 1999; Hatzidimitriou et al., 2005), which suggests that even if massive O and B type stars, the primary contributors to stellar feedback, are no longer present inside the HI holes,

we should still see remnant stellar populations (assuming a universal IMF).

While the stellar feedback hypothesis of HI hole creation is appealing due to its intuitive simplicity, observational and theoretical studies do not provide much supporting evidence. The close proximity of dwarf galaxies in the Local Group (LG) has permitted detailed studies of correlation between stars and HI holes. In the LMC, Kim et al. (1999) compared the positions of 103 giant or supergiant HI shells with Hα, and found a weaker correlation than expected given the young ages of the shells. Similarly, Book et al. (2008) find that while Hα traces sites of secondary triggered SF around supergiant HI shells in the LMC, it is not exclusively associated with stars interior to the holes. Hatzidimitriou et al. (2005) cross-correlated the locations of 509 HI holes in the SMC with known catalogs of OB associations, supergiants, Cepheids, Wolf-Rayet (WR) stars, SN remnants, and stars clusters, finding 59 HI shells with no stellar component, and that holes without associated OB stars exceed those with them by factor of ~ 1.5. Further, in the LG dwarf irregular galaxy (dI) IC 1613, Silich et al. (2006) find that even the HI structures that do contain young stars do not have the observed properties consistent with the traditional stellar feedback theory.

The studies of the origins of HI holes in galaxies beyond the LG show similarly mixed results when testing the stellar feedback hypothesis. In the pioneering study of M31, Brinks & Bajaja (1986) found a strong correlation between OB associations and HI shells smaller than ~ 300 pc. Correlating high resolution HI imaging of the M81 Group dI Holmberg II with Hα, Puche et al. (1992) found strong evidence for a stellar feedback origin to the 51 HI holes. In a follow up study of Ho II, Rhode et al. (1999) used integrated BVR photometry to search for stars within the HI holes and found only 14% had a stellar component. A third study of Ho II concludes that Hα does not adequately trace the progenitor stellar populations; however, detected FUV emission associated with HI holes supports the stellar feedback model (Stewart et al., 2000). In another M81 Group dI, IC 2574, Pasquali et al. (2008) use integrated colors from imaging from the Large Binocular Telescope to show that there is not a one to one correspondence between stars and HI holes, while an evaluation of alternative models by Sánchez-Salcedo (2002) finds that HI holes in IC 2574 are likely formed by stellar feedback.

Although a number of studies of select individual holes have found associated young

stars (e.g., Oey & Massey, 1995; van der Hulst, 1996; Weisz et al., 2009), the overall evidence for a stellar feedback origin for all HI holes is not as compelling and a variety of alternate explanations have been proposed. For example, gamma ray bursts (GRBs) have sufficient energy to create holes in the HI without leaving a remnant stellar cluster (e.g., Loeb & Perna, 1998). Similarly, collisions between high velocity HI clouds and a galaxy (e.g., Tenorio-Tagle et al., 1986) or ram pressure stripping from the intergalactic medium (e.g., Bureau et al., 2004) could provide the means to create observed ISM features. Rhode et al. (1999) suggest that modified energetics, either by an overestimation in the energies necessary to evacuate HI holes or by a non-standard IMF, could explain the observed discrepancies, although they acknowledge the latter is not likely. An alternate possibility is that gravitational instabilities and/or turbulence naturally give rise to structure in the ISM (e.g., Elmegreen, 1997; Dib & Burkert, 2005). The study of Constellation III by Harris & Zaritsky (2004) has cast doubt upon a number of these alternate theories and favors structure creation by numerous SF events. While it is likely that many of these mechanisms play a role in shaping the ISM at some level, quantifying the impact of stellar feedback on the ISM can give key insights into the feedback processes and self-regulation of SF.

A further alternative is that the traditional theory linking stellar feedback to the creation of HI holes is not complete. Specifically, the most rigorous observational test of the stellar feedback model (Rhode et al., 1999) assumed that single age stellar clusters generated the SNe energy necessary to evacuate the HI holes. This is a reasonable assumption based on an extrapolation from the theoretical models of the explosion and expansion of a single SN in the ISM (e.g., Chevalier, 1974; Weaver et al., 1977). In this scenario, SNe from a single generation of stars (i.e., a cluster) explode, releasing energy into to an isotropic ISM, thus creating the observed hole and quenching future SF, by sweeping up and heating of the gas interior to the hole. However, the study of spatially resolved SFHs in nearby dwarf galaxies has provided evidence that SF within ~ 500 Myr can return to the same locations (Dohm-Palmer et al., 1997; Dohm-Palmer & Skillman, 2002a; Weisz et al., 2009), demonstrating the SF does not always suppress subsequent generations of SF. The creation of HI holes by multiple generations of SNe is a scenario that would likely have complicated dynamics, but preserves the intuitive simplicity linking the energy production of stars with the structures in the ISM.

In this paper, we use HST/ACS imaging of Ho II to detect and study the resolved stellar populations within the HI holes independently catalogued by Puche et al. (1992) and The HI Nearby Galaxy Survey (THINGS; Walter et al., 2008; Bagetakos et al., 2009). Nearby dIs, such as Ho II (roughly a solid body rotator in the inner 2 kpc; Puche et al., 1992), are excellent environments for both the study of resolved stars and ISM features. Because the HI disks of dIs are typically solid body rotators, and thus lack sheer and differential rotation, HI holes and potential progenitor stellar components travel in unison for time scales on order of $\sim 10^8$ yr (e.g., Skillman et al., 1988; Skillman, 1996). Further, the low metallicities of nearby dIs minimize internal extinction effects, which allow us to take a precise census of individual stars.

From the resolved stellar populations of Ho II, we construct color-magnitude diagrams (CMDs) and measure star formation histories (SFHs) corresponding to catalogued HI holes that fall into our ACS field of view. Using the SFHs we can compute the energy associated with stellar feedback and compare it to the energy required to evacuate an HI hole, allowing us to quantify the efficiency of stellar feedback and compare it to predictions from models. We further compare the stellar populations of the HI holes to those of select control fields, similar in size to the HI holes, which span a wide range in HI surface density and do not overlap with catalogued HI holes. The resolved stellar populations also permit us to directly test the conclusions of previous studies of Ho II by Puche et al. (1992) and Rhode et al. (1999), including comparisons to Hα, 24μm, and UV imaging of the same regions. Using the results of the stellar populations in the HI holes located within the ACS field of view, we use simulated CMDs to demonstrate the plausibility of HI hole creation due to stellar feedback in regions of low gas and stellar densities, such as the outer regions of galaxies. We then apply this method of analysis to the SMC and discuss how observations of apparently empty holes does not rule out the possibility of a stellar feedback origin.

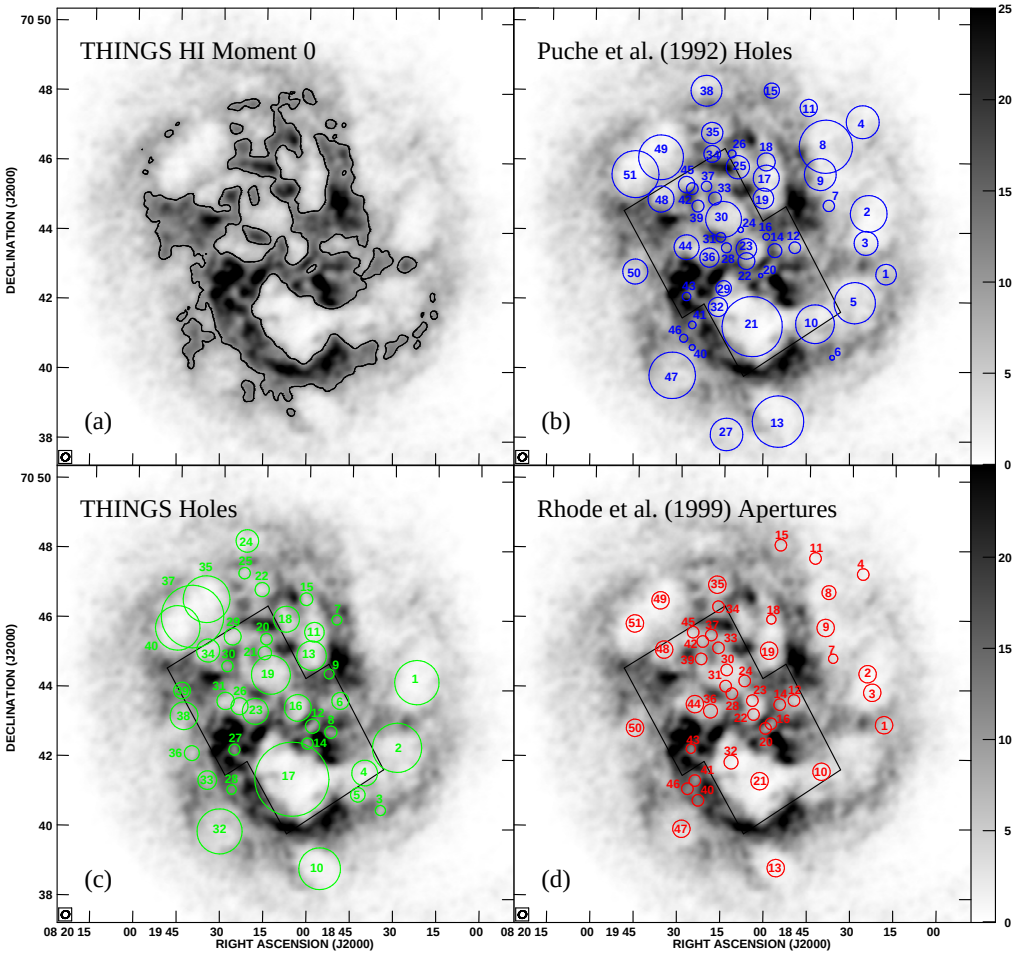

Figure 6.1 (a) HI surface density image of Ho II processed by the THINGS program (THINGS; Walter et al., 2008) with a contour of 10^{-21} cm^{-2} overlaid; (b) HI holes catalogued by Puche et al. (1992); (c) HI holes from the THINGS catalog (Bagetakos et al., 2009); (d) apertures used by Rhode et al. (1999) with the ACS footprint overlaid in black. Note the 'shredded' appearance of the HI distribution as well as the numerous separate holes cataloged in regions of low HI column density.

6.2 Observations and Photometry

As part of a larger HST program aimed at imaging multiple dIs in the M81 Group (GO-10605), we observed Ho II on 2006, December 30 using HST/ACS (Ford et al., 1998). To capture most of the optical galaxy, we used two ACS fields, observing each field for 4660 sec in F555W (V) and 4660 sec in F814W (I), with a CR-split in order to reduce the impact of cosmic rays, and a dithering strategy to cover the chip gap. The images were processed with the HST pipeline and we performed photometry and artificial star tests using DOLPHOT, a version of HSTphot (Dolphin, 2000) optimized for ACS observations[1] . Photometry was carried out as part of a larger program and the specific details, e.g., rejection criteria, completeness, can be found in Weisz et al. (2008). Following the photometric cuts, we merged the two fields into a single photometric list, appropriately removing duplicate stars, resulting in a total of 388,945 well measured stars for the combined fields. The deep photometry that is used in this paper has a limiting magnitude of $M_V \sim 0$, which allows us to see main sequence stars (MS) up to $\sim$ 300 Myr and Blue Helium Burning stars (BHeBs) up to $\sim$ 1 Gyr in age (Gallart et al., 2005; Weisz et al., 2008). To quantify the accuracy of the photometry we ran artificial star tests on the entire galaxy and found 50% completeness limits of $m_{F555W} = 27.8$ ($M_{F555W} = +0.15$) and $m_{F814W} = 27.3$ ($M_{F814W} = -0.15$), assuming a distance modulus of 27.65 (Karachentsev et al., 2002). A number of HI holes in nearby galaxies have inferred kinematic ages (from HI observations) as old as a $\sim 10^8$ yr (e.g., Puche et al., 1992; Walter & Brinks, 1999). If some of the older HI holes were created by SF on this time scale, only deep photometry of resolved stellar populations would probe faint enough limits to detect the remaining stars.

The HI image we used in our analysis (panel (a) of Figure 6.1) was observed with the VLA using the B, C, D configurations in 1990 and 1991 (the full details of the observations are available in Puche et al. 1992). As part of the THINGS program (Walter et al., 2008), the observations were reprocessed with their software pipeline, achieving a final spatial resolution of $\sim$ 6" and a velocity resolution of 2.6 km s^{-1}. Both P92 and the THINGS team independently constructed catalogs of HI holes in Ho II by examining

[1] Photometry and artificial star tests for the HST/ACS imaging of Ho II is available via the ACS Nearby Galaxy Survey Treasury program (ANGST; Dalcanton et al., 2009): http://www.nearbygalaxies.org

them in the position-velocity (PV) cuts and radius-velocity space in the HI data cube. Hole identification was done by eye using the following criteria as a guide: presence of the hole with a stationary center in multiple channel maps, sufficient contrast between the hole and its immediate surroundings, and the shape of the hole in radius-velocity space must be described by an ellipse (Puche et al., 1992; Bagetakos et al., 2009). Both catalogs contain the locations, diameters, expansion velocities of each of the holes (see Tables 6.1 − 6.4 and Figure 6.1). Additionally, the THINGS catalog classifies each hole such that a type 1 hole has completely blown out of the disk of the galaxy, i.e, a break in the PV diagram, a type 2 hole only shows an approaching or receding side, and a type 3 hole has both sides present in PV space. While the P92 and THINGS holes catalogs are generally similar, the sizes, locations, and measured expansion velocities are not identical. For example, the THINGS catalog assigns an expansion velocity of 7 km $s^{-1}$to any blown out hole, while P92 lists expansion velocities for each hole, and does not indicate a blow out. Because of the high stellar density, slight differences in the hole locations and size can lead to different stellar populations. We explore this further in §6.4.3.

With a distance of 3.40 Mpc, measured from the TRGB (Karachentsev et al., 2002), the high spatial resolution of HST/ACS (1 pixel = 0.05"; 1" ∼ 16.5 pc) allows us to probe scales much smaller than the minimum detectable HI hole size (∼ 100 pc). Treating each hole as circular and using the central coordinates and diameters from each hole catalog, we overlaid these apertures over the HST/ACS drizzled image and found that 23 of the 51 holes from P92 and 19 of the 39 THINGS holes were within ACS coverage (Figure 6.2). In the P92 catalog, a portion of holes 10, 21, 25, 34, and 48 are outside our ACS field of view. We included those that primarily overlapped with the ACS data (10, 21, and 48), but excluded the others from the sample (25 and 34). From the THINGS catalog, we excluded holes 18 and 38 for the same reason. For consistency we used the HI hole numbering systems presented in the P92 and THINGS catalogs. Additionally, we selected nine control fields, regions in comparable size to the HI holes that do not overlap cataloged HI holes and span a range in HI column densities, and number them c1 − c9 (Figures 6.1 and 6.2).

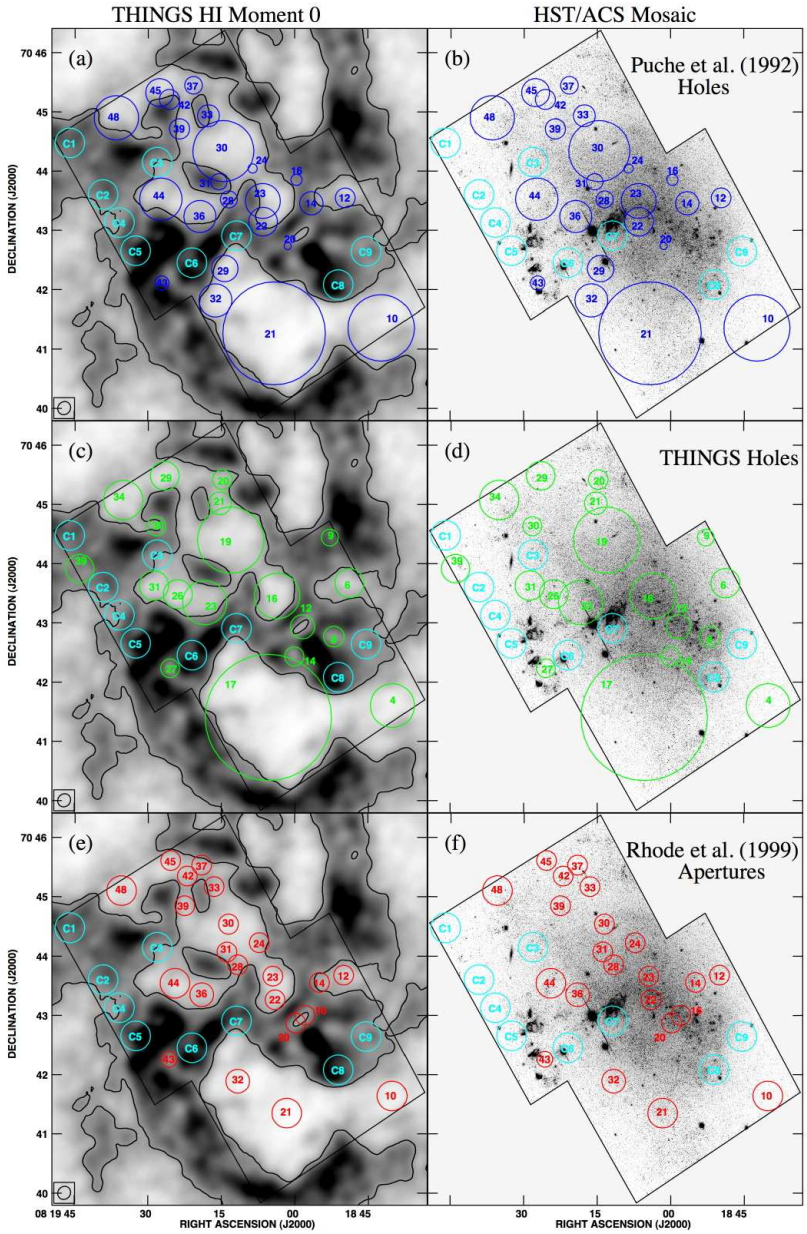

Figure 6.2 (a) THINGS processed HI image of Ho II (Walter et al., 2008) with a contour of 10^{-21} cm^{-2} overlaid and (b) ACS drizzled image of Ho II with Puche et al. (1992) holes in blue and control fields in cyan; (c) and (d) THING holes catalog (Bagetakos et al., 2009) in green and control fields in cyan; (e) and (f) Rhode et al. (1999) apertures in red and control fields in cyan.

Table 6.1: Photometric Properties of Puche et al. (1992) HI Holes

Hole Number (1)	α (B1950.0) (2)	δ (B1950.0) (3)	Diameter (arcsec) (4)	Stars in CMD (5)	Integrated m_{F555W} (6)
10	8 13 27.7	+70 50 59	72.96	4149	17.68
12	8 13 37.3	+70 53 02	22.15	2065	18.65
14	8 13 42.3	+70 52 55	26.67	3907	17.47
16	8 13 45.4	+70 52 22	12.59	948	19.00
20	8 13 47.3	+70 52 14	7.95	383	20.19
21	8 13 49.4	+70 50 43	115.3	39153	14.72
22	8 13 51.5	+70 52 38	32.19	6443	16.65
23	8 13 51.9	+70 53 02	39.26	9477	16.22
24	8 13 54.6	+70 53 36	10.24	579	19.37
28	8 13 59.1	+70 53 14	19.12	1934	17.93
29	8 14 02.0	+70 51 44	26.74	4517	17.58
30	8 14 00.9	+70 53 55	68.62	20614	15.77
31	8 14 01.3	+70 53 27	18.32	1625	18.37
32	8 13 59.4	+70 51 16	36.90	3782	17.83
33	8 14 03.8	+70 54 33	24.58	2140	18.34
36	8 14 06.6	+70 52 44	36.70	5945	16.98
37	8 14 06.3	+70 54 55	19.80	1011	19.12
39	8 14 09.9	+70 54 14	22.76	1971	18.24
42	8 14 09.3	+70 54 44	22.49	1383	18.75
43	8 14 13.5	+70 51 39	16.16	549	18.75
44	8 14 12.1	+70 52 56	47.67	7566	16.82
45	8 14 12.7	+70 54 60	31.45	2344	18.08
48	8 14 22.9	+70 54 30	49.83	4695	16.93

Table 6.2: Photometric Properties of the THINGS HI Holes

Hole Number (1)	α (J2000) (2)	δ (J2000) (3)	Hole Diameter (arcsec) (4)	No. of Stars in CMD (5)	Integrated m_{F555W} (6)
4	8 18 40.1	+70 41 36.3	44	1733	18.81
6	8 18 48.8	+70 43 40.3	29	3781	17.98
8	8 18 52.0	+70 42 46.2	21	2636	17.26
9	8 18 52.8	+70 44 26.6	17	1067	19.35
12	8 18 58.4	+70 42 56.3	24	4067	16.75
14	8 19 00.1	+70 42 26.2	19	2289	18.13
16	8 19 03.6	+70 43 27.5	46	16146	15.67
17	8 19 05.4	+70 41 24.4	128	61244	14.37
19	8 19 13.1	+70 44 24.0	67	25053	15.66
20	8 19 14.8	+70 45 25.4	20	1644	18.44
21	8 19 15.3	+70 45 01.4	23	2312	18.40
23	8 19 18.4	+70 43 20.7	45	11644	16.24
26	8 19 23.9	+70 43 29.3	29	4253	17.54
27	8 19 25.5	+70 42 14.2	19	1126	18.89
29	8 19 26.6	+70 45 29.2	29	2202	18.28
30	8 19 28.3	+70 44 38.1	19	1590	18.62
31	8 19 28.8	+70 43 38.0	30	3190	18.05
34	8 19 35.1	+70 45 04.6	40	3673	17.33
39	8 19 44.0	+70 43 55.0	29	640	19.31

Table 6.3 Derived Properties of Puche et al. (1992) HI Holes

Hole Number (1)	Diameter (pc) (2)	DV km s^{-1} (3)	Kinematic Age Myr (4)	E_{Hole} (P92) (10^{50} erg) (5)	E_{Hole} (new) (10^{50} erg) (6)	E_{SFKA} (10^{50} erg) (7)	Putative Efficiency$_{KA}$ (8)
10	1171	8.8	65	500	364	2400	15%
12	349	7.7	22	18.0	16	130	12%
14	421	3.9	53	15.0	19	2700	0.7%
16	199	1.0	97	0.30	0.5	1000	<0.1%
20	125	6.5?	9.4	0.4	2.0	10	20%
21	1820	6.6	135	2800	7700	60000	13%
22	508	6.5	38	48.0	230	1600	15%
23	619	4.5	67	60	211	3300	6.4%
24	162	7.5?	11	1.66	5.0	20	27%
28	302	7.2?	21	11.0	83	220	37%
29	469	3.9	59	21.4	190	1300	15%
30	1083	8.1	65	737	2200	5700	39%
31	289	2.5?	56	2.20	13	900	1.4%
32	583	4.8	59	48.4	420	2600	16%
33	388	3.5	54	10.2	17	780	2.2%
36	579	8.3	34	119	990	1800	55%
37	312	11.9	13	28.8	34	45	74%
39	359	3.5	50	8.00	16	1500	1.1%
42	355	10.1	17	34.0	39	75	52%
43	255	4.8	26	3.73	25	90	28%
44	752	7.9	47	217	1200	7300	17%
45	596	6.6	37	53.5	51	930	6%
48	786	14.1	27	649	560	450	120%

Table 6.4 Derived Properties of the THINGS HI Holes

Hole Number (1)	Diameter (pc) (2)	DV km s^{-1} (3)	Kinematic Age Myr (4)	E_{Hole} (THINGS) (10^{50} erg) (5)	E_{Hole} (new) (10^{50} erg) (6)	E_{SFKA} (10^{50} erg) (7)	Putative Efficiency$_{KA}$ (8)	(Type) (9)
4	731	7	51	100	170	500	34%	1
6	486	7	34	50	180	600	31%	1
8	345	10	17	32	140	500	28%	3
9	279	10	14	13	54	15	360%	3
12	403	11	18	63	450	330	140%	3
14	318	15	10	40	310	20	1600%	2
16	761	7	53	200	2100	4600	45%	1
17	2110	7	147	3200	18000	100000	18%	1
19	1107	7	77	500	3200	9500	34%	1
20	329	12	13	25	56	100	56%	3
21	378	9	21	20	88	300	29%	3
23	738	16	23	630	2900	2400	120%	2
26	483	7	34	50	133	2200	6%	1
27	312	7	22	20	25	190	13%	1
29	479	7	33	32	43	900	5%	1
30	318	13	12	32	40	150	26%	2
31	491	7	34	50	83	1000	8%	1
34	657	7	46	80	79	730	11%	1
39	474	18	13	160	66	50	130%	2

6.3 Stellar Components of HI holes in Ho II

6.3.1 Luminous Main Sequence Stars Within the HI Holes

From our photometry we constructed CMDs of the stars in each of the 23 holes in the P92 catalog, 19 holes in the THINGS catalog, and nine control fields (Figures 6.3 − 6.5 and Tables 6.1, 6.2, & 6.5). Notably, we found that all holes in both catalogs contain a significant number of young stars; enough to easily identify CMD features by visual inspection and compare with the models of Marigo et al. (2008) (see Figure 6.6). However, these CMDs are not consistent with the expected CMD for a single age stellar cluster. The holes also have red giant (RGB) and asymptotic giant branch (AGB) stars with ages < 1 Gyr, as expected given that the older stars are fairly smoothly distributed throughout the optical galaxy (see Figure 11 in Weisz et al. 2008).

Young stellar clusters (e.g., OB associations) are traditionally associated with the formation of HI holes (e.g., Brinks & Bajaja, 1986; Hatzidimitriou et al., 2005), and we tested this notion by making a census of the youngest and brightest stars. We identified young stars based on the stellar evolution models of Marigo et al. (2008), which suggest that the brightest 10 Myr old MS star at its turnoff has $M_{F555W} \sim -5$, or $m_{F555W} \sim 22.65$ in Ho II. We found 302 MS stars with $m_{F555W} < 22.65$ that also lay within holes in the P92 catalog. Further, restricting the color to be less than 0.05, i.e., $m_{F555W} - m_{F814W} < 0.05$, (to exclude Red Helium Burning stars (RHeBs), bright foreground stars, and most BHeBs) we find 109 stars that match our criteria. Of these 109 stars, 21 of them belong to hole 21, which is the largest and most populated hole with a diameter of ~ 2 kpc and $\sim 40{,}000$ stars in the CMD. Applying the above criteria for luminous MS stars to the remaining 21 holes, we found that all the holes have fewer than 10 bright MS stars and 20 holes have fewer than two bright MS stars. Similarly for the HI holes in the THINGS catalog, we found 347 stars with $m_{F555W} < 22.65$, and 104 stars with $m_{F555W} < 22.65$ and $m_{F555W} - m_{F814W} < 0.05$. Of these 104 stars, 30 belong to the largest hole (number 17). The other 18 holes all have fewer than 10 young MS stars, and 13 have fewer than two young MS stars. For the stars located in the control fields (Figure 6.5), we found that 32 match the bright MS star criteria, with c7 containing 21 of these stars, and six of the nine control fields containing two or less bright MS stars. The control field have more bright MS stars by a factor of ~ 1.5 when

compared to the HI holes. We explore the impact of small number statistics, stochastic effects on the SFR, and production of massive stars in §6.5.

From these basic calculations, it seems that the location of young OB type stars are not a reliable tracer of the locations of HI holes, nor do they accurately represent the presence of young remnant stellar populations inside HI holes. We will discuss the spatial distribution of these stars further in §**??**.

Table 6.5: Photometric Properties of the Control Fields

Hole Number (1)	α (J2000) (2)	δ (J2000) (3)	Hole Diameter (arcsec) (4)	No. of Stars in CMD (5)	Integrated m_{F555W} (6)
c1	8 14 33.7	+70 50 50	30	839	19.38
c2	8 14 26.9	+70 52 59	30	1309	19.20
c3	8 14 15.7	+70 52 33	30	4089	17.64
c4	8 14 23.6	+70 52 30	30	1549	18.78
c5	8 14 20.3	+70 52 02	30	1863	18.08
c6	8 14 08.8	+70 15 49	30	3598	17.96
c7	8 14 02.9	+70 52 57	30	5183	17.40
c8	8 13 30.3	+70 52 07	30	1988	18.72
c9	8 13 39.7	+70 52 31	30	2147	17.74

6.3.2 The SFHs of Stars Within the HI Holes

Upper MS stars and BHeBs offer the opportunity to age date stellar populations more than 10 Myr old. To extract a more complete picture of the recent SF within the HI holes, we measured the SFHs for the stars inside each HI hole and compared the timing of SF activity to the inferred kinematic ages, i.e., the radius of the hole divided by its expansion velocity. We derived the SFHs, from the CMDs, using SFH recovery code of Dolphin (2002). This method constructs synthetic CMDs, using the stellar evolution models of Marigo et al. (2008), and compares them to the observed

CMD using a maximum likelihood technique. To obtain this solution, we used a combination of fixed (e.g, binary fraction, IMF) and searchable (e.g., distance, extinction) parameters. We allowed the program to search for the best fit metallicity per time bin, with the condition that the metallicity must monotonically increase with time toward the present. We found the mean metallicity in the most recent time bins from the SFHs to be consistent with the observed value of $\sim$ 10% $Z_{\odot}$ (Miller & Hodge, 1996), which is best fit by Z=0.002 isochrones (Figure 6.6). Throughout this paper, we use the following values when measuring SFHs or simulating CMDs: a standard power law IMF with x = -2.3 from 0.1 to 100 $M_{\odot}$, a binary fraction = 0.35, the stellar evolution models of Marigo et al. (2008), a distance of 3.40 Mpc, a foreground extinction of A_{F555W} = 0.11 (Schlegel et al., 1998), and 50% completeness limits of m_{F555W} = 27.9 and m_{F814W} = 27.4 (Weisz et al., 2008). To quantify the errors in the SFHs, we added the systematic uncertainties from the isochrones and the statistical uncertainties from Monte Carlo tests in quadrature. Quantifying the best fit solution and associated uncertainties from synthetic CMD matching has been subject to a number of extensive studies (e.g., Tosi et al., 1989; Tolstoy & Saha, 1996; Gallart et al., 1996; Mighell, 1997; Holtzman et al., 1999; Hernandez et al., 1999; Dolphin, 2002; Ikuta & Arimoto, 2002; Yuk & Lee, 2007), which explore the nuances of this method beyond the scope of this paper. Full details on the method we used in this paper to measure the SFHs and quantify the associated errors can be found in Dolphin (2002).

As an example we present the observed, model, residual, and significance of the residual CMDs from the code of Dolphin (2002) for hole 23 in the THINGS catalog (Figure 6.7). Visual inspection of the observed and model CMD show broad agreement of features such as the young MS, BHeBs, RHeBs, and the RGB. The difference between the model and the observed CMD can been seen in the lower two panels, where black points indicate more real stars than synthetic stars, and white points indicating more synthetic than real stars. The residual significance diagram (panel (d)), reveals no distinct patterns of black or white points, indicating that the model CMD describes the data quite well.

We chose to focus on SF over the past 200 Myr in each of the holes (Figures 6.8 $-$ 6.10) and control fields (Figure 6.11) based on the inferred kinematic ages of the holes derived from both hole catalogs. The time resolution of our SFHs is $\sim$ 10 Myr up to a

look back time of 50 Myr and then $\sim$ 25 Myr from 50 $-$ 200 Myr. These choices provide an adequate look back time and time resolution to see potential SF events responsible for the creation of the HI holes. Note that kinematic ages for HI holes are traditionally considered an upper limit to the age of the HI holes, as the expansion velocities were most likely higher in the past (e.g., Tenorio-Tagle & Bodenheimer, 1988). We discuss the accuracy of inferred kinematic ages in more detail in §6.5.

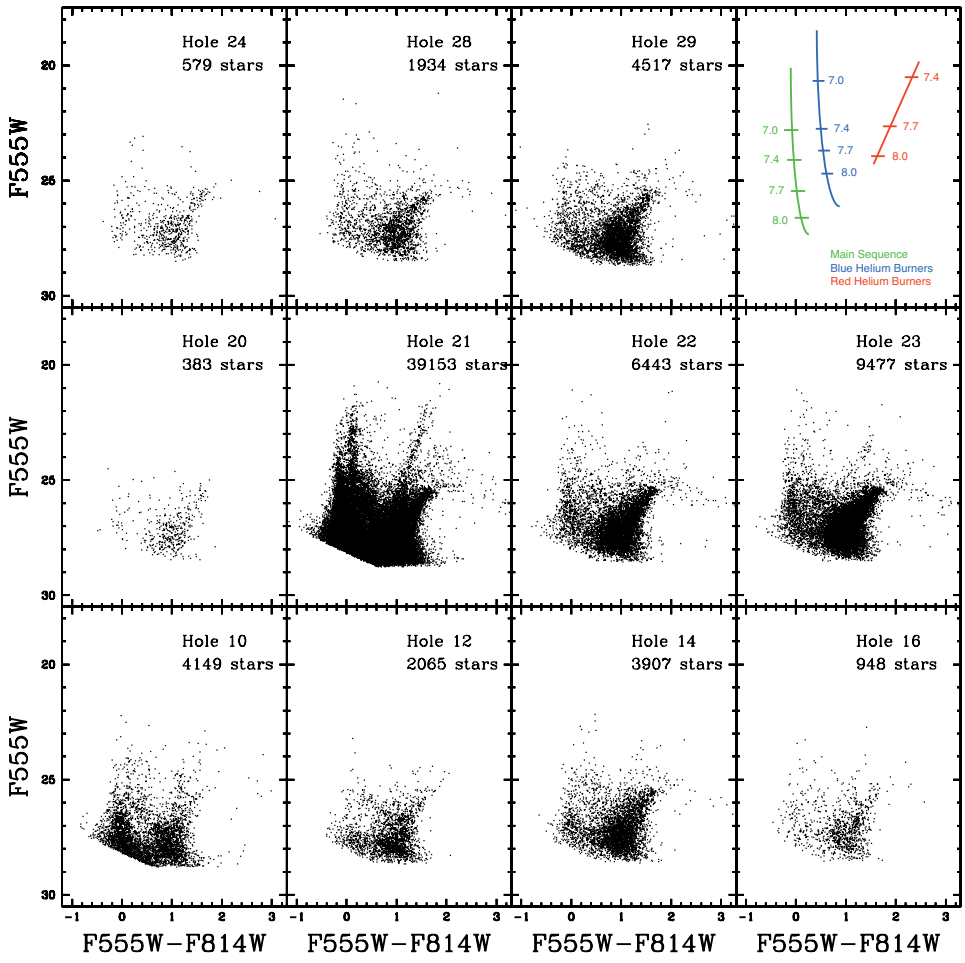

Figure 6.3 HST/ACS CMDs of the stars inside the HI holes cataloged by Puche et al. (1992), corrected for foreground reddening, $A_V = 0.11$ (Schlegel et al., 1998). The schematic in the upper right hand corner shows the ages of each type of star, MS (green), BHeB (green), and RHeB (red), with the logarithm of the ages (turn off age for the MS) shown as a function of magnitude and color on the CMD. Although sparse in some fields, note the presence of young MS and BHeB stars in all the CMDs. The fact the the BHeBs span a range in magnitudes indicate that multiple episodes of recent SF must have taken place, as different age BHeBs do not overlap on the CMD. In contrast, BHeBs from a single age cluster would have an over-density at only one magnitude.

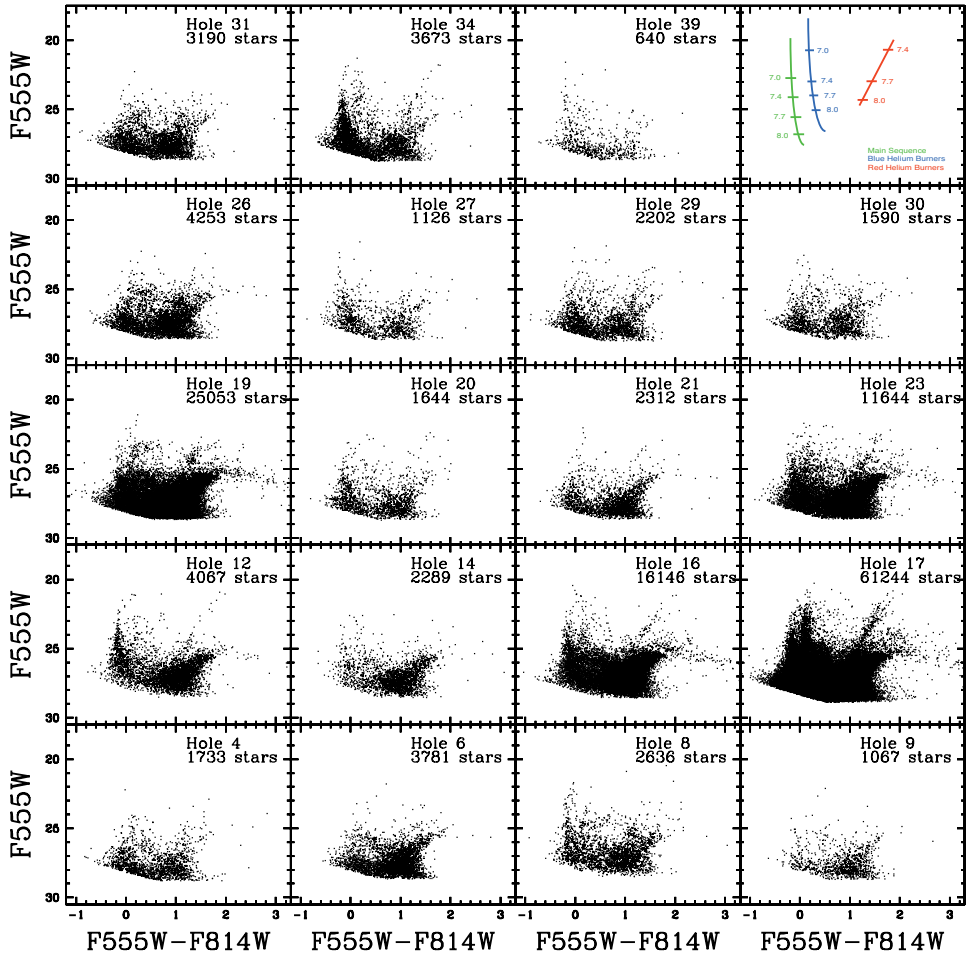

Figure 6.4 HST/ACS CMDs of the stars inside the HI holes cataloged by Bagetakos et al. (2009), corrected for foreground reddening, $A_V = 0.11$ (Schlegel et al., 1998). The schematic in the upper right hand corner shows the ages of each type of star, MS (green), BHeB (green), and RHeB (red), with the logarithm of the ages (turn off age for the MS) shown as a function of magnitude and color on the CMD. Although sparse in some fields, note the presence of young MS and BHeB stars in all the CMDs. The fact the the BHeBs span a range in magnitudes indicate that multiple episodes of recent SF must have taken place, as different age BHeBs do not overlap on the CMD. In contrast, BHeBs from a single age cluster would have an overdensity at only one magnitude.

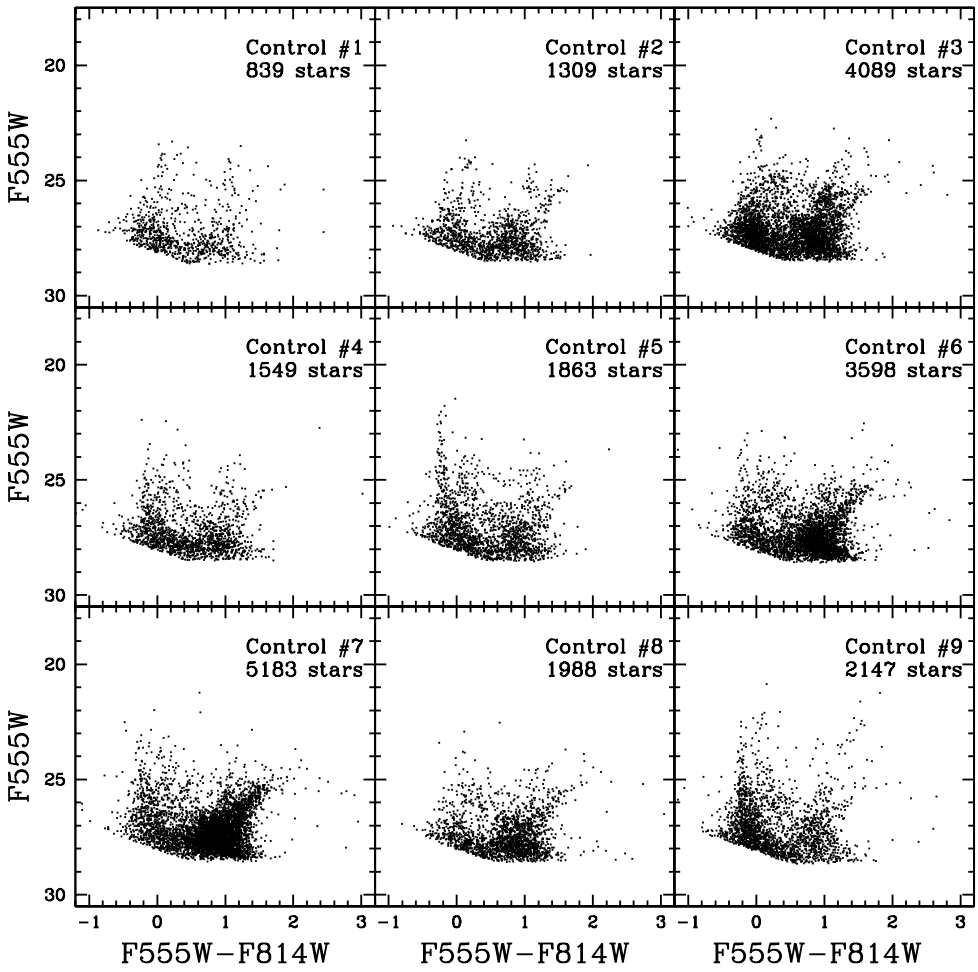

Figure 6.5 HST/ACS CMDs of the nine control fields in Ho II (Table 6.3 and Figure 6.2), corrected for foreground reddening, $A_V = 0.11$ (Schlegel et al., 1998). Although sparse in some fields, note the presence of young MS and BHeB stars in all the CMDs. The fact the the BHeBs span a range in magnitudes indicate that multiple episodes of recent SF must have taken place, as different age BHeBs do not overlap on the CMD. In contrast, BHeBs from a single age cluster would have an overdensity at only one magnitude. Comparing the CMDs of the control fields to those associated with the HI holes (Figure 6.3 − 6.4), there is not a clear difference in the composition of the two stellar populations despite having vastly different HI column densities.

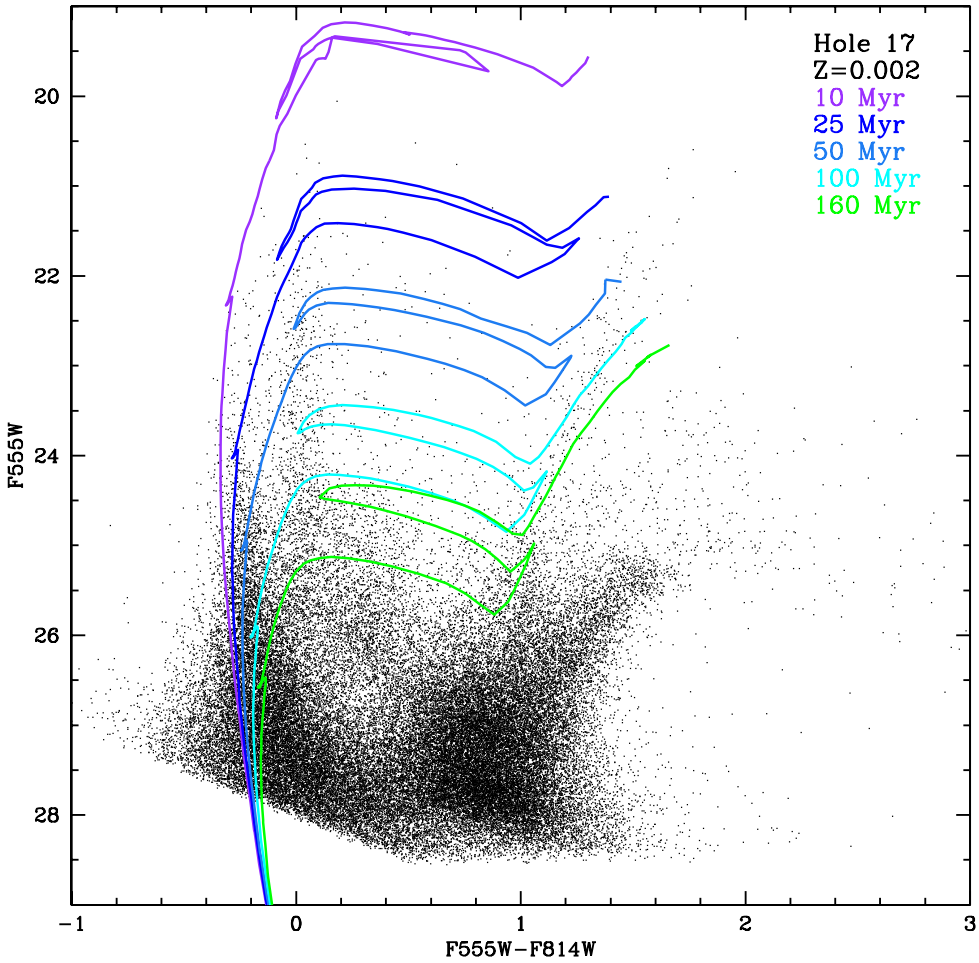

Figure 6.6 HST/ACS CMD of THINGS hole 17 with the Z=0.002 isochrones from Marigo et al. (2008) overlaid. The observed CMD has been corrected for foreground reddening. Notice that although the observed MS and isochrones show excellent agreement, the BHeB models become increasingly redder with age, when compared with the data. This is not an effect of metallicity, as we matched the isochrones to the measured nebular abundance (Miller & Hodge, 1996). Instead, this is an example of the color mismatch for BHeB models at metallicites greater than $\sim$ 10% $Z_{\odot}$.

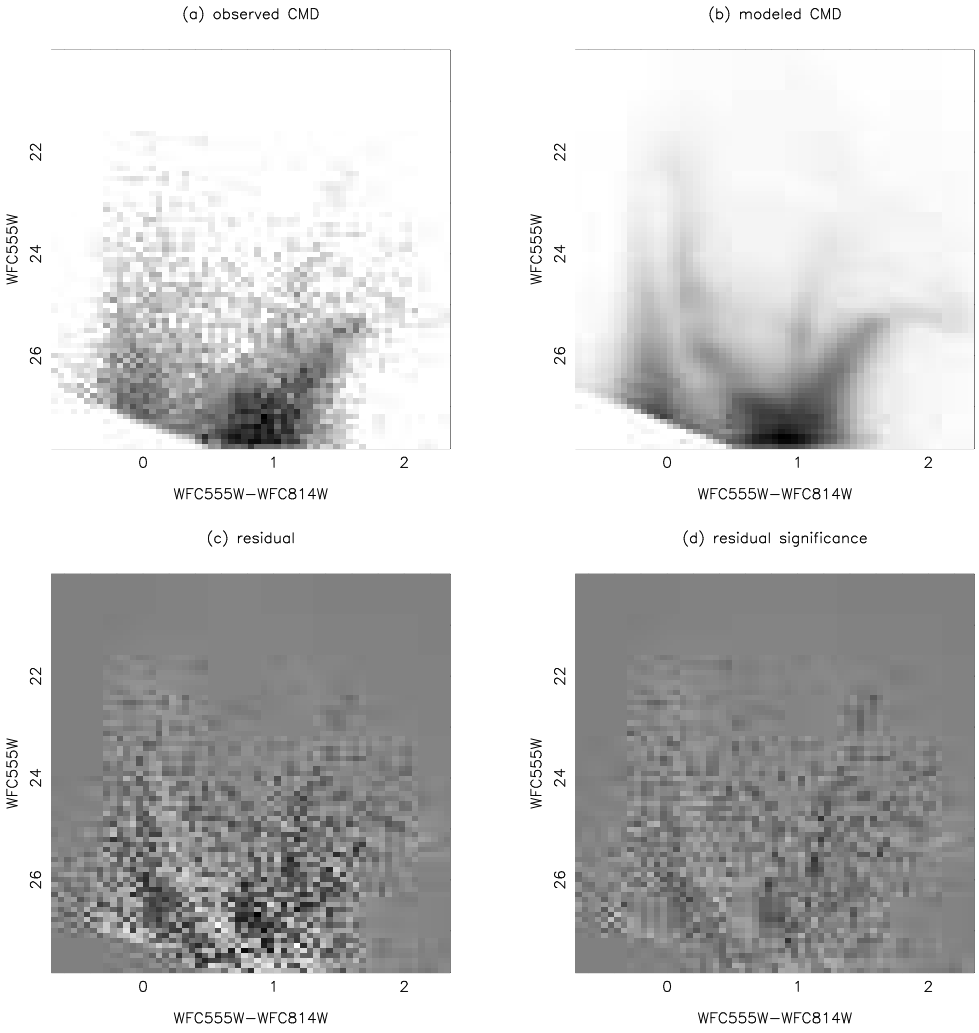

Figure 6.7 Comparison of the observed (panel (a)) and model CMDs (panel (b)) for THINGS hole 23 as measured using the code of Dolphin (2002). The bottom panels show the residual CMD (panel (c)) and the significance of the residuals (panel (d)). In the bottom panels black points indicate many more observed stars than synthetic star, while white points have more synthetic than observed stars. From the residual significance diagram we do not see any particularly poorly matched areas, indicating the synthetic CMD matches the data quite well.

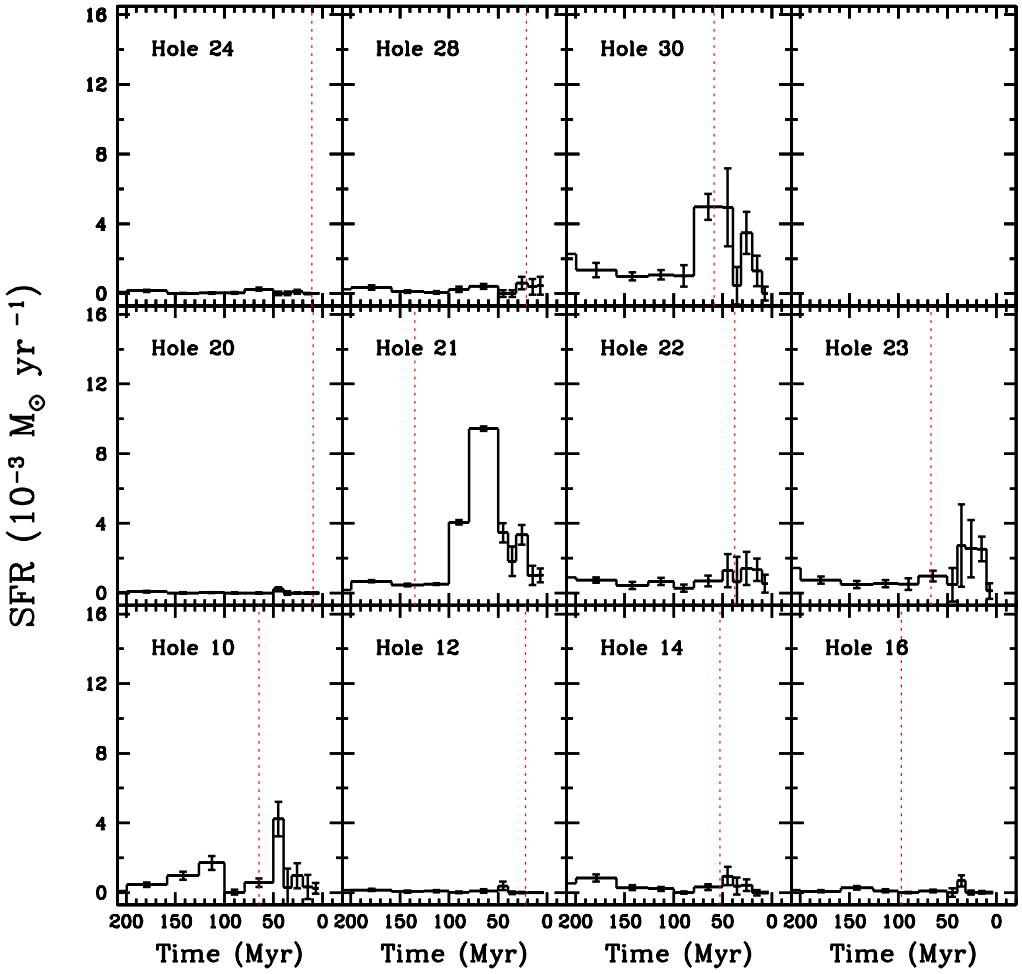

Figure 6.8 The recent SFHs of the stars inside the HI holes cataloged by Puche et al. (1992) over the last 200 Myr. The time resolution is $\sim$ 10 Myr until 50 Myr ago, and then $\sim$ 25 Myr there after. The red dotted line indicates the inferred kinematic age of each hole (Table 6.3). Note that the SFH of hole 21 has been scaled down by a factor of 10. In most cases, the majority of SF has taken place more recently than the inferred kinematic age, however, this is not always the case.

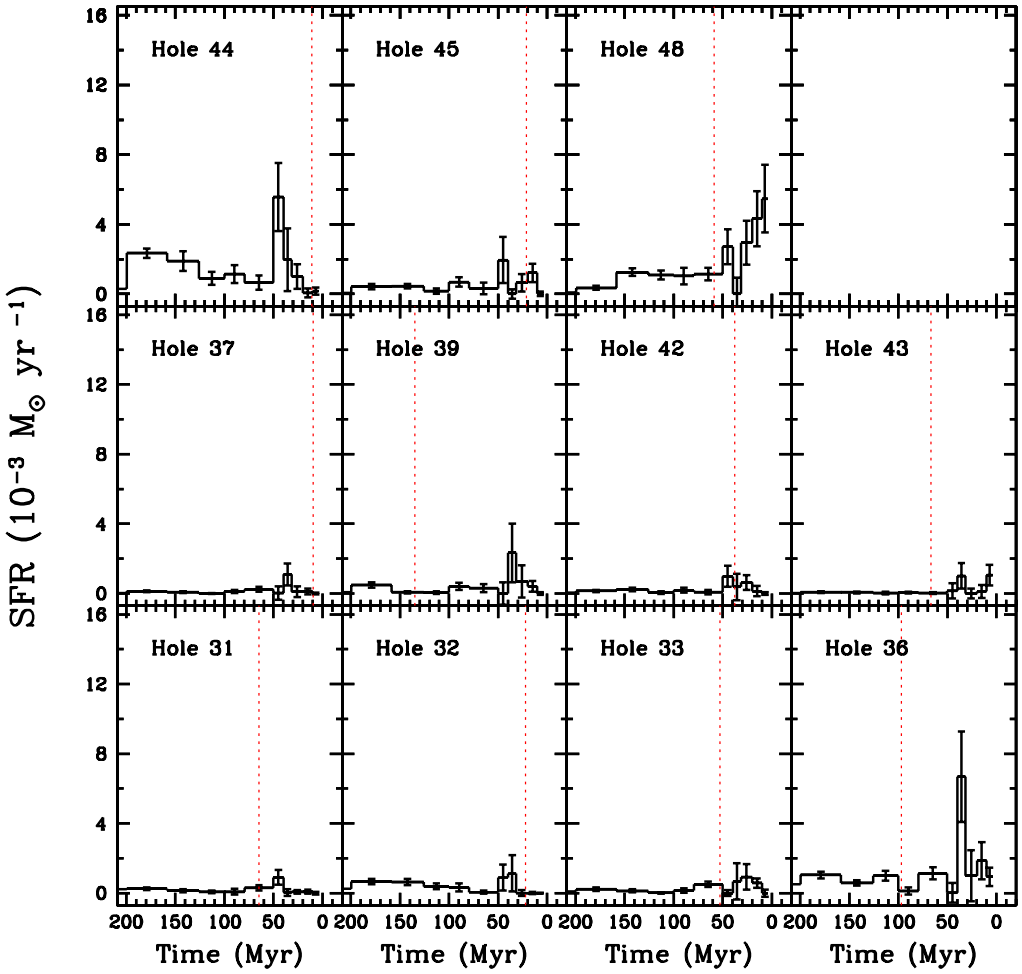

Figure 6.9 The recent SFHs of the stars inside the HI holes cataloged by Puche et al. (1992) over the last 200 Myr. The time resolution is $\sim$ 10 Myr until 50 Myr ago, and then $\sim$ 25 Myr there after. The red dotted line indicates the inferred kinematic age of each hole (Table 6.3). In most cases, the majority of SF has taken place more recently than the inferred kinematic age, however, this is not always the case.

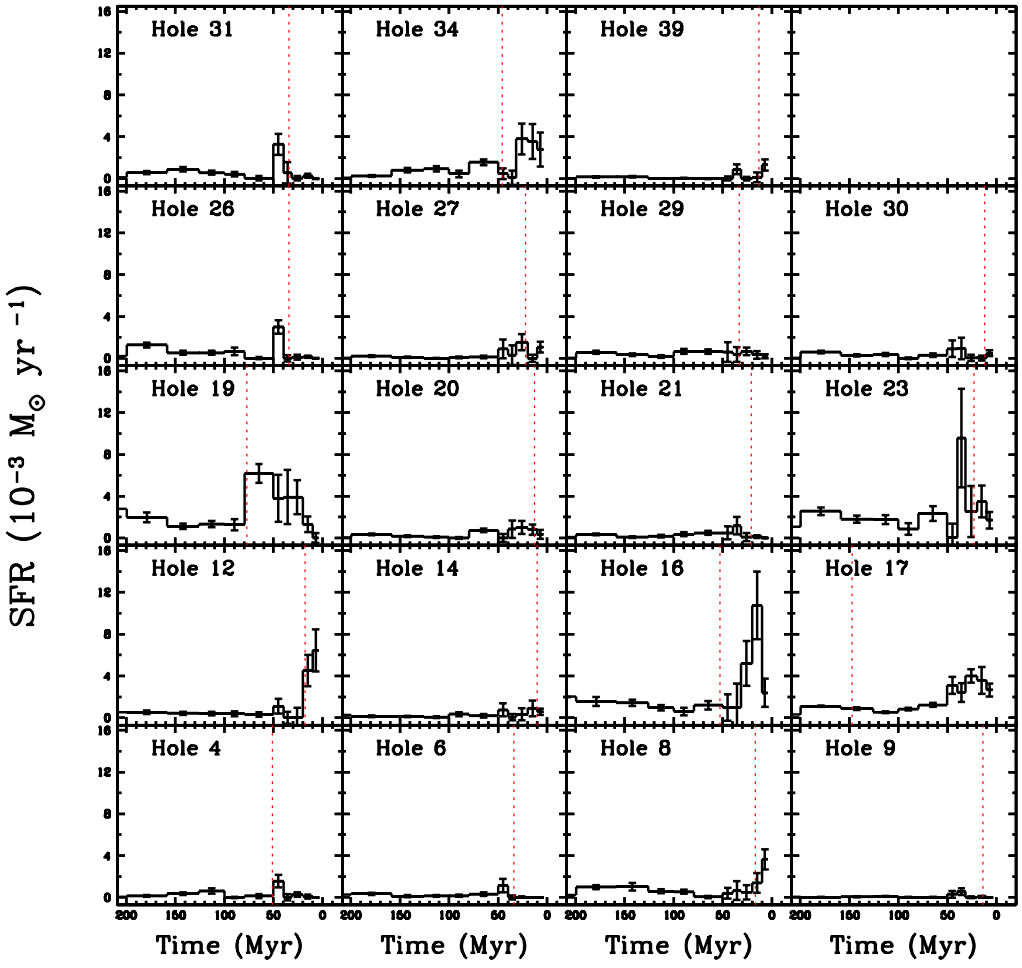

Figure 6.10 The recent SFHs of the stars inside the HI holes cataloged by Bagetakos et al. (2009) over the last 200 Myr. The time resolution is $\sim$ 10 Myr until 50 Myr ago, and then $\sim$ 25 Myr there after. The red dotted line indicates the kinematic age of each hole (Table 6.4). Note that the SFH of hole 17 has been scaled down by a factor of 10. In most cases, the majority of SF has taken place more recently than the inferred kinematic age, however, this is not always the case.

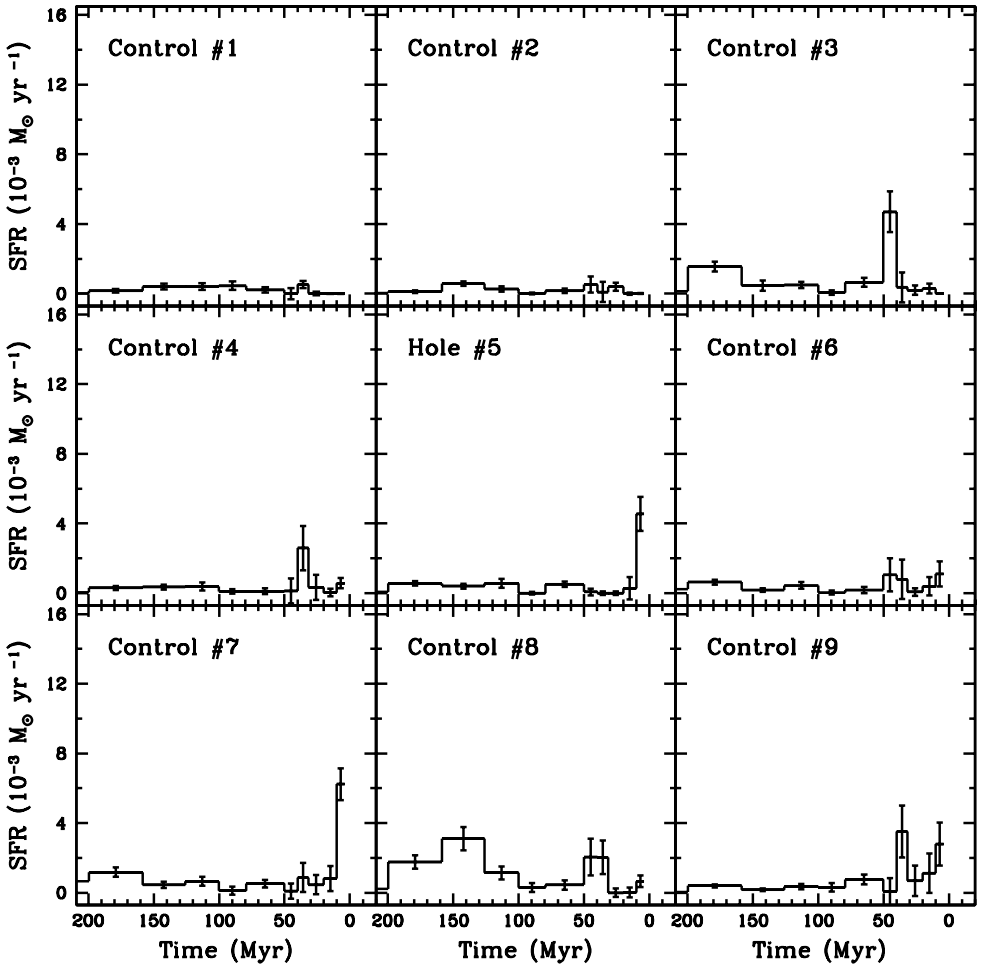

Figure 6.11 The recent SFHs of each control field in Ho II over the last 200 Myr. The time resolution is ∼10 Myr ber bin until 50 Myr and ∼ 25 Myr there after.

As a check for accuracy of SFHs between the two hole catalogs, we compared the SFHs and CMDs from overlapping holes. The CMD of P92 hole 44 significantly overlaps with THINGS holes 26 and 31. The CMD of P92 hole 44 has 7566 stars, where as the two THINGS holes have 4253 and 3190, respectively. In terms of the SFHs, the peak SFR for P92 hole 44 occurs in the $40 - 50$ Myr bin with a peak values of 5.6×10^{-3} $M_{\odot}$ yr^{-1}. Both the THINGS holes how peak SFRs in the same time bin, with values of 3.0×10^{-3} $M_{\odot}$ yr^{-1} and 3.2×10^{-3} $M_{\odot}$ yr^{-1}, or co-adding them, we find a peak SFR of $\sim 6.2\times10^{-3}$ $M_{\odot}$ yr^{-1}, consistent with the values for the single P92 hole. Similar tests were carried out for several other overlapping holes, and all were found to have consistent SFRs where expected. It is important to note that because the stellar density is not uniform in Ho II, even small differences in the location or radius of a hole, may result in significant differences in the stellar populations and SFHs.

We searched for differences between the stellar populations of the control fields and the HI holes by comparing their cumulative SFHs (i.e., fraction of stars formed as a function of time) over the past 14.1 Gyr (lifetime) and 200 Myr (recent) by performing a KS test comparing the average cumulative SFHs for the holes and control fields (red lines in Figure 6.12). As expected, the majority of the holes and control fields share a common old stellar population, i.e., at least 50% of the stars were formed greater than 6 Gyrs ago), and the fraction of stars formed in the last 6 Gyrs is also consistent between the hole and control field samples. Although the past 200 Myr is likely more influential when it comes to hole formation, again we see no discernible difference between the recent cumulative SFHs of the two samples. The KS test confirmed these impressions, indicating that, on both the lifetime and recent time scales, the stellar populations of the holes and control fields have the same parent distribution. From the perspective of the traditional stellar feedback hypothesis, this is an unanticipated result, as the theory would expect young stars associated with remnant clusters to be predominantly located inside the HI holes, and not control fields. This is discussed in more detail in §6.5.

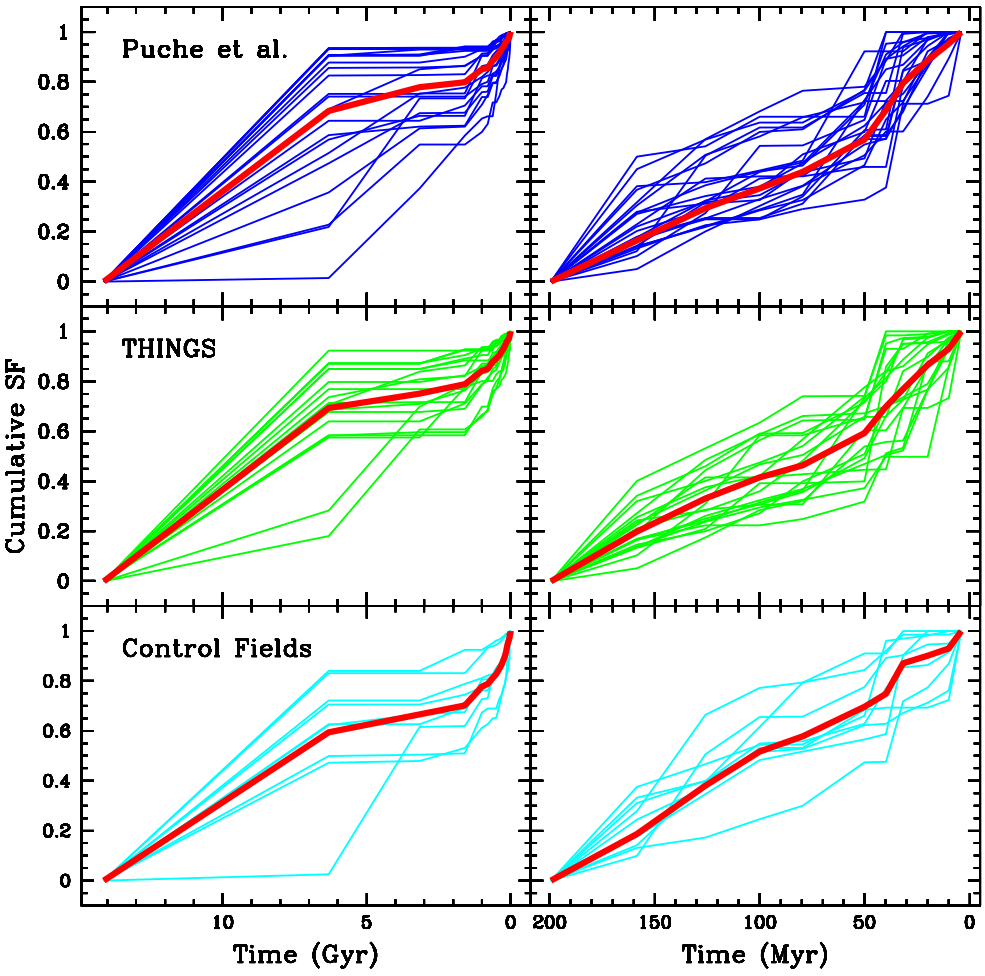

Figure 6.12 Comparison of the cumulative SF of stars within the holes from the Ho II for the Puche et al. (1992) catalog (blue) and the THINGS catalog (Bagetakos et al., 2009) (green) with the control fields cyan. The left panels show the cumulative SF over the the past 14.1 Gyr, while the panels on the right show the cumulative SF over the past 200 Myr. Although any given cumulative SFH is unique, a comparison of the HI holes and control fields suggest that the SFHs of the stars inside HI holes and the control fields are indistinguishable. For reference, the globally averaged SFR for the galaxy is 3.6×10^{-2} $M_\odot$ yr^{-1}, and the full SFH of the entire galaxy was measured by Weisz et al. (2008).

6.4 Comparing the Energy from SF to the Energy Needed to Create an HI Hole

Quantifying the energy generated from SF and the energy necessary to create an HI hole is of particular importance in understanding the role stellar feedback plays in creating HI holes. Fortunately, the interaction of a single SN and the surrounding ISM has been modeled in great detail (e.g., Chevalier, 1974; Weaver et al., 1977; Heiles, 1979). In addition, energy associated with SF is computed by the galaxy evolution modeling code STARBURST99 (Leitherer et al., 1999). STARBURST99 takes a SFH as input and uses stellar evolution models to produce predictions for spectrophotometric, chemical, and stellar energy output properties of galaxies that have had episodes of SF within the last 1 Gyr. For the particular case of stellar feedback, STARBURST99 can compute the energy profiles (i.e., energy produced by stellar winds and SNe) using the SFHs for individual holes, which allows us to directly connect stellar feedback to the creation and evolution HI holes. In this section, we apply each of these methods to the HI holes in Ho II and their stellar populations, and compare them to expected stellar feedback efficiencies from a variety of hydrodynamical simulations.

6.4.1 Energy Required to Evacuate an HI Hole

??

The minimum amount of energy required to evacuate an HI hole is given by the single blast model of Chevalier (1974):

$$E_{Hole} = 5.3 \times 10^{43}\ n_0^{1.12}\ (\frac{d}{2})^{3.12}\ v^{1.4} \tag{6.1}$$

where E_{Hole} is in the units of 10^{50} ergs, n_0 is the HI volume density (cm^{-3}) at the mid-plane of the galaxy, d is the diameter of the HI hole in pc, and v is the expansion velocity in km s^{-1}. While the expansion velocity and diameter of the hole are independently measured quantities, n_0 is dependent upon the HI column density, N_{HI}, and scale height of the gas, h, in the following way:

$$n_0 = \frac{N_{HI}}{\sqrt{2\pi}h} \tag{6.2}$$

The denominator, $\sqrt{2\pi}h$ is the effective thickness of the gas assuming a Gaussian distribution, with h being the 1σ scale height.

One of the challenges in determining E_{Hole} is accurately measuring n_0. Both P92 and Bagetakos et al. (2009) use a rotation curve to estimate the total mass in a gravitationally bound spherical system. This value was averaged over the volume of a sphere with a radius, $R_{V_{max}}$ and multiplied by a factor of two. Measuring $\sigma_v = 6.8$ km s^{-1}(HI velocity dispersion), P92 found $h = 625$ pc, and Bagetakos et al. (2009) find $h = 600$ pc. P92 used this method to compute the scale height of M31, and found it to be in agreement with the mass-model based method of Brinks & Burton (1984). However, P92 acknowledged that wide-field, deep photometry of Ho II, would produce an accurate mass model of Ho II, and a more precise knowledge of h, n_0, and E_{Hole}.

Fortunately, we had access to high quality 3.6μm imaging of Ho II through the Local Volume Legacy Survey (LVL; Lee et al., 2008; Dale et al., 2009) taken with the *Spitzer Space Telescope*, which allowed us to construct such a mass model. The LVL team provided a calibrated (including foreground star subtraction) 3.6μm image of Ho II. From this image, we used the ISOPHOT package in IRAF[2] to perform surface photometry, accounting for inclination and position angle effects ($i = 47°$, PA = 177°; Puche et al., 1992) starting at the dynamical center of the galaxy (α = 08:19:18, δ = +70:42:37; J2000), which yielded a surface brightness profile as a function of galactocentric radius (Figure 6.13). Following the method described in § 4 of Oh et al. (2008) and assuming the 3.6μm mass to light ratio, $\Gamma_\star = 0.5$ (comparable to other dwarf irregulars; Walter et al., 2008), we converted the surface brightness profile into a surface mass density profile, Σ.

The isothermal gas scale height equation (Equation 3) derived by Kellman (1970) (and used by Kim et al. 1999 for the LMC) relates the surface mass density, Σ and the HI velocity dispersion, σ_v, to the HI scale height, h. For Ho II, Bureau & Carignan (2002) derived σ_v as a function of galactrocentric radius, allowing us to compute the HI scale height as a function of radius.

$$h = \frac{\langle\ \sigma_v^2 \rangle}{\pi G \Sigma} \tag{6.3}$$

[2] IRAF is distributed by the National Optical Astronomy Observatory, which is operated by the Association of Universities for Research in Astronomy (AURA) under cooperative agreement with the National Science Foundation.

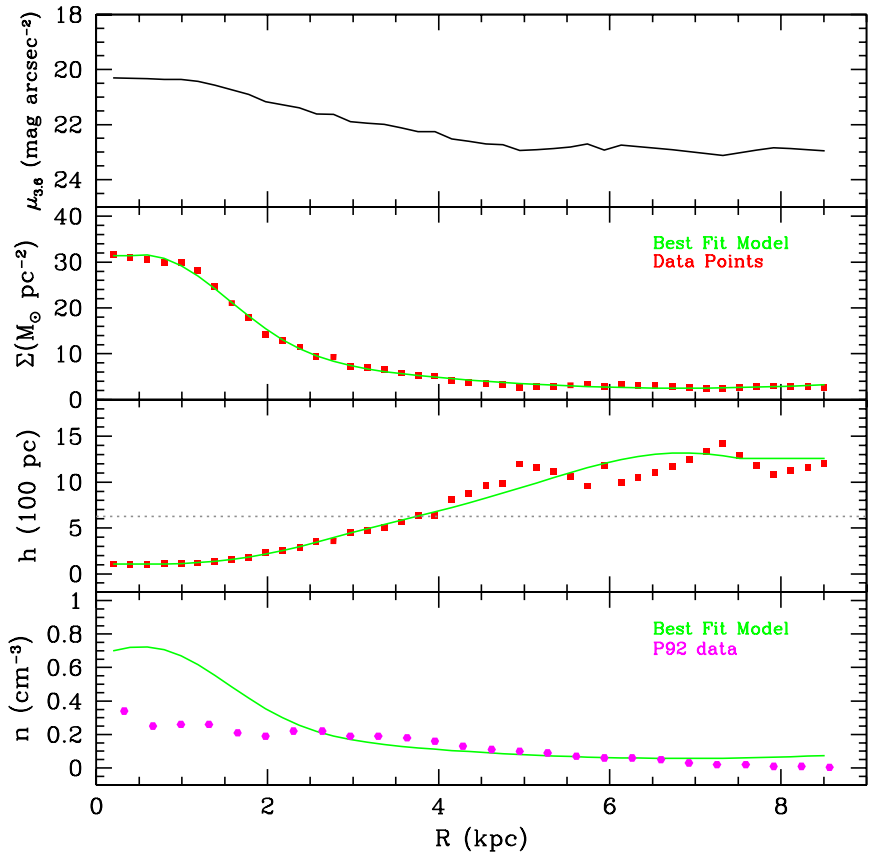

Figure 6.13 *Top panel*: Surface brightness profile of Ho II as measured from 3.6μm imaging from the Local Volume Legacy program (LVL; Lee et al., 2008; Dale et al., 2009) as a function of radius; *Second Panel*: The mass surface density derived from the surface brightness profile following the method of Oh et al. (2008). The red points are the data points and the green line is the best fit analytic function; *Third panel*: The gas scale height of Ho II as a function of radius assuming an isothermal disk derived using the method of (Kellman, 1970; Kim et al., 1999). Data points are in red and the best fit analytic function is the green line. The grey dotted line is the constant value gas scale height used by (Puche et al., 1992); *Bottom Panel*: The present day HI volume density, n, as a function of radius (green line) with the values used by Puche et al. (1992) in magenta. Note the difference in the values of n between the best fit model obtained via surface photometry and the values used by Puche et al. (1992) in the inner $\sim$ 2 kpc. Because $E_{Hole} \propto n_0^{1.12}$ (where n_0 is the average volume density prior to hole formation), an increase in the volume density leads to an increase in the minimum energy necessary to create an HI hole. In this case n_0 measures the average value of the HI volume density, however, SF is more likely to occur at HI peaks, thus E_{Hole} is likely a lower bound (See §**??** for more details).

We now have two independent estimates of the gas scale height, namely the HI scale height of P92 and that inferred from surface photometry. We found the HI scale height derived by P92 to be larger by a factor of $\sim 3-5$ in the innermost 2 kpc of the galaxy, and in agreement at ~ 4 kpc. At radii larger than 2 kpc, h is in better agreement between the different methods.

We computed new values of n_0, as a function of radius, using Equation (2) along with the newly calculated HI scale height and the values of N_{HI} measured by P92. Because the P92 N_{HI} values showed multiple large fluctuations in the inner region of the galaxy, likely due to the presence a number of HI holes, we interpolated over the regions of large fluctuations to ensure a smooth, continuous distribution. Effectively, the largest difference in the P92 and new estimated values are due to the differences in the HI scales heights. The HI scale height derived from surface photometry effectively increases the values of n_0 by a factor of ~ 3 compared to the P92 and Bagetakos et al. (2009) values, which in turn increases E_{Hole} by approximately the same amount.

It is important to note that the values of E_{Hole} are likely lower limits on the energy necessary to evacuate an HI hole. The values of n_0 are the *average* HI volume density at a given radius. However, observationally, SF occurs at higher than average values of n_0, suggesting that to get a true sense of E_{Hole} we would need to measure a peak value of N_{HI} inside the HI holes. Although this is not observationally plausible, we can get a sense of how a larger values of N_{HI} would affect E_{Hole}. As an example, we examined control field 5, which is located near one of the highest regions of current SF in Ho II. From Equation (3) and the peak N_{HI} measured inside c5, we find an increase by a factor of ~ 8 in the the peak value of n_0 versus the average value. This translates into an increase in E_{Hole} by a factor of ~ 10, suggesting that E_{Hole} values present here are likely lower limits.

6.4.2 Energy Associated with Star Formation

A basic criteria of the stellar feedback model is that the energy associated with SF must exceed the energy necessary to evacuate a given HI hole. To calculate the available energy due to SF, we used the galaxy evolution modeling software STARBURST99 (Leitherer et al., 1999). We simulated a single instantaneous burst of SF with a fixed mass of 10^6 $M_{\odot}$using STARBURST99 parameters that matched those described in

§6.3.2, including a metallicity of Z = 0.002, a SN cutoff mass of 8 $M_{\odot}$, and a time sampling of 5 Myr.

Because the energy output from STARBURST99 scales linearly with the input mass, we ran one simulation (with a stellar mass of 10^6 $M_{\odot}$), and then subsequently scaled it by the integrated stellar mass from the SFHs of stars inside each hole, sampled at 5 Myr intervals. The cumulative distribution of the energy generated from SF from the present (t = 0) to 200 Myr for the stars inside each HI hole are shown in Figures 6.14 − 6.19. The inferred kinematic ages are denoted by the grey dashed line, and efficiencies (see §6.4.3) of 100%, 10%, and 1% are indicated by the red, green, and blue dashed lines, respectively.

We have examined the efficiency over the inferred kinematic age for both catalogs as a function of galactrocentric radius, hole radius, expansion velocity, and inferred kinematic age (Figure 6.20). For both hole catalogs the clearest trend we found is that efficiency seems to increase with expansion velocity. However, this result is likely misleading, because of the differences in assigning expansion velocities. In the THINGS, catalog, if a hole was blown out, it was assigned an expansion velocity of 7 km s^{-1}, whereas P92 attempted to measure the best fit expansion velocity for each hole. Thus, if we assigned each P92 hole with an expansion velocity lower than 7 km s^{-1}, the value of 7 km s^{-1}, there would be no trend in the P92 sample, consistent with the THINGS sample. Based on the THINGS catalog classification (see §6.2) of hole types, we found that holes that have not blown out (type 2 or 3), tend to have efficiencies higher than expected from models (see §6.4.3 for a description of the models), in some cases exceeding 100%. In contrast, holes that have blown out generally fall within the expected range. Again, this trend is likely due to the measurement techniques of the HI expansion velocities. In general, a blown out hole has stalled expansion, and its expansion velocity is not detectable above the random HI motions. Thus, the measurements of E_{Hole} are highly uncertain for blown out holes as are the efficiencies. The underlying implication is that the creation of an HI hole is a complex event that cannot be accurately represented by a simple kinematic age or efficiency, rather a more complex model is necessary (see §6.5 for more discussion).

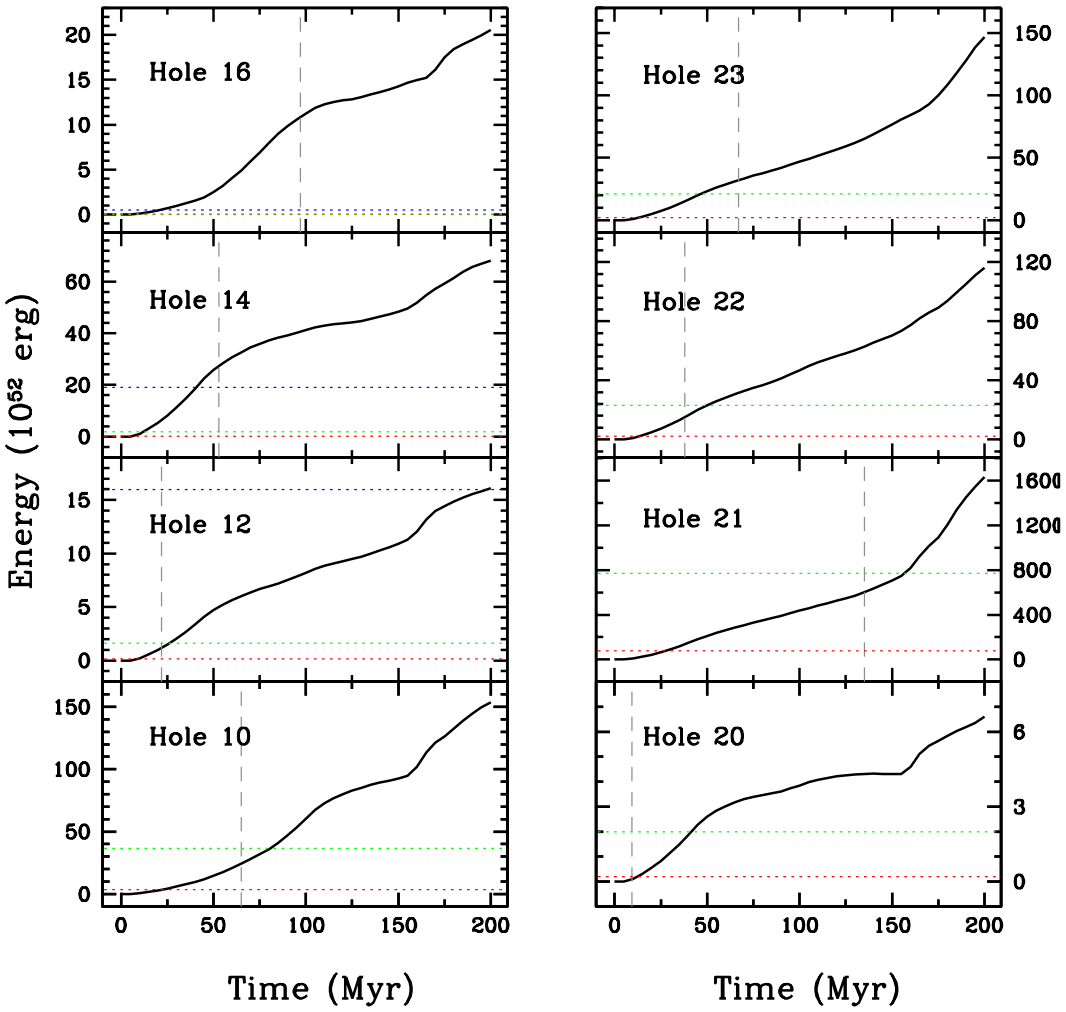

Figure 6.14 The cumulative energies of the stars inside the HI holes of Puche et al. (1992) computed using STARBURST99 (Leitherer et al., 1999) with the measured SFHs as input. The energies are integrated from the present (t = 0) over the past 200 Myr. The vertical grey dashed line is the kinematic age of each hole. The horizontal dotted lines are E_{Hole} assuming 100% (red), 10% (green), and 1% (blue) efficiencies. The intersection of the grey line with the energy profile indicates the putative feedback efficiency over the inferred kinematic age. In several cases, this falls outside the expected range, and may even be greater than 100%. This suggests that inferred kinematic age may not represent the true age of the hole. If instead, we use the intersection 10% efficiency line (green) and the energy profile as a guide, we can get a rough sense of how old the hole may be, if it formed from multiple generations of SNe.

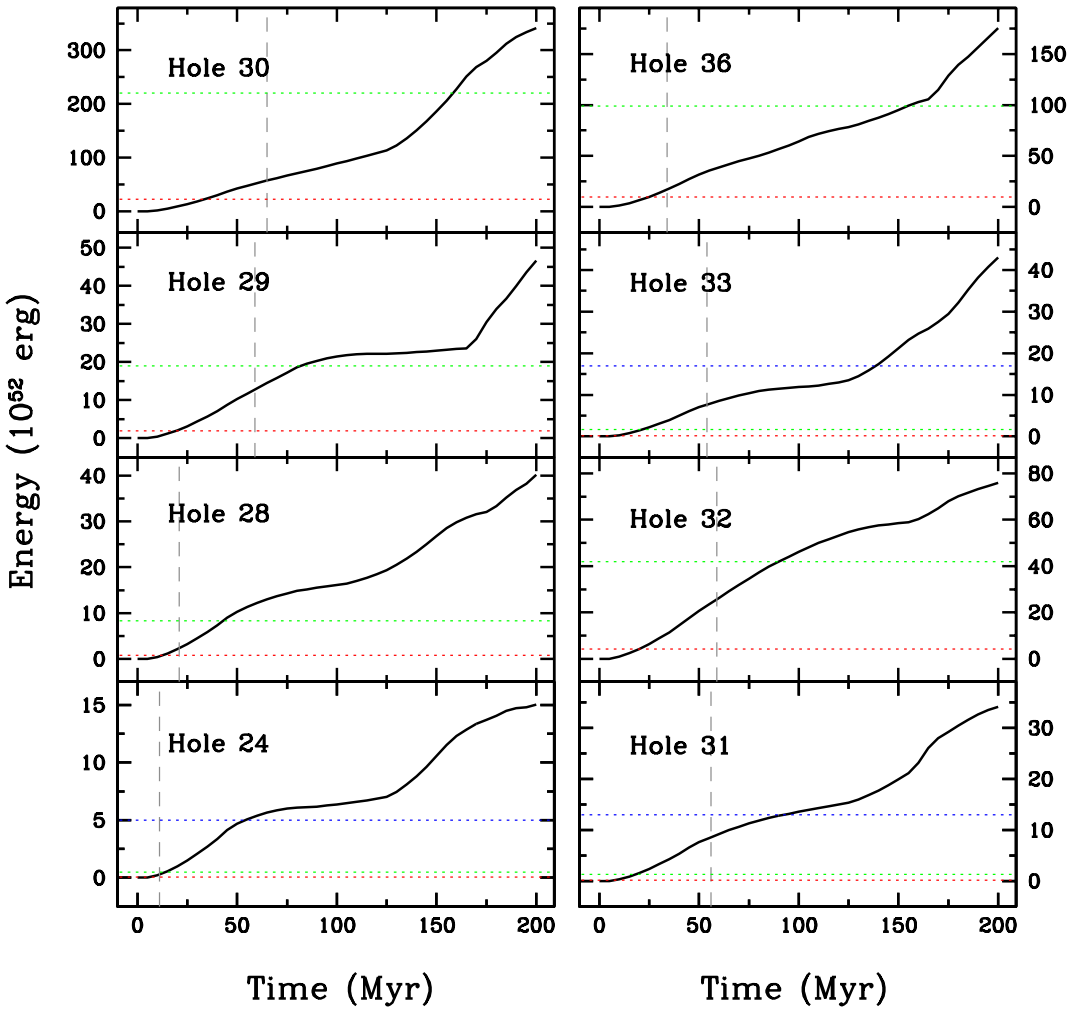

Figure 6.15 The cumulative energies of the stars inside the HI holes of Puche et al. (1992) computed using STARBURST99 (Leitherer et al., 1999) with the measured SFHs as input. The energies are integrated from the present (t = 0) over the past 200 Myr. The vertical grey dashed line is the kinematic age of each hole. The horizontal dotted lines are E_{Hole} assuming 100% (red), 10% (green), and 1% (blue) efficiencies. The intersection of the grey line with the energy profile indicates the putative feedback efficiency over the inferred kinematic age. In several cases, this falls outside the expected range, and may even be greater than 100%. This suggests that inferred kinematic age may not represent the true age of the hole. If instead, we use the intersection 10% efficiency line (green) and the energy profile as a guide, we can get a rough sense of how old the hole may be, if it formed from multiple generations of SNe.

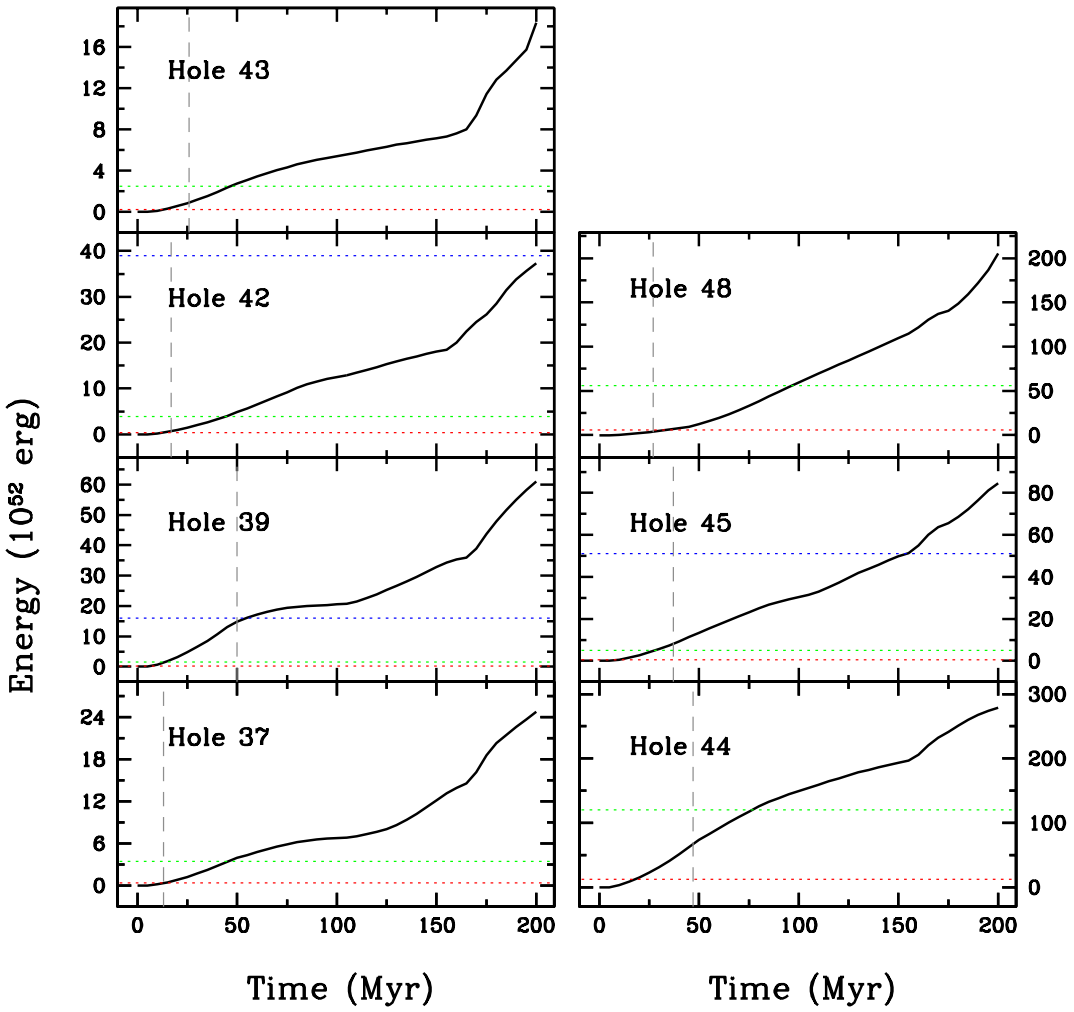

Figure 6.16 The cumulative energies of the stars inside the HI holes of Puche et al. (1992) computed using STARBURST99 (Leitherer et al., 1999) with the measured SFHs as input. The energies are integrated from the present (t = 0) over the past 200 Myr. The vertical grey dashed line is the kinematic age of each hole. The horizontal dotted lines are E_{Hole} assuming 100% (red), 10% (green), and 1% (blue) efficiencies. The intersection of the grey line with the energy profile indicates the putative feedback efficiency over the inferred kinematic age. In several cases, this falls outside the expected range, and may even be greater than 100%. This suggests that inferred kinematic age may not represent the true age of the hole. If instead, we use the intersection 10% efficiency line (green) and the energy profile as a guide, we can get a rough sense of how old the hole may be, if it formed from multiple generations of SNe.

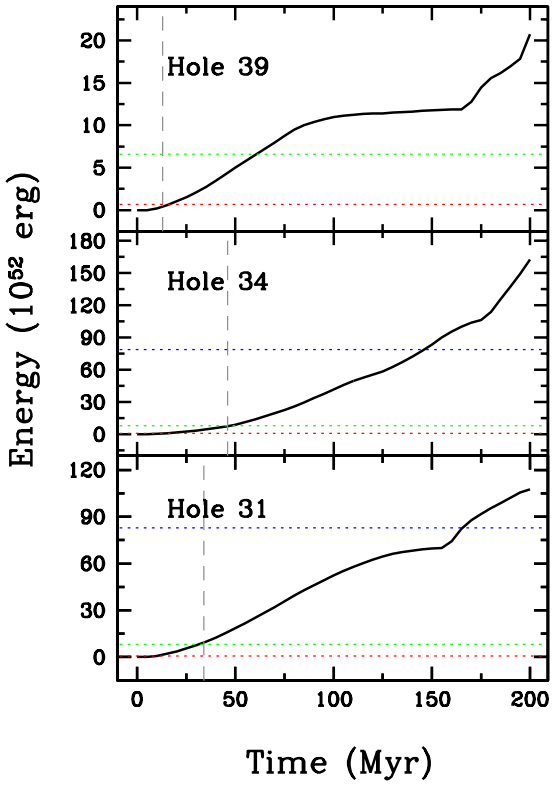

Figure 6.17 The cumulative energies of the stars inside the HI holes of Bagetakos et al. (2009) computed using STARBURST99 (Leitherer et al., 1999) with the measured SFHs as input. The energies are integrated from the present (t = 0) over the past 200 Myr. The vertical grey dashed line is the kinematic age of each hole. The horizontal dotted lines are E_{Hole} assuming 100% (red), 10% (green), and 1% (blue) efficiencies. The intersection of the grey line with the energy profile indicates the putative feedback efficiency over the inferred kinematic age. In several cases, this falls outside the expected range, and may even be greater than 100%. This suggests that inferred kinematic age may not represent the true age of the hole. If instead, we use the intersection 10% efficiency line (green) and the energy profile as a guide, we can get a rough sense of how old the hole may be, if it formed from multiple generations of SNe.

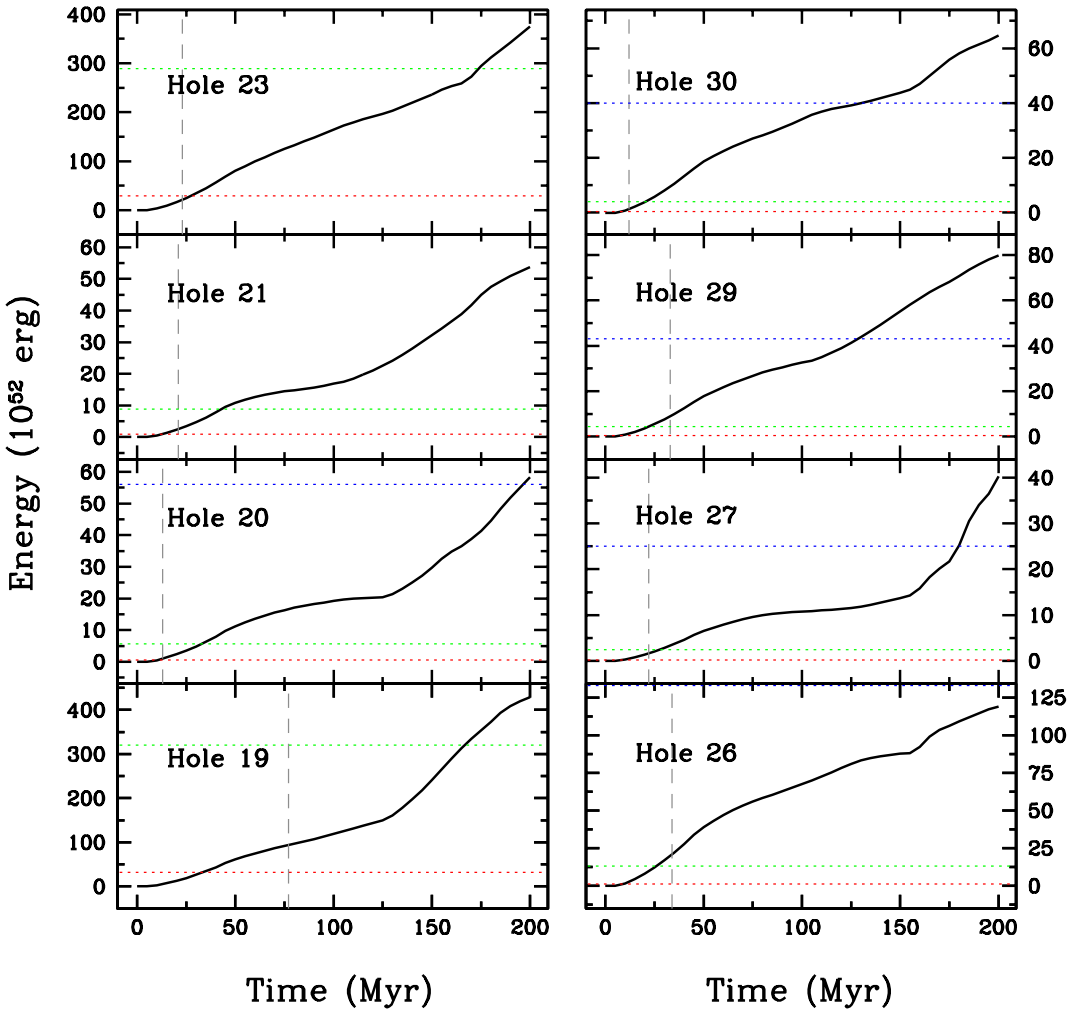

Figure 6.18 The cumulative energies of the stars inside the HI holes of Bagetakos et al. (2009) computed using STARBURST99 (Leitherer et al., 1999) with the measured SFHs as input. The energies are integrated from the present (t = 0) over the past 200 Myr. The vertical grey dashed line is the kinematic age of each hole. The horizontal dotted lines are E_{Hole} assuming 100% (red), 10% (green), and 1% (blue) efficiencies. The intersection of the grey line with the energy profile indicates the putative feedback efficiency over the inferred kinematic age. In several cases, this falls outside the expected range, and may even be greater than 100%. This suggests that inferred kinematic age may not represent the true age of the hole. If instead, we use the intersection 10% efficiency line (green) and the energy profile as a guide, we can get a rough sense of how old the hole may be, if it formed from multiple generations of SNe.

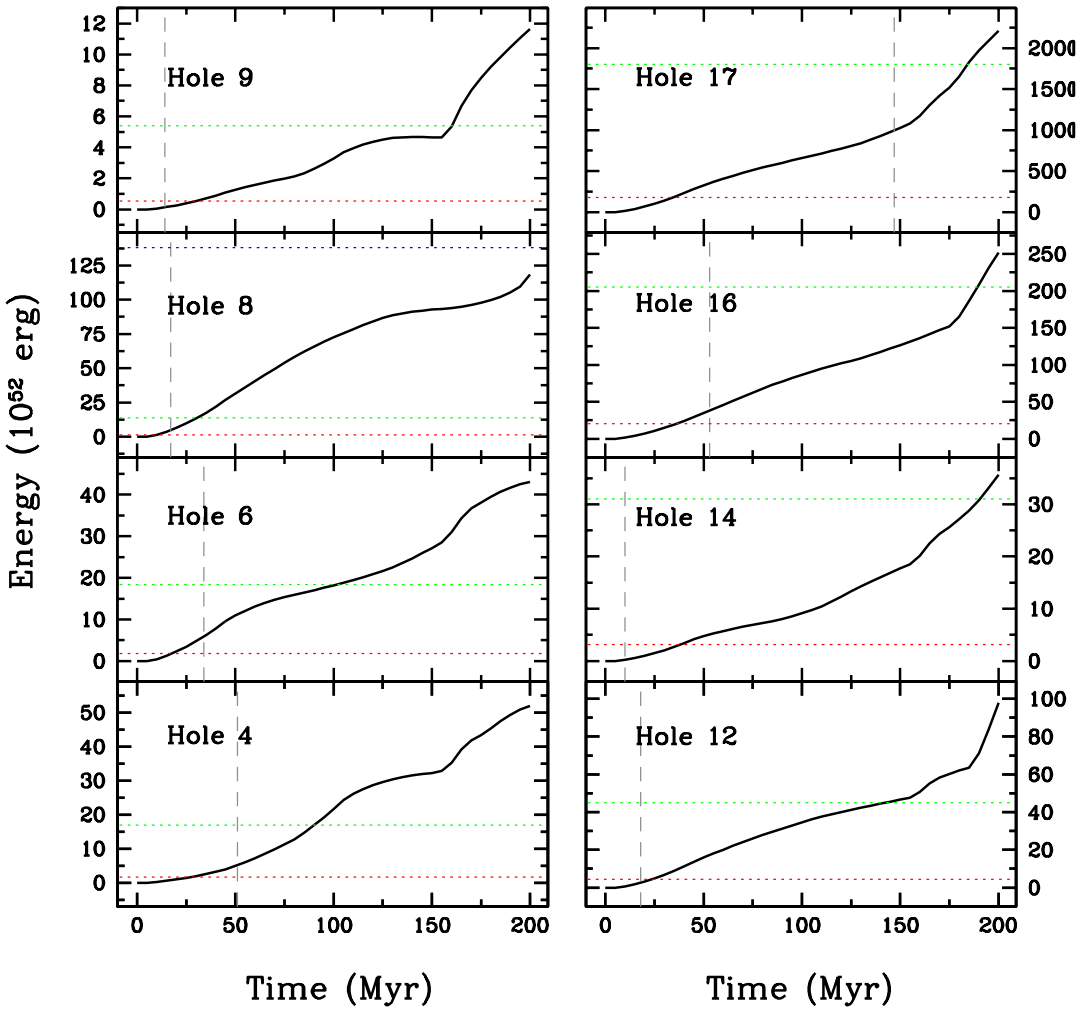

Figure 6.19 The cumulative energies of the stars inside the HI holes of Bagetakos et al. (2009) computed using STARBURST99 (Leitherer et al., 1999) with the measured SFHs as input. The energies are integrated from the present (t = 0) over the past 200 Myr. The vertical grey dashed line is the kinematic age of each hole. The horizontal dotted lines are E_{Hole} assuming 100% (red), 10% (green), and 1% (blue) efficiencies. The intersection of the grey line with the energy profile indicates the putative feedback efficiency over the inferred kinematic age. In several cases, this falls outside the expected range, and may even be greater than 100%. This suggests that inferred kinematic age may not represent the true age of the hole. If instead, we use the intersection 10% efficiency line (green) and the energy profile as a guide, we can get a rough sense of how old the hole may be, if it formed from multiple generations of SNe.

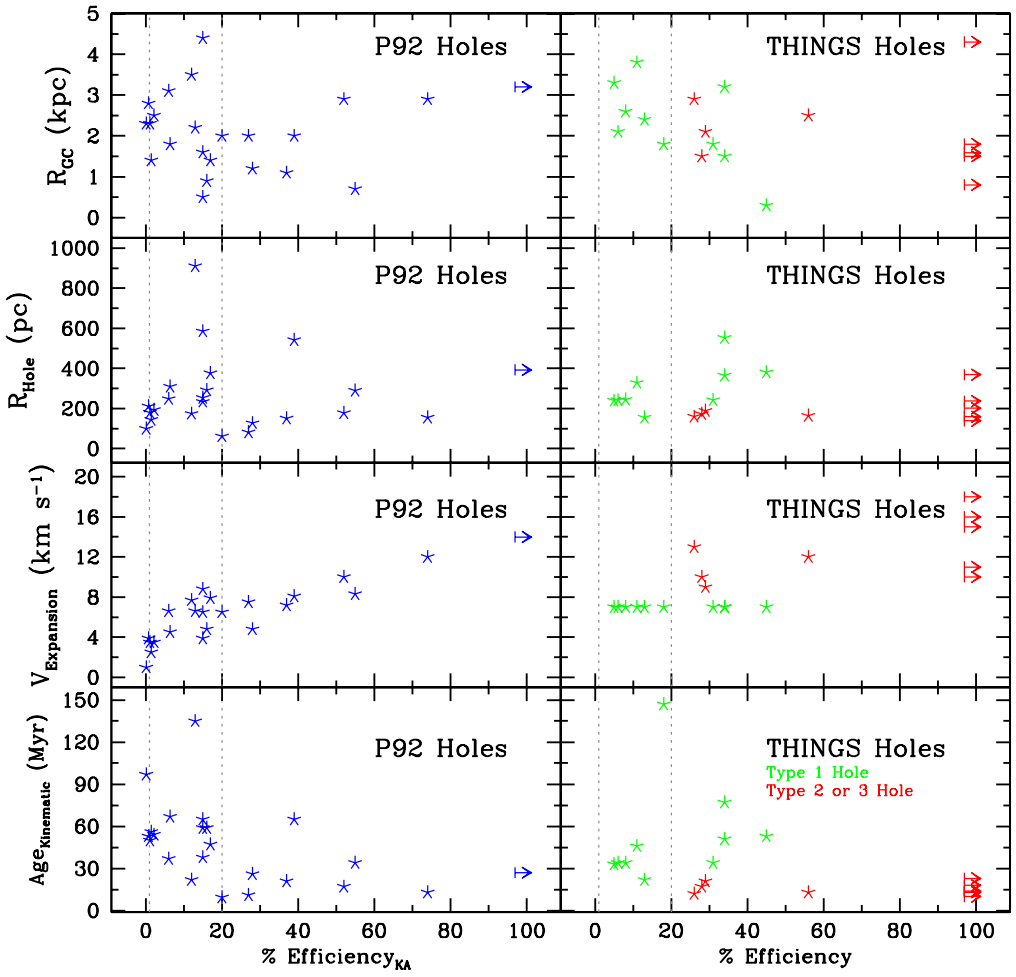

Figure 6.20 Putative stellar feedback efficiencies (E_{sfka}/E_{Hole}; Tables 6.3 and 6.4) plotted versus the galactrocentric radius (R_{GC}), hole radius (R_{Hole}), HI expansion velocity ($V_{Expansion}$), and kinematic age of each hole for the Puche et al. (1992) and the THINGS HI hole catalogs. For the THINGS holes, green stars are type 1 holes (blown out), the red stars are type 2 or 3 (not blown out), and the arrow indicate holes that have efficiencies greater than 100% and have been moved to fit the plot scale. The vertical grey dashed lines indicate the range of efficiencies predicted by various models, 1% − 20% (Theis et al., 1992; Cole et al., 1994; Padoan et al., 1997; Thornton et al., 1998). Note that the type 2 and 3 holes in the THINGS hole sample do not fall in to the expected range of putative feedback efficiency. These holes also tend to be young, expanding quickly, and are generally smaller in size. Arrows indicate lower limits on the efficiency for both hole catalogs.

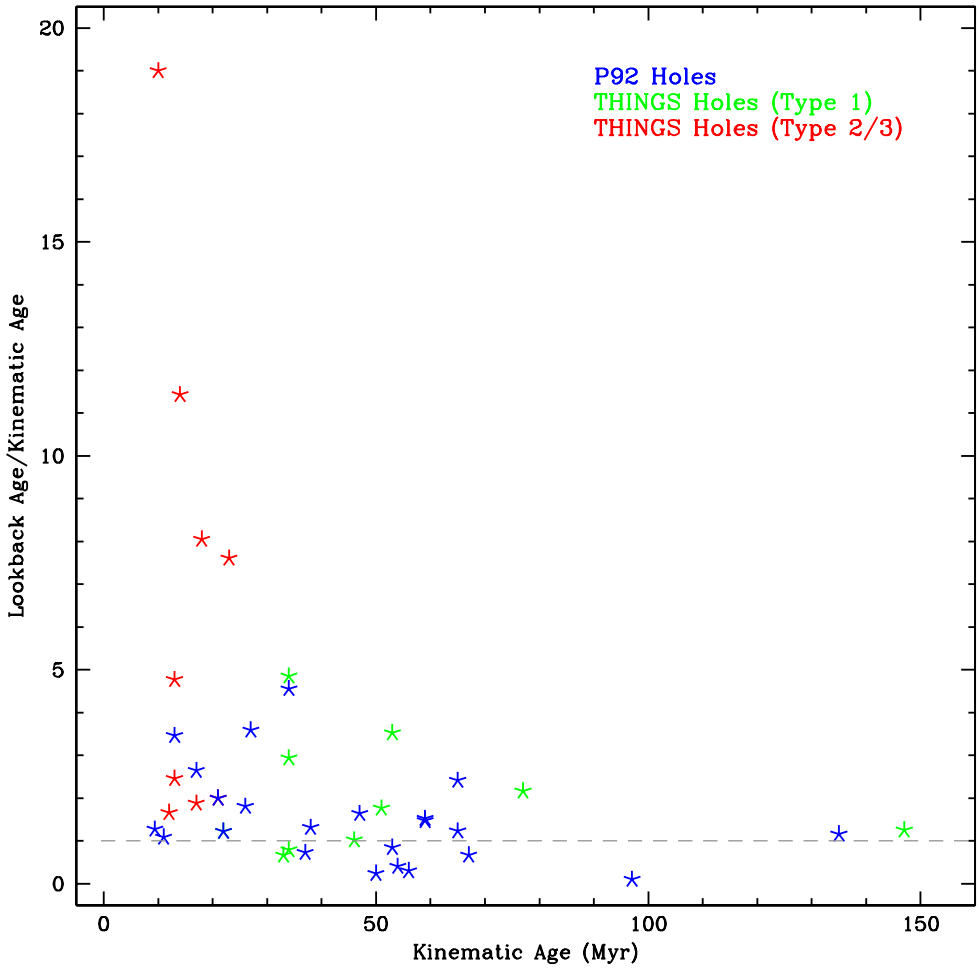

Figure 6.21 The ratio of look back age to inferred kinematic age for the HI holes from the Puche et al. (1992) and Bagetakos et al. (2009) as a function of the inferred kinematic age. The look back age is defined as the time at which the line of 10% efficiency intersects the energy profiles in Figures 6.14 − 6.19. The spread of values greater than unity (grey dashed line) implies that the inferred kinematic age often underestimates the age of HI holes, suggesting that the concept of an age for an HI hole created by multiple generations of SF is intrinsically ambiguous.

6.4.3 Comparing Energies and Feedback Efficiencies

We then compared the inferred energy from SF over the kinematic age of each hole, E_{SFKA}, to the energy needed to produce the observed properties of each hole, E_{Hole}. The ratio of E_{Hole} to E_{SFKA} allows us to calculate the a 'putative' stellar feedback efficiency, ϵ, over the inferred kinematic age of each hole (see Tables 6.3 and 6.4). Models of SF including feedback and interactions with the ISM expect such efficiencies to range from $\sim 1\% - 20\%$ (Theis et al., 1992; Cole et al., 1994; Padoan et al., 1997; Thornton et al., 1998). 15 of the 23 P92 holes and 6 of the 19 THINGS holes have putative efficiencies between $1 - 20\%$, in agreement with the models. Overall, a higher fraction of P92 holes are within the expected efficiency range than THINGS holes. While this may seem to be an unexpected result, this actually underlines the complexity of the connection between stars and HI holes. For example, P92 hole 42 and THINGS hole 27 are roughly the same size, but slightly different central coordinates, which results in the the THINGS hole having more stars in its CMD by a factor of ~ 2, in turn influencing the SFH and feedback efficiency. Of the holes that are not consistent with the expected range, one P92 hole (number 48) has an efficiency greater than 100%, while five THINGS holes (9, 12, 14, 23, 39) also have efficiencies greater than 100% (Figure 6.20). These outliers suggest that perhaps energy from stellar feedback is not sufficient to have created these holes.

For example, P92 hole 14 (Figure 6.14) has an efficiency of $\sim 1\%$ where the inferred kinematic age intersects the cumulative energy profile. In comparison, P92 hole 30 (Figure 6.15) has a kinematic age efficiency of 39%, outside the theoretical range predicted by models. Further, ratios that require $\epsilon > 100\%$ indicate that there has not been enough energy for SF during the inferred kinematic age of each hole. However, Figures $6.14 - 6.19$ show that there has been sufficient energy available during the most recent 200 Myr even in these extreme cases, suggesting that perhaps the inferred kinematic ages do not truly represent the ages of the holes, or that the concept of an HI hole age is intrinsically ambiguous for holes that contain multiple generations of stars.

To explore this possibility, instead of using the inferred kinematic age as a guide, we assumed a nominal 10% efficiency and recalculated the age of the hole to match the time scale needed to give sufficient energy input from SF. For example, while P92 hole 48 (Figure 6.16) has a kinematic age efficiency of 120%, the energy profile shows

that over the past 200 Myr, enough energy was generated from SF to have created the hole, if the hole is $\sim$ 100 Myr old (assuming a nominal 10% efficiency). Similarly, for the other P92 and THINGS holes that have efficiencies outside the theoretical range, the same analysis shows that there is ample energy from SF to have created each of those holes in the past 200 Myr. We defined a 'look back age' as the time at which the line of 10% efficiency intersects the energy profiles in Figures 6.14 $-$ 6.19. We then compared the ratio of the look back age to the inferred kinematic age, and found that the inferred kinematic ages are generally lower than the look back times (Figure 6.21). While perhaps not the most rigorous definition of the age of a hole, the look back age suggests that the inferred kinematic age may not accurately represent the true age of HI holes, even as an upper limit. We explore the kinematic age discrepancy in greater detail in §6.5.

6.4.4 Connecting the Spatially Resolved Star Formation History to the HI Surface Density

In addition to the measuring the SFR as a function of time, we can use spatial information from the resolved stellar populations to qualitatively compare the location of SF episodes with HI column densities. Following a method of analysis similar to Dohm-Palmer et al. (1997), we used BHeBs from the entire HST/ACS CMD of Ho II (Weisz et al., 2008) and constructed movies of the spatially resolved recent SFH over the past $\sim$ 200 Myr. The initial masses of BHeBs range from $\sim 2 - 20$ $M_{\odot}$, giving them lifetimes between $\sim 5 - 500$ Myr. More importantly, BHeBs have a one-to-one correspondence between luminosity and age. BHeBs of a single age therefore occupy a *unique* location on a CMD, making them superb tracers of recent SF. In contrast, multiple generations of MS stars can occupy the same location on the CMD, making age dating of most individual MS stars from the CMD virtually impossible (see Dohm-Palmer et al., 1997; Gallart et al., 2005; Weisz et al., 2008, for a more in depth discussion of age dating stars from CMDs).

By measuring its magnitude, we can assign a unique age to each BHeB, using the models of stellar evolution. We can then trace the location of SF as a function of age based on BHeB positions in the ACS image. While it is true that many young star clusters dissolve into the field on time scales of $\sim$ 10 Myr (e.g., Lada & Lada, 2003), the

stars can maintain spatial coherence for much longer. Empirically, CMD-based studies of the SMC and LMC find that star forming structures (such as associations) can remain coherent for up to a couple hundred Myr (Gieles et al., 2008; Bastian et al., 2009).

We were able to isolate the BHeBs on the CMD by visual inspection because Ho II has a large number of BHeBs, and low foreground and internal reddening values. We constructed a smooth analytic function mapping the magnitudes of the BHeB track to unique ages, using the stellar evolution models of Marigo et al. (2008). Applying this function to the observed BHeBs, we assigned each star an individual age, with an uncertainty of $\lesssim 20\%$. We created density maps of the BHeBs by placing the stars into 5 Myr bins and converting their x and y coordinates to RA and Dec. We then smoothed the resulting images with a Gaussian kernel with a FWHM $\sim$ 15".

To convert the BHeB density maps (stars pixel^{-1}) to SFR/area ($M_\odot$ yr^{-1} kpc^{-2}), we first divided each frame (i.e., 5 Myr binned density maps) by the sum of the pixel values to determine the fractional contribution of each pixel to the total stellar density in each frame. That is, if a normalized pixel had a value of 0 it did not contribute to the SF in the frame, while a pixel with a value of 0.01 contributed to 1% of the SF in that frame. The density maps were then connected to the SFH of the field (Weisz et al., 2008).

First, we re-binned the SFH with different time resolutions: 10 Myr for a look back time of $\sim$ 100 Myr and 20 Myr for a look back time of $\sim$ 200 Myr, in order to match the decreasing time resolution at older ages. We then interpolated each to a 5 Myr time sampling to match the temporal resolution of the stellar density maps. We then multiplied each stellar density map by the corresponding SFR and divided by the physical area of the ACS field of view, thus converting the images from units of stars pixel^{-1} to SFR/area. We then performed bilinear interpolation over time and space to ensure smooth and continuous movies. The result is two movies of the spatially resolved SFHs of Ho II with units of SFR/area, with look back times of $\sim$ 100 and $\sim$ 200 Myr, and a spatial resolution of $\sim$ 15" ($\sim$ 250 pc). Figures 6.22 and 6.23 show select still frames of the two movies with HI contours overlaid.

The general trends presented by the spatially resolved SFHs are that low level SF has dominated the galaxy in the most recent $\sim$ 200 Myr, with only a substantial rise in the SF activity in the last $\sim$ 40 Myr. The smoothness of the SFH implies that the HI holes

were not produced by a series of intense episodes of SF, instead the holes were created due to low level SF with some variation above a constant value, which has steadily input energy into the ISM. As a comparison, we integrated the spatial resolved SFH of the region corresponding to THINGS hole 17 and found general agreement between the two. For example, both SFHs show a peak at $\sim$ 40 Myr, and from the integration of the spatially resolved SFH we found the SFR at this time to be 3.0×10^{-2} $M_{\odot}$ yr^{-1}, whereas the SFH from Figure 6.4 shows a SFR of 4.0×10^{-2} $M_{\odot}$ yr^{-1}. While this difference of 30% may seem large, in fact, the systematic and statistical uncertainties from the two methods are $\sim$ 20% from the temporal SFH and 50% from the spatial SFH, which implies these are consistent values.

These movies allow us to investigate the correlation between HI density and SF on different time scales. Within the last $\sim$ 40 Myr, the SF is well correlated with high HI surface density, as has been seen in Hα, and UV imaging (see §6.5.2 for a discussion on Hα and UV imaging). On longer timescales, we note that the SF patterns do not adhere to the locations of high HI column densities. In particular, there is a relatively high level of SF activity in the large HI void, corresponding to P92 hole 21 and THINGS hole 17, $\sim$ 40 Myr ago, which has been preceded by low level activity for at least the past $\sim$ 200 Myr.

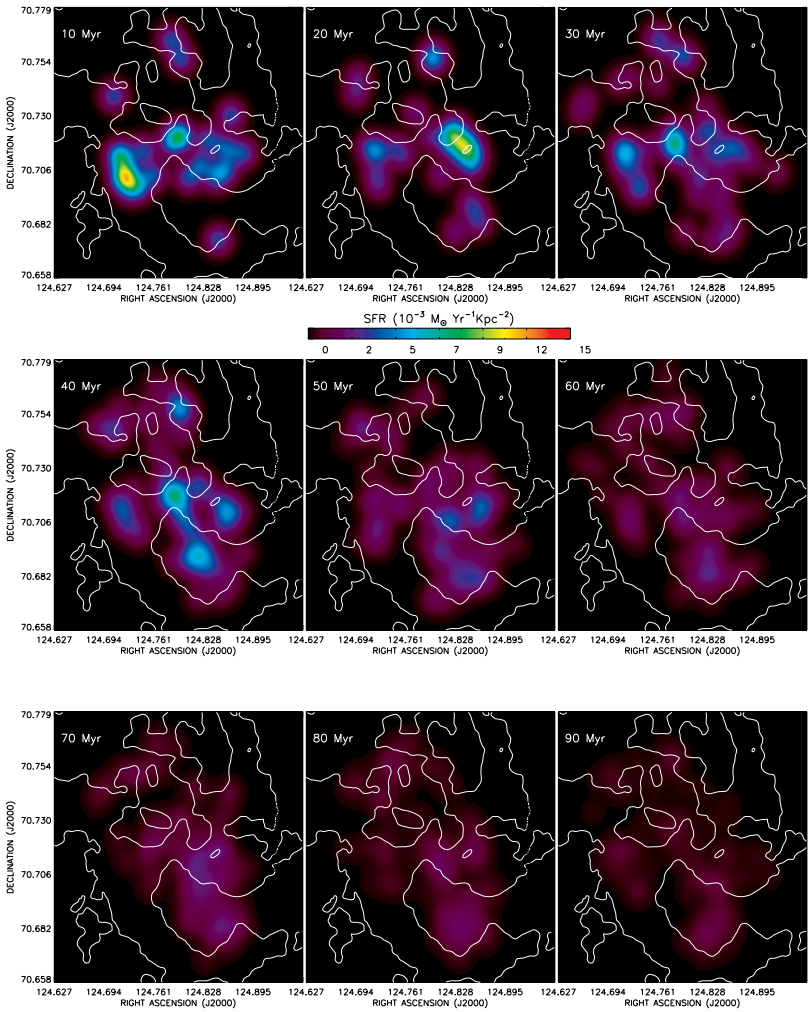

Figure 6.22 The spatially resolved recent SFH of Ho II over the last 90 Myr with 10 Myr time resolution as seen on the sky in units of SFR/area. The HI 10^{-21} cm^{-2} contour is overlaid in white. Note that majority of the galaxy is dominated by constant low level SF, while only a few regions have experienced elevated episodes of SF. As expected, the most recent frame shows the peaks of SF coincident with the peaks of the HI distribution.

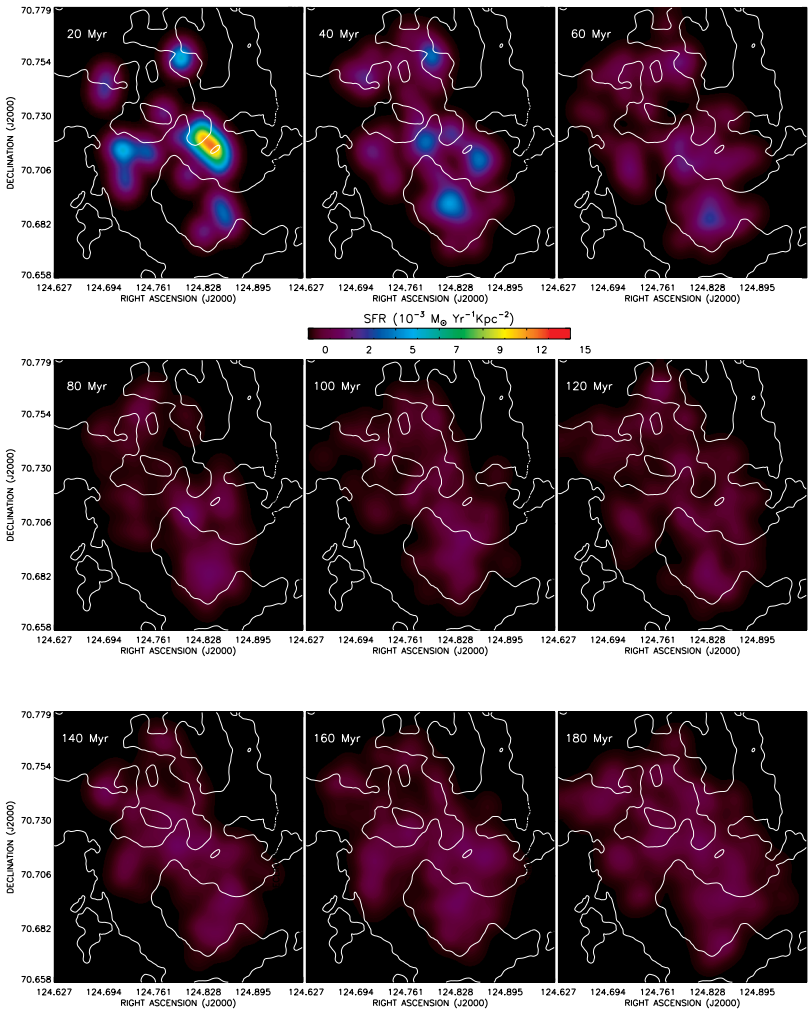

Figure 6.23 The spatially resolved recent SFH of Ho II over the last 180 Myr with 20 Myr time resolution as seen on the sky in units of SFR/area. The HI 10^{-21} cm^{-2} contour is overlaid in white. Note that majority of the galaxy is dominated by constant low level SF, while only a few regions have experienced elevated episodes of SF. As expected, the most recent frame shows the peaks of SF coincident with the peaks of the HI distribution.

6.5 Discussion

6.5.1 The Paradoxical Results of Rhode et al. (1999)

The study of Ho II by Rhode et al. (1999) is perhaps one of the most rigorous observational tests of the stellar feedback model of HI hole creation. Despite the appeal of the stellar feedback theory of HI hole formation, Rhode et al. (1999) found no compelling evidence supporting this hypothesis, and their conclusions seriously challenged the standard model of HI hole formation. The non-detection of stars in the majority of HI holes contradicted expectations for stellar feedback as a universal mechanism of hole creation, although Rhode et al. (1999) did not rule out stellar feedback as the source of small HI holes in the central regions of Ho II.

Rhode et al. (1999) searched for single age stellar clusters, but likely did not find them because the single age cluster model can overestimate the surface brightness of the remnant stars by a significant amount, for a variety of reasons we explore in the following sections. Further, using only integrated light, it can be difficult to distinguish between a single age stellar cluster and a mixed age stellar population, which can make it difficult to age date stars that are detected. As a comparative test, we computed the integrated magnitudes of each of the Rhode et al. (1999) apertures from the HST/ACS CMDs. Our integrated photometry is in agreement with that of Rhode et al. (1999). A histogram of the resulting integrated magnitudes reveals that the six regions where Rhode et al. (1999) did detect stars are among the brightest in the sample (Figure 6.26). The rest of the regions were classified as non-detections, despite containing significant numbers of young stars.

Using the HST/ACS photometry of Ho II we constructed CMDs of the apertures (panel (d) of Figure 6.1 and Table 6.6) defined by Rhode et al. (1999). Figures 6.24 and 6.25 unequivocally show well-populated CMDs of mixed age stellar populations, including young MS stars and HeBs, which are likely the remnant stars Rhode et al. (1999) attempted to detect using integrated light. Our interpretation is that single age stellar populations do not produce a majority of the HI holes in Ho II, confirming the conclusions of Rhode et al. (1999).

Table 6.6: Photometric Properties of the Rhode et al. (1999) Apertures

Hole Number (1)	α (B1950.0) (2)	δ (B1950.0) (3)	Diameter (arcsec) (4)	Stars in CMD (5)	Hole Type (6)	Integrated m_{F555W} (7)
10	8 13 27.7	+70 50 59	30.00	893	a	19.75
12	8 13 37.3	+70 53 02	20.00	1989	b	18.63
14	8 13 42.3	+70 52 55	20.00	2810	c	18.12
16	8 13 45.4	+70 52 22	20.00	2740	d	17.12
20	8 13 47.3	+70 52 14	20.00	2639	c	17.44
21	8 13 49.4	+70 50 43	30.00	4077	d	17.18
22	8 13 51.5	+70 52 38	20.00	3064	d	17.24
23	8 13 51.9	+70 53 02	20.00	3051	c	17.85
24	8 13 54.6	+70 53 36	20.00	2825	c	18.08
28	8 13 59.1	+70 53 14	20.00	2526	c	18.01
30	8 14 00.9	+70 53 55	20.00	2062	c	18.59
31	8 14 01.3	+70 53 27	20.00	2374	c	18.09
32	8 13 59.4	+70 51 16	24.00	2615	c	18.31
33	8 14 03.8	+70 54 33	20.00	1628	c	18.81
36	8 14 06.6	+70 52 44	24.00	3324	d	17.65
37	8 14 06.3	+70 54 55	20.00	1205	b	19.04
39	8 14 09.9	+70 54 14	20.00	1893	c	18.29
42	8 14 09.3	+70 54 44	20.00	1336	b	18.76
43	8 14 13.5	+70 51 39	16.00	805	e	19.40
44	8 14 12.1	+70 52 56	30.00	4229	d	17.60
45	8 14 12.7	+70 54 60	20.00	1023	c	19.04
48	8 14 22.9	+70 54 30	30.00	1892	d	18.14

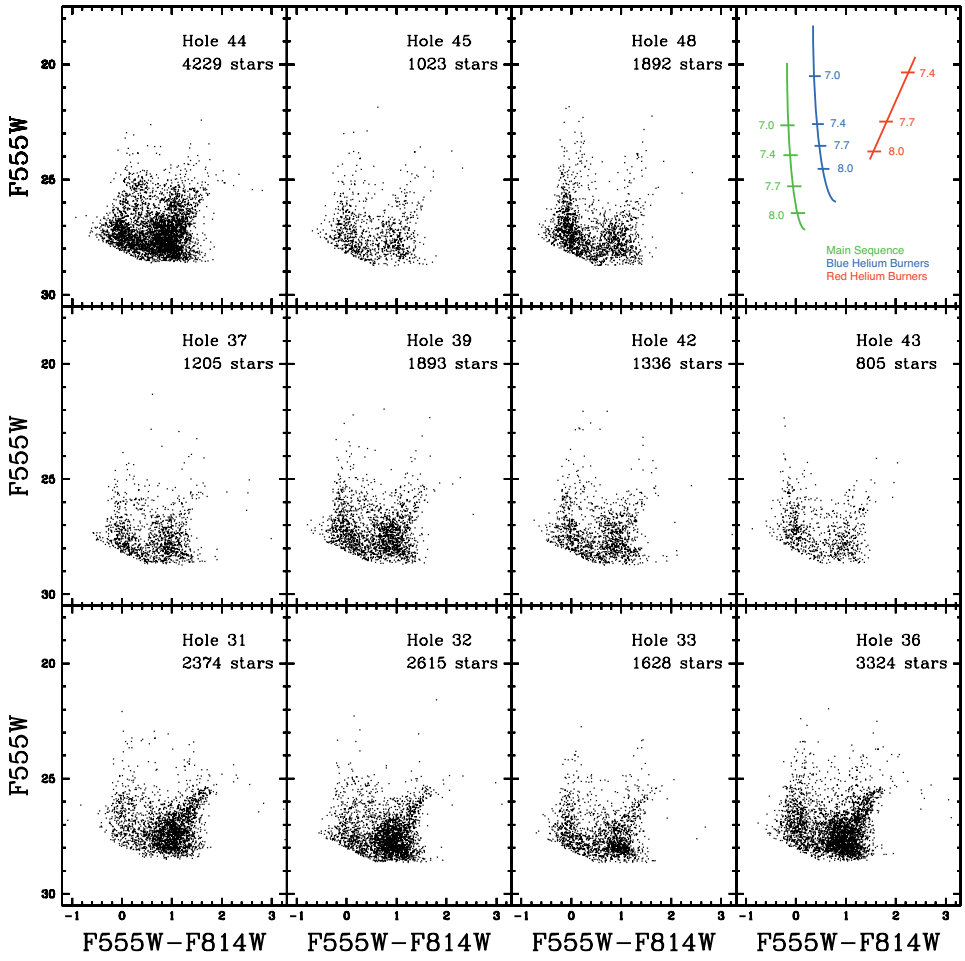

Figure 6.24 HST/ACS CMDs of the photometric apertures used by Rhode et al. (1999), corrected for foreground reddening, $A_V = 0.11$ (Schlegel et al., 1998). The schematic in the upper right hand corner shows the ages of each type of star, MS (green), BHeB (green), and RHeB (red), with the logarithm of the ages shown as a function of magnitude. Although sparse in some fields, note the presence of young MS and BHeB stars in all the CMDs. The fact the the BHeBs span a range in magnitudes indicate that multiple episodes of recent SF must have taken place, as different age BHeBs do not overlap on the CMD. In contrast, BHeBs from a single age cluster would have an overdensity at only one magnitude.

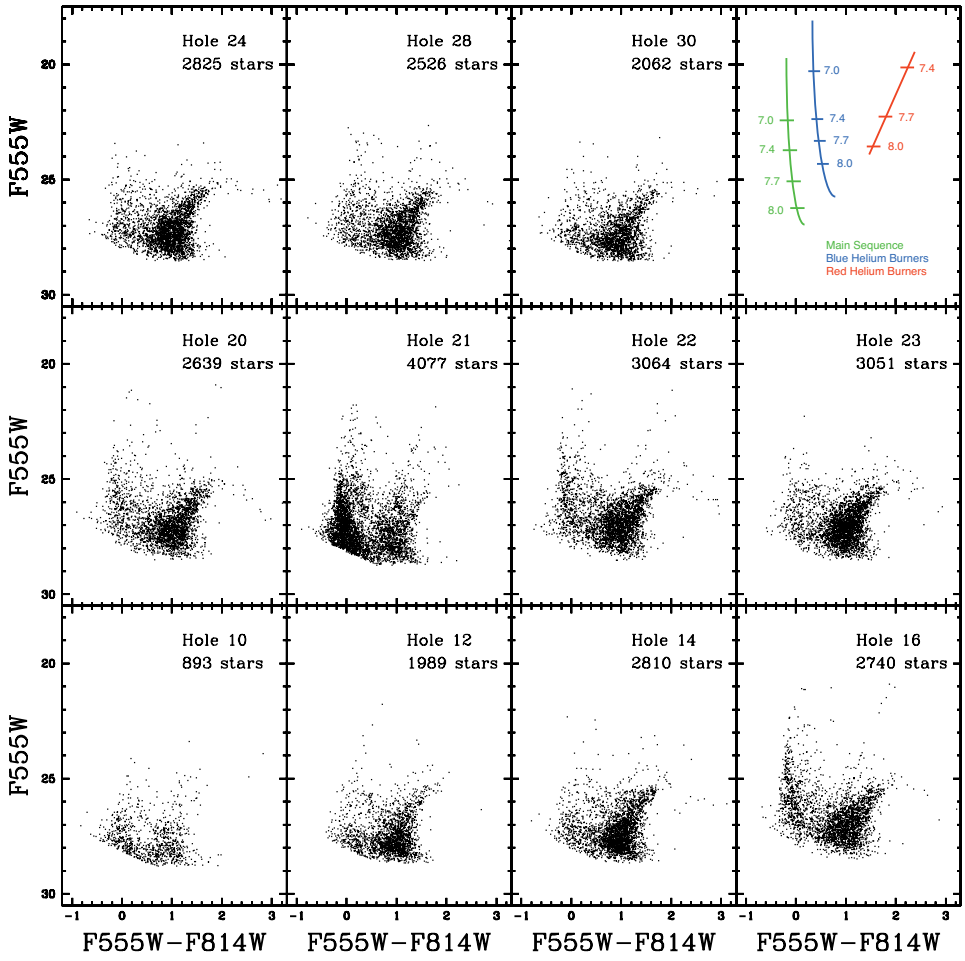

Figure 6.25 HST/ACS CMDs of the photometric apertures used by Rhode et al. (1999), corrected for foreground reddening, $A_V = 0.11$ (Schlegel et al., 1998). The schematic in the upper right hand corner shows the ages of each type of star, MS (green), BHeB (green), and RHeB (red), with the logarithm of the ages shown as a function of magnitude. Although sparse in some fields, note the presence of young MS and BHeB stars in all the CMDs. The fact the the BHeBs span a range in magnitudes indicate that multiple episodes of recent SF must have taken place, as different age BHeBs do not overlap on the CMD. In contrast, BHeBs from a single age cluster would have an overdensity at only one magnitude.

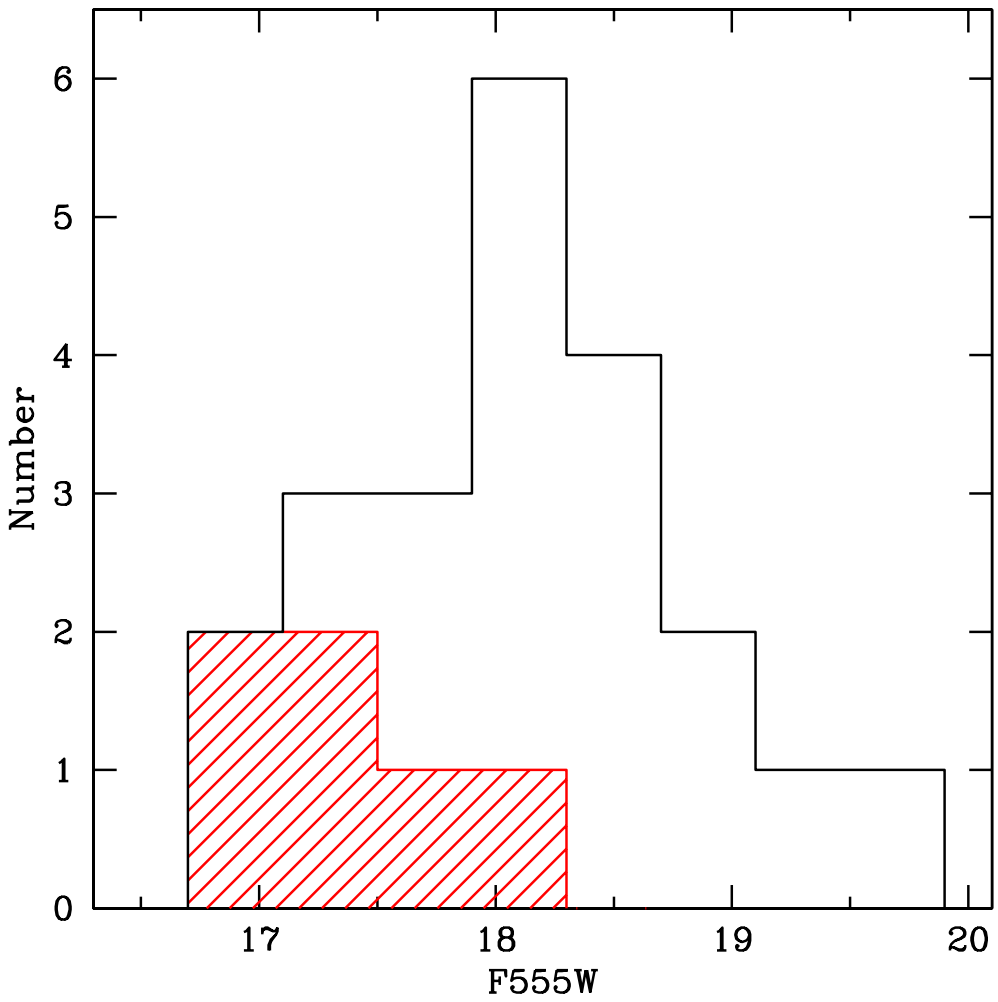

Figure 6.26 A histogram of the integrated ACS m_{F555W} magnitudes from the HST/ACS CMDs corresponding to the photometric apertures used by Rhode et al. (1999). The red shaded region represents the apertures that Rhode et al. (1999) classify as containing putative star clusters (Table 6.6). Note that they regions containing putative stellar clusters are among the brightest in the sample.

6.5.2 A New Model

Instead of assuming that a single age cluster was responsible for the creation of HI holes, we explored the possibility that a mixed age stellar population producing SNe tens or hundreds of Myr apart was responsible for the creation of HI holes. Specifically, we asked how a remnant mixed age stellar population would differ from a single age cluster in terms of the integrated light properties, location of stars inside HI holes, and energetics associated with this different mode of SF.

To illustrate this, we generated synthetic CMDs, with the same parameters (e.g., IMF, binary fraction, distance, etc.) used to measure the SFHs in §6.3.2, and computed the mean expected integrated magnitudes of different stellar populations. To ensure that we were not in a regime where stochastic effects are important, we fixed the integrated mass of the simulations to be 10^6 $M_\odot$, $\sim 1\%$ of the stellar mass of Ho II and at least a factor of 100 greater than the stellar mass within any given hole. We limited the simulations to the most recent 100 Myr, the approximate age regime of the majority of HI holes in Ho II. The simulations were run 100 times, which produced an average statistical error of ~ 0.01 mags. Effects of completeness and photometric error are similarly ~ 0.01 mags. Neither source of error has a large impact on the results at magnitudes this bright.

The first model assumed that all the stellar mass was formed in a ~ 5 Myr period 50 Myr ago, with no subsequent SF. For this, 'burst' model, we found the mean integrated magnitude and color to be $m_{F555W} = 15.88$ and $m_{F555W} - m_{F814W} = 0.48$. For comparison, we distributed the same integrated stellar mass with a constant SFR over the period of $50 - 100$ Myr and found $m_{F555W} = 16.07$ and $m_{F555W} - m_{F814W} = 0.51$.

We further considered a two component SFH model. We distributed 10^6 $M_\odot$ in stellar mass with a constant SFR from $50 - 90$ Myr ago, no SF from $35 - 50$ Myr ago, constant SFR from $25 - 35$ Myr ago, and quiescence for the most recent 25 Myr. This multiple episode model produced stars with integrated properties of $m_{F555W} = 15.86$ and $m_{F555W} - m_{F814W} = 0.54$. Comparing the single age, constant, and multiple episode models of the same integrated stellar mass, we found they produced results that were indistinguishable in terms of integrated light.

To illustrate this point empirically, we compared the stellar populations of P92 holes 42 and 43, which both have integrated magnitudes of $m_{F555W} = 18.75$, but differ in other

properties. For example, hole 42 contains 1383 stars and has an inferred kinematic age of 17 Myr, but hole 43 has 549 stars and an inferred kinematic age of 26 Myr. The SFHs of stars within the two holes differ significantly in the last 10 Myr. SF in hole 42 had been more prominent $>$ 10 Myr ago, however within the last 10 Myr, hole 43 has a higher SFR, likely producing young bright stars that dominate the integrated light of the stellar population. These findings suggest that integrated light can only serve as an indicator of recent SF, but cannot give an accurate account of the SFH.

The dissolution of stellar clusters into the field further complicates integrated light observations and analysis of clusters. Lada & Lada (2003) note that the most common stellar clusters contain only dozens of stars and disperse into the field within $\sim$ 10 Myr, which is the so-called 'infant mortality' scenario of cluster dissolution. Detailed studies of structure of stellar groups in the SMC and LMC show that only $\sim 3-7\%$ of young stars survive in clusters past the age of $\sim$ 10 Myr (Gieles et al., 2008; Bastian et al., 2009). Applying this idea to Ho II, it suggests that the remnant stellar populations would not be highly clustered, but instead would be distributed across the HI hole, resulting in fainter integrated magnitudes than expected for clustered stars. To look for this effect we selected MS stars from the HST/ACS photometry by applying magnitude and color restrictions that isolated young MS stars ($<$ 10 Myr (red) and $<$ 75 Myr (blue)) and plotted their positions relative to the HI holes catalogs, Rhode et al. (1999) apertures, and control fields (Figure 6.27). While there is some clustering of young stars, particularly those $<$ 10 Myr in age, the clusters of stars are typically on the edges of the HI holes where triggered secondary SF due to the expansion of the hole is likely taking place (e.g., Tenorio-Tagle & Bodenheimer, 1988). The majority of the MS stars $<$ 75 Myr in age are not clustered, which makes the integrated light of these stellar populations appear fainter than had they been bound or appeared as unresolved stellar clusters.

One of the most interesting cases presented by Rhode et al. (1999) is that of P92 hole 10. Based on its HI properties at least several dozen SNe would be necessary to have created hole 10. The remnant stars from a burst should be well above the detection criteria used by Rhode et al. (1999) in a single cluster model, but none were detected. Rhode et al. (1999) assumed a single remnant cluster would be in the center of the hole and used an aperture smaller than the hole to search for the stars. Comparing the

CMD between the actual hole and the aperture shows why the stars likely responsible for creating hole 10 were not detected by Rhode et al. (1999). The CMD of the entire hole has $\sim$ 4200 stars and an integrated magnitude of $m_{F555W} = 17.68$, while the CMD of the Rhode et al. (1999) hole 10 aperture contains 893 stars and has an integrated magnitude of $m_{F555W} = 19.75$. Furthermore, the spatial distribution of MS stars < 75 Myr in age (Figure 6.27) show that the photometric aperture of hole 10 has no stars, while the hole itself contains a number of young stars. It appears that the bright stars either did not form centrally in hole 10 or they have rapidly diffused out of the center, if they did form there. Although this hole was considered among the strongest evidence against the stellar feedback theory of HI hole creation, it now only seems to confirm that the single age cluster model of hole formation is not the appropriate mechanism for HI hole creation.

If HI holes form via multiple generations of SNe, understanding the underlying physics becomes more complicated. We have to go beyond the simple single blast model of HI hole creation and consider the complex interplay between the local ISM and stellar feedback, which seems to be the dominant mechanism behind structure formation in the ISM (e.g., Harris & Zaritsky, 2008). Heiles (1990) considers the case of 'clusters of clusters' of SNe present within an HI hole, noting that sequential explosions would contribute to the mechanical energy expanding the hole as well as significantly alter the gas density inside the hole. Oey & Clarke (1997) also conclude that multiple OB associations would increase the mechanical power and time scale of energy input into expanding the shell. Recchi & Hensler (2006) present a model demonstrating how two separate SF events inside an HI hole would delay the onset of the hole refilling with cold gas with time scales from $\sim 100 - 600$ Myr depending on local conditions, indicating the multiple episodes of SF spread out over time can help extend the life of an HI hole. Projection effects could cause generations of stars along a line of site appear to be spatially co-incident within a given HI hole. However, this is likely a small effect because the disk-like nature of Ho II implies that the stellar scale height is much less than that of the HI, suggesting a reasonable assumption is that the young stars are primarily located in the mid-plane of the disk.

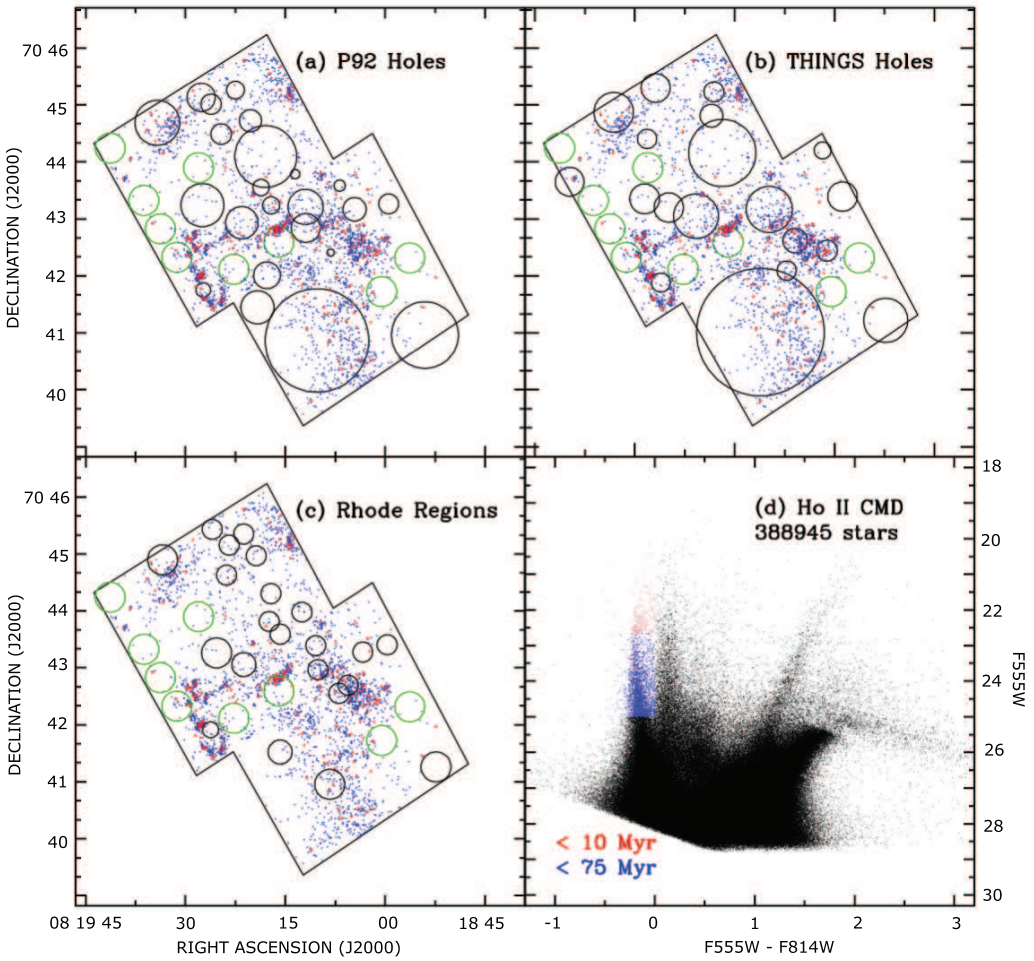

Figure 6.27 The spatial distribution of young MS stars (red < 10 Myr, blue < 75 Myr) plotted over (a) HI holes from the Puche et al. (1992) catalog; (b) HI holes from the THINGS catalog (Bagetakos et al., 2009); (c) photometric apertures of Rhode et al. (1999); Panel (d) is the CMD of the entire galaxy of Ho II with the young MS stars color-coded to match the spatial distributions with MS stars < 10 Myr in age in red and < 75 Myr in blue. Note the tendency of the red points to appear highly clustered, while the blue points are more widely distributed. Further, note that most of the HI holes do not contain highly clustered regions of young stars, rather these are found near the edges of the holes or near HI peaks.

Quantitative modeling of the impact of the complex scenarios presented by multiple generations of SF inside HI holes has yet to be carried out in detail. Presently, the single blast approximation and kinematic age estimations of HI holes are dependent upon quantities (e.g., expansion velocity, volume density) that likely have varied over the history of a given hole. Quantifying the precise impact of these parameters on HI hole formation and energetics is beyond the scope of this paper. For example, while why control fields and HI holes contain similar stellar populations, but vastly different HI column densities, is an open question. However, Ho II may not be the best galaxy to answer this question, because we are not sensitive to HI hole smaller than $\sim$ 100 pc. Thus, if it is the case that larger holes are mergers of multiple smaller holes, we simply may not be sensitive to the small holes forming inside the control fields. Analysis similar to that presented in this paper using galaxies with smaller resolvable HI holes (e.g., LMC or SMC) along with computer modeling that accounts for the effects of an anisotropic ISM and multiple generations of SNe could lend insight into the fundamental physical processes that are responsible for shaping the ISM and driving HI hole formation.

6.5.3 HI Holes in the Outer Regions of Ho II

Of particular interest to Rhode et al. (1999) are the presence of HI holes outside the the optical body of the galaxy. While they do not rule out the possibility that the inner holes could have formed from SF, the typical HI densities in the outer regions of Ho II are relatively low, which is not very conducive to SF (Kennicutt, 1989). However, the properties of holes in outer regions of galaxies do not differ from those in inner regions (Brinks & Bajaja, 1986; Puche et al., 1992; Hatzidimitriou et al., 2005; Bagetakos et al., 2009), suggesting that the same underlying mechanism, namely stellar feedback, is responsible for HI holes in both environments. To this end, we used a Monte Carlo method to compute expected stellar populations in the outer holes of Ho II to see if their creation via stellar feedback is possible.

From E_{Hole} we can calculate the SFR over the kinematic age, SFR_{KA}, for a typical outer HI hole and then use it to construct simulated CMDs to determine properties of the expected stellar populations. We find that the 19 holes from Bagetakos et al. (2009) located outside our ACS coverage have a mean diameter $\sim$ 800 pc, an expansion velocity $\sim$ 8 km s^{-1}, a kinematic age $\sim$ 50 Myr, an HI volume density of 0.1 cm^{-3},

and $E_{Hole} \sim 100 \times 10^{50}$ erg. Assuming 10^{51} erg per SN (McCray & Kafatos, 1987) and that 10% of this energy goes into moving the ISM (Theis et al., 1992; Cole et al., 1994; Padoan et al., 1997; Thornton et al., 1998), ~ 100 SN are needed to create an HI hole with these properties, equivalent to a SN rate over the kinematic age of $\sim 10^{-6}$ SN yr^{-1}. Assuming that the SNe come from stars with M $>$ 8 M$_{\odot}$, we find SFR$_{KA} \sim 2\times10^{-5}$ M$_{\odot}$ yr^{-1} for all stars, using our standard IMF (§6.3.2). This SFR implies an integrated stellar mass of $\sim 10^3$ M$_{\odot}$ over the kinematic age.

With this SFR as input, we constructed simulated CMDs, via a Monte Carlo process using either a constant or a burst model. The input for the constant SFR model had a SFR = 2×10^{-5} M$_{\odot}$ yr^{-1} from 50 Myr to 100 Myr. This focuses on the brightest stars and most recent SF likely to have created the HI hole. The burst model assumed a burst of SF 50 Myr ago, producing 1000 M$_{\odot}$. We ran each simulation 100 times to account for the statistical fluctuations. For the constant model, we find that the average CMD of the remnant stars has ~ 7 stars and an integrated magnitude of m$_{F555W} = 24.00$, assuming a limiting photometric depth equal to the 50% completeness limit (Weisz et al., 2008). For the burst model, the average CMD of the remnant stars had ~ 8 stars and a integrated magnitude of m$_{F555W} = 23.75$. Both cases results in integrated magnitudes fainter than the predictions by Rhode et al. (1999) as well as the hole and control fields presented in this paper. The remnant stellar populations in the outer holes are likely only detectable with deep photometry of resolved stars.

Other common methods of searching for stellar populations inside HI holes include the use of Hα, 24μm, and UV imaging (e.g., Puche et al., 1992; Stewart et al., 2000; Muller et al., 2003). UV traces a stellar population with initial masses $\gtrsim 3$ M$_{\odot}$ and time scales of ~ 100 Myr, while Hα (and 24μm in more dusty environments) traces ionizing photons from MS stars with initial masses of $\gtrsim 20$ M$_{\odot}$ and ages $\lesssim 10$ Myr (see Kennicutt, 1998, for a full review of different SFR indicators and their properties). A number of studies aimed at testing the stellar feedback theory of hole creation via this type of imaging have have done so with a mixed degree of success (Puche et al., 1992; Kim et al., 1999; Rhode et al., 1999; Stewart et al., 2000; Muller et al., 2003; Cannon et al., 2005; Book et al., 2008). Given the low SFRs we have derived ($10^{-4} - 10^{-5}$ M$_{\odot}$ yr^{-1}) within many of the HI holes, it is not entirely surprising that these imaging techniques have yielded such mixed results. Simulations have shown that for SFRs below $\sim 10^{-4}$ M$_{\odot}$

yr^{-1} stochastic processes become important and Hα is no longer a reliable tracer of SF (Tremonti et al., 2007; Thilker et al., 2007; Meurer et al., 2009). Although a similar study in the UV has yet to be conducted, given the small number of stars expected in any given CMD, it is likely that the UV has a similar cut-off SFR. Indeed, Stewart et al. (2000) used FUV imaging of Ho II to show that there is some agreement between HI hole locations and bright UV regions, but did not find a good one to one correlation.

We can test for UV-bright stellar populations within the outer holes using data from the Local Volume Legacy sample (Lee et al., 2008; Dale et al., 2009), which contains FUV and NUV imaging originating from the GALEX Nearby Galaxies Survey (Gil de Paz et al., 2007), and the Hα and 24μm images from the Spitzer Infrared Nearby Galaxies Survey (SINGS Kennicutt et al., 2003). Overlaying the HI hole and Rhode et al. (1999) aperture locations over these images, we compared the location of bright regions with known HI holes (Figures 6.28 − 6.30). Because the correlation between low SFRs and Hα, 24μm, and UV is not well understood, we are only able to make qualitative conclusions. From all the images, it is evident that there is not a one to one correlation between any of these fluxes and the stellar populations inside the HI holes as shown in the HST/ACS based CMDs. This simple test demonstrates that deep photometry is necessary to understand the formation and histories of HI holes.

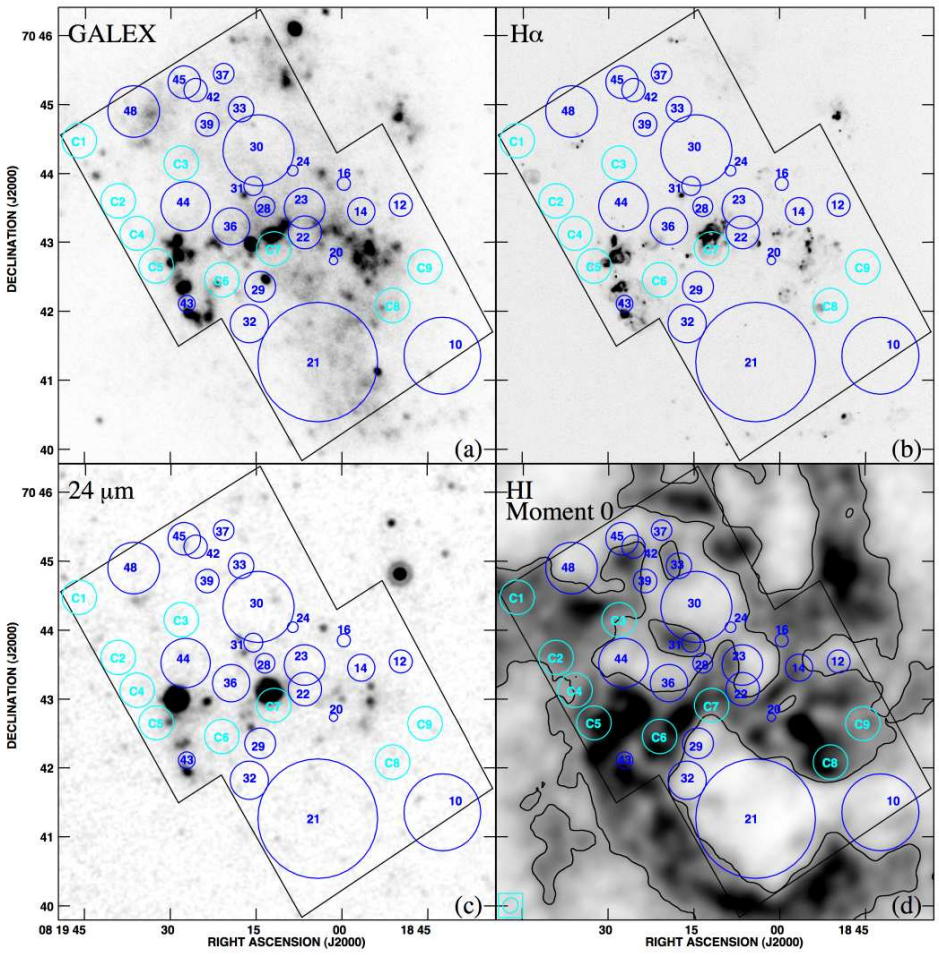

Figure 6.28 HI holes of Puche et al. (1992) (blue) and control fields (cyan) overlaid on Ho II images of (a) GALEX NUV (Gil de Paz et al., 2007); (b) LVL Hα (Lee et al., 2008); (c) SINGS 24μm Kennicutt et al. (2003); (d) THINGS HI (Walter et al., 2008). Despite that fact that all the HI holes contain hundreds or thousands of stars, from these images alone, it would seem that the HI holes are void of stars. At low SFRs ($< 10^{-4}$) $M_{\odot}$ yr^{-1}, it seems that these tracers of recent SF no longer reliably correlate with the underlying stellar populations (see §6.5.3 for further discussion).

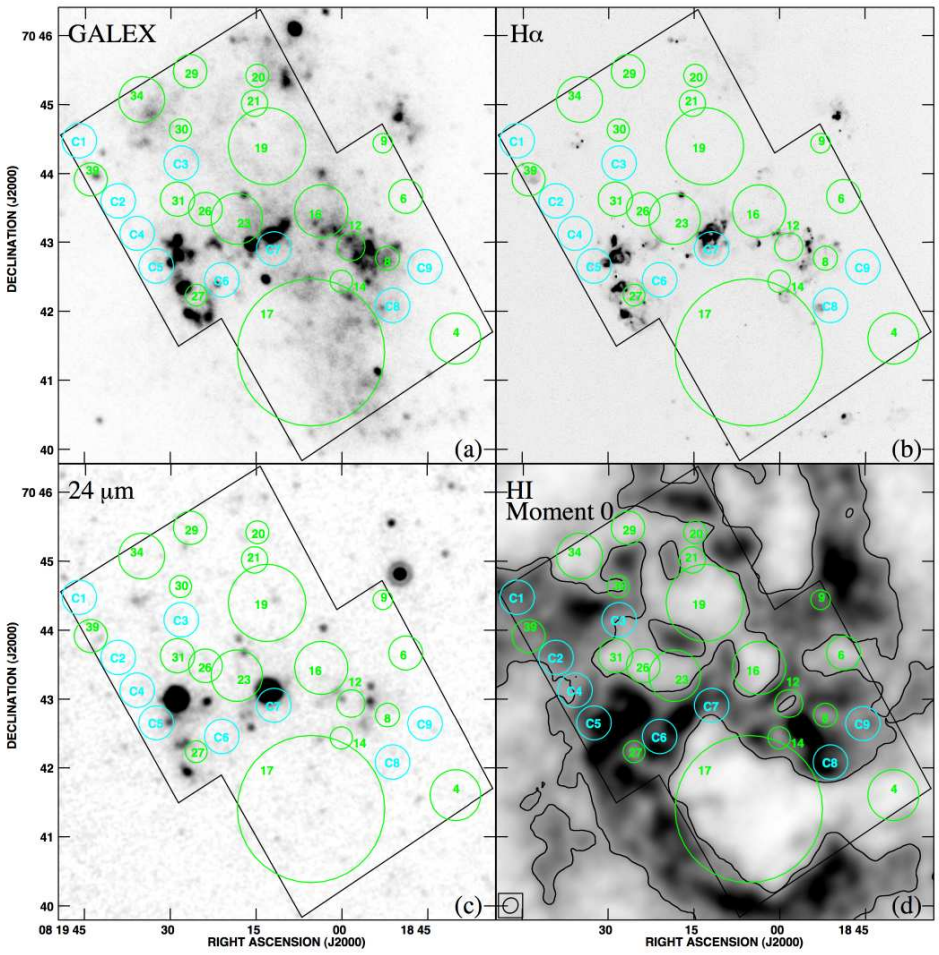

Figure 6.29 HI holes of Bagetakos et al. (2009) (green) and control fields (cyan) overlaid on Ho II images of (a) GALEX NUV (Gil de Paz et al., 2007); (b) LVL Hα (Lee et al., 2008); (c) SINGS 24μm Kennicutt et al. (2003); (d) THINGS HI (Walter et al., 2008). Despite that fact that all the HI holes contain hundreds or thousands of stars, from these images alone, it would seem that the HI holes are void of stars.At low SFRs ($< 10^{-4}$) $M_{\odot}$ yr^{-1}, it seems that these tracers of recent SF no longer reliably correlate with the underlying stellar populations (see §6.5.3 for further discussion).

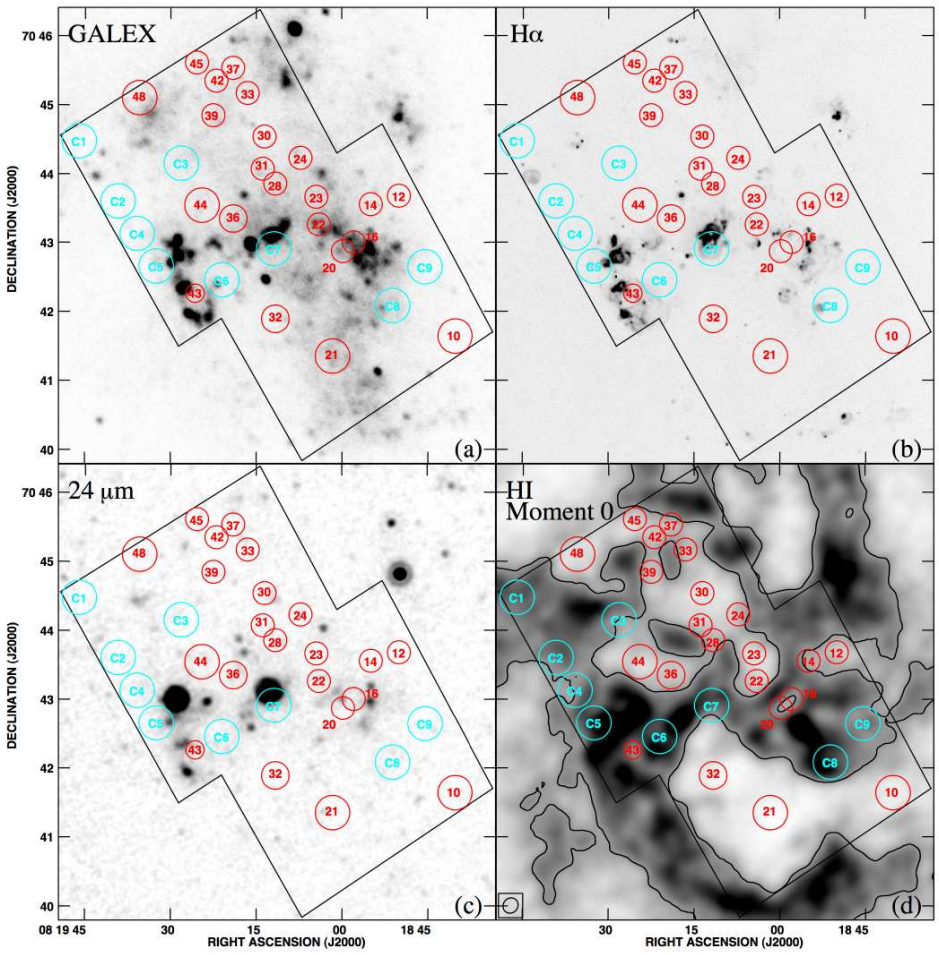

Figure 6.30 Photometric apertures of Rhode et al. (1999) (red) and control fields (cyan) overlaid on Ho II images of (a) GALEX NUV (Gil de Paz et al., 2007); (b) LVL Hα (Lee et al., 2008); (c) SINGS 24μm Kennicutt et al. (2003); (d) THINGS HI (Walter et al., 2008). Despite that fact that all the HI holes contain hundreds or thousands of stars, from these images alone, it would seem that the HI holes are void of stars. At low SFRs ($< 10^{-4}$) $M_{\odot}$ yr^{-1}, it seems that these tracers of recent SF no longer reliably correlate with the underlying stellar populations (see §6.5.3 for further discussion).

6.5.4 Comparison with the SMC and LMC

Perhaps the biggest challenge to the stellar feedback model of HI hole creation comes from observations of some of the closest galaxies. The proximity of the SMC and LMC allow for detailed observations, including high resolution HI imaging, which probes physical scales as small as $\sim$ 15 pc (Kim et al., 1999). Matching catalogs of young stellar objects (e.g., OB associations, supergiants, WR stars) and Hα imaging to HI hole catalogs, three recent studies of the LMC (Kim et al., 1999), the SMC (Hatzidimitriou et al., 2005), and the Magellanic Bridge (Muller et al., 2003) do not find strong correlations between the locations of young stellar objects and HI holes. The largest challenge to the stellar feedback creation hypothesis posed by these studies are the presence of young HI holes ($\sim$ 2$-$10 Myr) with no associated young stellar objects (Stanimirović, 2007). This is particularly problematic in the SMC, where Hatzidimitriou et al. (2005) identified 59 young holes ($\sim$ 5 $-$ 10 Myr) that appear to be void of young stellar objects. Hatzidimitriou et al. (2005) further find that the physical characteristics of these particular holes are no different than those with stellar components. Further, Hatzidimitriou et al. (2005) conclude that the properties of the HI holes in the inner and outer region are indistinguishable and that from their analysis there is no evidence to suspect a different creation mechanism for inner and outer holes.

Using the same type of analysis as in §6.5.3, and the assumption that inner and outer holes are indistinguishable in their HI properties Hatzidimitriou et al. (2005), we can compute the properties of the expected stellar populations if these young holes were formed due to stellar feedback. For the 59 empty HI holes in the SMC, we find that the mean size is $\sim$ 128 pc, the expansion velocity is 7.5 km s^{-1}, and the inferred kinematic age is 8 Myr. We also compute $E_{Hole} \sim 56 \times 10^{50}$, assuming an HI volume density of 1.0 cm^{-3}, and find that SFR$_{KA} = 7\times10^{-5}$ M$_\odot$ yr^{-1}. We simulate 100 CMDs assuming a distance modulus of 19, photometric completeness limits of $m_V = 22$ and $m_I = 21.7$ (Harris & Zaritsky, 2004), and the parameters listed in §6.3.2 We chose to only consider a burst model of SF at 8 Myr, since the differences between a burst and constant model of SF over such a short time scale are minimal. We ran 100 simulations, to account for small number statistics, and found that the typical CMD contained $\sim$ 40 stars (within the completeness limits) and the mean magnitude of the brightest star in the CMD was $m_{F555W} \sim 14.80$. We found that only 25 out of the 100 simulated CMDs contained at

least one star with $m_{F555W} < 14$, i.e., a bright OB type star. For $m_{F555W} < 15$, we found 72 CMDs contained at least one such star. This test signifies that for a episode of SF 8 Myr ago, only 25% of the time we would expect to find a star brighter than $m_{F555W} = 14$, and 72% of the time for $m_{F555W} = 15$.

Applying these statistics to the 509 holes cataloged by Hatzidimitriou et al. (2005), we expect 128 HI holes with at least one star brighter than $m_{F555W} = 14$, or 367 holes for $m_{F555W} = 15$. In comparison, Hatzidimitriou et al. (2005) find 330 HI holes with at least one star cluster, young star, or WR star. Initially, they also found 80 holes that appeared void of stars, however follow up observations revealed that 21 of the 80 holes appeared to have A spectral-type stars, leaving 59 holes without detected stellar companions, which is consistent with the 143 of holes we predict will appear void of MS stars at $m_{F555W} = 15$. The uncertainties in our calculation are at least 50%, due to uncertainties in E_{Hole}, the stellar evolution models, and statistical error. Further, we are not able to test out results directly as we cannot reasonably compare our predicted stellar populations to the various catalogs used for correlations by Hatzidimitriou et al. (2005). However, we have demonstrated that even without the detection of a bright object inside a young HI hole, it is possible that the hole was created by stellar feedback.

6.6 Conclusions

In summary:

- The HST/ACS based CMDs of stars within HI holes from the catalogs of Puche et al. (1992) and Bagetakos et al. (2009) revealed significant stellar populations, including young MS and BHeBs with ages less than $\sim$ 50 Myr, in *all* holes. We found that $\ll 1\%$ of the stars in the composite stellar population of either holes catalog were luminous MS stars less than $\sim$ 10 Myr in age. This indicates that young OB associations are not reliable tracers of the locations of HI holes.

- We searched for differences in the stellar populations inside HI holes and those in selected control fields, regions similar in size to holes, but that span a wide range in HI column density. We found that, on average, the control fields have twice as many luminous (i.e., young) MS stars as the HI holes, however this is consistent

with statistical fluctuations from small number statistics tests. We measured the SFHs and cumulative SFHs of both samples (holes and control fields) and found no significant differences. However, because we are not sensitive to holes less than $\sim$ 100 pc in size, it could be that smaller holes are already forming in control fields. Only further similar studies involving an even wider range of hole sizes (e.g., SMC or LMC) can address this question with the requisite level of precision.

- Using the SFHs for stars in each hole as input into STARBURST99, we calculated the energy associated with SF over the past 200 Myr. From this we computed the energy input over the inferred kinematic age of each hole and calculated the feedback efficiency. Compared to theoretical values, 8 of the 23 P92 and 13 of the 19 THINGS holes have efficiencies greater 20%, with several exceeding 100%. Looking at the energy profiles over the last 200 Myr, we found that stellar feedback did produce enough energy, in principle, to have created all the HI holes, just not necessarily within the inferred kinematic age. This finding suggests that the inferred kinematic age (which is poorly constrained from observations) may not represent the true age of an individual HI hole. Indeed, the concept of an age for an HI hole created by multiple generations of SF is intrinsically ambiguous.

- Using the BHeBs from the full HST/ACS CMD of Ho II, we constructed two spatially resolved recent SFH movies of Ho II with look back times of $\sim$ 100 Myr and $\sim$ 200 Myr. Comparing these movies with the HI distribution, we found that low levels of SF have been common, and only in the past $\sim$ 40 Myr has the SF rate elevated significantly. Since many of the holes are older than $\sim$ 40 Myr, this suggests that holes are formed through a series of small SF events as opposed to a larger event at a single epoch.

- From the HST/ACS photometry, we constructed CMDs corresponding to the apertures used by Rhode et al. (1999). In all cases, we found mixed age stellar populations of hundreds or thousands of stars. Using Monte Carlo tests of synthetic CMDs and empirical comparisons from the HST/ACS photometry, we demonstrated that integrated light does not accurately trace the SFHs of stellar populations inside HI holes. We also show that young MS stars ($<$ 75 Myr) are not highly clustered, which may imply that the single age stellar cluster method of

HI formation is not the most likely model. This assumption can account for why Rhode et al. (1999) did not detect a greater number of holes with stars inside.

- Using the Monte Carlo technique, we computed expected stellar populations for HI holes outside the optical body of Ho II and found that low levels of SF ($\sim 10^{-5}$ $M_{\odot}$) could account for the presence of those holes. The remnant populations would be quite faint as only a handful of young stars would remain to be seen at the present time. We also examine the use of other SF tracers, Hα, 24μm, and UV, and find that at such low SFRs, they do not reliably correlate with the stellar populations of HI holes.

- We applied similar analysis to the 59 young ($\sim$ 8 Myr) HI holes that appear empty in the SMC (Hatzidimitriou et al., 2005), finding $SFR_{KA} = 7{\times}10^{-5}$ $M_{\odot}$ yr^{-1}. Using the integrated stellar mass, we assume a burst of SFH at 8 Myr, and construct 100 simulated CMDs. The resulting synthetic stellar populations show that only 25% of the CMDs have at least one MS stars brighter than $m_{F555W} = 14$ and 72% have at least one MS star brighter than $m_{F555W} = 15$. Applying this to the 509 holes in the sample, we expect 128 HI holes with at least one bright star in the 25% case, 367 holes in the 72% case, and 143 holes to be without any MS star brighter than $m_{F555W} = 15$. Hatzidimitriou et al. (2005) find 330 holes that have at least one bright object, and 59 HI holes that do not have any objects. While this comparison is subject to large uncertainties, it demonstrates the plausibility of a stellar feedback origin for young HI holes without a bright stellar companion.

The evidence presented by the HST/ACS observations of Ho II suggests that stellar feedback provides enough energy, in principle, to create the observed HI holes in Ho II. The traditional theory that single epoch episodes of SF, and singled aged clusters, are responsible for HI hole creation is unlikely, because of the presence of mixed age stellar populations inside all of the holes, including holes with younger inferred ages. The conclusions of Rhode et al. (1999) and those in this paper are not contradicting, rather they both seem to reinforce the idea that HI holes are not often created by single aged stellar populations. The summation of the evidence is that the likely mechanism for the creation of HI holes is stellar feedback from SNe due to multiple generations of SF. An important caveat is found in the similarity of the stellar populations in control fields

and the HI holes. While this detracts from the potential casual relationship between stellar feedback and HI hole creation, this result could simply be explained by the fact that we are not sensitive to holes smaller than $\sim$ 100 pc. Applying similar analysis to galaxies with a wider range in HI holes sizes (e.g., SMC or LMC) could reveal the extent of this effect and provide further insight into the potential link between stellar feedback and the formation and growth of HI holes.

References

Aloisi, A., Tosi, M., & Greggio, L. 1999, AJ, 118, 302

Aloisi, A., van der Marel, R. P., Mack, J., Leitherer, C., Sirianni, M., & Tosi, M. 2005, ApJL, 631, L45

Angeretti, L., Tosi, M., Greggio, L., Sabbi, E., Aloisi, A., & Leitherer, C. 2005, AJ, 129, 2203

Aparicio, A., & Hidalgo, S. L. 2009, AJ, 138, 558

Babul, A., & Ferguson, H. C. 1996, ApJ, 458, 10

Bagetakos, I., Brinks, E., Walter, F., de Blok, W. J. G., Rich, J. W., Usero, A., & Kennicutt, R. C., Jr. 2009, submitted.

Barnes, J. E., & Hernquist, L. 1992, Nature, 360, 715

Bastian, N., Gieles, M., Ercolano, B., & Gutermuth, R. 2009, MNRAS, 392, 868

Begum, A., Chengalur, J. N., Karachentsev, I. D., Kaisin, S. S., & Sharina, M. E. 2006, MNRAS, 365, 1220

Begum, A., Chengalur, J. N., Karachentsev, I. D., Sharina, M. E., & Kaisin, S. S. 2008, MNRAS, 386, 1667

Belokurov, V., et al. 2006, ApJL, 647, L111

Bertelli, G., Bressan, A., Chiosi, C., Fagotto, F., & Nasi, E. 1994, A&AS, 106, 275

Binggeli, B. 1986, Star-forming Dwarf Galaxies and Related Objects, 53

Binggeli, B. 1994, Panchromatic View of Galaxies. Their Evolutionary Puzzle, 173

Blanton, M. R., et al. 2001, AJ, 121, 2358

Book, L. G., Chu, Y.-H., & Gruendl, R. A. 2008, ApJS, 175, 165

Bouchard, A., Da Costa, G. S., & Jerjen, H. 2009, AJ, 137, 3038

Boyce, P. J., et al. 2001, ApJL, 560, L127

Brinks, E., & Bajaja, E. 1986, A&A, 169, 14

Brinks, E., & Burton, W. B. 1984, A&A, 141, 195

Bullock, J. S., Kravtsov, A. V., & Weinberg, D. H. 2000, ApJ, 539, 517

Bureau, M., & Carignan, C. 2002, AJ, 123, 1316

Bureau, M., Walter, F., van Gorkom, J., & Carignan, C. 2004, Recycling Intergalactic and Interstellar Matter, 217, 452

Caldwell, N., Armandroff, T. E., Da Costa, G. S., & Seitzer, P. 1998, AJ, 115, 535

Calzetti, D., et al. 2007, ApJ, 666, 870

Cannon, J. M., Dohm-Palmer, R. C., Skillman, E. D., Bomans, D. J., Côté, S., & Miller, B. W. 2003, AJ, 126, 2806

Cannon, J. M., et al. 2005, ApJL, 630, L37

Cash, W., Charles, P., Bowyer, S., Walter, F., Garmire, G., & Riegler, G. 1980, ApJL, 238, L71

Chandar, R., Leitherer, C., Tremonti, C. A., Calzetti, D., Aloisi, A., Meurer, G. R., & de Mello, D. 2005, ApJ, 628, 210

Chevalier, R. A. 1974, ApJ, 188, 501

Chiboucas, K., Karachentsev, I. D., & Tully, R. B. 2009, AJ, 137, 3009

Chu, Y.-H. 2008, IAU Symposium, 250, 341

Cignoni, M., & Tosi, M. 2010, Advances in Astronomy, 2010

Cole, S., Aragon-Salamanca, A., Frenk, C. S., Navarro, J. F., & Zepf, S. E. 1994, MNRAS, 271, 781

Cole, A. A., Tolstoy, E., Gallagher, J. S., III, & Smecker-Hane, T. A. 2005, AJ, 129, 1465

Cole, A. A., et al. 2007, ApJL, 659, L17

Côté, S., Freeman, K. C., Carignan, C., & Quinn, P. J. 1997, AJ, 114, 1313

Côté, S., Draginda, A., Skillman, E. D., & Miller, B. W. 2009, AJ, 138, 1037

Cowie, L. L., Songaila, A., Hu, E. M., & Cohen, J. G. 1996, AJ, 112, 839

da Costa, G. S. 2007, From Stars to Galaxies: Building the Pieces to Build Up the Universe, 374, 247

Dalcanton, J. J., et al. 2009, ApJS, 183, 67

Dalcanton, J. J., et al. 2010, In Prep.

Dale, D., et al. 2009, accepted to ApJ

de Vaucouleurs G., de Vaucouleurs A., Corwin H.G., Buta R.J., Paturel G., & Fouque P., 1991, Third Reference Catalog of Bright Galaxies (New York: Springer)

Dekel, A., & Silk, J. 1986, ApJ, 303, 39

Dekel, A., & Woo, J. 2003, MNRAS, 344, 1131

Denicoló, G., Terlevich, R., & Terlevich, E. 2002, MNRAS, 330, 69

Dellenbusch, K. E., Gallagher, J. S., III, Knezek, P. M., & Noble, A. G. 2008, AJ, 135, 326

Deul, E. R., & den Hartog, R. H. 1990, A&A, 229, 362

Dib, S., & Burkert, A. 2005, ApJ, 630, 238

Dijkstra, M., Haiman, Z., Rees, M. J., & Weinberg, D. H. 2004, ApJ, 601, 666

Dohm-Palmer, R. C., et al. 1997, AJ, 114, 2527

Dohm-Palmer, R. C., & Skillman, E. D. 2002, AJ, 123, 1433

Dohm-Palmer, R. C., Skillman, E. D., Mateo, M., Saha, A., Dolphin,A., Tolstoy, E., Gallagher, J. S., & Cole, A. A. 2002, AJ, 123, 813

Dolphin, A. E. 2000, PASP, 112, 1383

Dolphin, A. E. 2002, MNRAS, 332, 91

Dolphin, A. E., et al. 2003, AJ, 126, 187

Dolphin, A. E., Weisz, D. R., Skillman, E. D., & Holtzman, J. A. 2005, ArXiv Astrophysics e-prints, arXiv:astro-ph/0506430

Dolphin, A. E., et al., 2010, In Prep.

Dressler, A. 1980, ApJ, 236, 351

Duc, P.-A., Brinks, E., Wink, J. E., & Mirabel, I. F. 1997, A&A, 326, 537

Duc, P.-A., Brinks, E., Springel, V., Pichardo, B., Weilbacher, P., & Mirabel, I. F. 2000, AJ, 120, 1238

Dunkley, J., et al. 2009, ApJS, 180, 306

Efstathiou, G. 1992, MNRAS, 256, 43P

Ellis, R. S. 1997, ARA&A, 35, 389

Elmegreen, B. G. 1997, ApJ, 477, 196

Ferrara, A., & Tolstoy, E. 2000, MNRAS, 313, 291

Ford, H. C., et al. 1998, , 3356, 234

Gallart, C., Aparicio, A., Bertelli, G., & Chiosi, C. 1996, AJ, 112, 1950

Gallart, C., Zoccali, M., & Aparicio, A. 2005, ARA&A, 43, 387

Gallart, C., & The Lcid Team 2007, IAU Symposium, 241, 290

Geha, M., Blanton, M. R., Masjedi, M., & West, A. A. 2006, ApJ, 653, 240

Gerola, H., & Seiden, P. E. 1978, ApJ, 223, 129

Gieles, M., Bastian, N., & Ercolano, B. 2008, MNRAS, 391, L93

Gilbert, K., et al. 2010, In Prep.

Girardi, L., Bertelli, G., Bressan, A., Chiosi, C., Groenewegen, M. A. T., Marigo, P., Salasnich, B., & Weiss, A. 2002, A&A, 391, 195

Girardi, L., et al. 2010, In Prep.

Gnedin, O. Y. 1999, Ph.D. Thesis

Gnedin, N. Y. 2000, ApJ, 542, 535

Gil de Paz, A., et al. 2007, ApJS, 173, 185

Gogarten, S. M., et al. 2010, ApJ, 712, 858

Grebel, E. K. 1997, Reviews in Modern Astronomy, 10, 29

Grebel, E. K., Gallagher, J. S., III, & Harbeck, D. 2003, AJ, 125, 1926

Harris, J., & Zaritsky, D. 2001, ApJS, 136, 25

Harris, J., & Zaritsky, D. 2004, AJ, 127, 1531

Harris, J., & Zaritsky, D. 2008, Publications of the Astronomical Society of Australia, 25, 116

Hatzidimitriou, D., Stanimirovic, S., Maragoudaki, F., Staveley-Smith, L., Dapergolas, A., & Bratsolis, E. 2005, MNRAS, 360, 1171

Heiles, C. 1979, ApJ, 229, 533

Heiles, C. 1990, ApJ, 354, 483

Hernandez, X., Valls-Gabaud, D.,& Gilmore, G. 1999, MNRAS, 304, 705

Hodge, P. 1989, ARA&A, 27, 139

Holtzman, J. A., Burrows, C. J., Casertano, S., Hester, J. J., Trauger, J. T., Watson, A. M., & Worthey, G. 1995, PASP, 107, 1065

Holtzman, J. A., et al. 1999, AJ, 118, 2262

Holtzman, J. A., Afonso, C., & Dolphin, A. 2006, ApJS, 166, 534

Hubble, E. P. 1926, ApJ, 64, 321

Hunter, D. A., & Wilcots, E. M. 2002, AJ, 123, 2449

Huchtmeier, W. K., Karachentsev, I. D., Karachentseva, V. E., & Ehle, M. 2000, A&AS, 141, 469

Ikuta, C., & Arimoto, N. 2002, A&A, 391, 55

Irwin, M. J., et al. 2007, ApJL, 656, L13

Jackson, D. C., Cannon, J. M., Skillman, E. D., Lee, H., Gehrz, R. D., Woodward, C. E., & Polomski, E. 2006, ApJ, 646, 192

Kamphuis, J., Sancisi, R., & van der Hulst, T. 1991, A&A, 244, L29

Karachentsev, I. D., et al. 2002, A&A, 383, 125

Karachentsev, I. D., et al. 2003, A&A, 404, 93

Karachentsev, I. D., Karachentseva, V. E., Huchtmeier, W. K., & Makarov, D. I. 2004, AJ, 127, 2031

Karachentsev, I. D., et al. 2006, AJ, 131, 1361

Karachentsev, I. D., & Kaisin, S. S. 2007, AJ, 133, 1883

Kauffmann, G., Li, C., & Heckman, T. M. 2010, arXiv:1005.1825

Kennicutt, R. C., Jr. 1984, ApJ, 287, 116

Kennicutt, R. C., Jr. 1989, ApJ, 344, 685

Kennicutt, R. C., Jr. 1998, ARA&A, 36, 189

Kennicutt, R. C., Jr., et al. 2003, PASP, 115, 928

Kennicutt, R. C., Jr., et al. 2007, ApJ, 671, 333

Kennicutt, R. C., Jr., Lee, J. C., Funes, S. J., José G., Sakai, S., & Akiyama, S. 2008, ApJS, 178, 247

Kellman, S. A. 1970, Ph.D. Thesis

Kereš, D., Katz, N., Weinberg, D. H., & Davé, R. 2005, MNRAS, 363, 2

Kim, S., Dopita, M. A., Staveley-Smith, L., & Bessell, M. S. 1999, AJ, 118, 2797

Koekemoer, A. M., Fruchter, A. S., Hook, R. N., & Hack, W. 2002, The 2002 HST Calibration Workshop : Hubble after the Installation of the ACS and the NICMOS Cooling System, Proceedings of a Workshop held at the Space Telescope Science Institute, Baltimore, Maryland, October 17 and 18, 2002. Edited by Santiago Arribas, Anton Koekemoer, and Brad Whitmore. Baltimore, MD: Space Telescope Science Institute, 2002., p.337, 337

Koribalski, B., Gordon, S., & Jones, K. 2003, MNRAS, 339, 1203

Klypin, A., Kravtsov, A. V., Valenzuela, O., & Prada, F. 1999, ApJ, 522, 82

Lada, C. J., & Lada, E. A. 2003, ARA&A, 41, 57

Lee, J. C., et al. 2008, Astronomical Society of the Pacific Conference Series, 396, 151

Lee, J. C., Kennicutt, R. C., Funes, S. J., José G., Sakai, S., & Akiyama, S. 2007, ApJL, 671, L113

Lee, J.C. 2006, University of Arizona, Ph.D. Thesis

Lee, J. C., et al. 2009, ApJ, 706, 599

Lee, H., Grebel, E. K., & Hodge, P. W. 2003, A&A, 401, 141

Lee, M. G., Freedman, W. L., & Madore, B. F. 1993, ApJ, 417, 553

Leitherer, C., et al. 1999, ApJS, 123, 3

Loeb, A., & Perna, R. 1998, ApJL, 503, L35

Mac Low, M.-M., & Ferrara, A. 1999, ApJ, 513, 142

Madau, P., Ferguson, H. C., Dickinson, M. E., Giavalisco, M., Steidel, C. C., & Fruchter, A. 1996, MNRAS, 283, 1388

Makarova, L. N., et al. 2002, A&A, 396, 473

Marcolini, A., D'Ercole, A., Brighenti, F., & Recchi, S. 2006, MNRAS, 371, 643

Marigo, P., Girardi, L., Bressan, A., Groenewegen, M. A. T., Silva, L., & Granato, G. L. 2008, A&A, 482, 883

Masegosa, J., Moles, M., & del Olmo, A. 1991, A&A, 249, 505

Mateo, M. L. 1998, ARA&A, 36, 435

Mayer, L., Governato, F., Colpi, M., Moore, B., Quinn, T., Wadsley, J., Stadel, J., & Lake, G. 2001, ApJL, 547, L123

Mayer, L., Governato, F., Colpi, M., Moore, B., Quinn, T., Wadsley, J., Stadel, J., & Lake, G. 2001, ApJ, 559, 754

Mayer, L., & Moore, B. 2004, MNRAS, 354, 477

Mayer, L., Mastropietro, C., Wadsley, J., Stadel, J., & Moore, B. 2006, MNRAS, 369, 1021

Mayer, L. 2010, Advances in Astronomy, 2010

McCray, R., & Kafatos, M. 1987, ApJ, 317, 190

McQuinn, K. B. W., Skillman, E. D., Cannon, J. M., Dalcanton, J. J., Dolphin, A., Stark, D., & Weisz, D. 2009, ApJ, 695, 561

McQuinn, K. B. W., et al. 2010, Submitted

Meurer, G. R., et al. 2009, ApJ, 695, 765

Mighell, K. J. 1997, AJ, 114, 1458

Miller, B. W., Dolphin, A. E., Lee, M. G., Kim, S. C., & Hodge, P. 2001, ApJ, 562, 713

Miller, B. W., & Hodge, P. 1994, ApJ, 427, 656

Miller, B. W., & Hodge, P. 1996, ApJ, 458, 467

Momany, Y., et al. 2005, A&A, 439, 111

Monelli, M., et al. 2010, arXiv:1002.4300

Mori, M., Ferrara, A., & Madau, P. 2002, ApJ, 571, 40

Mueller, M. W., & Arnett, W. D. 1976, ApJ, 210, 670

Muller, E., Staveley-Smith, L., Zealey, W., & Stanimirović, S. 2003, MNRAS, 339, 105

Navarro, J. F., & Steinmetz, M. 1997, ApJ, 478, 13

Oey, M. S., & Massey, P. 1995, ApJ, 452, 210

Oey, M. S., & Clarke, C. J. 1997, MNRAS, 289, 570

Oey, M. S., Groves, B., Staveley-Smith, L., & Smith, R. C. 2002, AJ, 123, 255

Oey, M. S., Watson, A. M., Kern, K., & Walth, G. L. 2005, AJ, 129, 393

Oh, S.-H., de Blok, W. J. G., Walter, F., Brinks, E., & Kennicutt, R. C. 2008, AJ, 136, 2761

Orban, C., Gnedin, O. Y., Weisz, D. R., Skillman, E. D., Dolphin, A. E., & Holtzman, J. A. 2008, ApJ, 686, 1030

Östlin, G. 2000, ApJL, 535, L99

Ott, J., Walter, F., Brinks, E., Van Dyk, S. D., Dirsch, B., & Klein, U. 2001, AJ, 122, 3070

Ott, J., Skillman, E., Dalcanton, J., Walter, F., Stilp, A., Koribalski, B., West, A., & Warren, S. 2008, The Evolution of Galaxies Through the Neutral Hydrogen Window, 1035, 105

Padoan, P., Jimenez, R., & Jones, B. 1997, MNRAS, 285, 711

Pasquali, A., et al. 2008, ApJ, 687, 1004

Pflamm-Altenburg, J., Weidner, C., & Kroupa, P. 2007, ApJ, 671, 1550

Pelupessy, F. I., van der Werf, P. P., & Icke, V. 2004, A&A, 422, 55

Peñarrubia, J., McConnachie, A. W., & Navarro, J. F. 2008, ApJ, 672, 904

Perlmutter, S., et al. 1998, Nature, 391, 51

Puche, D., Westpfahl, D., Brinks, E., & Roy, J.-R. 1992, AJ, 103, 1841

Recchi, S., & Hensler, G. 2006, A&A, 445, L39

Relaño, M., Beckman, J. E., Daigle, O., & Carignan, C. 2007, IAU Symposium, 237, 467

Reddy, N. A., Steidel, C. C., Pettini, M., Adelberger, K. L., Shapley, A. E., Erb, D. K., & Dickinson, M. 2008, ApJS, 175, 48

Revaz, Y., et al. 2009, A&A, 501, 189

Rhode, K. L., Salzer, J. J., Westpfahl, D. J., & Radice, L. A. 1999, AJ, 118, 323

Ricotti, M., & Gnedin, N. Y. 2005, ApJ, 629, 259

Sabbi, E., Gallagher, J. S., Smith, L. J., de Mello, D. F., & Mountain, M. 2008, ApJL, 676, L113

Sakai, S., & Madore, B. F. 2001, ApJ, 555, 280

Salpeter, E. E. 1955, ApJ, 121, 161

Sánchez-Salcedo, F. J. 2002, Revista Mexicana de Astronomia y Astrofisica, 38, 39

Sancisi, R., Fraternali, F., Oosterloo, T., & van der Hulst, T. 2008, A&AR, 15, 189

Scalo, J. M. 1986, Fundamentals of Cosmic Physics, 11, 1

Schlegel, D. J., Finkbeiner, D. P., & Davis, M. 1998, ApJ, 500, 525

Schmidt, B. P., et al. 1998, ApJ, 507, 46

Silich, S., Lozinskaya, T., Moiseev, A., Podorvanuk, N., Rosado, M., Borissova, J., & Valdez-Gutierrez, M. 2006, A&A, 448, 123

Simon, J. D., & Geha, M. 2007, ApJ, 670, 31

Skillman, E. D., Terlevich, R., Teuben, P. J., & van Woerden, H. 1988, A&A, 198, 33

Skillman, E. D., Terlevich, R. J., Kennicutt, R. C., Jr., Garnett, D. R., & Terlevich, E. 1994, ApJ, 431, 172

Skillman, E. D., & Bender, R. 1995, Revista Mexicana de Astronomia y Astrofisica Conference Series, 3, 25

Skillman, E. D. 1996, The Minnesota Lectures on Extragalactic Neutral Hydrogen, 106, 208

Skillman, E. D. 1997, Revista Mexicana de Astronomia y Astrofisica Conference Series, 6, 36

Skillman, E. D., & Gallart, C. 2002, Observed HR Diagrams and Stellar Evolution, 274, 535

Skillman, E. D., Côté, S., & Miller, B. W. 2003, AJ, 125, 593

Skillman, E. D., Tolstoy, E., Cole, A. A., Dolphin, A. E., Saha, A., Gallagher, J. S., Dohm-Palmer, R. C., & Mateo, M. 2003, ApJ, 596, 253

Stanimirović, S. 2007, IAU Symposium, 237, 84

Stewart, S. G., et al. 2000, ApJ, 529, 201

Stinson, G. S., Dalcanton, J. J., Quinn, T., Kaufmann, T., & Wadsley, J. 2007, ApJ, 667, 170

Tenorio-Tagle, G., Bodenheimer, P., Rozyczka, M., & Franco, J. 1986, A&A, 170, 107

Tenorio-Tagle, G., & Bodenheimer, P. 1988, ARA&A, 26, 145

Theis, C., Burkert, A., & Hensler, G. 1992, A&A, 265, 465

Thilker, D. A., et al. 2007, ApJS, 173, 572

Thornton, K., Gaudlitz, M., Janka, H.-T., & Steinmetz, M. 1998, ApJ, 500, 95

Thomas, D., Maraston, C., Bender, R., & Mendes de Oliveira, C. 2005, ApJ, 621, 673

Thoul, A. A., & Weinberg, D. H. 1996, ApJ, 465, 608

Tolstoy, E., & Saha, A. 1996, ApJ, 462, 672

Tosi, M., Greggio, L., & Focardi, P. 1989, , 156, 295

Tremonti, C. A., Calzetti, D., Leitherer, C., & Heckman, T. M. 2001, ApJ, 555, 322

Tremonti, C. A., Lee, J. C., van Zee, L., Kennicutt, R. C., Gil de Paz, A., Sakai, S., Funes, J., & Akiyama, S. 2007, Bulletin of the American Astronomical Society, 38, 894

Tolstoy, E., & Saha, A. 1996, ApJ, 462, 672

Tolstoy, E., et al. 1998, AJ, 116, 1244

Tolstoy, E., Hill, V., & Tosi, M. 2009, ARA&A, 47, 371

Toomre, A., & Toomre, J. 1972, ApJ, 178, 623

Tosi, M., Greggio, L., & Focardi, P. 1989, Ap&SS, 156, 295

van den Bergh, S., Abraham, R. G., Ellis, R. S., Tanvir, N. R., Santiago, B. X., & Glazebrook, K. G. 1996, AJ, 112, 359

van den Bergh, S. 2000, The galaxies of the Local Group, by Sidney Van den Bergh. Published by Cambridge, UK: Cambridge University Press, 2000 Cambridge Astrophysics Series Series, vol no: 35, ISBN: 0521651816.

van der Hulst, J. M. 1979, A&A, 75, 97

van der Hulst, J. M. 1996, The Minnesota Lectures on Extragalactic Neutral Hydrogen, 106, 47

van Driel, W., Kraan-Korteweg, R. C., Binggeli, B., & Huchtmeier, W. K. 1998, A&AS, 127, 397

van Zee, L., Skillman, E. D., & Salzer, J. J. 1998, AJ, 116, 1186

van Zee, L., Salzer, J. J., Haynes, M. P., O'Donoghue, A. A., & Balonek, T. J. 1998, AJ, 116, 2805

Walter, F., Kerp, J., Duric, N., Brinks, E., & Klein, U. 1998, ApJL, 502, L143

Walter, F., & Brinks, E. 1999, AJ, 118, 273

Walter, F., & Heithausen, A. 1999, ApJL, 519, L69

Walter, F., et al. 2007, ApJ, 661, 102

Walter, F., Brinks, E., de Blok, W. J. G., Bigiel, F., Kennicutt, R. C., Thornley, M. D., & Leroy, A. 2008, AJ, 136, 2563

Weaver, R., McCray, R., Castor, J., Shapiro, P., & Moore, R. 1977, ApJ, 218, 377

Weidner, C., & Kroupa, P. 2006, MNRAS, 365, 1333

Weisz, D. R., Skillman, E. D., Cannon, J. M., Dolphin, A. E., Kennicutt, R. C., Jr., Lee, J.C.,& Walter, F. 2008, ApJ, 689,160

Weisz, D. R., Skillman, E. D., Cannon, J. M., Walter, F., Brinks, E., Ott, J., & Dolphin, A. E. 2009, ApJL, 691, L59

Weisz, D. R., et al., 2010, In Prep.

Williams, B. F., et al. 2010, ApJ, 709, 135

Williams, B. F., et al. 2010, In Prep.

Willman, B., et al. 2005, ApJL, 626, L85

Woo, J., Courteau, S., & Dekel, A. 2008, MNRAS, 390, 1453

Wyder, T. K. 2001, AJ, 122, 2490

Young, L. M., Skillman, E. D., Weisz, D. R., & Dolphin, A. E. 2007, ApJ, 659, 331

Yuk, I.-S., & Lee, M. G. 2007, ApJ, 668, 876

Yun, M. S., Ho, P. T. P., & Lo, K. Y. 1994, Nature, 372, 530

Yun, M. S. 1999, Galaxy Interactions at Low and High Redshift, 186, 81

Zucker, D. B., et al. 2004, ApJL, 612, L121

Zwicky, F. 1956, Ergebnisse der exakten Naturwissenschaften, 29, 344